THERAPEUTIC APPROACHES TO APOE

by

Lucas Kraft

A THESIS SUBMITTED IN PARTIAL FULFILLMENT OF THE REQUIREMENTS FOR THE DEGREE OF

DOCTOR OF PHILOSOPHY

in

BIOCHEMISTRY

UNIVERSITY OF SUSSEX

APRIL 2019

DECLARATION OF AUTHORSHIP

I, Lucas Kraft declare that this thesis and the work presented in it are my own and has been generated by me as the result of my own original research. I confirm that this work was done wholly while in candidature for a research degree at the University of Sussex; where any part of this thesis has previously been submitted for a degree or any other qualification at this University or any other institution, this has been clearly stated; where I have consulted the published work of others, this is always clearly attributed; where I have quoted from the work of others, the source is always given and with the exception of such quotations, this thesis is entirely my own work; I have acknowledged all main sources of help; where the thesis is based on work done by myself jointly with others, I have made clear exactly what was done by others and what I have contributed myself.

Lucas Kraft

ABSTRACT

Apolipoprotein E4 (ApoE4) is the major genetic risk factor in Alzheimer's disease (AD) and homozygous individuals are at 12-fold greater risk developing the disorder. Three ApoE isoforms exist that differ by a cysteine-arginine interchange at sites 112 and 158. While the most common ApoE3 variant has a cysteine at site 112 and an arginine at site 158, ApoE2 has two cysteines and ApoE4 two arginines, respectively. The difference in primary structure is believed to alter ApoE tertiary/quaternary structure and its function and is presumably therefore responsible for ApoE4's increased risk for AD. However, the exact mechanism whereby ApoE4 differs functionally from ApoE3 (and ApoE2) is still elusive. In this thesis, isoform dependent differences in the binding ability to heparin, a natural analogue to heparan sulphate proteoglycans (HSPGs) that are physiological receptors of ApoE and important in brain lipoprotein metabolism, as well as new ApoE tool compounds are identified. ApoE4 binds stronger to heparin compared to ApoE2 and ApoE3 and induces substantial conformational changes as measured using small angle X-ray scattering (SAXS). The isoform-dependent difference in the heparin interaction suggests altered ApoE4 binding ability to HSPGs. Meanwhile, L-Thyroxine and it's analogue Tafamidis, as well as the selective estrogen receptor modulators (SERMs) Clomiphene, Tamoxifen, Toremifene, and the non-steroidal anti-inflammatory drug (NSAID) Meclofenamic acid were identified as novel ApoE binders by biophysical screening using the Corning® Epic® label-free, followed by microscale thermophoresis (MST) and isothermal titration calorimetry (ITC). Although none of these drugs showed selectivity for the ApoE4 versus ApoE2 and ApoE3 isoforms, they can nevertheless be used to investigate ApoE function and may also provide starting points for future attempts to identify and develop molecules which interact selectively with ApoE4 and which might therefore be of therapeutic utility.

PREFACE

A version of Chapter 2 is currently under revision; **Lucas Kraft***, Ana-Caroline Raulin*, Youssra K. Al-Hilaly, John E. McGeehan, John R. Atack, Louise Serpell (*equally contributed). The molecular basis of the major risk factor for Alzheimer's disease: structural studies of ApoE isoforms. This work was carried out primarily in the laboratories of Prof. Louise Serpell and Prof. John R. Atack in collaboration with Prof. John McGeehan at the University of Portsmouth, UK and the B21 beamline at the Diamond Lightsource, UK. Ana-Caroline Raulin and I equally contributed to the work and were responsible for the experimental design and concepts, as well as experimental work, data analysis and figure generation. Dr. Youssra K. Al-Hilaly collected the diffraction data. Ana-Caroline Raulin, Prof. Louise Serpell and I wrote the manuscript. Prof. John McGeehan assisted with the analytical ultracentrifugation and edited the manuscript. Prof. John R. Atack assisted with editing the manuscript.

A version of Chapter 3 is currently under revision; **Lucas Kraft**, Nathan Cowieson, Ana-Caroline Raulin, Louise Serpell, John R. Atack. Differential binding of ApoE isoforms to heparin investigated by small angle X-ray scattering. This work was carried out primarily in the laboratory of Prof. John R. Atack in collaboration with the B21 beamline at the Diamond Lightsource, UK. I was responsible for experiment design and concepts, the majority of experimental work, data analysis, figure generation, and writing of the manuscript. Prof. Louise Serpell, Prof. John R. Atack and Dr. Nathan Cowieson assisted with editing the manuscript. Dr. Nathan Cowieson also assisted with data collection and data analysis at the B21 beamline. Ana-Caroline Raulin and Dr. Youssra K. Al-Hilaly assisted with CD measurements.

A version of Chapter 4 has been published; **Lucas Kraft**, Louise Serpell, John R. Atack. A biophysical approach to the identification of novel ApoE chemical probes. **Biomolecules, 2019, 9, 48**. This work was carried out primarily in the laboratory of Prof. John R. Atack. I was responsible for experiment design and concepts, the majority of experimental work, data analysis, figure generation, and writing of the manuscript. Prof. Louise Serpell and Prof. John R. Atack assisted with editing the manuscript.

TABLE OF CONTENTS

LIST OF TABLES

LIST OF FIGURES

ABBREVIATIONS

AD	Alzheimer's disease
11C-PiB	11C Pittsburgh compound B
18F	Florbetapir
ADAM	a disintegrin and metalloproteinase
AEX	anion exchange chromatography
AICD	APP intracellular domain
AMPA	α-amino-3-hydroxy-5-methyl-4-isoxazolepropionic acid
AMPAR	α-amino-3-hydroxy-5-methyl-4-isoxazolepropionic acid receptor
ApoE	Apolipoprotein E
APP	β-amyloid precursor protein
AUC	analytical ultracentrifugation
Aβ	amyloid β
BACE1	β-site APP cleaving enzyme 1
BBB	blood brain barrier
CAA	cerebral amyloid angiopathy
CD	circular dichroism
CEX	cation exchange chromatography
CHD	1,2-cyclohexanedione
CM	chylomicron
CNS	central nervous system
CSF	cerebrospinal fluid
CTEP	cholesteryl ester transfer protein
CTF	carboxyl terminal fragment
DMPC	dimyristoylphosphatidylcholine
DPPC	dipalmitoylphosphatidylcholine
DTT	dithiothreitol
E. coli	Escherichia coli
EDTA	ethylenediaminetetraacetic acid
EGFP	enhanced green fluorescent protein
EPR	electron paramagnetic resonance
FPLC	fast-performance liquid chromatography
FRET	fluorescence energy transfer
GAG	glycosaminoglycan
GST	glutathione S-transferase
GWAS	genome wide association studies
HAC	heparin affinity chromatography
HCl	hydrochloride or hydrochloric acid
HDL	high-density lipoprotein
HDX MS	hydrogen−deuterium exchange and mass spectroscopy
HEPES	4-(2-hydroxyethyl)-1-piperazineethanesulfonic acid
HL	hepatic lipase
HS	heparan sulphate
HSPGs	heparan sulphate proteoglycans
ICD-11	11th version of the International Statistical Classification of Diseases and Related Health Problems
IDE	insulin-degrading enzyme

IMAC	immobilized metal ion affinity chromatography
iPSCs	induced pluripotent stem cells
IPTG	isopropyl β-D-1-thiogalactopyranoside
ISF	interstitial fluid
ITC	isothermal titration calorimetry
kDa	kilodalton
LB	Luria-Bertani
LCAT	lecithin cholesterol acyltransferase
LCP	lipid cubic phase
LDL	low density lipoprotein
LDLR	low density lipoprotein receptor
LPL	lipoprotein lipase
LPS	lipopolysaccharide
LRP1	low density lipoprotein receptor-related protein 1
LXR	liver X receptor
MALS	multi angle (laser) light scattering
MAPT	microtubule-associated protein tau
MCI	mild cognitive impairment
MRI	magnetic resonance imaging
MST	microscale thermophoresis
Mw	molecular weight
MWCO	molecular weight cut-off
NCD	neurocognitive disorder
Ndst1	*N*-acetyl-D-glucosamine *N*-deacetylase/*N*-sulfotransferase 1
NEP	neprilysin
NFTs	neurofibrillary tangles
NF-κB	nuclear factor-κB
NMDA	*N*-methyl-D-aspartate
NMDAR	*N*-methyl-D-aspartate receptor
NMR	nuclear magnetic resonance
NSAID	nonsteroidal anti-inflammatory drug
NSE	neuron-specific enolase
OG	octyl β-glucoside
OTG	octyl β-D-1-thioglucopyranoside
PET	positron emission tomography
pI	isoelectric point
PSEN 1/2	presenilin 1 or 2
RAP	receptor-associated protein
RFP	red fluorescence protein
RMSD	root-mean-square deviation
RT	room temperature
RXR	retinoid X receptor
sAPP	soluble ectodomain of APP
SAXS	small angle X-ray scattering
SDS PAGE	sodium dodecyl sulphate polyacrylamide gel electrophoresis
SEC	size exclusion chromatography
SERM	selective estrogen receptor modulator
SPR	surface plasmon resonance

TCEP	tris(2-carboxyethyl)phosphine
VHDL	very high-density lipoprotein
VLDL	very low-density lipoprotein
VLDLR	very low-density lipoprotein receptor
WT	wild type

ACKNOWLEDGMENTS

This work was possible with the generous funding support from the Alzheimer's Society UK. This PhD thesis was performed from September 2015 to March 2019 at the School of Life Sciences in the Sussex Drug Discovery Centre (SDDC), University of Sussex under supervision of Prof. Louise Serpell and Prof. John R. Atack. I am very grateful to my supervisors who have given me the freedom to explore my passion for science, but also my passion for public engagement and widening participation that has shaped me into the scientist I am today. I am feeling lucky to have completed my research in the SDDC with all the scientific and personal support. Thank you to all the SDDC for providing mentorship, guidance, technical support and particularly fellow PhD students and friends Dr. Thalia Carreno-Velazquez, Dr. Chloe Koulouris, James W. Noble, Torri Miller, Fiona Scott and Gareth Williams who have gone with me through highs and lows. To my fellow PhD students in the Alzheimer's Society Doctoral training Centre Luca Biasetti, Orla Bonnar and Rebecca Atkinson for supporting me with all challenges and for keeping my spirits up. To all lab members of the Serpell lab, in particular Ana-Caroline Raulin for providing invaluable contributions to this work.

I have also received incredible support from many mentors during my PhD. I would like to thank all members of my thesis committee Prof. Louise Serpell, Dr. Mark Roe and Dr. Antony Oliver for their input and guidance. I would also like to thank all my collaborators Prof. John McGeehan at the University of Portsmouth for helping with the analytical ultracentrifugation, Dr. Isabel Moraes at the Membrane Protein Lab and all B21 beamline scientist at the Diamond Lightsource for assisting with small angle X-ray data collection and analysis. I am also profoundly indebted to Dr. Katy Petherick who has sparked and supported my passion for public engagement and outreach work.

Finally, I am grateful for the unconditional support, encouragement and love of my partner Jamie Deane, my parents Barbara Salvi-Kraft and Hans Kraft, as well as my siblings Stefan, Claudia and Adrian Kraft. I could not have done this journey without them.

“The trouble with having an open mind, of course,

is that people will insist on coming along and trying to put things in it.”

- Terry Pratchett, *Diggers*

1 INTRODUCTION

1.1 Definition of Alzheimer's disease

In 1906, Alois Alzheimer received brain material from Auguste Deter, a woman who died of a clinically unusual dementia at the age of 51. By using Bielschowsky's improved staining method, Alzheimer described new pathological features in the patient's brain and observed tangles of fibrils within the cytoplasm of neurons that stained differently from normal neurofibrils, as well as a pronounced plaque pathology (1). Today we know that the plaques and neurofibrillary tangles (NFTs) are formed by aggregated amyloid beta (Aβ) peptide and tau protein that are characteristic lesion of Alzheimer's disease (AD) (2).

Alzheimer's disease is the main cause of dementia and represents a rapidly growing burden to the healthcare system (3). An estimated 47 million people worldwide were living with dementia in 2015 and this figure is projected to double every 20 years to approximately 131 million in 2050 (4). Dementia is an umbrella term and describes a group of symptoms that occur when the brain is affected by certain diseases or conditions. According to the 11th version of the International Statistical Classification of Diseases and Related Health Problems (ICD-11, World Health Organization) dementia falls under the category of mental, behavioural and neurodevelopmental disorders and is an "*acquired brain syndrome characterized by a decline from a previous level of cognitive functioning with impairment in two or more cognitive domains (such as memory, executive functions, attention, language, social cognition and judgment, psychomotor speed, visuoperceptual or visuospatial abilities)*" (5). Dementia can be attributed to a neurological or medical condition and is not a normal part of aging (5). Dementia due to Alzheimer's disease is the most common form of dementia and is often accompanied by other mental or behavioural symptoms such as depression, psychoses and seizures at later stages (6).

With novel imaging methods and advancements in biomarker research for Aβ and tau deposition, the definition of AD in a living person is starting to shift from a clinicopathological entity to a biological construct (7). Definite certainty on the cause of dementia however requires histopathological confirmation at autopsy (2). NFTs and neuritic plaques are the most characteristic lesion of AD and its neuropathology remains defined around these characteristic hallmarks (8).

1.2 Neuropathology of Alzheimer's disease

1.2.1 Amyloid plaques

Amyloid plaques or senile plaques are extracellular deposits of the Aβ peptide that were initially isolated and sequenced by Glenner & Wong and Master's *et al* (9–11). The Aβ peptide is derived by sequential proteolytic cleavage of the β-amyloid precursor protein (APP) (12). APP is a glycosylated type I transmembrane protein with its amino terminal domain positioned in the extracellular space and its carboxyl terminus within the cytosol (13, 14). APP is processed via two principle pathways that either generate Aβ (amyloidogenic pathway) or prevent Aβ formation (anti-amyloidogenic pathway) (Figure 1.1). APP is most commonly cleaved within the Aβ sequence by α-secretases that are members of the ADAM (a disintegrin and metalloproteinase) family and thus initiate the non-amyloidogenic pathway (15–17). A soluble ectodomain of APP (sAPP-α) is released into the lumen and leaves a membrane-bound carboxyl terminal fragment (α-CTF) behind that is further cleaved by the γ-secretase complex yielding a non-toxic p3 peptide and APP intracellular domain (AICD) (18–21). Alternatively, APP can be cleaved by β-secretase, also referred to as β-site APP cleaving enzyme 1 (BACE-1) that releases a truncated APP soluble domain (sAPP-β) and β-CTF of 99 amino acids (22–24). The carboxyl terminal fragment β-CTF is further processed by the γ-secretase complex to liberate Aβ peptides between 38-46 amino acids in length (25–27). Of particular interest are the Aβ peptides $A\beta_{40}$ and $A\beta_{42}$. While the $A\beta_{40}$ peptide is most abundant in the brain and cerebrospinal fluid (CSF) (26, 28, 29) the longer and less soluble $A\beta_{42}$ peptide is far more prone to oligomerization and to formation of amyloid fibrils as demonstrated by *in vitro* assembly studies (30, 31). Immature diffuse plaques are exclusively composed of the longer amyloid peptide which may serve as a starting point to recruit more soluble $A\beta_{40}$ to form mature neuritic plaques (32).

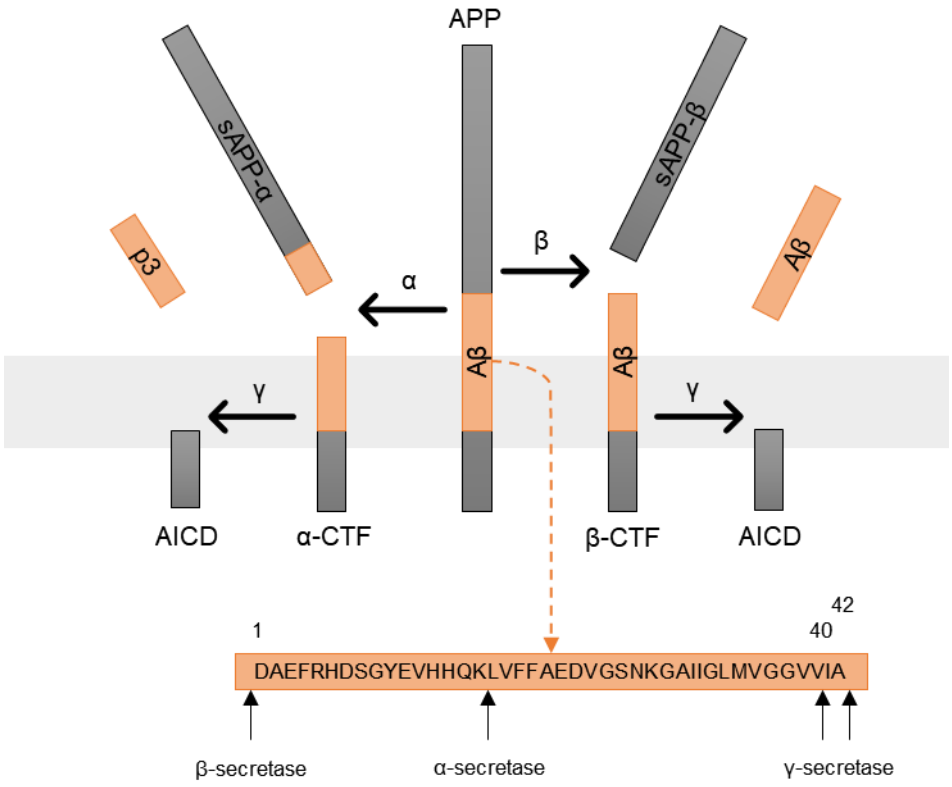

Figure 1.1. APP processing through the amyloidogenic and non-amyloidogenic pathway. The non-amyloidogenic pathway (left) is initiated by α-secretase mediated cleavage of β-amyloid precursor protein (APP) that enables secretion of the large and soluble ectodomain of APP (sAPP-α) into the lumen and retention of the 83 amino acid long carboxyl terminal fragment in the membrane (α-CTF). The α-CTF fragment can be further processed by γ-secretase to release p3 peptide and retain APP intracellular domain (AICD). The amyloidogenic pathway (right) on the other hand is initiated by cleavage of APP by β-secretase, also referred to as β-site APP cleaving enzyme 1 (BACE-1), that releases a slightly truncated ectodomain of APP (sAPP-β) and the 99-residue carboxyl terminal fragment (β-CTF). B-CTF can undergo heterogeneous cleavage by γ-secretase that releases Aβ of various length. The Aβ sequence is shown on the bottom with cleavage sites of α, β and γ secretases.

The identification of dominantly inherited missense mutations flanking and within the Aβ sequence, as well as in the presenilin 1 and 2 (*PSEN1* and *PSEN2*) genes that encode core subunits of the γ-secretase complex support a dominant role of Aβ in AD. These mutations are inherited in a fully penetrant, autosomal-dominant fashion and result in the early onset of AD that account for approximately 5% of AD cases (33, 34). To date, 51 mutations have been reported for the *APP* gene, 219 for *PSEN1* and 16 for *PSEN2* and can be accessed on the Alzheimer Disease and Frontotemporal Dementia Database (35). Most of these mutations result in altered processing of the APP protein that increase the ratio of aggregatory, longer forms of the Aβ peptide or directly increase the aggregatory properties of Aβ (36–39). On the other hand, an APP missense mutation reported by Jonsson *et al* (40) decreases APP cleavage by β-secretase and the generated Aβ peptide seems to possess slower aggregation kinetics (41, 42).

The focus has recently shifted from amyloid plaques to soluble Aβ oligomers. Particularly, in the more common, late-onset form of AD there is poor correlation between the severity of dementia and density of fibrillary plaque load. Reports have shown substantial amounts of plaques in non-demented individuals (43–48) and synapse loss, as well as levels of soluble Aβ provide a better pathological correlate of memory decline in AD (43, 49–51). Evidence suggests that soluble Aβ oligomers rather than insoluble Aβ fibrils in form of plaques may be the toxic species and are hypothesized to be early effectors on synaptic efficacy, inflammatory response and tangle formation (52–57).

1.2.2 Neurofibrillary tangles

Neurofibrillary tangles (NFTs) are intraneuronal cytoplasmic paired helical filaments that are formed by abnormally hyperphosphorylated tau protein (58–60). Six tau isoforms are expressed in the human brain as a result of alternative mRNA splicing of transcripts from the microtubule-associated protein tau (*MAPT*) gene that is located on chromosome 17 (61, 62). Tau protein is predominantly found in axons where it performs its functions including initiation of tubulin polymerization and microtubule growth, as well as regulation of microtubule-dependent axonal transport (63–65). Tau protein undergoes post-translational modifications of which its phosphorylation is best characterized (66). Physiological tau phosphorylation weakens the binding of tau protein to tubulin and results in destabilization of microtubules (Figure 1.2) (67–69). In AD, phosphorylation levels of tau protein are increased three to four fold compared to control brains (70). Tau hyperphosphorylation is believed to decrease its solubility and to promote its self-aggregation, as well as to promote misfolding of normal tau and co-aggregation into filaments (71–73).

Similar to amyloid plaques, it has been assumed that only insoluble NTFs are responsible for tau's cytotoxic effects; however, intermediate aggregates of abnormal tau or other soluble lower-mass species seem to have neurotoxic properties and were shown to lead to behavioural abnormalities, as well as synaptic dysfunction in animal models of tauopathies (74–76). Tau oligomers have been detected in brains of AD patients (77, 78) and were shown to have substantial tau seeding capacity (i.e. ability of tau aggregate to recruit monomeric tau) and that seeding is enriched in the synapses as compared to the cytosol (79). This data supports the pathogenic role of tau oligomers and their ability to propagate from affected to unaffected brain regions during disease progression. However, the exact mechanisms by which tau oligomers cause neurodegeneration and propagate across the brain remain to be elucidated (80).

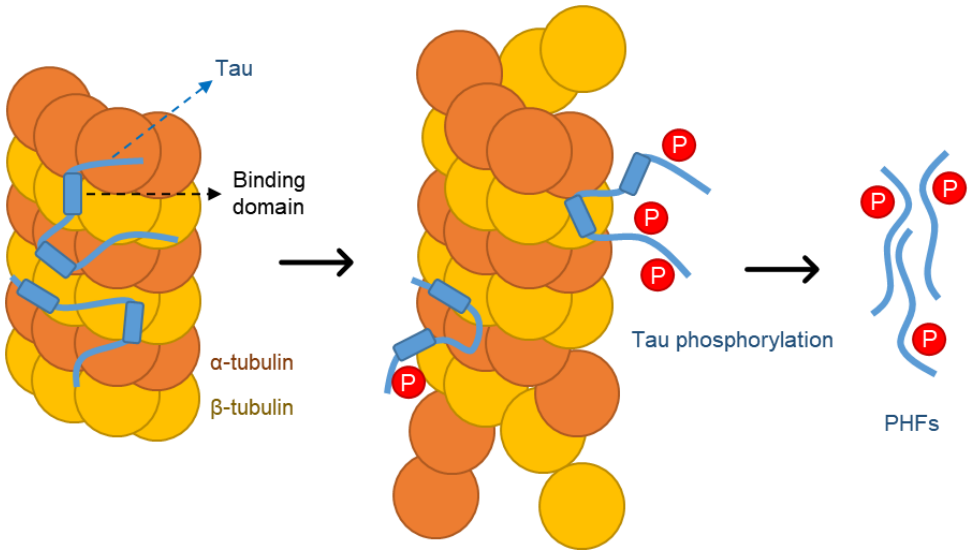

Figure 1.2. Intraneuronal aggregation of tau protein. Microtubules form part of the cytoskeleton and are cylindrical polymers that are composed of the two globular proteins α- and β-tubulin. Tau protein is one of the major microtubule-associated proteins (MAPs) that stabilizes microtubule architecture by interaction through its microtubule-binding repeats. Phosphorylation of tau protein at specific serine or threonine sites by different kinases attenuates tau binding to microtubules that results in their destabilization. Highly phosphorylated tau dissociates from the microtubule array and accumulates in paired helical filaments (PHFs). Figure adapted with permission from Springer Nature: Mazanetz and Fischer, Nature Reviews Drug Discovery, 2007, 6(6):464-79 (81).

1.2.3 Synapse loss

Synapse loss is a neuropathological change in AD that correlates most closely with symptoms (43) and was shown with immunohistochemical markers directed against pre- or postsynaptic proteins as well as with electron microscopy studies (8, 82). Immunohistochemical quantification of the presynaptic protein synaptophysin showed significant decrease (up to 50%) in the density of the protein immunoreaction in different brain sections and ultrastructural studies revealed a decline in synapse numbers between controls and AD subjects (83–85). Aβ, as well as tau were shown to impair synapse functioning that is likely to result in synapse loss (86). Neurochemical analyses in the late 1970s and early 1980s revealed a substantial reduction of acetylcholine generating and metabolizing enzyme levels in AD brain tissue compared to controls, as well as degeneration in the cholinergic cell bodies of the basal forebrain that project to the cortex and hippocampus (87–91). These observations, in conjunction with pharmacological evidence linking the cholinergic system to learning and memory in animals and man led to the conclusion that in particular dysfunction and degeneration of cholinergic neurons contribute to the cognitive decline and the early symptoms in AD. Currently available and approved symptomatic drug therapies in AD are therefore cholinesterase inhibitors such as donepezil, galantamine and rivastigmine (92), but also the glutamate *N*-methyl-D-aspartate (NMDA) receptor antagonist memantine (as a blocker of excitotoxicity) (93).

1.3 Genetics of Alzheimer's disease

AD is commonly classified into early (< 65 years) and late (> 65 years) onset forms (94, 95). According to family history, AD cases can be further divided into autosomal dominant, familial or sporadic* AD (96). Most cases of autosomal dominant AD have an early onset with a heritability ranging between 92 to 100% (97). To date, three genes are known in which mutations are associated with autosomal dominant early onset AD: *APP*, *PSEN1* and *PSEN2* (Section 1.2.1). These mutations have nearly complete genetic penetrance and ultimately cause AD (33). Late onset familial or sporadic AD is the most common form of the disease. Although, twin studies showed a substantial genetic component and a clear heritability in AD with late onset (98, 99), the pattern of inheritance seems far more complex in which genetic risk factors work together with environmental factors and life style (33). Genome wide association studies (GWAS) have significantly contributed to our current understanding of late onset AD and identified novel genetic risk loci (100, 101). Most risk loci cluster within three pathways including cholesterol and lipid metabolism, immune system and inflammatory response, and endosomal vesicle trafficking (102). Out of all the genetic risk loci revealed over the last decades, only one has a striking effect on AD risk and was identified before the availability of GWAS. The inheritance of the ε4 allele of the apolipoprotein E gene (*APOE)* is considered to be the major genetic risk factor for late onset AD (103–105).

1.4 Introduction to Apolipoprotein E

Apolipoprotein E (ApoE) was identified by Shore and Shore in 1973 as a major protein constituent of very low density lipoproteins (VLDLs) and was initially termed "arginine-rich protein" (106). Two years later, Utermann *et al* (107) further characterized this arginine-rich protein, differentiated it from previously identified apolipoproteins B and C that are also present on VLDLs and coined it apolipoprotein E. Subsequent electrophoresis studies in the late 1970s and early 1980s showed distinct electrophoretic patterns of plasma VLDL-derived ApoE as a result of genetic polymorphism in the human population (108–113). The electrophoresis pattern revealed six different ApoE phenotypes that could be explained by three alleles at a single genetic locus. Amino acid analysis and sequencing in the same era by Weisgraber, Mahley and colleagues at the Gladstone Institute in California, USA demonstrated that ApoE's heterogeneity is due to differences in primary structure and comprises cysteine-arginine

* Autosomal dominant, familial and sporadic AD are defined by the American College of Medical Genetics and the National Society of Genetic Conselors (96) as follows:

1 Autosomal dominant AD is characterized by disease that occurs in at least three individuals in two or more generations, with two of the individuals being first degree relatives.
2 Familial AD is characterized by disease that occurs in more than one individual, and at least two of the affected individuals are third-degree relatives.
3 Sporadic AD is characterized by an isolated case in the family or cases separated by more than three degrees of relationship.

interchanges (114, 115). A common nomenclature system to describe ApoE allelic variance was introduced in 1982 and was based on the electrophoretic behaviour of ApoE isoforms (116). The three major *APOE* alleles were termed ε2, ε3 and ε4; the corresponding proteins as seen in plasma by two-dimensional gel electrophoresis were named ApoE2, ApoE3 and ApoE4[*].

In humans, the three different *APOE* alleles (ε2, ε3 and ε4) are found on chromosome 19 and result in six possible genotypes (homozygous genotypes ε2/ε2, ε3/ε3, ε4/ε4 and heterozygous genotypes ε2/ε3, ε2/ε4, ε3/ε4) (117). The ε3 allele and therefore the ε3/ε3 genotype is most frequent with an allelic frequency of approximately 78% in the Caucasian population; ε2 and ε4 have frequencies of 8% and 14% respectively (118). Notably, the ε4 variant of *APOE* is overrepresented in patients with AD and increases the risk for the disease in a gene dose-dependent fashion (103–105). Corder *et al* (105) in their 1993 landmark study investigated the gene dose effect of the ε4 allele in 42 families with late onset AD and showed that the proportion of individuals with AD to healthy subjects increased with the number of ε4 alleles. While approximately 21% of subjects with an ε3/ε3 genotype developed AD, the number of affected individuals increased to 48% of subjects with ε3/ε4 and 91% with ε4/ε4 genotype respectively. Additionally, Corder *et al* (105) showed that the ε4 allele drastically reduces the age at onset to a younger age. Individuals without the ε4 allele had a mean age at onset of 84 years; one copy of the ε4 allele shifted the age at onset to 76 years, two copies to 68 years respectively. Meta-analysis by the ApoE and Alzheimer Disease Meta-Analysis Consortium (118) confirmed the odds and notably showed that women across all *APOE* genotypes are more likely to develop AD than men. The magnitude of the ε4 allele on the risk to develop AD should further be established with the upraise of GWAS that consistently confirmed *APOE* ε4 as the major risk locus for late onset AD (100, 101).

As mentioned, ApoE's heterogeneity is due to cysteine-arginine interchanges and correspond to combinations of amino acids at residues 112 and 158. ApoE3 has a cysteine at site 112 and an arginine at position 158, ApoE2 has two cysteine and ApoE4 two arginine at both sites respectively (114, 115). ApoE is a 299 amino acid glycoprotein (M_R 34,200 Da) that is predominantly expressed in the liver and brain as determined by immunohistochemistry and mRNA analysis in human tissue and other species (119–122). In the liver, ApoE is expressed by hepatocytes (119, 123) and in the brain mostly by astrocytes (124, 125). ApoE is the major lipid, as well as cholesterol carrier in the brain and is involved in lipoprotein metabolism through

[*] What happened to ε1 and ApoE1? As mentioned, the ApoE nomenclature system from 1982 is based on electrophoretic patterns. ApoE isoforms are separated by isoelectric focusing and bands with different isoelectric point and/or molecular weight are assigned a group number. A band observed at position 1 is normally caused by either sialylated ApoE2, E3 or E4 (116). However, a very rare ApoE variant was identified by Weisgraber *et al* (469) in 1984 that migrates to the E1 band (not due to sialylation) and was therefore coined ApoE1. It differs from ApoE2 at site 127 (Gly127 → Asp).

interaction with its receptors such as low density lipoprotein (LDL) receptor (LDLR), LDL related protein 1 (LRP1) and heparan sulphate proteoglycans (HSPGs) (117, 126).

1.4.1 Lipoprotein metabolism and physiological role of ApoE in the periphery

The primary function of ApoE is to transport lipids and cholesterol in our body. Lipids are highly insoluble in aqueous solutions and therefore become associated with proteins (i.e. apolipoproteins) to form water soluble lipoprotein complexes (Figure 1.3) (127). The role of plasma lipoproteins and apolipoproteins in the periphery of our bodies has been studied extensively, whereas central nervous system (CNS) lipoproteins are less well characterized and differ from those in the periphery with respect to lipid as well as apolipoprotein composition (Section 1.4.2).

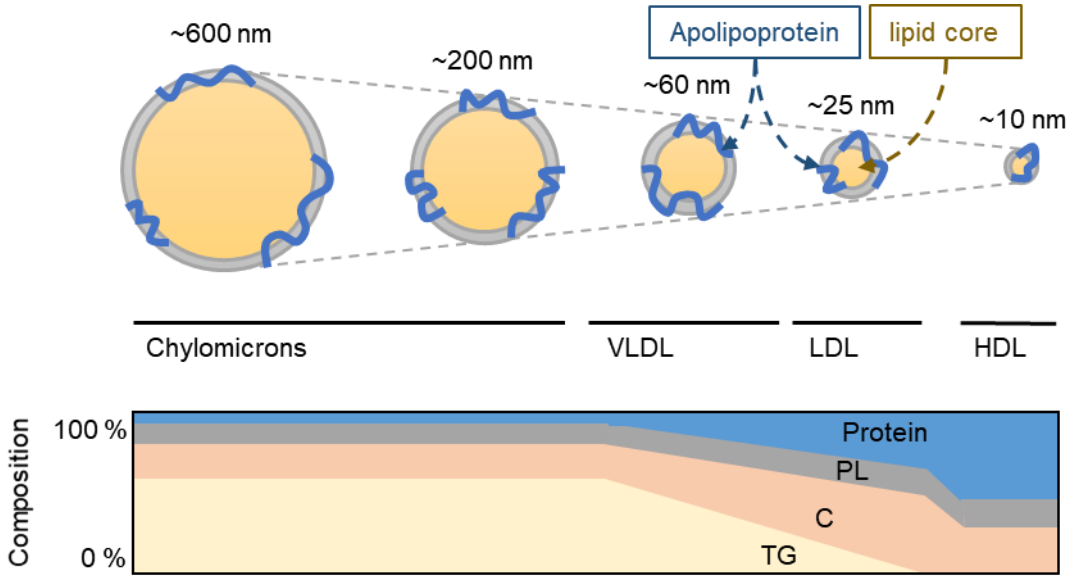

Figure 1.3. Classification and constituents of plasma lipoproteins. Lipoproteins are a complex of lipids, cholesterol and proteins. All lipoproteins share a similar structural organization. Phospholipids (PL) enclose a core of triacylglycerols (TG), cholesteryl esters and cholesterol (C). Integrated into PL bilayer are apolipoproteins such as ApoE. Lipoprotein classes are based on their densities and diameters and can range from 600 nm to 10 nm. Chylomicrons and very low-density lipoproteins (VLDLs) contain a large core of triacylglycerols and 1-10% of apolipoprotein by weight. Low-density lipoproteins (LDLs) and high-density lipoproteins (HDLs) on the other hand have highest cholesterol and cholesteryl ester contents, as well as up to 50% protein. Figure adapted with permission from Elsevier: Jonas and Phillips, Biochemistry of Lipids, Lipoproteins and Membranes, 2008, 348:485-506 (127).

The principal function of lipoproteins in the periphery of our body is determined by their lipid and apolipoprotein composition. Lipid-rich chylomicrons (CM) are derived from the intestine and transport dietary-derived lipids to various tissues. CM undergo lipolysis (i.e. lipids are extracted from their core) while circulating in the blood stream and the CM remnants are eventually catabolized in the liver by hepatocytes via ApoE-receptor mediated endocytosis (128, 129). Very low-density lipoproteins (VLDLs) are synthesized in the liver and deliver

endogenous triglycerides, as well as cholesteryl esters from the liver to other tissues. VLDLs like CM are subject to lipolysis in the blood stream that results in the generation of low-density lipoproteins (LDLs). The most protein-rich and smallest high-density lipoprotein (HDL) particles take part in the reverse cholesterol transport. The reverse cholesterol transport is important in maintaining cholesterol homeostasis and forms a mechanism by which the body transports cholesteryl esters to steroid hormone synthesizing tissues, as well as by which it eliminates excessive cholesterol from the periphery (Figure 1.4) (128, 130).

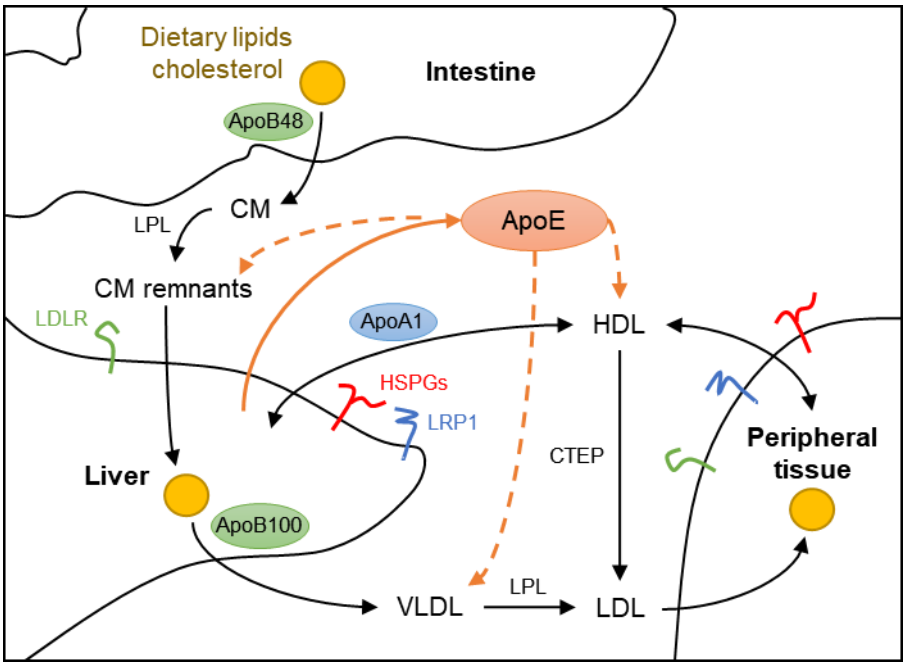

Figure 1.4. Peripheral lipoprotein metabolism. Dietary lipids, as well as cholesterol are combined into chylomicrons (CM) with apolipoprotein B48 (ApoB48) and secreted into circulation. Lipids are extracted by interaction with lipoprotein lipase (LPL) and CM remnants are eventually internalized by hepatocytes in the liver. Liver-derived lipids and sterols are packed into VLDLs with apolipoprotein B100 (ApoB100) and similar to CMs are catabolized in circulation by LPL. Processing results in the generation of LDLs. Reverse cholesterol transport is initialized by the secretion of lipid-poor apolipoprotein A1 (ApoA1) from the liver. ApoA1 acquires phospholipids and cholesterol in circulation, as well as from peripheral tissues that results in the formation of HDL particles. Cholesterol in the HDLs is then transported to peripheral tissues (e.g. where needed for steroid hormone synthesis), back to the liver or transferred by cholesterol ester transfer protein (CTEP) to other lipoproteins. ApoE is synthesized in the liver (but also intestine) and is transferred to most lipoproteins in circulation including CM, CM remnants, VLDLs and HDLs. ApoE, as well as ApoB48 and ApoB100 mediate the internalization of lipoproteins into the liver and peripheral tissues via interaction with LDLR, LRP1 and HSPGs.

ApoE is a critical ligand for the clearance of lipoproteins via ApoE receptors and HSPGs. Intravenous infusion of recombinant human ApoE or ApoE isolated from rabbit plasma markedly reduced lipoprotein levels in cholesterol-fed rabbits by directing lipoproteins into the liver and transgenic animals overexpressing ApoE were shown to have accelerated CM remnant clearance (131–133). ApoE-knockout mice on the other hand show defective

lipoprotein clearance, subsequent cholesterol accumulation and phenotypically develop atherosclerotic plaques (134).

Compelling evidence of ApoE's role in lipoprotein metabolism comes from patients with type III hyperlipoproteinemia; a rare genetic disorder that is characterized by elevated cholesterol, as well as triglyceride plasma levels due to accumulation of lipoproteins and affected individuals are predisposed to premature development of atherosclerosis (135). Type III hyperlipoproteinemia is a result of rare ApoE mutants that have defective receptor binding ability. A naturally occurring ApoE4 variant that has a cysteine at site 142 instead of an arginine is associated with the dominant transmission of type III hyperlipoproteinemia (136, 137). The variant was shown to have approximately 20% of normal binding to LDLR, as well as strongly reduced binding to HSPGs (137). Expression of the ApoE4 variant (Arg142Cys) in mice reproduced the hyperlipidemic effects with accumulation of VLDLs, hypercholesterolemia and impaired lipoprotein clearance (138). Rare cases of complete ApoE deficiency in humans have been reported and deficiency has identical outcomes on lipoprotein metabolism as type III hyperlipoproteinemia (139). The ApoE2 variant has also a defective receptor binding site (Section 1.4.3) and is a susceptibility factor for the disorder; however, development of overt hyperlipoproteinemia requires homozygous ε2/ε2 genotype and additional pathology such as obesity or diabetes (135).

Several steps are involved in the uptake of lipoproteins in the liver and particularly involve the interaction of ApoE with HSPGs (Figure1.5) (126, 140–142). Lipoprotein uptake is initialized by sequestration or capture through the interaction of ApoE to HSPGs in the perisinusoidal space (or space Disse; location in the liver between sinusoid and hepatocyte). Other enzymes such as hepatic lipase (HL) (143) and lipoprotein lipase (LPL) (144) were shown to bind to HSPGs and further process the particles. Internalization into hepatocytes involves the interaction of ApoE with cell surface receptors LDLR, LRP1 and HSPGs (126). Treatment of HepG2 hepatocytes or LDLR-negative familial hypercholesterolemic fibroblasts with heparinase, a heparin and HSPG degrading enzyme, impaired the binding and uptake of CM (145) and infusion of heparinase into mice *in vivo* resulted in reduced VLDL plasma clearance, as well as liver uptake (146). Internalization of lipoproteins by LRP1 seems to require the presence of HSPGs and LRP1 was shown to coimmunoprecipitate with proteoglycans (147). Studies by MacArthur *et al* (148) in mice with inactive HSPG biosynthetic enzyme *N*-acetyl-D-glucosamine *N*-deacetylase/*N*-sulfotransferase 1 (Ndst1) proofed an independent role of HSPGs in lipoprotein uptake. Ndst1 is involved in HSPG synthesis by transferring sulphate to free amino groups of *N*-acetyl-D-glucosamine. Hepatic knockout of the *Ndst1* gene in mice was shown to decrease HSPG sulfonation in the liver and mice accumulated ApoE containing triglyceride-rich lipoproteins (i.e. CM remnants and VLDLs) in the presence of LDLR and LRP1

which suggests an independent role of HSPGs in lipoprotein clearance. The relative contribution of HSPGs, LDLR and LRP1 was confirmed by the same research group in a follow-up study by producing mice lacking various combinations of the three receptors (149). HSPGs and LDLR were shown to be the dominant receptors in mediating triglyceride-rich lipoprotein clearance under fasting conditions, whereas LRP1 plays a minor role. Notably, mice lacking HSPGs accumulated particles of smaller size (20-50 nm in diameter) that are enriched in ApoE compared to mice lacking the LDLR family members (30-60 nm in diameter) (149, 150). Cross-breeding of the *Ndst1* knockouts with ApoE deficient mice resulted in greater accumulation of plasma triglycerides compared to either single mutant alone (150). These studies establish the importance of ApoE in lipoprotein metabolism by HSPGs and suggest that HSPGs mediate the uptake of a subset of smaller, ApoE enriched triglyceride-rich lipoproteins (149, 150). One goal of this thesis is to expand our knowledge in the interaction of ApoE to HSPGs and evaluate isoform dependent differences.

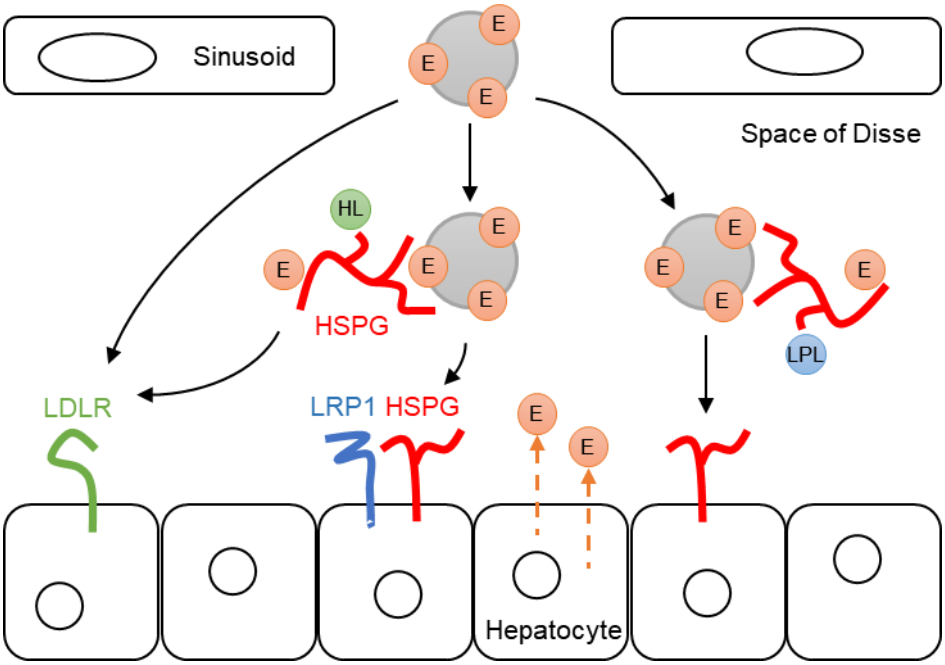

Figure 1.5. Lipoprotein clearance pathways in the liver. ApoE-containing lipoproteins enter the space of Disse (or perisinusoidal space) that is enriched with HSPGs, ApoE (E) and other enzymes such as hepatic lipase (HL) and lipoprotein lipase (LPL). Remnants are sequestered by HSPGs via ApoE and internalized into hepatocytes by LDLR, by the HSPG-LRP1 complex and/or by HSPGs alone. Figure adapted with permission from the American Society for Biochemistry and Molecular Biology: Mahley and Ji, Journal of Lipid Research, 1999, 40(1):1-16 (126).

1.4.2 Lipoprotein metabolism and physiological role of ApoE in the brain

The brain is the most cholesterol-rich organ in the body and contains approximately 20% of the whole body's cholesterol of which the majority is found in myelin (151–153). Such a large pool of cholesterol would presumably require uptake of plasma lipoproteins across the blood brain barrier (BBB). However, unlike hepatic sinusoids there are no fenestrations as a result of tight junctional attachments of endothelial cells that would allow paracellular transport (153, 154). Cholesterol metabolism in the brain is thus insulated from changes in circulating cholesterol and comes entirely from local synthesis (155–158). Cholesterol alters the biophysical properties of membranes and influences synaptic function, integrity and development (159). Efficient cholesterol transport in the CNS is therefore essential and unlike in the periphery, where cholesterol transport is mediated by additional apolipoproteins ApoB48 and ApoB100 (Figure 1.4), cholesterol transport in the brain is controlled by ApoE and ApoA1

Several apolipoproteins have been detected in human cerebrospinal fluid (CSF), of which ApoE and ApoA1 are the most abundant with CSF concentrations around 4 µg/mL, or 4% and 0.3% of their respective plasma levels (160). ApoE is the major apolipoprotein in the brain and is mostly synthesized and secreted by astrocytes in form of nascent lipoprotein particles (124, 125). It is also expressed in microglia, as well as in neurons particularly under stress conditions or injury as assessed in mice expressing enhanced green fluorescent protein (EGFP) under control of the endogenous ApoE promoter (161). Studies in mice, as well as studies in human patients who received liver transplants of different *APOE* genotype to their own suggest that ApoE does not cross the BBB and therefore must come from local synthesis in the brain (162, 163). ApoA1 on the other hand is not produced in the CNS, but instead is transferred from the periphery to the CSF (164). The exact mechanism and the specific transporter for the ApoA1 transfer remains to be elucidated.

Freshly synthesized ApoE-containing lipoproteins from astrocytes are lipidated by adenosine triphosphate (ATP) binding cassette A1 (ABCA1) shortly after their secretion (Figure 1.6) (165). Lipidation of ApoE by ABCA1 is critical in the regulation of ApoE levels and function in the CNS. Knockout *ABCA1* mice have considerably lowered ApoE, as well as cholesterol levels in plasma and CSF due to abnormal lipidation and processing of ApoE (165). Conversely, overexpression of ABCA1 in transgenic mice results in an increased ApoE lipidation state (166). Astrocyte-secreted particles are discoid in shape with a diameter of 8-15 nm and lack a lipid core (167, 168). Human CSF lipoproteins on the other hand tend to be spherical (10-20 nm in diameter) and resemble plasma HDLs (160). As suggested by LaDu *et al* (167) astrocyte-secreted lipoproteins in brain parenchyma may accumulate cholesterol and develop a lipid core through the activity of various enzymes including lecithin cholesterol acyltransferase (LCAT). The ApoE-containing lipoproteins circulate within the CNS and transport cholesterol,

as well as lipids to neurons and are internalized by interaction of ApoE with the superfamily of LDLR proteins which are abundantly found in the brain (Figure 1.6) (169). Knockout of *LDLR* in mice was shown to increase levels of ApoE in brain parenchyma and CSF which suggests impaired metabolism of ApoE containing lipoproteins and deletion of *LRP1* in mouse forebrain neurons had similar effects (170, 171). Overexpression of LDLR in transgenic mice on the other hand resulted in the opposite effects with a significant decrease in brain ApoE levels being observed (172). HSPGs and other proteoglycans are also widely expressed in brain tissue and are important for brain development, synaptogenesis and axonal growth (173). Similar to the periphery, HSPGs are likely involved in ApoE mediated uptake of lipoprotein particles in the brain. Astrocyte-secreted ApoE particles were shown to bind to heparin and require HSPGs for cellular uptake (174). Additionally, internalization of VLDLs isolated from rabbit plasma by rat hippocampal neurons and human astrocytoma cells was impaired after cells were treated with proteoglycan degrading enzymes (175).

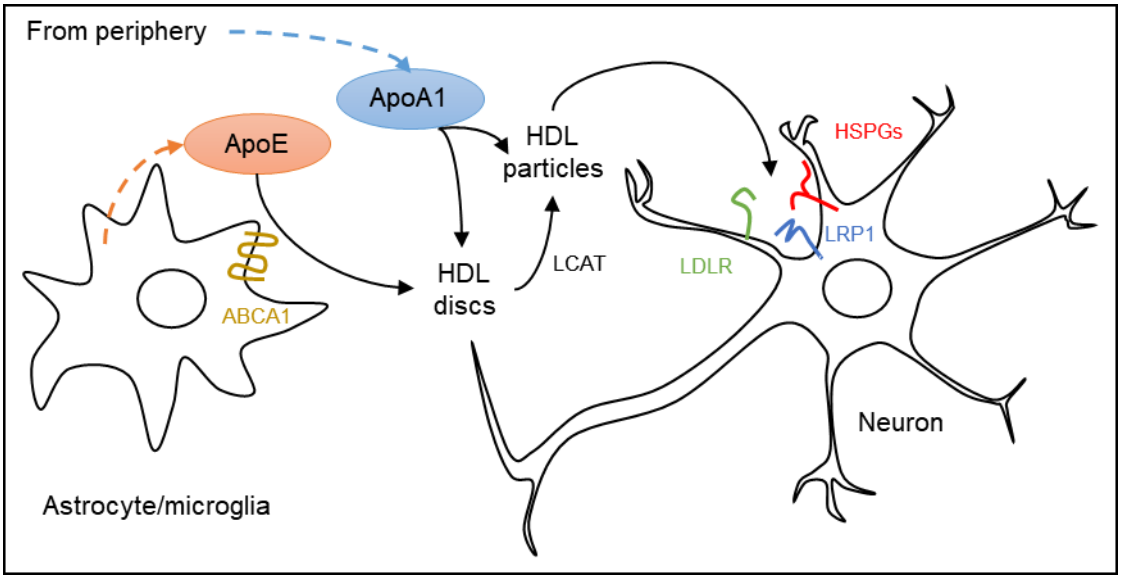

Figure 1.6. Central nervous system lipoprotein metabolism. ApoE is the major cholesterol and lipid transporter in the CNS. ApoE is secreted by astrocytes or microglia and further lipidated by ABCA1 to form HDL discs. The unesterified cholesterol in the discoidal HDLs is esterified by LCAT. ApoA1 after having crossed the blood brain barrier is also transferred to the HDLs. The ApoE and ApoA1 containing particles are then taken up by neurons via interaction with LDLR proteins and HSPGs where cholesterol and lipids are used for regeneration, axonal growth and synaptogenesis.

ApoE and ApoE receptor-mediated lipid redistribution is important for synaptic plasticity and neuronal repair. In terms of neuro- and synaptic plasticity, the effect of ApoE on neurite outgrowth has been extensively investigated. Studies have shown that ApoE-containing lipoproteins promote neurite outgrowth in a variety of cultured cell types including rabbit dorsal root ganglions, mouse hippocampal neurons and mouse neuroblastoma cells (176–180). On the other hand, cortical neurons derived from *APOE* knockout mice had significantly shorter

neurites compared to wild type mice and hippocampal slice cultures from *APOE* knockout mice showed reduced sprouting of mossy fibres (178, 181). Importantly, the effects of ApoE containing lipoproteins on neurite outgrowth were stopped by blocking the interaction with LRP1 through anti-LRP1 antibodies or receptor-associated protein (RAP), a LRP1 antagonist (176–180).

In addition, ApoE plays a critical role in neuronal repair and CNS inflammatory response. Secretion of ApoE by macrophages was observed to be strongly increased after peripheral, as well as optic nerve injury in rats, reaching a maximum number of ApoE positive cells at two weeks after lesion (182–184). Increased expression of ApoE by microglia was confirmed *in vivo* by treating EGFP-ApoE transgenic mice with kainic acid, a potent kainate receptor agonist that is known to activate microglia and induce gliosis (161). Similarly, increased ApoE levels were observed in rat and mouse brains following experimentally induced ischaemia and traumatic brain injury with glia cells being the major site of ApoE synthesis, as well as neuronal cells to a minor extent (185–187). Notably, *APOE* knockout mice were shown to have cognitive impairment and greater neurological damage compared to control animals after experimental head injury (188). Knockout animals had slower recovery rates, performed worse in the Morris water test and had higher hippocampal neuronal death compared to control mice (188). These data support the hypothesis that ApoE confers a neuroprotective and regenerative effect by redistributing lipids and cholesterol after nerve injury (185, 188). Respectively, the ApoE promoter region holds binding sites for several inflammatory transcription factors including a nuclear factor-κB (NF-κB) binding site that are likely to regulate ApoE expression and secretion during immune response (189–191). HSPGs were shown to participate in the nerve injury response, however, their interplay with ApoE in this scenario is not well characterized. HSPG synthesis was identified to be upregulated in astrocytes after brain injury in mice and rats and an increase in HSPG quantity was especially observed around the injury site (192, 193). Increased HSPG expression and secretion may enhance capture of ApoE containing lipoproteins, as well as other growth factors that are secreted by microglia, astrocytes and neurons and therefore promote neuron regeneration (194).

1.4.3 Apolipoprotein E structure and biochemistry

As introduced in Section 1.4, three major ApoE isoform exist due to allelic variance that differ at site 112 and 158 (ApoE2 Cys112/Cys158, ApoE3 Cys112/Arg158, ApoE4 Arg112/Arg158, Figure 1.7) (114, 115). All ApoE isoforms have in their lipid-free state an independently folded amino terminal and carboxyl terminal domain that are linked by a flexible hinge region (195, 196). The hinge region is prone to proteolysis and is cleaved by a variety of enzymes generally generating 22 kDa amino and 10 kDa carboxyl terminal domain digestion products (196).

The amino and carboxyl terminal domain harbour the receptor and lipid binding regions that have characteristic basic and hydrophobic residues (Figure 1.7). Chemical modification of lipoprotein particles revealed that arginine and lysine residues are critical for ApoE mediated uptake of lipoproteins into human fibroblasts via LDLR (197, 198). The first indication that the central region of ApoE (residues 136-158) was involved in receptor binding emerged when the amino acid interchange in ApoE isoform was determined and ApoE2 with its cysteine at site 158 was identified to possess impaired LDLR binding ability (114, 115, 199). Population based studies in patients with type III hyperlipoproteinemia revealed several naturally occurring mutations around the central region that should further help to define the receptor binding residues (200). Eventually, the receptor binding site was narrowed down to residues 134-150; an arginine and lysine rich region located on helix 4 of the amino terminal domain (Figure 1.7) (201–203). However, later studies revealed that full receptor binding activity additionally requires an arginine at site 172 (204). The lipid binding site on the other hand was predicted to be located on the carboxyl terminal domain based on primary structure (115). Apolipoproteins A, C and E have the same genomic structure and likely evolved from a common ancestral gene (205). Similar to other apolipoproteins, the ApoE carboxyl terminus contains amino acid sequences with amphipathic regions that are assumed to take an α-helical conformation. Segrest *et al* (206) hypothesized that these regions have a large apolar face that associates with the fatty acid side chains of phospholipids and a polar face with positively, as well as negatively charged amino acids that interact with the zwitterionic phospholipid polar head group. Assessment of lipid and lipoprotein binding ability of carboxyl terminally truncated ApoE, as well as various carboxyl terminal peptides located the lipid binding region around residues 244-272 (Figure 1.7) (207, 208). Interestingly, the receptor, as well as the lipid binding region seem to both be involved in heparin binding (209–213).

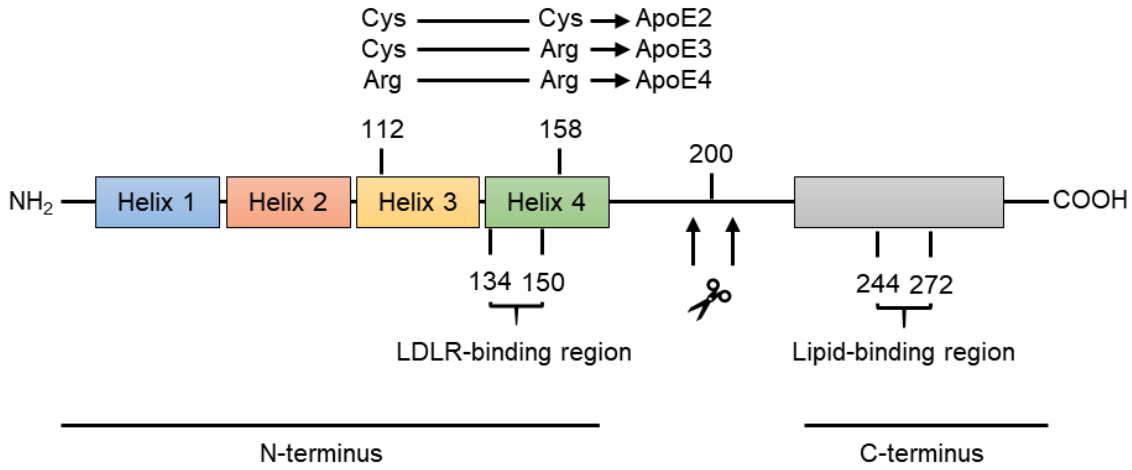

Figure 1.7. ApoE domain structure. A linear model of ApoE structure is shown. ApoE consists of two independently folded domains. A four α-helix bundle that contains the receptor binding site (residues 134-150) and an α-helical carboxyl terminus that harbours the lipid-binding region (residues 244-272). ApoE isoforms differ at sites 112 and 158. ApoE isoforms are prone to proteolysis and are cleaved by a set of proteases such as trypsin and chymotrypsin. Cleavage sites are found between the amino and carboxyl terminus located around site 200.

ApoE is physiologically present on lipoprotein particles and is associated with lipids and cholesterol. The actual amount of lipid-free ApoE is expected to be small. On lipid binding and lipoprotein association, ApoE undergoes substantial conformational changes, firstly inferred from observations made that ApoE's binding affinity to LDLR increases upon lipid binding (214). Further studies showed that binding affinity is also dependent on the presence of other apolipoproteins on the particles. C apolipoproteins (in particular ApoC1 that is also present in the brain) can oppose ApoE function in hepatic clearance of CM remnants, as well as VLDLs as assessed in studies with perfused rat liver (215–217) and presence of C apolipoproteins on VLDLs interferes with ApoE's ability to interact with LRP1 (218, 219). These findings suggest that C apolipoproteins may displace ApoE from VLDLs and/or that they might induce conformational changes of ApoE and abolish its ability to bind to its receptors (216, 219). That ApoE may undergo conformational changes during lipoprotein metabolism was inferred by Sehayek *et al* (220) who investigated the effects of VLDL lipolysis on lipoprotein uptake and degradation in cultured fibroblasts, as well as hepatocytes. Incubation of human plasma derived ApoE-containing VLDLs with exogenous LPL enhanced their uptake and metabolism compared to untreated lipoproteins indicating that lipolysis may induce conversion of ApoE from a "receptor-inactive" to a "receptor-active" conformation. Notably, lipolysis was accompanied by the loss of ApoC1 on VLDLs that would be in accordance of its influence on ApoE conformation (220).

In order to study the conformation of physiologically lipid-bound ApoE, synthetic lipoproteins were used and analysed by fluorescence energy transfer (FRET), electron paramagnetic

resonance spectroscopy (EPR), small angle X-ray scattering (SAXS) and X-ray diffraction. These studies suggest that ApoE folds upon phospholipid binding into an α-helical hairpin-like structure (Figure 1.8) (221–225). Synthetic lipoproteins are ApoE-phospholipid complexes either made with dimyristoylphosphatidylcholine (DMPC) or dipalmitoylphosphatidylcholine (DPPC) and resemble HDLs in terms of density and metabolism (214, 221, 222). X-ray diffraction and SAXS data of ApoE bound to DPPC suggest an ellipsoidal to spheroidal particle surface that holds two horseshoe resembling ApoE molecules (221, 222). The α-helical hairpin model provides an explanation for why lipid association is important for high affinity LDLR binding. In ApoE's lipid-free state, residues that form the receptor binding domain and arginine at site 172, which as mentioned is important for receptor binding activity, are separated by more than 15 Å. However, in the hairpin model all required residues are close together and therefore would result in full receptor binding activity (Figure 1.8) (222, 225).

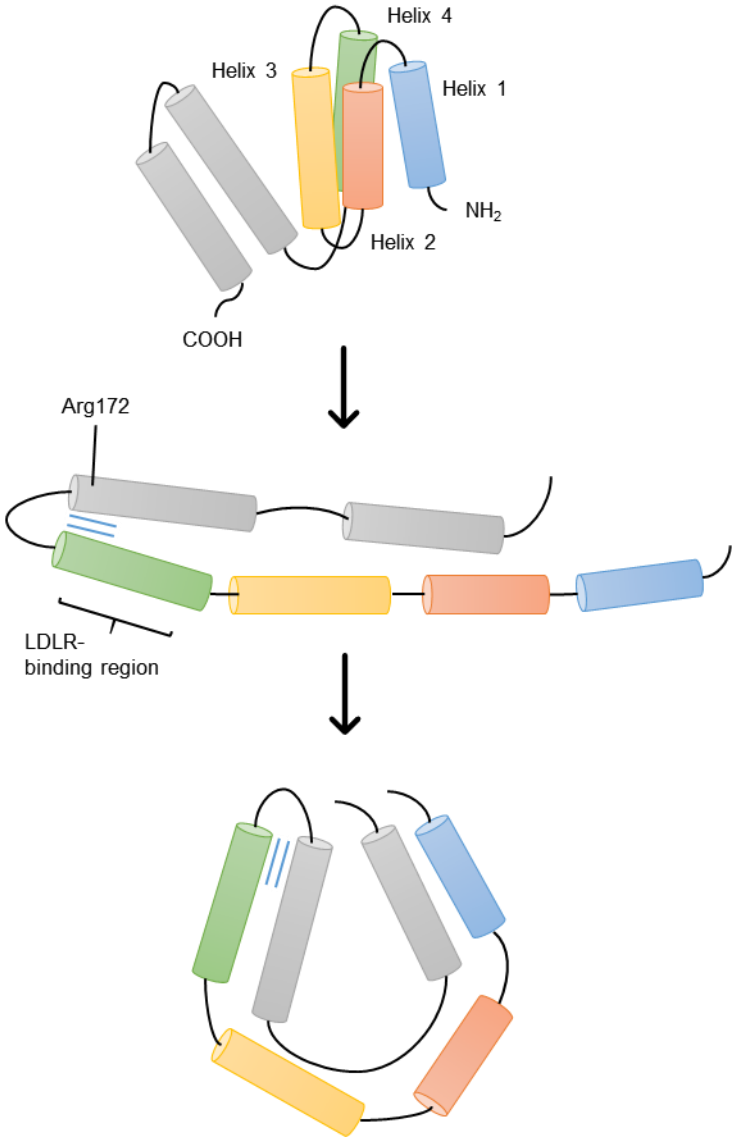

Figure 1.8. The α-helical hairpin-like and horseshoe-like conformation model in ApoE-DPPC particles. Amino terminal helices are highlighted in colours (helix 1 in blue, helix 2 in red, helix 3 in yellow and helix 4 in green), while the carboxyl terminus is shown in grey. Upon lipoprotein binding, ApoE unfolds and adopts a horseshoe-like structure with residues involved in LDLR binding being in close proximity to each other (blue bars indicating alignment of crucial LDLR binding residues). Figure adapted with permission from Elsevier: Hatters, Peters-Libeu, Weisgraber, Trends in Biochemical Sciences, 2006, 31(8):445-454 (226).

Observations made by isothermal titration calorimetry (ITC) (227), surface plasmon resonance (SPR) (228) and fluorescence analysis of ApoE labelled with fluorophores at its amino or carboxyl terminus (229) suggest a two-step binding mechanism of ApoE to small and large emulsions. Initially, ApoE binds to a lipid surface through its carboxyl terminal domain followed by a slower conformational reorganization of its amino terminal helix bundle. This model likely applies for binding of ApoE to large emulsion particles such as VLDLs. Interestingly, not only ApoE-lipid, but also the interaction of ApoE with resident proteins seems to be important for binding to HDLs (228–230). Removal of the carboxyl terminus by site directed mutagenesis

was shown to have minor effects on binding of ApoE to HDLs but had a substantial impact on VLDL binding (230). Most of the HDL particle surface is covered with proteins whereas in VLDLs most of the surface is phospholipids (127). The lipid interaction may therefore play a minor role in binding of ApoE to HDLs compared to other large phospholipid-rich particles (229, 230).

1.4.4 Structural and functional differences between apolipoprotein E isoforms

The amino acid substitutions in ApoE isoforms are thought to have profound effects on their structure and properties. As previously mentioned, ApoE2 is associated with type III hyperlipoproteinemia and was identified as susceptibility factor in the late 1970s (108, 111). ApoE2 isolated from ε2/ε2 homozygotes, as well as from patients with overt hyperlipoproteinemia showed impaired binding to LDLR compared to ApoE3 and ApoE4 (199, 231). Notably, the binding ability of the isoform could be rescued by chemical modification of its cysteine residues into cysteamines that mimic positively charged lysine residues (199). Chemical modification of ApoE3 on the other hand showed no effect on receptor binding ability which suggests the importance of a positive charge at site 158 (199). The high-resolution crystal structure of the ApoE2 amino terminal domain revealed that substitution of arginine to cysteine eliminates a salt bridge that normally forms between Arg158 and Asp154. Asp154 interacts instead with Arg150 and perturbs the electrostatic potential within the receptor binding region, therefore reducing ApoE2's ability to interact with LDLR (232, 233). Elimination of the Asp154 – Arg150 salt bridge in ApoE2 by mutation of Asp154 into alanine increased receptor binding activity of ApoE2 to normal levels and demonstrated the salt bridge to be a key determinant of the defective ApoE2-LDLR binding interaction (232).

The additional arginine at site 112 in ApoE4 compared to ApoE3 is postulated to introduce more rigorous interactions between the amino and carboxyl terminus. This concept termed "ApoE4 domain interaction" is a prevailing hypothesis that postulates an intramolecular salt bridge between Arg61 and Glu255 in ApoE4 (Figure 1.9) (234). Although studies suggest this intramolecular salt bridge as an intrinsic property of ApoE4, there is no direct proof in form of a crystal structure and the theory remains unproven. Other reports propose altered receptor binding ability of ApoE4 or altered quaternary structure as a result of the amino acid interchange. It remains to be elucidated how exactly ApoE4 differs in terms of structure to ApoE2 and ApoE3. Following paragraphs discuss the evidence for and against the ApoE4 intramolecular domain interaction.

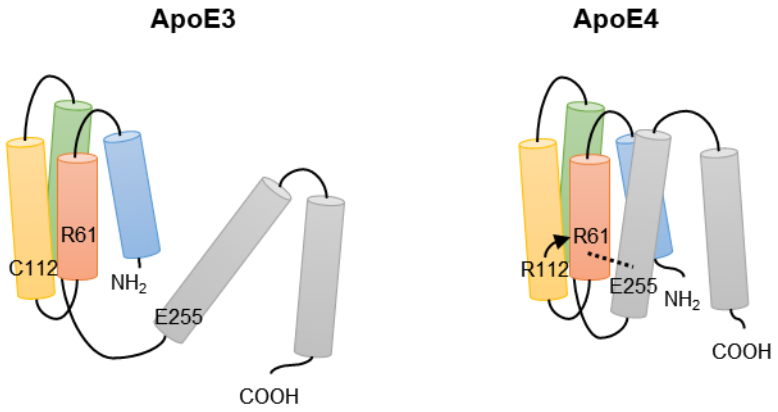

Figure 1.9. ApoE4 domain interaction. The arginine at site 112 in ApoE4 is postulated to orient the side chain of Arg61 so that a salt bridge forms to Glu255, resulting in more rigorous interactions between the amino and carboxyl terminus. In ApoE3 on the other hand, Arg61 is buried between helix 2 (red) and 3 (yellow) which hinders the formation of an intramolecular salt bridge.

ApoE4 was shown to preferentially bind to large lower-density lipoproteins (VLDLs and LDLs) in comparison to ApoE3 that preferably associates with smaller and cholesterol-rich HDLs (235–237). The altered lipoprotein distribution seems to be mediated by the positive charge at site 112. Chemical modification of ApoE3's cysteine into a positively charged cysteamine was shown to shift its binding preference from HDLs to VLDLs, similar to ApoE4 (237). Based on this observation and the fact that the carboxyl terminal domain in ApoE mediates lipid association, Karl Weisgraber at the Gladstone Institute suggested in 1990 that both domains may interact via an ApoE4-specific salt bridge (237). Comparison of lipoprotein distribution of canine ApoE (arginine at equivalent position 112) and rabbit ApoE (cysteine at equivalent position 112) demonstrated however that both mammal apolipoproteins preferentially associate with HDLs identical to human ApoE3 (238). This indicated that ApoE4's preferred binding to VLDLs involved additional residues other than Arg112. The high-resolution crystal structure of the ApoE4 amino terminal domain revealed that Arg112 interacts via a salt bridge with Glu109, leading to conformational changes of the second helix that contains Arg61; while Arg61 is buried in between helix 2 and 3 in ApoE3, it points away in ApoE4 and may interact with acidic residues located on the carboxyl terminus (238). Mutation of Arg61 into threonine resulted in identical lipoprotein distribution of ApoE4 compared to ApoE3 (238). Site directed mutagenesis of acidic residues on the carboxyl terminal domain identified Glu255 as potential interaction partner and its substitution with alanine shifted ApoE4's binding preference from VLDL to HDL particles (239). These studies formed the basis of the ApoE4 domain interaction concept that suggests the Arg61 – Glu255 salt bridge as an intrinsic property of ApoE4 giving it a more compact structure compared to the other two isoforms (Figure 1.9) (237–239). According to Segrest *et al* (206), the length of the amphipathic, lipid binding α-helix in apolipoproteins influences the lipoprotein association. The intramolecular ionic interaction in

ApoE4 may stabilize an extended helical structure in the carboxyl terminus such that it may preferentially bind to less curved VLDLs instead of HDLs (238, 239).

Further biophysical characterization was undertaken to evaluate the ApoE4 domain interaction. To assess the distance between amino and carboxyl terminus in living neurons, ApoE3 and ApoE4 were both fused with yellow and cyan fluorescent protein at their amino and carboxyl terminal domains respectively and the FRET between both fluorescent proteins was measured. Consistent with the domain interaction concept, a greater FRET signal was observed in the ApoE4 fusion protein (240). Additional studies on recombinant ApoE3 and ApoE4 using FRET and EPR support a closer distance of amino and carboxyl terminal domains in ApoE4 (224). Notably, only human ApoE has an arginine at site 61. In other species such as mouse, a threonine is found at the equivalent position (200). Thus, domain interaction in mouse ApoE is not observed, regardless of a cysteine or arginine at site 112 and therefore behaves like human ApoE3 in terms of lipoprotein association. However, substitution of Thr61 with an arginine in mouse ApoE introduced postulated domain interaction and resulted in ApoE4-like properties, with preferred binding to VLDL and LDL over HDL (241).

Although data suggest an Arg61 – Glu255 mediated domain interaction in ApoE4, there is no high-resolution crystal structure of full length ApoE4 available that could directly prove the salt bridge. Arginine at site 61 was identified in the ApoE4 amino terminal domain crystal structure and Arg61 being surface exposed was confirmed in the study to have high flexibility as assessed by its B-factor* (238). To draw conclusions solely based on the crystal structure of the amino terminal domain is difficult and it remains speculative whether Arg61 interacts with Glu255. In fact, a published full length mutant ApoE3 nuclear magnetic resonance (NMR) structure may suggest no interaction between the two residues in ApoE4 (242). Single amino acids were substituted in the carboxyl terminal domain of this ApoE3 mutant to prevent oligomerization and to enable structure determination. These mutations were confirmed not to affect receptor binding activity and biochemical properties (242, 243). The NMR structure revealed an overall six helix bundle with extensive amino and carboxyl terminal domain interactions (242). Arg61 forms a hydrogen bond with Thr194 and Glu255 a salt bridge with Lys95. Notably, solvent exposed Arg61 and Glu255 are separated by a carboxyl terminal helix that mostly contains hydrophobic residues (242, 244). The LDLR binding region located on helix 4 interacts with the carboxyl terminus and all lysine, as well as arginine residues involved in receptor binding are shielded. This is in accordance with observations made that LDLR binding affinity of lipid-free ApoE is reduced (214). Based on these findings Frieden & Garai (245) suggested an alternative pathway that may cause the structural differences between

* The B-factor or sometimes referred as the temperature factor is a parameter that reflects the mobility of each atom in space. High B-factors represent high mobility (470).

ApoE3 and ApoE4. The Cys112 – Arg112 interchange in ApoE4 would affect movement of additional residue Arg114 that in turn would perturb ionization of His140. This eventually would affect the charge distribution in the receptor binding region on helix 4 and cause the functional differences between both isoforms (245).

Other studies using improved cellular FRET systems to evaluate ApoE4 domain interaction have confirmed the greater FRET signal in the ApoE4 constructs (246, 247). However, this may be the result of altered intermolecular interactions between ApoE4 molecules instead of an intramolecular salt bridge. A more recent study by Kara *et al* (247) has shown substantial intermolecular interaction of ApoE in HEK cells, as well as astrocytes as assessed by FRET of GFP and red fluorescence protein (RFP). Intermolecular interactions between ApoE4 molecules and therefore its FRET signal were much stronger compared to ApoE2 and ApoE3 suggesting that ApoE4 molecules come either closer together, have altered quaternary structure or may form larger complexes (247). Consistently, expression of the monomeric ApoE3 mutant that was used to solve the NMR structure showed much lower intermolecular interaction and therefore reduced FRET signal within cells (247).

ApoE isoforms seem also to differ in terms of chemical and thermal stability. ApoE4 was shown to be the least resistant to thermal and chemical denaturation, while ApoE2 shows highest and ApoE3 intermediate resistance (ApoE4 < ApoE3 < ApoE2) (248–250). These studies indicated a three-state denaturation process (folded/intermediate/unfolded) with a thermodynamically stable intermediate in ApoE4 that possesses structural characteristics of a molten globule[*] (248, 250). ApoE4's decreased stability and molten globule formation seem to drive its propensity to form soluble, fibril-like oligomers; ApoE2 and ApoE3 on the other hand do not form high molecular weight species to such extent (251). Aggregation does not seem to be an effect of postulated ApoE4 domain interaction. Mutation of Glu255 into alanine did not alter ApoE4 aggregation behaviour, however, substitution of Arg61 with a threonine markedly reduced self-association into higher molecular weight species (251).

The amino acid substitutions in ApoE isoforms clearly have pronounced effects on their structure and properties. While the amino acid change in ApoE2 has a well-defined effect on its receptor binding activity, the effect of the arginine interchange in ApoE4 seems less clear. A secondary objective of this thesis is to compare the structure of ApoE isoforms in solution, as well as attempt crystallization of full length ApoE4. Decreased conformational stability, as

[*] Molten globules can be described as reactive intermediates that are a *"highly dynamic form with native-like secondary structure and a loose protein core that admits solvent. The related (but still controversial) dry molten globule is an expanded form of the native protein with largely intact topology but a tighter protein core that excludes solvent."* (471).

well as altered structure of ApoE4 are hypothesized to influence its lipid and receptor binding properties and to contribute to ApoE4's pathophysiological role in AD (252).

1.5 Role of Apolipoprotein E4 in Alzheimer's disease

Although data suggest that ApoE4 contributes to AD pathogenesis through both Aβ-dependent and independent pathways (Table 1.1, Figure 1.11), the precise pathogenic nature of ApoE4 in AD remains elusive. Co-localization *in vivo* of ApoE and Aβ was shown by immunostaining analysis (104, 253, 254) and pathological studies indicated a positive correlation between plaque density and ε4 allele dose in AD patients (255–257). Several PET studies using ^{11}C Pittsburgh compound B (^{11}C-PiB) or Florbetapir (^{18}F) matched these histological findings and demonstrated that cognitively normal and demented ApoE4 carriers have higher cortical Aβ deposition than non-carriers (258–263). These findings strongly suggest an interplay between ApoE4 and Aβ in AD pathology but the mechanism by which ApoE isoforms modulate Aβ metabolism on the molecular and cellular level is still unclear.

Table 1.1. Effects of ApoE3 versus ApoE4.

Protective effects of ApoE3	Detrimental effects of ApoE4
Stimulates neurite outgrowth	Inhibits neurite outgrowth
Protects from neurodegeneration	Causes neurodegeneration
Protects from cognitive decline	Causes cognitive decline
Protects tau from phosphorylation	Stimulates tau phosphorylation
Antioxidative effect	Disrupts neuronal cytoskeleton
Stimulates cholesterol efflux	Causes neurodegeneration by ApoE4 fragments
Stimulates Aβ clearance	Enhances Aβ deposition
Stimulates synaptic plasticity	Potentiates Aβ-induced lysosomal leakage and apoptosis

Table adapted from Mahley, Weisgraber, Huang, National Academy of Sciences, 2006, 103(15):5644-51 (234).

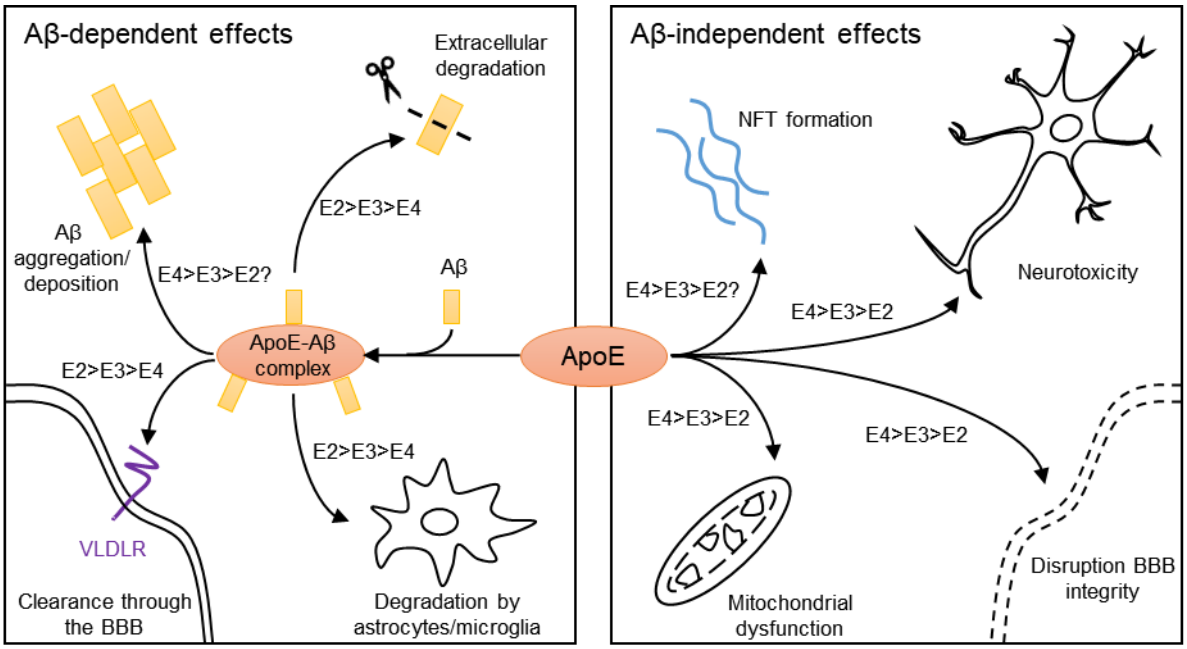

Figure 1.10. Aβ-dependent and Aβ-independent effects of ApoE4 in Alzheimer's disease. Shown are presumed effects of ApoE4 on Aβ aggregation and clearance (left) and Aβ-independent effects (right). Aβ associates with ApoE-containing lipoproteins that promotes Aβ clearance through the BBB mediated by the VLDL receptor (VLDLR), degradation by immune cells and extracellular degradation by proteases. Clearance and degradation are impaired when complexed with ApoE4-containing lipoproteins. Additionally, ApoE4 seems to promote Aβ aggregation and deposition. Independent of the amyloid peptide, ApoE4 seems to promote tau fibril and therefore NFT formation, disrupt BBB integrity as well as mitochondrial function and was shown to have neurotoxic properties.

1.5.1 Effects of Apolipoprotein E4 on Aβ aggregation and deposition

Studies on the interaction between ApoE and Aβ and the effects of ApoE isoforms on Aβ aggregation are contradictory. Interaction *in vitro* between ApoE and Aβ was shown by using synthetic Aβ peptides and ApoE either secreted from mammalian cells (264, 265), purified from human CSF (266) or human plasma (267, 268). Studies using ApoE derived from human plasma that is delipidated in the purification process demonstrated that lipid-free ApoE forms detergent-stable complexes with the amyloid peptide and that binding occurs faster in ApoE4 than in ApoE3 (267, 268). Conversely, other studies demonstrated that lipid associated ApoE3 binds greater to Aβ than ApoE4 (264, 265, 269–271). LaDu and colleagues (269) investigated the discrepancy and confirmed that delipidation of ApoE attenuates the isoform-specific binding to Aβ. Lipoproteins secreted by ApoE3-expressing mammalian cells or native VLDLs from ε3/ε3 homozygotes showed increased binding of the amyloid peptide compared to ApoE4 containing lipoproteins. However, isolation of ApoE and removal of lipids resulted in an increase in Aβ binding to ApoE4 (269). Follow-up binding studies of ApoE containing lipoproteins isolated by various cell lines confirmed higher binding affinity of ApoE3 to the

amyloid peptide compared to ApoE4 whereas delipidation decreased affinity, as well as abolished isoform-specificity (270).

Numerous studies also investigated the effects of ApoE on Aβ aggregation. ApoE isoforms readily form high molecular weight complexes with the amyloid peptide that can be isolated by gel filtration chromatography and ApoE4 seems more likely to promote Aβ aggregation and fibrillogenesis *in vitro* than ApoE3 (272–275). However, many other studies obtained the opposite results and reported that both ApoE3 and ApoE4 delay or inhibit Aβ fibrillogenesis *in vitro* (276–280). Studies by Strittmatter *et al* (267) identified the carboxyl terminus lipid binding region of ApoE to be critical for complex formation with Aβ. Later studies additionally demonstrated that amyloid peptide interacts with ApoE through its receptor binding region and was shown to compete for the metabolism of ApoE-containing VLDLs by binding to HSPGs (281). It has been speculated that ApoE may sequester soluble amyloid peptide and therefore interfere with Aβ nucleation and aggregation into insoluble fibrils (282). Data from Cerf *et al* (283) suggest that ApoE inhibits amyloid peptide fibril formation by stabilizing Aβ in its oligomeric conformation. Notably, ApoE4 seems to have greater tendency to block Aβ in its oligomeric state compared to ApoE3 (283). As Aβ oligomers were postulated to be the toxic species in AD (Section 1.2.1), the observation by Cerf and colleagues (283) proposes an Aβ-dependent role of ApoE4 in AD by promoting oligomer formation. Collectively, the *in vitro* binding studies do not answer whether ApoE4 is either more likely to promote Aβ aggregation or to inhibit fibrillogenesis. Differences in ApoE and Aβ preparations, the origin and state of ApoE (e.g. plasma derived, lipoprotein-bound, lipid-free etc), as well as differences in the conditions used to induce Aβ aggregation may have caused the conflicting results between the *in vitro* studies (284).

The effects of ApoE isoforms on Aβ deposition in transgenic mice are more conclusive. Initial studies using PDAPP transgenic mice that overexpress human APP and develop characteristic Aβ pathology (285), showed a significant decrease in Aβ deposition when lacking murine ApoE (286, 287). Following these knockout models, several transgenic mice were generated either expressing murine ApoE, human ApoE isoforms or no ApoE. Primarily studies by Holtzman *et al* (287) observed suppression of early Aβ deposition in 9 month old mice expressing human ApoE3 or ApoE4, suggesting that human ApoE isoforms decrease Aβ deposition or increase its clearance. However, in a follow up study, Holtzman *et al* (288) showed that most ApoE4-positive and some ApoE3-positive mice at the age of 15 months began to develop Aβ plaques with greater deposition in ApoE4-expressing mice. Interestingly, endogenously expressed murine ApoE resulted in significantly more Aβ deposition compared to human ApoE (288). Similarly, Fagan *et al* (289) observed over a longer period markedly delayed Aβ deposition in aged mice (18 – 24 months) when expressing human ApoE isoforms instead of mouse ApoE.

But, analysis of the older animals revealed an earlier age at onset of Aβ pathology and increased Aβ plaque formation in ApoE4 mice compared to their ApoE3 counterparts (289). Gene delivery of human *APOE* into APP transgenic mice confirmed the ApoE isoform-specific differences in Aβ deposition with the expression of ApoE4 resulting in higher plaque load (290, 291).

1.5.2 Effects of Apolipoprotein E4 on Aβ clearance

Besides influencing Aβ aggregation and fibril formation, evidence suggests that ApoE may alter transport and metabolism of Aβ in brain. Aβ production and secretion is not unique to AD pathology, but is a constitutive process that is product of normal cell metabolism throughout life (25–27). Aβ is efficiently cleared under physiological conditions via three major pathways including (i) proteolytic degradation, (ii) cellular clearance through lysosomal degradation by microglia and astrocytes and (iii) cerebrovascular system-mediated clearance through the interstitial fluid (ISF) and across the BBB (292).

Several studies identified a large set of zinc-metalloproteases, as well as serine and aspartyl proteases that are involved in intracellular and extracellular degradation of the amyloid peptide. Most prominent examples that have extensively been investigated include the zinc-metalloproteases neprilysin (NEP), as well as insulin-degrading enzyme (IDE) (293). Deletion, inhibition or knockout of these enzymes in mice or rats was shown to increase Aβ levels and to promote accumulation of the amyloid peptide in the brain (294–296). Overexpression of NEP or IDE on the other hand was demonstrated to decrease Aβ pathology and plaque formation in mouse models of amyloidosis (297, 298). Notably, proteolytic degradation of Aβ peptide seems to be enhanced when it was in complex with ApoE. Treatment of microglia isolated from *APOE* deficient mice with ApoE-containing HDLs markedly increased degradation of soluble Aβ; ApoE2-HDLs and ApoE4-HDLs being the most and least efficient respectively. Modulation of ApoE lipidation status by influencing ABCA1 expression showed that increased levels of lipidated ApoE enhanced the capacity of NEP and IDE to degrade the amyloid peptide (299). It has been speculated that the proteases are more likely to recognize Aβ when complexed with ApoE-containing lipoproteins (292).

Activated microglia, as well as astrocytes are found closely associated with amyloid plaques in patients with AD and electron microscopy studies revealed that microglia ingest amyloid fibrils and store them in phagosomes (300–303). As outlined in Section 1.4.3, expression and secretion of ApoE in microglia is highly increased in CNS inflammatory response and clearance, as well as degradation of Aβ by immune cells seems influenced by the ApoE genotype. Primary astrocytes from *APOE* knockout mice, as well as macrophages were shown to have impaired ability to degrade Aβ from plaque bearing PDAPP mouse brain sections and

degradation by wild-type immune cells was blocked by inactivation of LDLR and related receptors (304, 305). Additionally, macrophage-mediated degradation was most efficient by ApoE2-expressing cells, not only *in vitro*, but also *in vivo* as assessed after direct intracerebral injection of macrophages into old PDAPP mouse brain (305). Microglial cells and macrophages can take on a classical activated status (M1) in which pro-inflammatory cytokines are released and an alternatively activated stage (M2) in which anti-inflammatory factors are produced (306). Decreased anti-inflammatory functions and increased activation, as well as release of pro-inflammatory cytokines by glial cells were shown in ApoE4 transgenic mice when injected with lipopolysaccharide (LPS) (307). Additionally, microglia from ApoE4 transgenic mice showed slower migration in an *in vitro* chemotaxis migration assay compared to ApoE3 microglia (308). This data indicates that ApoE4 may be less effective in mediating Aβ clearance by microglia due to impaired ability to activate phagocytosis and migration (292).

Levels of CSF $A\beta_{42}$ were consistently shown to be lower in AD patients that is likely a result of $A\beta_{42}$ being sequestered into amyloid plaques (309). Low CSF $A\beta_{42}$ levels are therefore biomarkers for amyloid plaque formation in the living person (7). Studies that accounted for *APOE* genotype showed markedly decreased levels of CSF $A\beta_{42}$ in ε4-positive healthy control groups, as well as AD patients compared to ε4-negative individuals (310, 311). This data suggests that ApoE4 influences Aβ metabolism and is likely to impair its clearance from the brain, therefore promoting its deposition into plaques. A study in PDAPP transgenic mice confirmed impaired metabolism of Aβ in ApoE4 PDAPP mice (311). Halting of Aβ production with the potent and selective γ-secretase inhibitor LY411,575 demonstrated a longer half-life of Aβ in the hippocampus of ApoE4 PDAPP mice compared to ApoE2 and ApoE3 transgenes suggesting impaired amyloid peptide clearance from the brain by ApoE4 (311).

Efflux of Aβ from the brain through the BBB is mediated by the superfamily of LDLR proteins, as well as HSPGs (292). LRP1 was identified as the major efflux receptor for Aβ at the BBB by a series of *in vivo* experiments in which radiolabelled amyloid peptide was injected into animal brain tissue and their clearance into plasma tracked in the absence of LRP1 function (312–315). The amyloid peptide binds with high affinity to LRP1 as determined by SPR binding studies and the aggregation-prone $A\beta_{42}$ peptide exhibits greatly reduced binding affinity compared to $A\beta_{40}$ (314). As a result, clearance of $A\beta_{42}$ across the BBB in mice was significantly slower compared to the shorter peptide (312, 314). Notably, $A\beta_{40}$ in complex with ApoE4 was cleared at a slower rate across the BBB in mice compared with the two other isoforms (312, 316). Transport of ApoE-containing lipoproteins across the BBB is very slow and occurs predominantly via VLDL receptor (VLDLR). Complexation of Aβ with ApoE shifted the clearance from the fast LRP1-mediated pathway to the slow VLDLR transport mechanism (316). Moreover, ApoE4 was reported in *APOE* knock-in mice to disrupt BBB integrity that

results in reduced cerebral blood flow (317, 318). This might further retard Aβ clearance across the BBB and potentially drive cerebral amyloid angiopathy (CAA) by deposition of Aβ into walls of the blood vessels. Respectively, studies and meta-analyses showed possible association and severity of CAA in carriers of the ε4 allele (319–321).

1.5.3 Aβ-independent effects

The influence of *APOE* genotype on CSF tau biomarkers in healthy individuals, as well as AD patients is less clear compared to amyloid peptide levels. AD patients generally present higher total and phosphorylated CSF tau levels, but no correlation with *APOE* genotype was found (259, 322, 323). A significant influence of ε4 genotype on total and phosphorylated CSF tau is however observed in patients with mild cognitive impairment (MCI) (322, 323). Expression of human ApoE4 in mice under control of a neuron-specific enolase promoter (NSE) markedly increased brain accumulation of phosphorylated tau compared to ApoE3 expressing mice (324). A recent study by the Holtzman group (325) provided direct evidence that ApoE4 influences tauopathy independent of Aβ. P301S mice that overexpress human tau were cross-bred with knock-in mice with different human *APOE* genotypes and significantly greater brain-atrophy was observed in P301S/ApoE4 mice compared to the ApoE2 and ApoE3 counterparts. Cultured P301S/ApoE4 microglia that were stimulated with LPS exhibited increased upregulation of proinflammatory genes compared to P301S/ApoE3 microglia and increased neuronal death occurred in P301S mouse primary neurons co-cultured with mixed glia cells derived from ApoE4 knock-in mice. Interestingly, the absence of ApoE in P301S mice attenuated brain atrophy and inflammatory response suggesting an ApoE, in particular ApoE4, gain of toxic function in tau-mediated neurodegeneration (325). However, a follow-up study by Zhao *et al* (326) came to opposite results and found significantly increased tau pathology in ApoE2 (> ApoE3 > ApoE4) transgenic mice expressing human tau protein bearing the P301L mutation. In contrast to the transgenic mice by the Holtzman group that were generated by cross-breeding (325), Zhao *et al* (326) introduced the tau P301L mutation via viral delivery in human ApoE targeted replacement mice. The discrepancy between the two studies is likely a result of the different model systems used that differ in terms of tau expression levels (transgenic versus viral mediated) and toxicity of the tau species (P301S versus P301L). Further studies are therefore necessary to investigate the effects of ApoE in different model systems (326).

Behavioural studies gave additional insight into ApoE4's effects in AD pathology. Especially female mice expressing the ApoE4 isoform under the NSE promoter showed impaired performance in the water maze test and only ApoE3 was neuroprotective against kainic acid-induced neurodegeneration as assessed by staining for synaptic markers (327, 328). Similarly,

human ApoE4 knock-in mice showed an age-dependent decrease in GABAergic neurons that correlated with impaired spatial learning and memory (329, 330).

ApoE4's Aβ independent neurodegenerative effects may be explained by its increased susceptibility for proteolytic cleavage in neurons. Higher levels of ApoE4 fragments were identified in NFTs and amyloid plaques of AD patients compared to matched controls and increased proteolysis of ApoE4 was confirmed *in vitro* in transfected neuronal cells, as well as *in vivo* in ApoE4 transgenic mice (331–333). Fragmentation seems to be caused by a chymotrypsin-like serine protease that results in the generation of ApoE carboxyl and amino terminal fragments. In particular the amino terminal fragment was found to be present in NFTs of AD patients and expression of ApoE4 lacking residues 272-299 in mouse neuroblastoma cells resulted in the formation of intracellular NFT-like inclusions (332). The fragments were demonstrated to escape the secretory pathway and to interact with subunits of the mitochondrial respiratory complexes (334, 335). ApoE4 seems to negatively affect mitochondrial respiratory capacity and reduced levels of all mitochondrial respiratory complexes was shown in primary neurons derived from ApoE4 transgenic mice compared to ApoE3 neurons (336). Toxicity of the ApoE4 carboxyl terminal truncated fragments was further investigated in ApoE transgenic mice (333). Mice expressing high levels of ApoE4 lacking residues 272-299 died at young age and displayed AD-like neuropathological alterations such as abnormally phosphorylated tau protein. Animals expressing moderate protein levels were viable, but showed impaired learning and memory as assessed by the Morris water maze compared to wild type littermates (333). It has been suggested that ApoE4 when expressed in neurons induced by stressors (e.g. injury, oxidative stress) is proteolytically cleaved to a greater extent than ApoE3. ApoE4 fragments enter the cytosol and interfere with cytoskeletal components such as tau protein and neurofilaments leading to cytoskeletal disruption, mitochondrial dysfunction and neurodegeneration (337, 338).

A recent study by Yadong Huang and colleagues (339) strongly suggests an ApoE4 gain of toxic function and confirmed many of ApoE4's pathophysiological effects presented in this section. Human induced pluripotent stem cells (iPSCs) were generated from ε3 or ε4 homozygotes and differentiated into mature neurons. A significantly higher ratio of ApoE fragments to full length protein was observed in ApoE4 neurons compared to ApoE3. ApoE4 neurons secreted more soluble Aβ as a result of altered APP metabolism and showed higher levels of phosphorylated tau. However, the effect of ApoE4 on tau phosphorylation was demonstrated to be independent of increased amyloid peptide secretion as increased phosphorylated tau levels were still measured after treatment of neurons with potent β- and γ-secretase inhibitors. Less GABAergic neurons were seen amongst neurons derived from ApoE4 iPSCs (which was not a developmental effect; the decrease in GABAergic neurons

occurred during late stages of neuronal differentiation) and ApoE4 GABAergic neurons showed higher levels of phosphorylated tau compared to the ApoE3 counterparts. Notably, gene editing of ApoE4 iPSCs into an isogenic ApoE3 cell line abolished the effects and lentiviral re-introduction of ApoE4 into *APOE* deficient neurons that were derived from an *APOE* deficient individual reproduced the pathophysiological effects on Aβ production, tau phosphorylation and GABAergic survival (339).

1.6 Therapeutic approaches to modulating ApoE function

Although the vast amount of biochemical, cell biological and animal studies provide explanations on how ApoE4 may contribute to AD pathology, many of these processes are still poorly understood and often remain speculative and, in some cases, contradictory. Recent data suggests an ApoE4 gain of toxic function, however, other studies provide evidence for a loss of normal function. Therefore, proposed therapeutic strategies either aim to decrease the toxic effects of ApoE4 by modulating its structure or to restore its physiological function by regulating its expression levels or lipidation state (Figure 1.11) (340, 341).

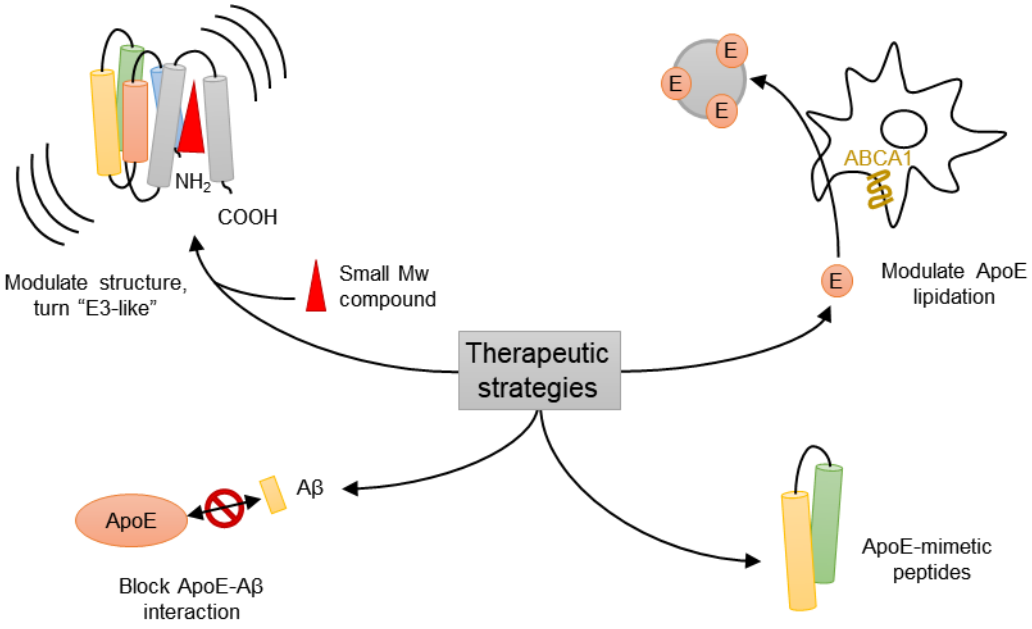

Figure 1.11. Therapeutic approaches towards ApoE. Therapeutic strategies aim to decrease the toxic effects of ApoE4 and/or restore its physiological function. Therapeutic approaches include (i) modulation of ApoE4 structure by small molecular weight (Mw) compounds and turn it "ApoE3-like", (ii) modulation of ApoE4 lipidation state through activation of ABCA1, (iii) blockage of the ApoE-Aβ interaction and (iv) ApoE-mimetic peptides that mimic beneficial effects of ApoE.

As outlined in Section 1.5.2, enzymatic degradation of Aβ is facilitated by ApoE and was shown to be dependent on ApoE lipidation status (299). ApoE is lipidated by ABCA1 (Section 1.4.2) and overexpression of ABCA1 in PDAPP transgenic mice markedly reduced amyloid peptide deposition as a result of increased ApoE lipidation (166). These observations gave rise to a

therapeutic approach to increase levels of functional and lipidated ApoE by modulation of ApoE, as well as ABCA1 expression. Transcription of ApoE and ABCA1 in macrophages, adipocytes and astrocytes is regulated by liver X receptors (LXRs) that form heterodimers with retinoid X receptors (RXRs) (342–345). LXRs are ligand-activated transcription factors and are strongly activated by oxysterols (i.e. oxidized cholesterols) (346, 347). Administration of nonsteroidal LXR agonists GW3965 (GlaxoSmithKline) or T0901317 (Tularik, now Amgen) were shown to increase ApoE, as well as ABCA1 expression levels in mouse models of amyloidosis and to reduce amyloid burden by promoting Aβ clearance; these effects were accompanied by an improvement in spatial memory (299, 348, 349). Unfortunately, direct LXR agonists are hepatotoxic and promote triglyceride synthesis in the liver, as well as VLDL secretion which complicated the development of LXR agonists for the clinic (350).

While some data suggests that increasing expression levels of functional ApoE via activation of the LXR pathway may be beneficial, other studies propose that decreasing, rather than increasing ApoE levels may be of therapeutic value (351). However, the physiological effects of reduced ApoE expression levels in humans remain unclear. In fact, a loss of expression and therefore loss of ApoE function may have toxic effects and needs further evaluation.

Another still controversial therapeutic approach is the use of ApoE-mimetic peptides that possess structural and biological features of the ApoE amino terminal domain. Most prominent peptides include COG133 (ApoE residues 133-149) and COG1410 (ApoE residues 138-149; 2-aminoisobutyric acid at position 141 and 145) that were shown to decrease LPS stimulated inflammatory response in primary mouse microglia, as well as *in vivo* in C57BL6/J mice (352–354). Subcutaneous administration of COG1410 to APP transgenic mice improved learning and memory compared to matched controls and decreased NFT-like pathology, as well as amyloid peptide brain pathology (355). Similar effects were demonstrated with COG133 in a *Drosophila* model of AD (356). Alternative synthetic peptides that block the ApoE/Aβ interaction were also proposed as potential therapeutic agents. These peptides such as $A\beta_{12\text{-}28}P$ (valine at position 18 substituted for proline) mimic the amyloid protein and bind with high affinity to ApoE (357). In APP/PS1 mice, $A\beta_{12\text{-}28}P$ reduced ApoE-positive plaque burden and resulted in improved working memory (357, 358). The effects of $A\beta_{12\text{-}28}P$ were additionally investigated in a noncontact neuron-astrocyte co-culture system (359). Hippocampal mouse primary neurons were shown to have a greater intraneuronal accumulation of exogenous Aβ when co-cultured with astrocytes compared to neuronal cultures alone. This observation suggested an increased uptake of amyloid peptide via ApoE-containing lipoproteins that were secreted by the astrocytes. Addition of $A\beta_{12\text{-}28}P$ to the co-culture medium reduced intraneuronal amyloid peptide accumulation and additionally prevented loss of synaptic proteins such as synaptophysin (359). As outlined in section 1.5.2, efflux of the amyloid peptide through the

BBB is mediated by LRP1, however, is shifted to the slow VLDLR pathway when complexed with lipid-associated ApoE (316). Blocking the ApoE-Aβ interaction would therefore enhance clearance of free Aβ from the brain (316). Further mapping of the ApoE/Aβ interaction by Liu *et al* (360) identified shorter peptide variants, as well as Congo Red dye and the X-34 dye derivate to be able to block the apolipoprotein – amyloid peptide interaction.

The structural difference amongst ApoE isoforms is believed to alter ApoE biology and function. As outlined in Section 1.4.4, the amino acid substitution in ApoE4 has been postulated to alter ApoE4 tertiary and/or quaternary structure that results in the ApoE4-associated neuropathology (234, 252). A structural difference between ApoE isoforms paved way for the therapeutic strategy to convert ApoE4 into an ApoE3-like molecule by small molecule "structure correctors" (234).

A first set of structure correctors was described by Ye *et al* (361) in 2005 who screened *in silico* for molecules that are potentially capable of binding to the amino terminal domain of ApoE4. Some of these *in silico* hits were observed to shift ApoE4's preferred VLDL binding affinity to HDLs, identical to ApoE3, and additionally, decreased Aβ production in APP overexpressing B103 rat neuroblastoma cells (361). These molecules named GIND (for Gladstone Institute of Neurological Diseases) were further characterized in follow-up studies and reported to restore expression levels of mitochondrial respiratory complexes in cultured brain cortical neurons (but not astrocytes) extracted from ApoE4 transgenic mice, as well as to restore processing of ApoE4 through the secretory pathway (336, 362). Members of the GIND series were shown to modulate ApoE4 structure in living neuronal cells as assessed by the intracellular FRET assay (Section 1.4.4) (240, 363). A second structure corrector series was published a few years later by Chen *et al* (246) that include molecules with a phthalazinone core structure. These molecules were demonstrated to modulate ApoE4 structure in cells and to abolish many of its detrimental effects on mitochondrial respiratory function, mitochondrial motility and neurite outgrowth (246). However, the phthalazinones caused significant toxicity in mice and alternative, non-toxic pyrazoline analogues were identified that are currently in pre-clinical trials (364). One goal of this thesis is to identify small molecules that preferentially bind to ApoE4 and that can be utilized as novel chemical probes.

1.7 Summary, Hypothesis and Objectives

ApoE is the major lipid and cholesterol carrier in the brain and therefore is important in brain development, synaptogenesis and regeneration. It re-distributes lipoprotein components by interacting with specific receptors that are members of the LDLR family of proteins, as well as via proteoglycans including HSPGs (365). Often, LDLRs cooperate with HSPGs to internalize lipoprotein particles and cooperation was particularly proven important for the LRP1-HSPG pathway (142). The interaction of ApoE with HSPGs has not been well characterised and comparative binding studies between ApoE isoforms to HSPGs are lacking. ApoE isoforms differ at their sites 112 and 158 by a cysteine-arginine interchange that affects their functionality. The cysteine in ApoE2 markedly reduces its binding affinity to LDLR, whereas the arginine in ApoE4 was shown to alter its structure and possibly introduce more rigorous domain interactions that may also influence its receptor binding ability (226). However, the exact mechanisms by which ApoE4 gains a toxic function compared to ApoE3 remains elusive but could most likely be receptor-mediated such as by HSPGs. Novel tool compounds that bind to ApoE4 and modulate its structure could be used to investigate these mechanisms and potentially be utilized to reverse its pathophysiological properties. **The overarching hypothesis of this thesis is that the structural difference in ApoE4 compared to ApoE3 confers its functional difference and in particular alters its receptor binding ability.** The main goal of this thesis is to investigate and compare the ApoE-HSPG interaction between the isoforms and to identify new ApoE small molecule tool compounds. *In vitro* biophysical techniques were used in this thesis to study the hypothesis and the main goal was achieved by the following specific objectives:

Aim 1. To develop a novel method for the expression and purification of recombinant ApoE and to compare their structure in solution, as well as to attempt ApoE crystallization.

Aim 2. To determine differences in heparin (as model of HSPGs) binding between ApoE isoforms by small angle X-ray scattering (SAXS).

Aim 3. To identify novel ApoE tool compounds that preferentially bind to ApoE4 over ApoE2 and ApoE3 by using biophysical assays.

2 ESTABLISHMENT OF A NOVEL APOE PURIFICATION PROTOCOL AND BIOPHYSICAL CHARACTERIZATION OF APOE ISOFORMS IN SOLUTION

2.1 Introduction and Objectives

ApoE can be isolated from plasma (366), CSF (160) or it can be recombinantly expressed in mammalian cell lines such as immortalized astrocytes (367) and hepatoma cells (123, 368). Large quantities can also be produced in *Escherichia coli* (*E. coli*) (369) that is particularly advantageous for biophysical studies such as SAXS and for protein crystallization since these methods require high amounts of protein. However, depending on the recombinant expression system, ApoE may differ in terms of glycosylation and lipidation state.

Unlike ApoE that is derived from plasma or secreted by astrocytes in form of nascent HDLs (367), the recombinant protein produced in *E. coli* is not associated with lipoproteins and additionally does not undergo posttranslational modifications. Sialylated forms of ApoE are present in plasma and CSF that can be resolved by gel electrophoresis (113, 116). The attachment of sialic acid-containing carbohydrates occurs at threonine 194 via *O*-linked glycosylation and results in a heterogeneous mixture of apparent higher molecular weight species (34 – 39 kDa) that can be resolved by 2D gel electrophoresis and isoelectric point focusing (113, 116, 370). It has been hypothesized that sialylated forms of ApoE play an important role in neuron regeneration after injury (371). For instance, increased secretion of a 37 kDa sialylated ApoE by macrophages was observed during immune response after peripheral, as well as optic nerve injury in rats (182–184). Sialylated forms are especially associated with neurons and account for approximately 50% of total neuronal ApoE as shown in neuron cultures isolated from transgenic mice (371). However, the importance of glycosylation on ApoE function is still unclear and a major proportion of human CSF and particularly plasma ApoE remains asialylated (372–374).

Recombinant, non-glycosylated ApoE expressed in *E. coli* was shown to behave in an identical manner to plasma-derived protein in terms of receptor binding affinity, lipid binding and stability (369, 375, 376). Recombinant ApoE retains its functionality *in vivo* and was shown to promote lipoprotein uptake into human fibroblasts, as well as accelerate plasma lipoprotein clearance when infused into rabbits (131, 218). Therefore, ApoE expressed and purified from *E. coli* not only appears functionally relevant but also provides a system that can produce large quantities of protein for subsequent biophysical characterisation (375). In this regard, SAXS and protein crystallization particularly require pure and monodisperse protein (377). Glycosylation of ApoE

in mammalian expression systems results in the production of heterogenous ApoE that can be disadvantageous for its biophysical characterization and crystallization (375).

Delipidated plasma-derived, as well as *E.coli* produced recombinant ApoE are tetrameric in solution, elongated in shape with oligomerization being mediated by the carboxyl terminal domain (195, 208, 378, 379). Other oligomeric species are present and formation of higher molecular weight species is dependent on ApoE concentration (378, 379). Self-association studies by measuring intermolecular tryptophan or protein label (i.e. Alexa dye) fluorescence and analytical ultracentrifugation (AUC) equilibrium studies are consistent with a monomer – dimer – tetramer equilibrium with tetrameric ApoE presenting the major component (379, 380). In particular ApoE4 seems more prone to form large species that were shown to assemble into fibril-like structures (251, 378). The tendency of ApoE to form high-molecular weight species, as well as being sensitive to proteolytic cleavage (196, 379) has hindered crystallization of the full-length protein. Crystal structures are available of the proteolytically-cleaved amino terminal domain that forms a four-helix bundle and is predominantly monomeric in solution (195, 232, 233). Generation of a monomeric ApoE mutant enabled determination of a full-length NMR structure (242). Specific residues (F257A, W264R, V269A, L279Q, V287E) were mutated in the carboxyl terminus of ApoE to prevent oligomerization without affecting LDLR binding affinity and lipid-binding (242, 243). ApoE in its monomeric form is globular in shape and forms a six-helix bundle with extensive interactions between the amino and carboxyl terminus (242). However, the monomeric NMR structure does not reflect the nature of tetrameric wild type ApoE in solution that is likely to differ substantially in tertiary structure. Mutations inserted to keep ApoE3 in its monomeric state are substantial and the very most C-terminal residues (277-299) in the NMR model are disordered and only loosely associated with the rest of the protein, making the validity of this NMR structure ambiguous (242).

A majority of available ApoE purification protocols include a chemical denaturing step with subsequent re-folding by extensive dialysis (369, 375, 376, 381, 382). High concentrations of urea or guanidine hydrochloride keep denatured ApoE in its monomeric state and help to isolate the protein from the void volume of the gel filtration column (381). However, the re-folding process is time consuming and can yield misfolded, as well as aggregated target protein (383). The objective of this chapter was to establish a novel method for the purification of full length ApoE isoforms, as well as the ApoE amino terminal domain (residues 1-191, $ApoE_{1-191}$) and monomeric ApoE ($ApoE_{mon}$) under non-denaturing conditions. ApoE isoforms were then characterized in solution, crystallized and used for SAXS studies (Chapter 3), as well as for the identification of small molecules that interact with ApoE (Chapter 4).

2.2 Materials and Methods

2.2.1 Materials

All materials were purchased from Sigma-Aldrich or Fisher Scientific and were the highest purity available. Isopropyl β-D-1-thiogalactopyranoside (IPTG, # I1003) and Tris(2-carboxyethyl)phosphine (TCEP, # GEN-TCEP) were purchased from Generon. Rosetta2(DE3) cells (# 71400-3) were purchased from Merck Millipore. Luria-Bertani (LB) broth (Lennox) was purchased from Formedium (# LBX0103). Roche ethylenediaminetetraacetic acid (EDTA) complete protease inhibitor Tablets (# 05056489001) and DNAse I (# D4527) were obtained from Sigma-Aldrich. Super optimal broth with catabolite repression (SOC, # 15544034) and the Gene JET miniprep kit (# K0502) were purchased from Thermo Fisher Scientific. QIAprep spin miniprep kit (# 27104) was retrieved from QIAGEN. The QuikChange Lightning Site-Directed mutagenesis kit (# 210518) that includes XL10-Gold ultracompetent cells (# 200314) were obtained from Agilent. TALON® metal affinity resin was purchased from clontech (# 635503).

The codon-optimized (i.e. optimized for the expression in *E. coli*) human ApoE4 gene preceded by a six-histidine tag, thioredoxin (TRX) sequence and human rhino-virus (HRV) 3C protease cleavage site was synthesized and cloned into the NdeI/HindIII site of a pET17b vector by Thermo Fisher Scientific (pET17b_ApoE4). A plasmid map is included in the Appendix (Figure 2.20E). The plasmid containing HRV 3C protease gene fused with glutathione *S*-transferase (GST; the HRV 3C-GST fusion protein is referred as PreScission protease) was provided by Dr Antony Oliver (Genome Damage and Stability Centre, University of Sussex).

2.2.2 Site directed mutagenesis

Codon optimized pET17b_ApoE4 (see above) was used as template to create the ApoE2 and ApoE3 full length variant by site directed mutagenesis. Additionally, truncated ApoE4 ($ApoE4_{1-191}$) was generated by mutating position 192 into a stop codon and monomeric ApoE4 ($ApoE4_{mon}$) as described by Zhang *et al* (243) by mutation of 5 hydrophobic amino acids (F257A, W264R, V269A, L279Q, V287E) in the lipid binding domain. Residues were mutated using the QuikChange lightning site directed mutagenesis kit (Agilent). Synthesis of mutated strands and *Dpn* I digestion was performed as per the kit's instructions.

Primers were synthesized by Eurofins to high purity salt free (HPSF) grade and were used for the site directed mutagenesis (Table 2.1). Primers were dissolved in nuclease-free water at a concentration of 100 pmol/µL and warmed to 50°C for 10 min. Stock solutions were further diluted 1:10 in nuclease-free water before use.

Table 2.1. Primers and annealing temperatures T_{m1} and T_{m2}.

Description	Forward primer Reverse primer	T_{m1}	T_{m2}
ApoE4 → ApoE3 (R112C)	5'-gggtgcagatatggaagatgtttgtggtcgtctgg-3' 5'-ccagacgaccacaaacatcttccatatctgcaccc-3'	60	65
ApoE3 → ApoE2 (R158C)	5'- gccgatgatctgcagaaatgtctggcagtttatcag-3' 5'- ctgataaactgccagacatttctgcagatcatcggc-3'	60 (see text body)	
To create truncated ApoE (A192STOP)	5'-tggtagaacagggtcgtgttcgttaagcaaccgttggt-3' 5'-accaacggttgcttaacgaacacgaccctgttctacca-3'	60	65
To create monomeric ApoE (F257A)	5'-gattcgtctgcaggcagaagcagctcaagcccgtct-3' 5'-agacgggcttgagctgcttctgcctgcagacgaatc-3'	60	65
To create monomeric ApoE (W264R)	5'-gcccgtctgaaaagccggtttgaaccgctgg-3' 5'-ccagcggttcaaaccggcttttcagacgggc-3'	61	66
To create monomeric ApoE (V269A)	5'-ctggtttgaaccgctggctgaagatatgcagcgtc-3' 5'-gacgctgcatatcttcagccagcggttcaaaccag-3'	60	65
To create monomeric ApoE (L279Q)	5'-cgtcagtgggcaggtcaggttgaaaaagtgcag-3' 5'-ctgcacttttttcaacctgacctgcccactgacg-3'	60	65
To create monomeric ApoE (V287E)	5'-gtgcaggcagcagagggcaccagcgcag-3' 5'-ctgcgctggtgccctctgctgcctgcac-3'	60	65

An altered polymerase chain reaction (PCR) program was used with specific annealing temperatures for each primer pair (Table 2.2). The PCR was performed in a T100™ Thermal Cycler (BioRad). Mutagenesis of ApoE3 to ApoE2 was performed by Ana Caroline-Raulin (Prof Louise Serpell lab, University of Sussex) as per the mutagenesis kit's instructions and using the kit's PCR program.

Table 2.2. PCR program for site-directed mutagenesis.

Segment	Type	Temperature [°C]	Time [sec]	Cycles
1	Initial denaturation	95	120	1
2	Denaturation	95	20	3
	Annealing 1	T_{m1} (Table 2.1)	10	
	Elongation	72	180	
3	Denaturation	95	20	15
	Annealing 1	T_{m2} (Table 2.1)	10	
	Elongation	72	180	
4	Final elongation	72	300	1
5	Store	8	∞	-

After amplification of the mutated strands, the template DNA was digested with *Dpn* I. Enzyme (2 µL) provided with the kit were added directly to each amplification reaction and incubated first at 37°C for 8 min, then at room temperature (RT) for 5 to 8 min. The digested DNA mix was directly used for the transformation of XL10-Gold ultracompetent cells as per the manufacturer's instructions. Hence, 50 µL of XL10-Gold cells were thawed on ice and 2 µL of β-mercaptoethanol provided with the kit were added to the XL10-Gold cells. Cells were incubated on ice for 10 min, then 5 µL of digested DNA were added and cells were again

incubated on ice for 30 min. Afterwards, cells were heat-pulsed at 42°C for 30 sec and cooled quickly on ice for 2 min. SOC medium (500 µL) was added and cells were incubated at 37°C for 1 h while shaking at 200 rpm. The transformation mixture was then plated on LB agar medium and incubated overnight at 37°C. The next day, colonies were picked from the agar plate to inoculate 8 mL of LB-medium supplemented with 100 µg/mL ampicillin and 35 µg/mL chloramphenicol and grown overnight at 37°C and 200 rpm. Plasmid DNA was isolated using the QIAprep spin miniprep kit (QIAGEN) or the GeneJET spin miniprep kit (Thermo Fisher Scientific) and confirmed by sequencing (Eurofins). Plasmids harbouring the wild type ApoE isoforms, as well as $ApoE4_{1-191}$ were sequenced using primer 5'-AAGGTGGAACAGGCCGTG-3'. The $ApoE4_{mon}$ containing plasmid was sequenced using the T7 terminator primer. Sequencing results are shown in the Appendix (Figure 2.20).

2.2.3 Transformation of Rosetta2(DE3) cells and glycerol stock preparation

Rosetta2(DE3) cells (20 µL) were thawed on ice and plasmid DNA to a final concentration of 2 ng/µL was added. Cells were incubated on ice for 5 min and then heat-pulsed at 42°C for 30 sec and then incubated on ice for 2 min. SOC medium (250 µL) was added and cells were incubated at 37°C for 1 h while shaking at 200 rpm. To select transformed cells, 30 µL of cells were plated on LB agar medium containing 100 µg/mL ampicillin and 35 µg/mL chloramphenicol and incubated overnight at 37°C.

Glycerol stocks of transformed cells were prepared by inoculating 8 mL of LB medium with a freshly transformed colony. The culture was incubated overnight at 37°C while constantly shaking at 200 rpm. The next day, 500 µL aliquots of cell suspension were mixed with 250 µL of 50% (v/v) sterile glycerol and stored at -80°C.

2.2.4 Expression trials

LB broth (10 mL) supplemented with 1% (v/v) glycerol and 100 µg/mL ampicillin were inoculated with transformed Rosetta2(DE3) (Section 2.2.3). Cells were grown for 6 h at 37˚C and 180 rpm, then stored overnight at RT. The next day, 500 µL of the pre-culture was used to inoculate 50 mL of LB broth supplemented with 1% (v/v) glycerol and 100 µg/mL ampicillin. Cells were grown at 180 rpm and 37˚C up to an optical density at 600 nm (OD_{600}) of ~0.6 and induced with 1 mM IPTG. A non-induced control culture was included. Samples (200 µL) were taken before induction, 1, 2, 4 and 6 h after induction. The temperature was then decreased to 25˚C and cells grown overnight at 180 rpm. A final sample (200 µL) was taken the next day. All samples were centrifuged at 16'000 x *g* for 2 min, the supernatant discarded, and the pellet stored at -4˚C until use. Pellets were dissolved in 20 µL Bugbuster® (Novex) per OD_{600} of 1 and per 100 µL sample taken, incubated at RT for 20 min and expression then analysed by sodium dodecyl sulphate polyacrylamide gel electrophoresis (SDS PAGE, Section 2.2.11).

2.2.5 Large-scale expression of ApoE isoforms, ApoE4$_{1-191}$ and ApoE4$_{mon}$

LB broth (200 mL) supplemented with 100 µg/mL ampicillin was inoculated with transformed Rosetta2(DE3) cells from glycerol stock (Section 2.2.3) and grown at 37˚C and 225 rpm until reaching an OD_{600} of 0.6 – 1.0. Cells were then stored overnight at RT. The next day, cells were centrifuged for 5 min at 2500 x *g*, re-suspended in 24 mL fresh LB broth and 2 mL of suspension used to inoculate 1 L of LB broth supplemented with 100 µg/mL ampicillin and 1% (v/v) glycerol. Typically, 8 – 12 L were grown as main culture. Cells were grown at 150 rpm and 37°C until reaching an OD_{600} of 0.7 – 0.9. Then, they were induced with 1 mM IPTG and incubated at 37°C and 180 rpm for 2 - 4 h. Cells were harvested by centrifugation at 4°C and 9600 x *g* (JLA 9.1000 rotor, Beckman Coulter) for 10 min and the pellet was stored at -80°C.

2.2.6 Purification of ApoE isoforms and ApoE4$_{mon}$

All ApoE isoforms and ApoE4$_{mon}$ were purified by a combination of immobilized metal ion affinity chromatography (IMAC), heparin affinity chromatography (HAC) and size exclusion chromatography (SEC). The final purification method is presented first; methodology for key purification trials are outlined after. Buffers for the final purification method are shown in Table 2.3.

Table 2.3. Buffers used for the purification of full length ApoE isoforms and monomeric ApoE4.

Description	Constituents
Lysis buffer	50 mM HEPES, 240 mM NaCl, 5 mM $MgCl_2$, 10 mM imidazole, 1 mM DTT, 10% (v/v) glycerol, 0.05% (v/v) Tween-20, 7 U/mL DNAse I, 1 protease inhibitor Tablet per 50 mL, pH 8.0
IMAC binding buffer	50 mM HEPES, 240 mM NaCl, 20 mM imidazole, 10% (v/v) glycerol, 0.05% (v/v) Tween-20, pH 8.0
IMAC elution buffer	50 mM HEPES, 240 mM NaCl, 300 mM imidazole, 10% (v/v) glycerol, 0.05% (v/v) Tween-20, pH 8.0
SEC buffer	20 mM HEPES, 300 mM NaCl, 10% (v/v) glycerol, 1 mM TCEP for ApoE2 and ApoE3 only, pH 8.0
Heparin binding buffer (ApoE2 only)	20 mM HEPES, 240 mM NaCl, 10% (v/v) glycerol, 1 mM TCEP, pH 8.0
Heparin elution buffer	20 mM HEPES, 1000 mM NaCl, 10% (v/v) glycerol, pH 8.0

The cell pellet was re-suspended in 200 mL ice-cold lysis buffer and cells disrupted by sonication (5 sec sonication, 5 sec break, 6 min total sonication time, 39% amplitude, Vibra cell sonicator VCX500, Sonics). Cell debris was separated from soluble protein by centrifugation for 10 min at 33'000 x *g* (JA 25.50 rotor, Beckman Coulter) and 4°C. The supernatant was filtered through a 0.45 µm filter and applied on 10-15 mL TALON® metal affinity resin (Clontech) that was equilibrated with IMAC binding buffer and placed into a 200 mL Econo®-column (BioRad). Beads were incubated at 4°C while rocking for 1 h. After, the metal affinity resin was washed with 4 x 50 mL of IMAC binding buffer and protein eluted with

5 x 10 mL IMAC elution buffer. Elution fractions were pooled and directly applied to a 5 mL HiTrap Heparin column (GE Healthcare, pre-equilibrated with SEC buffer for ApoE3, ApoE4 and $ApoE4_{mon}$; pre-equilibrated with heparin binding buffer for ApoE2) at a flow rate of 1 mL/min. An ÄKTA purifier (GE Healthcare) was used to perform all fast-performance liquid chromatography (FPLC) steps. The column was extensively washed with SEC buffer (ApoE3, ApoE4 and $ApoE4_{mon}$) or heparin binding buffer (ApoE2) until the absorbance measured at 280 nm (A_{280}) stabilized to baseline. The HiTrap Heparin column was then disconnected from the ÄKTA purifier and 320 µg PreScission protease (Section 2.2.9) manually injected. The HiTrap Heparin column was sealed, and an on-column digestion performed at 4°C for 16 h while rocking. The next day, the HiTrap Heparin column was re-connected to the ÄKTA purifier and digested TRX removed by washing the column with 3 column volumes of SEC buffer (ApoE3, ApoE4 and $ApoE4_{mon}$) or heparin binding buffer (ApoE2) at a flow rate of 1.5 mL/min. ApoE was then eluted by applying a linear NaCl gradient over 15 min at a decreased flow rate of 1 mL/min. ApoE elution fractions from the heparin column were pooled and loaded to a HiLoad Superdex 26/600 200 pg column (GE Healthcare) that was pre-equilibrated with SEC buffer. Protein was eluted at a flow rate of 1.5 mL/min. ApoE containing fractions were pooled, concentrated by using VivaSpin 20 concentrators (Sartorius, molecular weight cut-off, MWCO 10'000 Da) at 4000 x *g* (SX4400 rotor, Beckman Coulter) and 4˚C, shock-frozen in liquid nitrogen and stored at -80˚C. All steps and purity of samples were analysed by SDS PAGE.

The following paragraphs outline the methodology for key purification trials that contributed to the development of the final protocol presented above. To test purification by anion exchange chromatography (AEX), HAC (without on-column digestion) or directly by SEC (omitting heparin affinity chromatography), the bacterial pellet was lysed by sonication and ApoE captured by IMAC as described above. Lysis buffer, IMAC binding and IMAC elution buffer contained only 150 mM NaCl. IMAC elution fractions were pooled, 0.01% (w/w) PreScission protease added and digestion performed overnight at 4°C. In the case of AEX and HAC, digested protein was applied to a HiTrap Q HP anion exchange (GE Healthcare) or HiTrap heparin HP column (GE Healthcare) at a flow rate of 1.5 mL/min that was pre-equilibrated with binding buffer (50 mM HEPES, 150 mM NaCl, 10% (v/v) glycerol, pH 8.0). The column was extensively washed with binding buffer and protein eluted by applying a linear salt gradient over 15 min at a flow rate of 1 mL/min (150 – 1000 mM NaCl). In the case of SEC, ApoE was concentrated below a volume of 10 mL using VivaSpin 20 concentrators (Sartorius, MWCO 10'000 Da) at 4000 x *g* (SX4400 rotor, Beckman Coulter) and 4˚C. Protein was then applied to a HiLoad 26/600 Superdex 200 pg column (GE Healthcare) pre-equilibrated with SEC buffer containing only 150 mM and gel-filtered at a flow rate of 1.5 mL/min.

To test purification without IMAC, the bacterial cell pellet was lysed by sonication as described above in lysis buffer containing 250 mM NaCl. Cleared cell lysate supernatant was then applied to a HiTrap heparin HP column (GE Healthcare) at a flow rate of 1.5 mL/min that was pre-equilibrated with binding buffer (20 mM HEPES, 250 mM NaCl, 10% (v/v) glycerol, pH 8.0). The column was extensively washed with binding buffer and on-column digestion performed overnight as described above. The next day, cleaved TRX tag was washed out with 3 column volumes of binding buffer and ApoE eluted by applying a linear salt gradient over 15 min at a flow rate of 1 mL/min (250 - 1000 mM NaCl). ApoE containing fractions were pooled and applied to a HiLoad 26/600 Superdex 200 pg column (GE Healthcare). Protein was gel-filtered in SEC buffer at a flow rate of 1.5 mL/min.

2.2.7 Purification of ApoE4$_{1-191}$

ApoE4$_{1-191}$ was purified by a combination of IMAC and SEC. Buffer constituents are shown in Table 2.4.

Table 2.4. Buffers used for the purification of ApoE4$_{1-191}$.

Description	Constituents
Lysis buffer	50 mM HEPES, 300 mM NaCl, 5 mM $MgCl_2$, 10 mM imidazole, 1 mM DTT, 10% (v/v) glycerol, 0.05% (v/v) Tween-20, 7 U/mL DNAse I, 1 protease inhibitor Tablet per 50 mL, pH 8.0
IMAC binding buffer	50 mM HEPES, 300 mM NaCl, 20 mM imidazole, 10% (v/v) glycerol, 0.05% (v/v) Tween-20, pH 8.0
IMAC elution buffer	50 mM HEPES, 300 mM NaCl, 300 mM imidazole, 10% (v/v) glycerol, 0.05% (v/v) Tween-20, pH 8.0
SEC buffer	20 mM HEPES, 300 mM NaCl, 10% (v/v) glycerol

The bacterial pellet was re-suspended in ice-cold lysis buffer, lysed by sonication and cleared from cell debris by centrifugation as described in Section 2.2.6. The clarified sonicate was then applied to a HiFliQ nickel-NTA column (Generon) and extensively washed with IMAC binding buffer at a flow rate of 1.5 mL/min. After overnight on-column digestion with PreScission protease at 4°C, cleaved ApoE4$_{1-191}$ was washed out with IMAC binding buffer at a flow rate of 1.5 mL/min whilst the TRX tag stayed immobilized to the nickel column. ApoE4$_{1-191}$ containing fractions were pooled, applied to a HiLoad Superdex 26/600 75 pg column (GE Healthcare) and gel filtered in SEC buffer at a flow rate of 1.5 mL/min. Protein containing fractions were concentrated in VivaSpin 20 concentrators (Sartorius, MWCO 5000 Da) and protein stored at -80°C.

2.2.8 Expression of PreScission protease

LB broth (200 mL) supplemented with 50 µg/mL ampicillin and 35 µg/mL chloramphenicol was inoculated with transformed Rosetta2(DE3) cells from glycerol stock (Section 2.2.3) and grown at 37°C and 200 rpm overnight. The next day, 20 mL of the cell suspension were used to

inoculate 2 L of LB broth supplemented with the same antibiotics as the pre-culture. Cells were grown at 150 rpm and 37°C until reaching an OD_{600} of ~0.6. Cells were then put on ice for 15 min, supplemented with 100 µg/mL ampicillin and induced with 0.4 mM IPTG. Cells were incubated overnight at 20˚C and 150 rpm. The next day, cells were harvested by centrifugation at 4°C and 9600 x *g* (JLA 9.1000 rotor, Beckman Coulter) for 20 min and the pellet was stored at -80°C.

2.2.9 Purification of PreScission protease

PreScission protease was purified by GST affinity chromatography using buffers shown in Table 2.5.

Table 2.5. Buffers used for the purification of PreScission protease.

Description	Constituents
Lysis buffer	50 mM HEPES, 1000 mM NaCl, 5 mM $MgCl_2$, 1 mM DTT, 7 U/mL DNAse I, 1 protease inhibitor Tablet per 50 mL, pH 8.0
GST binding buffer	50 mM HEPES, 1000 mM NaCl, 1 mM EDTA, 1 mM DTT, pH 8.0
GST elution buffer	50 mM HEPES, 1000 mM NaCl, 1 mM EDTA, 1 mM DTT, 10 mM reduced glutathione, pH 8.0
Storage buffer	50 mM HEPES, 1000 mM NaCl, 1 mM EDTA, 1 mM DTT, 20% (v/v) glycerol, pH 8.0

The cell pellet was re-suspended in 50 mL ice-cold lysis buffer and disrupted by sonication for 3 min as described in Section 2.2.6. Cell debris was separated from soluble protein by centrifugation for 10 min at 33'000 x *g* (JA 25.50 rotor, Beckman Coulter) and 4°C. The supernatant was filtered through a 0.45 µm filter and applied to a GSTrap FF column (GE Healthcare) at a flow rate of 1 mL/min. The column was extensively washed with GST binding buffer and PreScission protease then eluted with 10 mM reduced glutathione. Protease containing fractions were pooled, concentrated as in Section 2.2.6, re-buffered into storage buffer and stored at -80˚C.

2.2.10 Residue modification of ApoE4

Lysine residues in ApoE4 were methylated as previously described (384). Reductive methylation was performed after overnight on-column digestion of the TRX tag by PreScission protease. Every two hours, 160 µL of 1 M dimethylamine borane (DMAB) complex and 320 µL of formaldehyde were added to 8 mL of pooled heparin-purified ApoE4 and incubated at 4°C. After 6 h, a final 160 µL of 1 M DMAB and 320 µL of formaldehyde were added and incubated overnight at 4°C. Methylated ApoE4 was then purified by a final SEC polishing step as described in Section 2.2.6, concentrated and stored at -80°C.

Modification of arginine residues with 1,2-cyclohexanedione (CHD) was also performed on ApoE4 after on-column digestion. The procedure was adopted from Busby and Gan (385).

Heparin-purified ApoE4 was concentrated to a volume of ~1 mL by using Vivaspin 6 concentrators (Sartorius, MWCO 5000 Da) and diluted into 6.2 mL of 100 mM sodium tetraborate decahydrate (borax), pH 9.0. Then, 800 µL of 1 M CHD in 100 mM borax, pH 9.0 was added and the mixture incubated at 38˚C in the dark at 150 rpm for 3 h. Arginine modified ApoE4 was purified by SEC as described in Section 2.2.6 and ApoE4 containing fractions concentrated and stored at -80°C.

2.2.11 Sodium dodecyl sulphate polyacrylamide gel electrophoresis

Protein fractions were analysed by sodium dodecyl sulphate polyacrylamide gel electrophoresis (SDS PAGE). NuPAGE® Novex® 4-12% Bis-Tris protein gels from Life Technologies were used. Electrophoresis occurred in 1 x NuPAGE® MES SDS running buffer (Life Technologies) at constant 200 V. Samples were denaturized at 70°C for 10 min in 4 x NuPAGE® LDS Sample Buffer (Life Technologies) + 10 x NuPAGE® sample reducing agent (Life Technologies) prior loading on the gels. Gels were stained in InstantBlue (Expedeon) overnight and de-stained in twice-distilled water.

2.2.12 Gel filtration studies

The high molecular weight protein standard (GE Healthcare, # 28-4038-42) was used to calibrate the HiLoad Superdex 26/600 200 pg column (GE Healthcare). All protein standards and dextran blue were dissolved in SEC buffer to the manufacturers recommended concentrations (0.4 mg/mL Ferritin, 4 mg/mL Aldolase, 3 mg/mL Conalbumin, 3 mg/mL Ovalbumin) and 1.6 mL of the protein calibration mixture applied to the SEC column at a flow rate of 1.5 mL/min. Stokes radius (R_S) values were calculated on the basis of ApoE elution volume using equation (2.1):

$$K_{av} = \frac{V_e - V_0}{V_t - V_0} \quad (2.1)$$

where V_e = elution volume for the protein, V_0 = Superdex 200 column void volume (112 mL), and V_t = total Superdex 200 column bed volume (320 mL). K_{av} values were calculated for each protein standard and a standard curve generated by plotting the $\sqrt{(-\log(K_{av}))}$ versus R_S of each standard (Ferritin 6.1 nm, Aldolase 4.8 nm, Conalbumin 4.04 nm, Ovalbumin 2.75 nm). ApoE's R_S was calculated using equation (2.2) representing the fit of the data:

$$y = 0.1058\,x + 0.2397\ (R^2 = 0.9552) \quad (2.2)$$

ApoE diffusion coefficient D was estimated from its R_S by equation (2.3):

$$D = \frac{RT}{N_A f} = \frac{kT}{6\pi\eta R_s} \quad (2.3)$$

where R [8.314 J K^{-1} mol^{-1}] is the gas constant, N_A [6.022 x 10^{23} mol^{-1}] is Avogadro's number, f is the frictional coefficient, k is the Boltzmann constant (1.38 x 10^{-23} m^2 kg s^{-2} K^{-1}; ratio R/N_A), T is the experimental temperature (277.15 K) and η is the solvent viscosity (1.4181 x 10^{-3} Pa s) at temperature T. The right-hand version of the equation was obtained by the Stokes relationship:

$$f = 6\pi\eta R_s \quad (2.4)$$

The frictional properties of a macromolecule are often expressed as the ratio of the frictional coefficient to that of a smooth sphere with identical mass and density, f/f_0 (386). The frictional ratio $f/f_0 = R_S/R_{min}$ was calculated by assuming the minimal radius (R_{min}) of a sphere that could contain the given mass of tetrameric ApoE (136800 Da) where R_{min} is defined according to Erickson *et al* (387) as:

$$R_{min} = 0.066\, M^{\frac{1}{3}} \; (for\ M\ in\ Dalton, R_{min}\ in\ nm) \quad (2.5)$$

2.2.13 Size exclusion multi angle light scattering

Multi angle (laser) light scattering (MALS) coupled with SEC has become one of the most widely used techniques to determine the molar mass and size of a particle in solution. When light hits a macromolecule, the electric field of the light induces an oscillating dipole within the macromolecule. This dipole will in turn re-radiate (i.e. scatter) light in any direction. The overall intensity of the light scattered by the macromolecule is directly proportional to its molecular weight and allows an estimate of its size (388, 389).

SEC-MALS experiments were performed at the B21 beamline (Diamond Lightsource, UK). ApoE isoforms were diluted to 5 mg/mL in 20 mM HEPES, 300 mM NaCl, 1 mM TCEP, pH 8.0 and delivered at RT via an in-line Agilent high performance liquid chromatography (HPLC) with a Shodex Kw-403 column. Refractive increments were determined by a Wyatt optilab T-rEX and scattering measured by a Wyatt Dawn Heleo equipped with a Quasi-Elastic Light Scattering (QELS) module. Data was analysed using the ASTRA software version 6.1.7 (Wyatt).

2.2.14 Analytical ultracentrifugation

Analytical ultracentrifugation (AUC) provides useful information on the size, shape and molecular weight of a macromolecule as determined by its sedimentation velocity. In AUC velocity experiments, movement of macromolecules is measured in high centrifugal fields. Macromolecules sediment away from the centre of rotation and form a concentration boundary that moves towards the bottom of the centrifuge cell as a function of time. Opposing the centrifugal force are the buoyant and diffusion forces as solvent is being displaced by the macromolecule. The sedimentation velocity of the macromolecule with respects to the

centrifugal field is given by the Svedberg equation that defines the sedimentation coefficient, s, of a macromolecule:

$$s = \frac{u}{\omega^2 r} = \frac{M(1 - v\rho)}{N_A f} = \frac{MD(1 - v\rho)}{RT} \quad (2.6)$$

where u is the radial velocity of the macromolecule, $\omega^2 r$ is the centrifugal field (with rotor angular velocity ω and distance r from the centre of rotation), M is the molar mass, v is the partial specific volume, ρ is the density of the solvent, N_A is Avogadro's number, f is the frictional coefficient, D is the diffusion coefficient, and R the gas constant. The right-hand version of the Svedberg equation was obtained by the relationship defined in equation (2.3). The sedimentation coefficient is reported in units of Svedberg (S) that corresponds to 10^{-13} sec. Values sought in a velocity experiment are the diffusion coefficient, D, and the sedimentation coefficient, s. These can be extracted by analysis programs that model the concentration distribution of a macromolecule as a function of time and radial position under influence of sedimentation and diffusion and fit it to the experimental data (386, 390, 391).

Sedimentation velocity experiments were performed in collaboration with Prof John McGeehan (University of Portsmouth) and were carried out in a Beckman model XL-A analytical ultracentrifuge (Beckman Coulter, Fullerton, CA) at 20ºC using an AnTi60 rotor. ApoE isoforms (400 µL) were used at a concentration of 8 µM in 20 mM HEPES, 300 mM NaCl, 10% (v/v) glycerol, pH 8.0. Experiments were performed at a rotor speed of 40,000 rpm, and absorbance at 280 nm was recorded in situ at time intervals of 25 min and radial intervals of 0.003 cm. Data was fitted to a continuous size distribution c(s) Lamm equation model in the range of 0.1-15 S using the programme Sedfit version 15.01b (392). The confidence interval (F-ratio) was set to 0.95. Buffer viscosity and density was calculated in Sednterp version 20120828 BETA (393).

2.2.15 Small angle X-ray scattering

An introduction to SAXS is provided in Chapter 3.

SAXS experiments were performed at the B21 beamline (Diamond Light Source, UK) and scattering acquired with an X-ray wavelength of 1 Å on a Pilatus 2M detector and at a camera length of 4.036 m. Static SAXS experiments were performed at protein concentrations of 8, 4, 2, 1 and 0.5 mg/mL in 20 mM HEPES, 300 mM NaCl, 4.4% (v/v) glycerol, pH 8.0. Measurements were performed at 15°C with 10 x 1 sec frames being recorded per sample. Data were reduced using the B21 beamline in-house *pypeline* software and further analysed in ScÅtter (Bioisis) version 3.1R.

For SAXS experiments coupled with SEC (SEC-SAXS), ApoE isoforms at a protein concentration of 10 mg/mL were delivered at 20°C and a flow rate of 0.16 mL/min via an in-line Agilent high performance liquid chromatography (HPLC) with a Shodex Kw-403 column and 20 mM HEPES, 300 mM NaCl, pH 8.0 as running buffer. In total 620 frames were acquired, and each frame exposed for 3 sec. Buffer subtraction, averaging and analysis was performed in ScÅtter version 3.1R. Analysis of SEC-SAXS data was also performed in ATSAS version 2.8.2 for comparison.

2.2.16 Crystallography

Protein crystals are grown in aqueous, so-called “mother” solutions. Nucleation and growth of crystals is dependent upon supersaturation of the mother liquor. Crystal growth starts with nucleation of protein aggregates on the nanometer scale. The protein forms small ordered assemblies (i.e. nuclei) that grow to crystals in a supersaturated environment. Supersaturation is a *“non-equilibrium condition in which some quantity of the macromolecule in excess of the solubility limit […] is nonetheless present in solution”* (394). The objective is therefore to keep the mother solution supersaturated so that crystals form and grow. Different techniques are available, however, most common are the hanging-drop and sitting-drop procedures for vapor diffusion that have the same principle: the sample mixed with the mother liquor is equilibrated in a small chamber that is filled with the mother liquor (= reservoir solution). The concentration of the mother solution in the droplet is less than that of the reservoir solution, hence, water evaporates from the droplet in a vapor phase. This concentrates the sample and increases supersaturation of the sample in the drop (395). In addition to the vapor diffusion method, proteins, in particular membrane proteins, can be stabilized and crystallized in lipid cubic phase (LCP). LCP is a liquid crystalline phase that forms spontaneously when mixing lipids (e.g. monoolein) with an aqueous protein solution at a certain ratio. The result is a complex, three-dimensional network of lipid bilayers that contain the lipid binding protein and enclose aqueous channels (396). Addition of a precipitant will alter the properties of the LCP in terms of microstructure and phase separation. In separated phases that are enriched in protein, nucleation and crystallization of the protein can occur (397).

The 96-well format Structure Screen 1 & 2, PACT screen, Morpheus screen and JCSG screen were purchased from Molecular Dimensions. Screening of crystallization conditions for full length ApoE4 and ApoE4$_{mon}$ was performed at various concentrations of protein (5–10 mg/mL) and in the presence of various additives, as well as mild detergents (i.e. 10 mM suramin, 1 mg/mL heparin, 25 mM octyl β-glucoside, OG, 30 mM octyl β-D-1-thioglucopyranoside, OTG) using the sitting drop method in MRC 2 Well Crystallization plates (Swissci) at 4°C or 20°C. Screening of lysine- and arginine-modified ApoE4 (Section 2.2.10) was performed at a concentration of 5 mg/mL using the sitting drop method in MRC 2 Well Crystallization plates

(Swissci) at 4°C and was compared to unmodified ApoE4. LCP crystallization trials were performed with full length ApoE4 and $ApoE4_{mon}$ in collaboration with the Membrane Protein Lab (Imperial College London, Diamond Light Source, UK) using the MemGold, MemGold 2, MemSys/MemStart and MemMeso crystallization screens (Molecular Dimensions). Proteins were buffer exchanged into 20 mM HEPES, 300 mM NaCl, 5% (v/v) glycerol, pH 8.0 using Vivaspin 2 concentrators (Sartorius, MWCO 10000) and adjusted to a concentration of ~25 mg/mL. LCP was then performed as described by Moraes and Archer (398).

To test the stability of ApoE4 over time, 20 µL aliquots of 1 µg/µL ApoE4, as well as 1 µg/µL ApoE4 + 25 mM OG were stored at RT for 2, 4 and 8 h, and 1, 2, 4, 5, 6, 7 and 8 d. Samples were then analysed by SDS PAGE.

Screening with $ApoE4_{1-191}$ was performed at a concentration of 10 mg/mL protein using the sitting drop method in MRC 2 Well Crystallization plates (Swissci). Protein was mixed at a 1:1 ratio with the mother solutions, the plates were sealed and stored at 20°C. Crystals were observed and documented using Leica microsystems. All crystals were transferred from 0 to 30% (v/v) glycerol in steps of 10% prior to flash cooling in liquid nitrogen and data collection. X-ray diffraction data was collected at the Diamond Light Source (Oxfordshire, United Kingdom) on the I04 beamline (λ = 0.9795 Å) using a Dectris Pilatus 6M-F detector. The crystals were cooled at 100 K during data collection by a Cryostream (Oxford Cryosystems Ltd). Data were integrated and scaled using the automatic Xia2 processing at the Diamond Light Source. Part of the structure was initially solved by molecular replacement using a previously determined structure (Protein Data Bank (PDB) (399) entry 1GS9) and data was processed with CCP4 (400). Data collection and processing were performed by Dr Mark Roe (University of Sussex). Figures were prepared in Maestro 10.3 (Schroedinger). The protein was prepared using Maestro's integrated protein preparation wizard before analysis: bond orders were assigned, hydrogens were added, zero-order bonds to metals and disulfide bonds were created, as well as water beyond 5 Å from hetero groups were deleted. Moreover, the protein was refined by assigning hydrogen bonds at pH 7.0.

2.3 Results

2.3.1 ApoE is only expressed over a short period of time in Rosetta2(DE3) cells

Full length ApoE isoforms, as well as $ApoE4_{1-191}$ and $ApoE4_{mon}$ were expressed as TRX fusion protein. The *E. coli* TRX has characteristics that make it very suitable as a fusion partner. It is a small redox protein with a molecular weight of 11 kDa and therefore represents only a small proportion of the fusion protein. Additionally, TRX was shown to increase solubility of various proteins and to promote release from the cell by osmotic shock or freeze/thaw treatments (401). With regards to the expression of ApoE in *E. coli*, TRX was shown to be advantageous in that high expression of soluble ApoE is achieved (375).

Small scale expression trials of ApoE isoforms in Rosetta2(DE3) cells revealed that ApoE is only expressed over a short period of time at a temperature of 37°C (Figure 2.1). Highest expression is observed 1 h and 2 h after induction with IPTG and significantly decreases after this period. Only a reduced band of the TRX-ApoE fusion protein is seen after 4 h and 6 h of induction and no expression was observed after leaving the cells to grow overnight at decreased temperature of 25°C. This suggests metabolism of ApoE in *E. coli* and/or plasmid loss after long periods of expression. All ApoE isoforms behaved in a similar manner. An example showing the growth (represented by the OD_{600}) of Rosetta2(DE3) cells expressing TRX-ApoE4 is presented in Figure 2.1A. As expected, cells that were not induced with IPTG reached higher optical densities at all time points compared to induced cells. Additionally, the OD_{600} of the induced culture after expression overnight fell below 1.0 which suggests lysis of cells. This effect was also confirmed for TRX-ApoE2 and TRX-ApoE3 (data not shown). For this reason, only short induction times were used for the large-scale expression of ApoE isoforms.

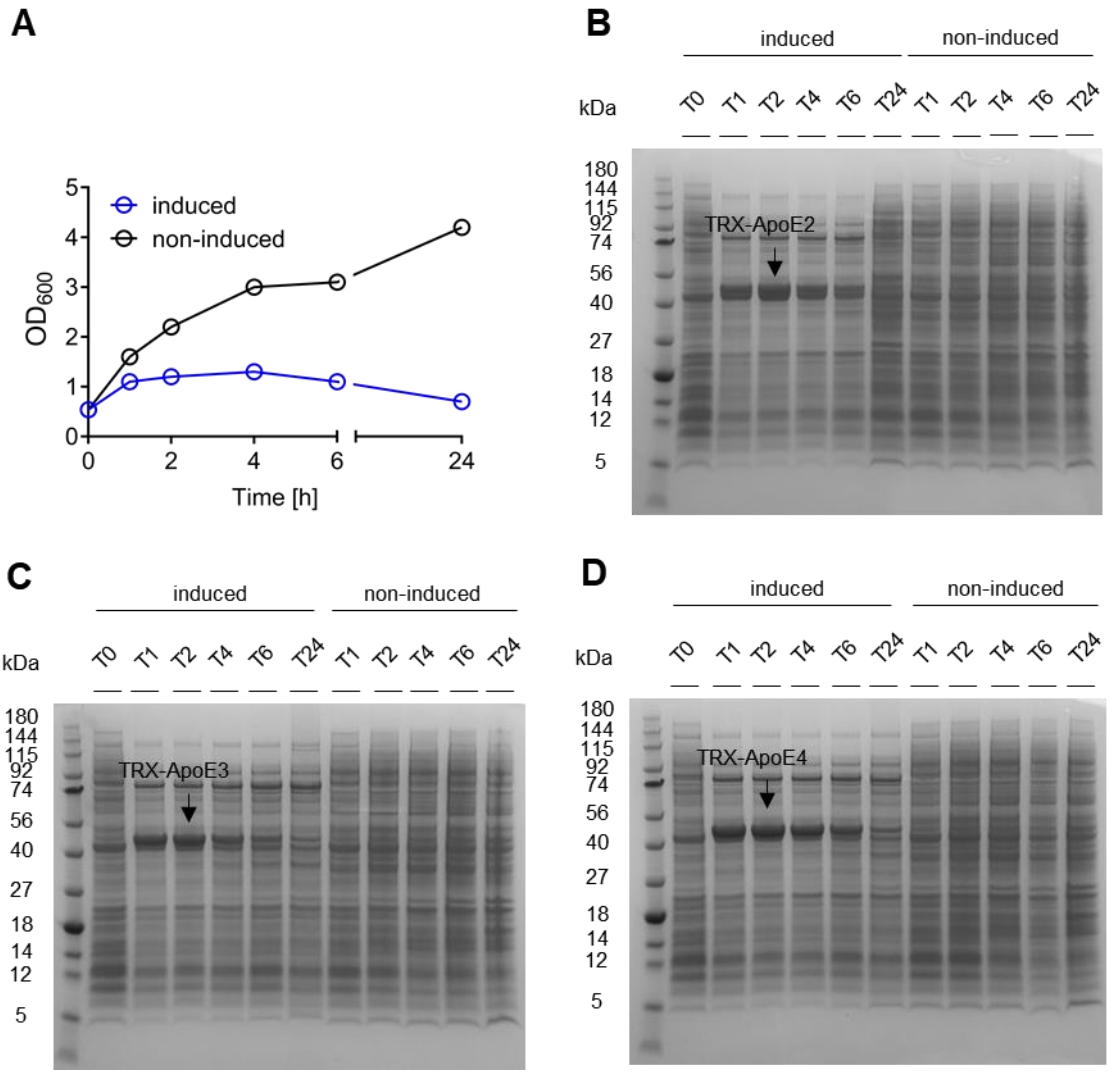

Figure 2.1. Expression of ApoE isoforms in Rosetta2(DE3) cells. (A) The OD_{600} is shown as a function of time for Rosetta2(DE3) cells expressing the TRX-ApoE4 fusion protein. Shown is the expression of the **(B)** TRX-ApoE2, **(C)** TRX-ApoE3 and **(D)** TRX-ApoE4 fusion protein (Mw ~45 kDa) in Rosetta2(DE3) cells over time. Cells were induced with 1 mM IPTG and samples taken before induction, after 1, 2, 4, 6 and 24 h. A non-induced control was included that shows no expression of TRX-ApoE.

The TRX ApoE4 amino terminal domain (TRX-ApoE4$_{1\text{-}191}$) and the monomeric ApoE4 fusion protein (TRX-ApoE4$_{mon}$) on the other hand seem more stable and are expressed up to 6 h after induction with peak expression at 4 h (Figure 2.2). However, similar to wild type ApoE isoforms, no band or only a minimal band is seen after growing the cells overnight. Expression of TRX-ApoE4$_{1\text{-}191}$ and TRX-ApoE4$_{mon}$ seems not to be as cytotoxic as the expression of wild type ApoE isoforms and induced cultures reach a similar OD_{600} compared to the non-induced controls after incubation overnight (Figure 2.2A and 2.2C). Therefore, expression times up to 4 h were adopted for the large-scale expression of TRX-ApoE4$_{mon}$ and TRX-ApoE4$_{1\text{-}191}$.

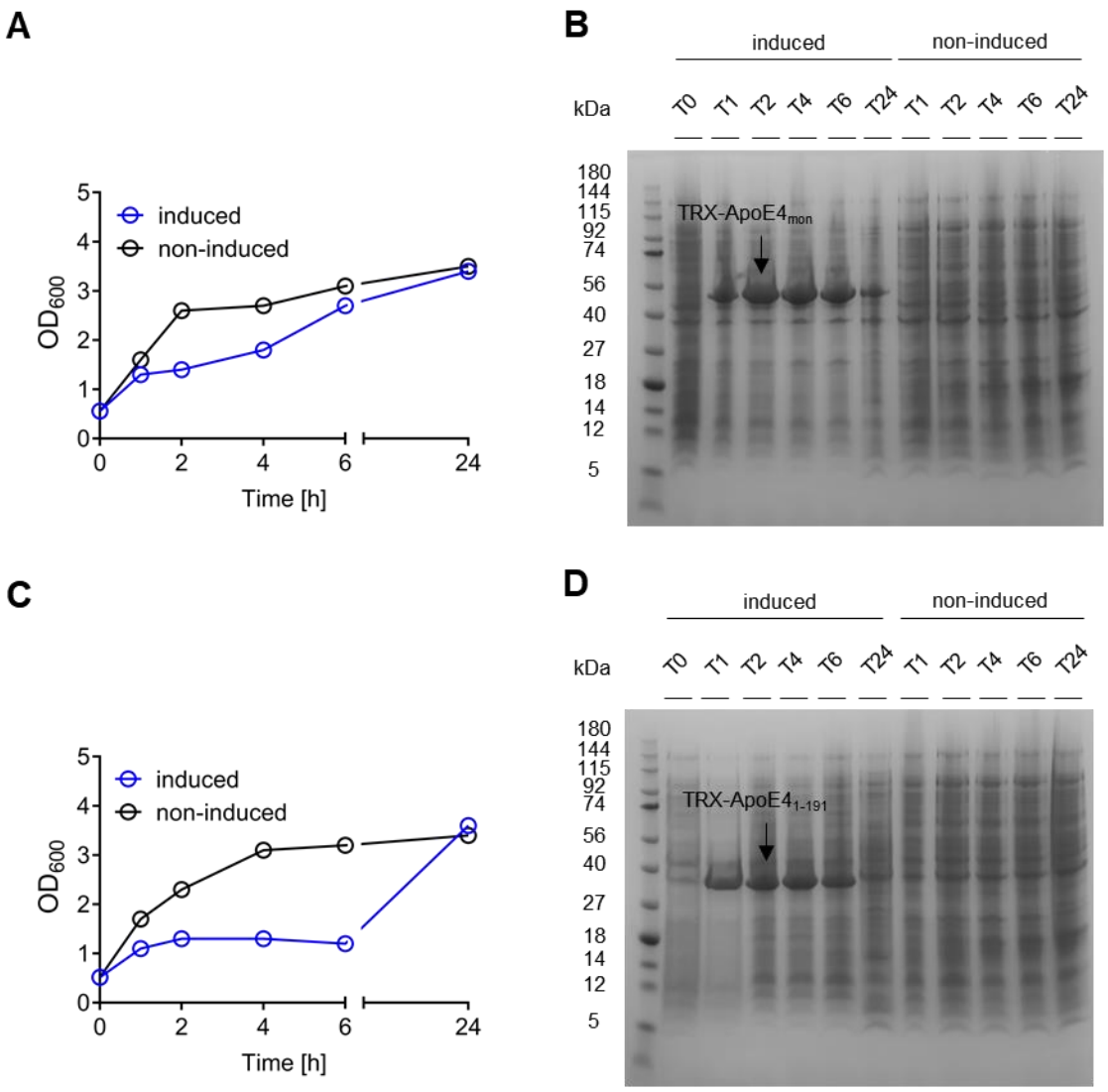

Figure 2.2. Expression of ApoE4$_{mon}$ and ApoE4$_{1-191}$ in Rosetta2(DE3) cells. (A) The OD_{600} as a function of time is shown for Rosetta2(DE3) cells expressing TRX-ApoE4$_{mon}$ as well as **(B)** the respective gel. **(C)** The OD_{600} as a function of time is shown for Rosetta2(DE3) cells expressing TRX-ApoE4$_{1-191}$ as well as **(D)** the respective gel. Cells were induced with 1 mM IPTG and samples taken before induction, after 1, 2, 4, 6 and 24 h. A non-induced control was included.

2.3.2 Development of a novel procedure for the purification of ApoE4

The purification protocol was developed using wild type ApoE4 and was then adopted for the two other isoforms (Section 2.3.3). Combinations of different affinity chromatography methods with SEC were tested under non-denaturing conditions and key trials that significantly contributed to the development of the final purification protocol are summarized in Table 2.6. A combination of IMAC followed by HAC and SEC were an ideal combination for the purification of ApoE4.

Table 2.6. Summary of key purification trials. The sequence of purification trials is shown that all include a capture step by IMAC (except #5) to enrich the protein of interest, digestion of the TRX tag by PreScission protease overnight, followed by an intermediate purification by either AEX or HAC and a final polishing by SEC.

#	Purification sequence	Comment
1	IMAC → SEC	Moderate purity (Appendix Figure 2.21)
2	IMAC → AEX	Only moderate binding affinity of ApoE to AEX column and moderate purity (Figure 2.3)
3	IMAC → HAC	High binding affinity of ApoE to heparin column and selection of functional protein; improved purity compared to AEX (Figure 2.4)
4	IMAC → HAC → SEC	Selection of functional protein and high purity (Figure 2.5)
5	HAC → SEC	Selection of functional protein, but only moderate purity (Appendix Figure 2.22)

A six-histidine tag is present at the amino terminus of the TRX-ApoE4 fusion protein. Therefore, a primary capture step by IMAC was always included to enrich the fusion protein and to remove major impurities. In the simplest purification trial, IMAC was followed by SEC, but the final purification product had only moderate purity (Appendix Figure 2.21). For this reason, intermediate purification steps by AEX and HAC were compared. With an isoelectric point (pI) of approximately 5.8 (109), ApoE4 should immobilize on AEX columns in buffers above its pI and on cation exchange chromatography (CEX) columns below its pI, respectively. Binding of ApoE4 to an AEX column was tested and as expected it immobilized to the column at a pH of 8.0 (Figure 2.3). Pleasingly, the cleaved TRX tag did not immobilize to the AEX column which enabled simple separation of the solubility tag. However, ApoE4 started to elute at a low salt concentration (~ 190 mM) and hence the protein sample was determined to be of poor purity as other proteins co-eluted.

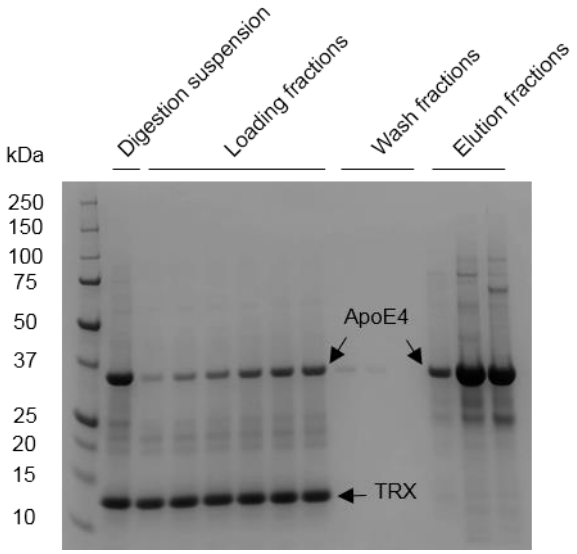

Figure 2.3. Purification of ApoE4 using immobilized metal affinity and anion exchange chromatography. After having captured TRX-ApoE4 by IMAC, the IMAC elution fractions were pooled and TRX-ApoE4 digested with PreScission protease overnight. Cleavage of the fusion protein was confirmed (digestion suspension) and the protein mixture was then applied to a HiTrap Q HP (GE Healthcare) anion exchange column. Elution of ApoE4 is observed during loading and the TRX tag is also found in the loading fractions. After having washed the column with binding buffer, ApoE4 was eluted with a linear salt gradient. Elution occurred at moderate salt concentration.

As outlined in Chapter 1, Section 1.4.3, ApoE contains two heparin binding sites that mediate the binding to cell-surface HSPGs. ApoE's heparin binding ability was exploited for high-resolution purification of ApoE by using affinity columns in which heparin is covalently coupled to highly cross-linked agarose beads. In a first test, the digested protein mixture was applied to a HiTrap heparin HP (GE Healthcare) column and then eluted by applying a linear salt gradient (Figure 2.4A). ApoE4 immobilized to the heparin column and eluted at high NaCl concentrations (~420 mM). Additionally, the TRX tag was found to be in the loading fractions and therefore was separated from ApoE4. In a second trial, the binding ability of the TRX-ApoE4 fusion protein to the heparin column was compared and cleavage of the TRX tag on the column was tested. The IMAC elution fractions were pooled and directly applied to the heparin column. PreScission protease was then manually injected and digestion performed overnight on the column. As can be seen on the gel in Figure 2.4B, cleavage on the column was successful and the TRX tag was removed by washing the column with a buffer containing low salt. ApoE4 on the other hand eluted at higher salt concentrations (~420 mM). HAC in combination with on-column digestion was selected as intermediate step in the final purification protocol, as it divides the purification process better in terms of work load; i.e. IMAC and loading of the heparin column are performed on Day 1 of the purification, elution of ApoE from the heparin column and SEC on Day 2.

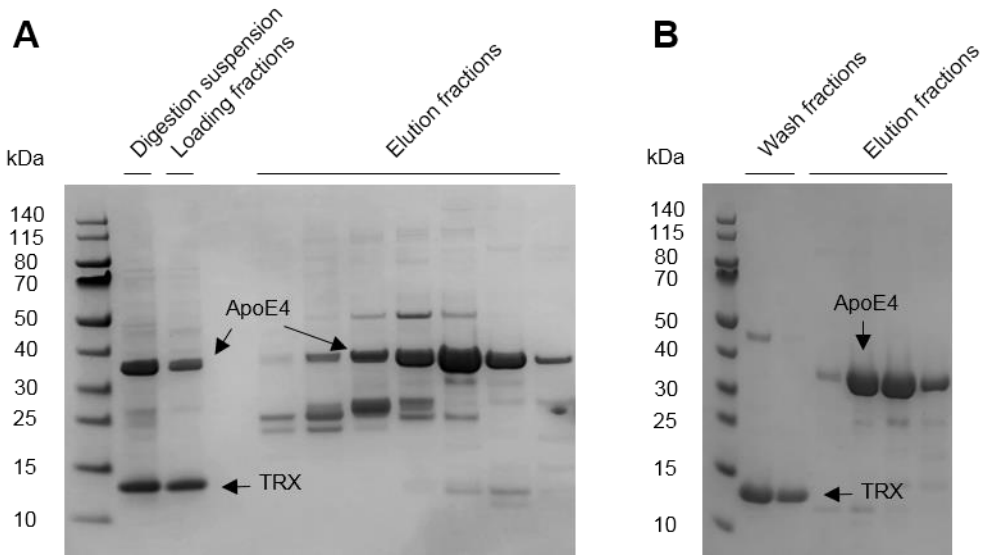

Figure 2.4. Heparin affinity chromatography in combination with off- or on-column digestion. The HAC of ApoE4 is shown. **(A)** Digestion of ApoE4 by PreScission protease was performed in suspension. Cleavage of the TRX solubility tag was confirmed (digestion suspension) and the mixture was applied to a HiTrap heparin HP (GE Healthcare) affinity column. Identical to AEX, TRX did not bind to the heparin resin and was found in the loading fractions. By applying a linear salt gradient, ApoE4 was then eluted from the heparin column and eluted at high salt concentrations. **(B)** In a similar approach, undigested TRX-ApoE4 was directly applied to the heparin column and digestion performed overnight on the column. TRX was found in the low salt wash fractions after digestion and ApoE4 on the other hand in the elution fractions with high salt content.

Each purification step included will result in a loss of protein of interest and reduce final yields. It was therefore of interest to test whether IMAC can be excluded and purification achieved by a combination of HAC and SEC only. Major impurities were found to be present after HAC and higher molecular weight species formed that eluted in the void volume of the SEC column (Appendix Figure 2.22). Final purity as assessed by SDS PAGE was determined to be only moderate. For this reason, IMAC was kept as a primary purification step in the final protocol.

The strong binding affinity of ApoE4 to the heparin column and the fact that it elutes at high NaCl concentration was exploited to increase purity of the final product by adjusting the salt concentration in the purification buffers. Results are summarized in Table 2.7. A combination of 240 mM NaCl for loading TRX-ApoE4 and 300 mM for washing the heparin column were identified to be optimal in terms of yield and purity. Example gels of the final purification protocol are shown in Figure 2.5. Typically, 8-12 mg of ApoE4 were yielded from an 8 L expression culture with purities > 95% as determined by densitometric scanning using the Image J image analysis software (402). Example chromatograms of HAC and SEC are found in Appendix Figure 2.23.

Table 2.7. Adjustment of NaCl concentration in purification buffers.

[NaCl] in buffers	Approximate yield	Comment
250 mM	0.3 mg final protein per 1 g wet pellet	Good purity (> 90%) of final product; impurities still visible
300 mM	0.12 mg final protein per 1 g wet pellet	High purity (> 95%); low yield
400 mM	---	ApoE4 does not immobilize to heparin column
240 mM / 300 mM	0.2 mg final protein per 1 g wet pellet	High purity (> 95%); increased yield compared to 300 mM NaCl in all buffers

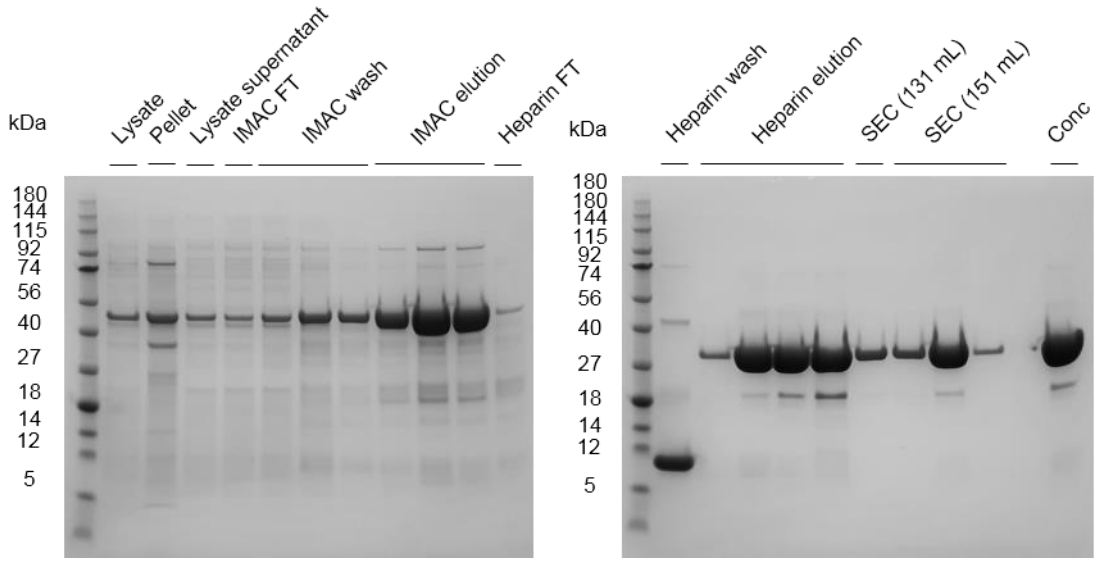

Figure 2.5. Representative gels summarizing ApoE4 purification. The TRX-ApoE4 fusion protein shows good solubility in the lysis buffer used and soluble protein is found in the lysate supernatant as demonstrated by the left gel. However, major TRX-ApoE4 is found in the pellet with the cell debris. A primary capture step by IMAC enriches the protein of interest and removes major impurities. Some of the fusion protein is found in the flow through (IMAC FT), as well as wash fractions (IMAC wash) of the IMAC resin, however, most is found in the elution fractions (IMAC elution). The TRX-ApoE4 fusion protein shows excellent heparin binding affinity as only minimal amounts of protein are seen in the flow through of the column (heparin FT). The right-hand figure shows a gel that demonstrates successful digestion of the solubility tag on the heparin column. TRX protein elutes at lower salt concentrations and is therefore found in the wash fractions (heparin wash). ApoE4 on the other hand elutes at higher salt concentrations (heparin elution). A final purification step by SEC eliminates last impurities and aggregates that may have formed. ApoE4 elutes at two apparent elution volumes (Appendix Figure 2.23B). One smaller fraction at 131 mL and the major fraction at 151 mL. This suggests that different oligomeric species are present. Only the major fractions at 151 mL were pooled and concentrated. The final concentrate (conc.) has high purity, with a minor impurity at 22 kDa being observed.

2.3.3 The purification procedure can be applied to ApoE2 and ApoE3

The purification protocol developed for ApoE4 was applied to ApoE2 and ApoE3. No adjustment was necessary for ApoE3 and an example gel that summarizes the purification process is shown in Figure 2.7B. The only difference compared to ApoE4 is the addition of TCEP to the SEC buffer as ApoE3 contains a cysteine that may form intermolecular disulphide bonds (381). Yields and purity were identical to ApoE4.

Sodium chloride concentrations for the purification of ApoE2 had to be adjusted. Washing the heparin column after loading the TRX-ApoE2 fusion protein with SEC buffer containing 300 mM NaCl resulted in elution of the fusion protein and therefore low yields (Figure 2.6). A comparison of the binding ability of ApoE isoforms to the HiTrap heparin HP column (GE Healthcare) revealed that ApoE2 elutes at lower a salt concentration compared to ApoE3 and ApoE4 (Chapter 3, Figure 3.12C). For this reason, sodium chloride concentrations were kept at 240 mM when washing the heparin column which prevented elution of TRX-ApoE2 during this stage. Due to lower concentrations of sodium chloride in buffers used for HAC, purity of the final ApoE2 product was slightly lower compared to the two other isoforms (Figure 2.7A). Final yields were similar to ApoE3 and ApoE4 (8-12 mg protein out of 8 L expression culture).

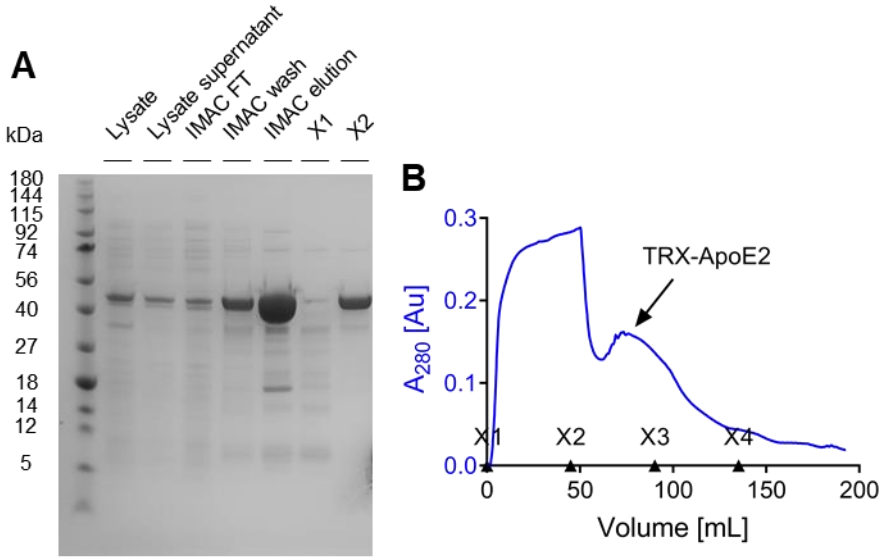

Figure 2.6. Loading of ApoE2 to a heparin column with increased sodium chloride. (A) The gel summarizes the ApoE2 purification steps. TRX-ApoE2 is like TRX-ApoE4 soluble in the lysis buffer and is found in the soluble fractions (lysate supernatant). The enriched protein after IMAC (IMAC elution) was then applied to a HiTrap heparin HP column (GE Healthcare) and washed with SEC buffer containing 300 mM NaCl. This resulted in elution of the TRX-ApoE2 fusion protein (X2) that could be followed in the absorbance chromatogram as shown in panel **(B)**. The absorbance at 280 nm is shown as a function of elution volume. X1-X2 represents the loading fraction. X2 – X4 are wash fractions during which the heparin column was flushed with SEC buffer.

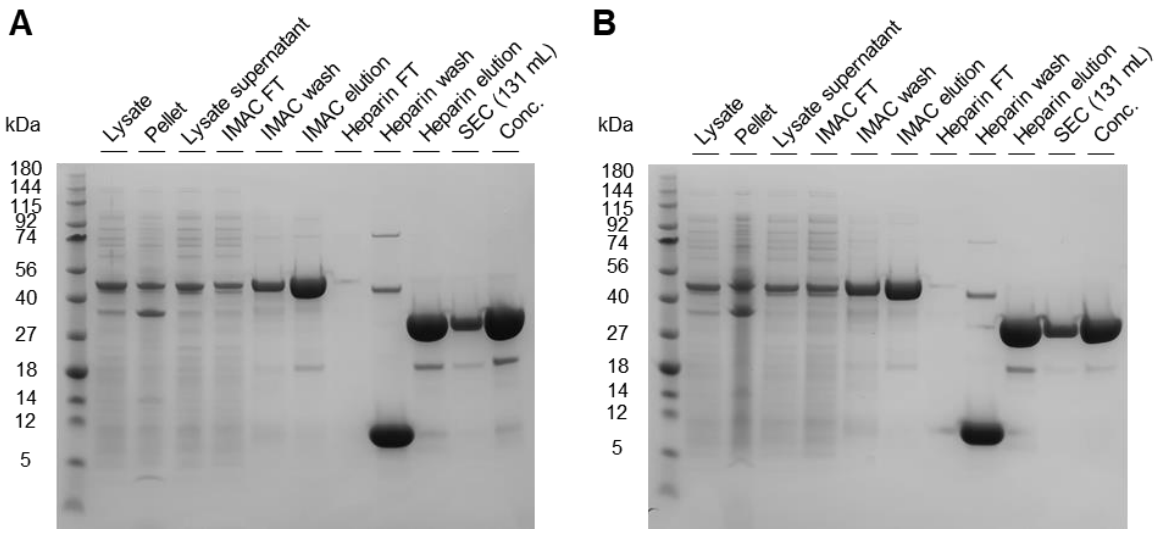

Figure 2.7. Representative gels summarizing ApoE2 and ApoE3 purification. Example gels of the **(A)** ApoE2 and **(B)** ApoE3 purification are shown. The TRX-ApoE2 and TRX-ApoE3 fusion protein are found in the soluble fraction of the lysate (lysate supernatant), however, some is found in the pellet with the cell debris (pellet). After enrichment of the fusion proteins by IMAC, they were applied to a heparin column. The fusion proteins show excellent heparin binding affinity as only minimal amount of protein is seen in the flow through of the column (heparin FT). Cleavage of the TRX solubility tag by PreScission protease was performed on the heparin column and TRX protein washed out the next day (heparin wash). Washing of the heparin column after loading the fusion protein, as well as after on column digestion was performed with reduced sodium chloride concentrations of 240 mM in the case of ApoE2 compared to 300 mM for ApoE3 and ApoE4. Elution of ApoE3 and ApoE2 was achieved by applying a linear salt gradient (heparin elution). Identical to ApoE4, two apparent elution peaks are observed for ApoE2 and ApoE3 in SEC; a minor shoulder at 131 mL and a major peak at 151 mL (Figure 2.10A). Fractions of the 151 mL peak were pooled and concentrated (conc.). The final concentrate has high purity, however, a minor impurity at 22 kDa is seen, in particular in the case of ApoE2.

2.3.4 Purification of ApoE4$_{mon}$ and ApoE4$_{1-191}$

The ApoE4$_{mon}$ mutant was purified using identical conditions to wild type ApoE4 (Section 2.3.2). Notably, the TRX-ApoE4$_{mon}$ fusion protein showed reduced binding affinity to the heparin column similar to ApoE2 and partly eluted during the wash with SEC buffer containing 300 mM NaCl (Figure 2.8). However, final yields were high (15-18 mg out of an 8 L expression culture) since ApoE4$_{mon}$ generally expressed better in Rosetta2(DE3) cells than wild type ApoE isoforms (Section 2.3.1). A similar purification protocol used for ApoE2 with reduced sodium chloride during HAC was therefore not adopted or tested. The elution profile of ApoE4$_{mon}$ during SEC was not reproducible. Peaks in purifications were generally very broad, and the peak maximum shifted to lower retention volumes the more protein was injected into the SEC column (Figure 2.8C). This suggests a concentration dependent effect on ApoE4$_{mon}$ oligomerization and therefore size. SAXS confirmed the concentration dependent effect on the size as determined by the radius of gyration (Rg) (Section 2.3.5).

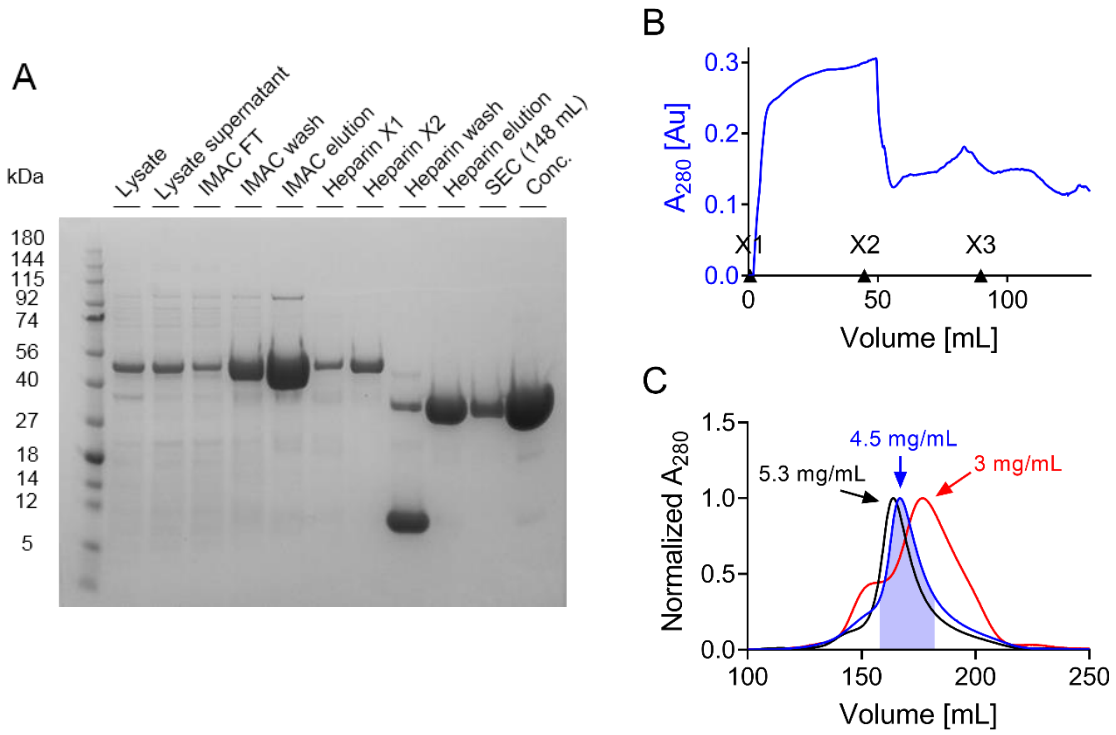

Figure 2.8. Summary purification of monomeric ApoE4. (A) An example gel of the ApoE4$_{mon}$ purification is shown. TRX-ApoE4$_{mon}$ fusion protein is found in the soluble fractions of the lysis supernatant and was enriched by IMAC (IMAC elution). IMAC elution fractions were then applied to a HiTrap heparin HP column (GE Healthcare) and washed with SEC buffer containing 300 mM NaCl. This resulted in partial elution of the TRX-ApoE4$_{mon}$ fusion protein (X2) that could be followed in the absorbance chromatogram as shown in panel **(B)**. The absorbance at 280 nm is shown as a function of elution volume. X1 represents the loading fraction. X2 and X3 are wash fractions during which the heparin column was flushed with SEC buffer. **(C)** SEC revealed a concentration dependent effect of ApoE4$_{mon}$ elution profile. Applying ApoE4$_{mon}$ at higher concentrations to the SEC column resulted in a shift of the elution peak maximum to lower volumes. The elution peak maximum was 164 mL, 167 mL and 177 mL when ApoE4$_{mon}$ was injected at concentrations of ~ 5.3 mg/mL, 4.5 mg/mL and 3 mg/mL respectively. In the purification presented here, ApoE4$_{mon}$ at a concentration of 4.5 mg/mL was applied to the column. Fractions around the 167 mL elution peak maximum were pooled (area under the curve highlighted in blue) and concentrated. Final product (conc.) as seen in panel **(A)** has very high purity (> 95%).

Primarily purifications of ApoE4$_{1\text{-}191}$ included batch IMAC using a cobalt resin followed by SEC. Although SEC separated the majority of the cleaved TRX tag from ApoE4$_{1\text{-}191}$, some TRX impurities were seen in the final product (Appendix Figure 2.24A). Additionally, high amounts of ApoE4$_{1\text{-}191}$ aggregate that eluted in the void volume of the SEC column formed during overnight digestion in suspension (Appendix Figure 2.24B) and reverse IMAC to remove residual TRX reduced yields of the amino terminal domain. An improved purification process was therefore adopted. The cleared lysate was loaded to a nickel column and digestion was performed on the column overnight. ApoE4$_{1\text{-}191}$ having lost its six-histidine tag was then washed out of the column with low imidazole concentrations while the TRX with the six-

histidine tag at its amino terminus remained immobilized to the column (Figure 2.9). This enabled easy separation of ApoE4$_{1-191}$ from TRX and no reverse IMAC was necessary to remove residual TRX. Moreover, fewer ApoE4$_{1-191}$ aggregates formed during on-column digestion. Purity and yields of the final product were very high (~10 mg per 1 L expression culture).

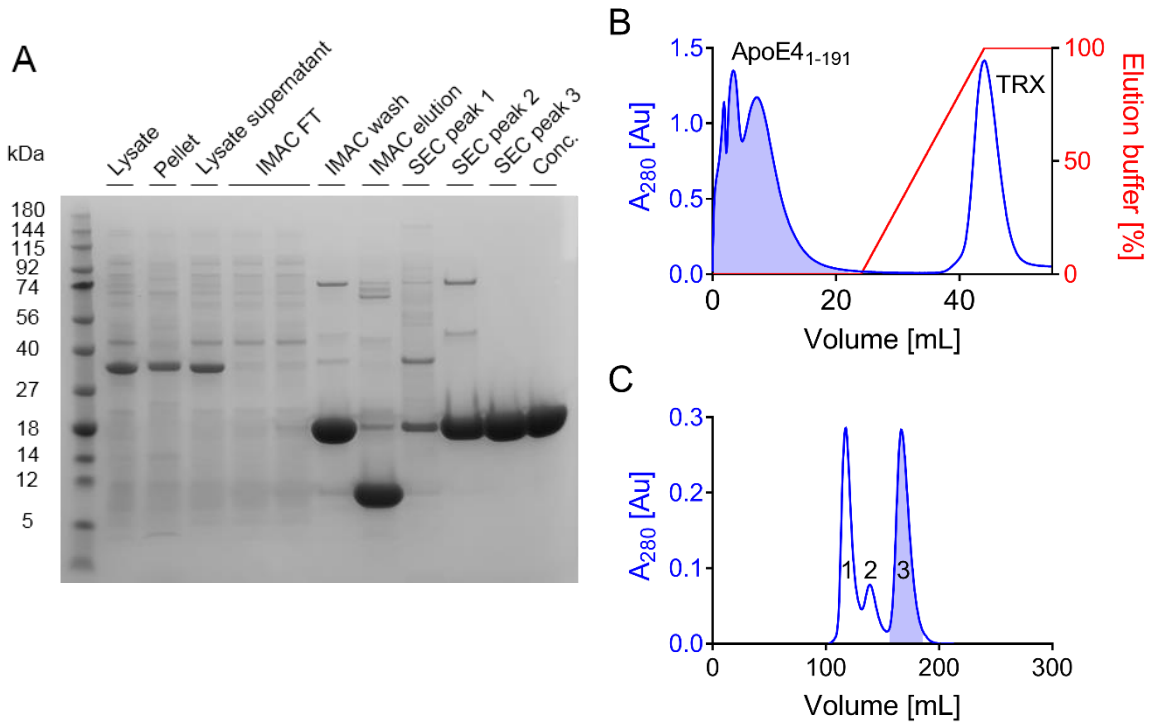

Figure 2.9. Purification of the ApoE4 amino terminal domain. (A) The gel summarizes the ApoE4$_{1-191}$ purification steps. The TRX-ApoE4$_{1-191}$ fusion protein is found in the soluble fractions of the lysate (lysate supernatant), although some is also seen in the cell debris pellet (pellet). The fusion protein bound to the nickel column and none was found in the flow through fractions (IMAC FT). After digestion overnight on the column, the column was washed with 20 mM imidazole (IMAC wash) and ApoE4$_{1-191}$ eluted with TRX remaining bound to the nickel column. TRX with the six-histidine tag was eluted by applying a linear imidazole gradient (IMAC elution). SEC excluded aggregates (SEC peak 1), as well as other higher oligomeric ApoE4$_{1-191}$ species (SEC peak 2) that formed during purification. The final product (conc.) has high purity as determined by densitometric scanning (> 95%). Panels **(B)** and **(C)** illustrate the respective IMAC and SEC chromatograms. The absorbance at 280 nm is shown as a function of elution volume. Three elution peaks were observed during SEC. An aggregate peak 1, higher ApoE4$_{1-191}$ species peak 2 and major ApoE4$_{1-191}$ peak 3 that was pooled to yield the final product (area under the curve highlighted in blue).

2.3.5 ApoE forms stable tetramers in solution and is elongated in shape

The structure of ApoE isoforms in solution was investigated using gel filtration, SEC MALS, AUC and SAXS. Since ApoE isoforms were isolated by a novel purification protocol, it was important to compare the behaviour of the proteins in solution with previous publications. ApoE isoforms were gel-filtered through a Superdex 200 column and all showed identical elution profiles with a minor shoulder at 131 mL and a major peak at 151 mL (Figure 2.10A). The ApoE retention volume was compared to the elution pattern of globular protein standards. From the standard curve for globular proteins, the Stokes radius (R_S) of ApoE was determined to be 5.8 nm that would correspond to a molecular mass of approximately 330 kDa (Figure 2.10). This much larger molecular weight of recombinant ApoE tetramer has already been observed in previous gel filtration studies (195, 379). A frictional ratio f/f_0 of 1.71 was calculated based on the R_S of 5.8 nm suggesting elongated shape in solution of ApoE. This elongation seems responsible for the discrepancy in molecular weight.

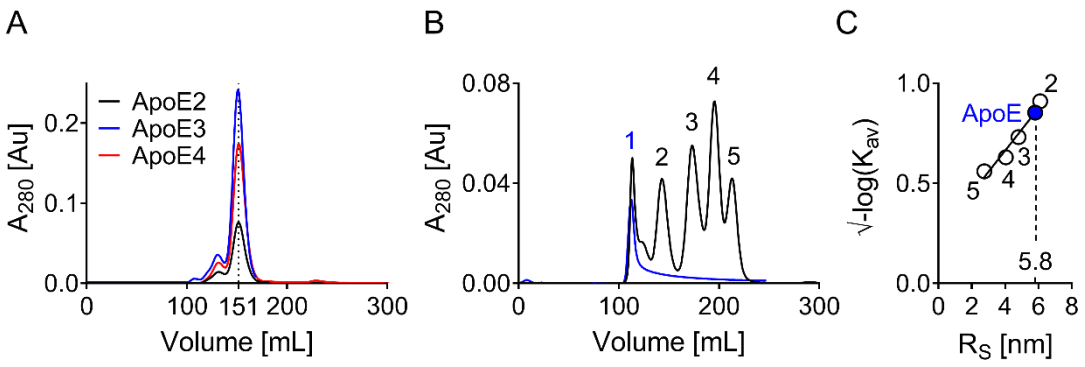

Figure 2.10. Gelfiltration studies on ApoE isoforms. The elution pattern of ApoE isoforms on the Superdex 200 column is shown in panel **(A)** as a function of absorbance at 280 nm versus the elution volume. All ApoE isoforms have a minor elution peak at 131 mL and a major at 151 mL. This suggests the presence of different oligomeric species. **(B and C)** A hydrodynamic radius of 5.8 nm, as well as a diffusion coefficient of 2.47 x 10^{-7} cm^2 s^{-1} was calculated for ApoE by calibration of the Superdex 200 column using commercially available protein standards (1 – dextran blue, 2 – ferritin, 3 – aldolase, 4 – conalbumin, 5 – ovalbumin).

To define the association state more accurately of the three ApoE isoforms in solution, their behaviour was analysed by SEC MALS and AUC. SEC MALS confirmed identical elution profile of all ApoE isoforms from a Kw-403 (Shodex) column (Figure 2.11). Molecular weights ranging from 139-151 kDa were calculated at the peak maximum suggesting tetramerization of ApoE isoforms in solution. The R_S was determined to be slightly higher compared to the value measured using gelfiltration (Table 2.8). However, values of 6.4 – 6.8 nm come closer to previous observations made for ApoE3 determined to have a R_S of 6.6 nm (195, 379).

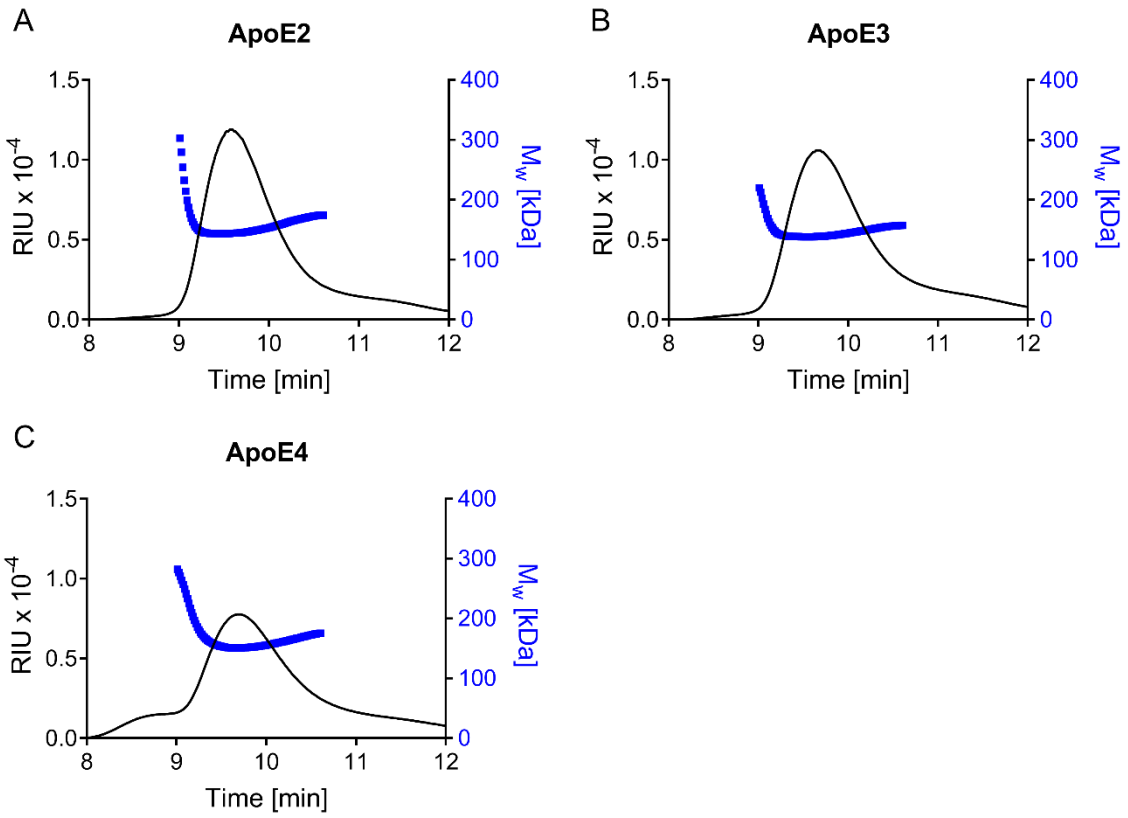

Figure 2.11. SEC MALS studies on ApoE isoforms. The differential refractive index (RIU) and the calculated molecular weight (M_w) across the peak are shown as a function of elution time for **(A)** ApoE2, **(B)** ApoE3 and **(C)** ApoE4.

Table 2.8. Hydrodynamic properties at elution peak determined by SEC MALS.

	ApoE2	ApoE3	ApoE4
Mw [kDa]	144	139	151
R_s [nm]	6.55	6.40	6.81
f/f_0	1.93	1.88	2.00
D [cm^2 s^{-1}] x 10^{-7}	3.78	3.88	3.64

AUC confirmed observations made in the SEC MALS study with respects to size and tetramerization. Sedimentation velocity analysis was performed by applying the continuous size distribution model c(S) (392). One major component around 3 S was identified after fitting the data which represents 92%, 75% and 91% of the soluble protein for ApoE2, ApoE3 and ApoE4 respectively (Figure 2.12 and Table 2.9). Higher molecular weight species are present and represent the rest of the soluble protein. In particular higher oligomeric species are seen in the ApoE3 sample at 4.5 S (Mw ~217 kDa). Normalization of sedimentation coefficients to standard conditions in water ($s_{20,w}$) result in values of 5.06 – 5.19 S (Table 2.9) that compare well to values obtained in previous studies of $s_{20,w}$ 5.3 – 5.7 S (195, 379).

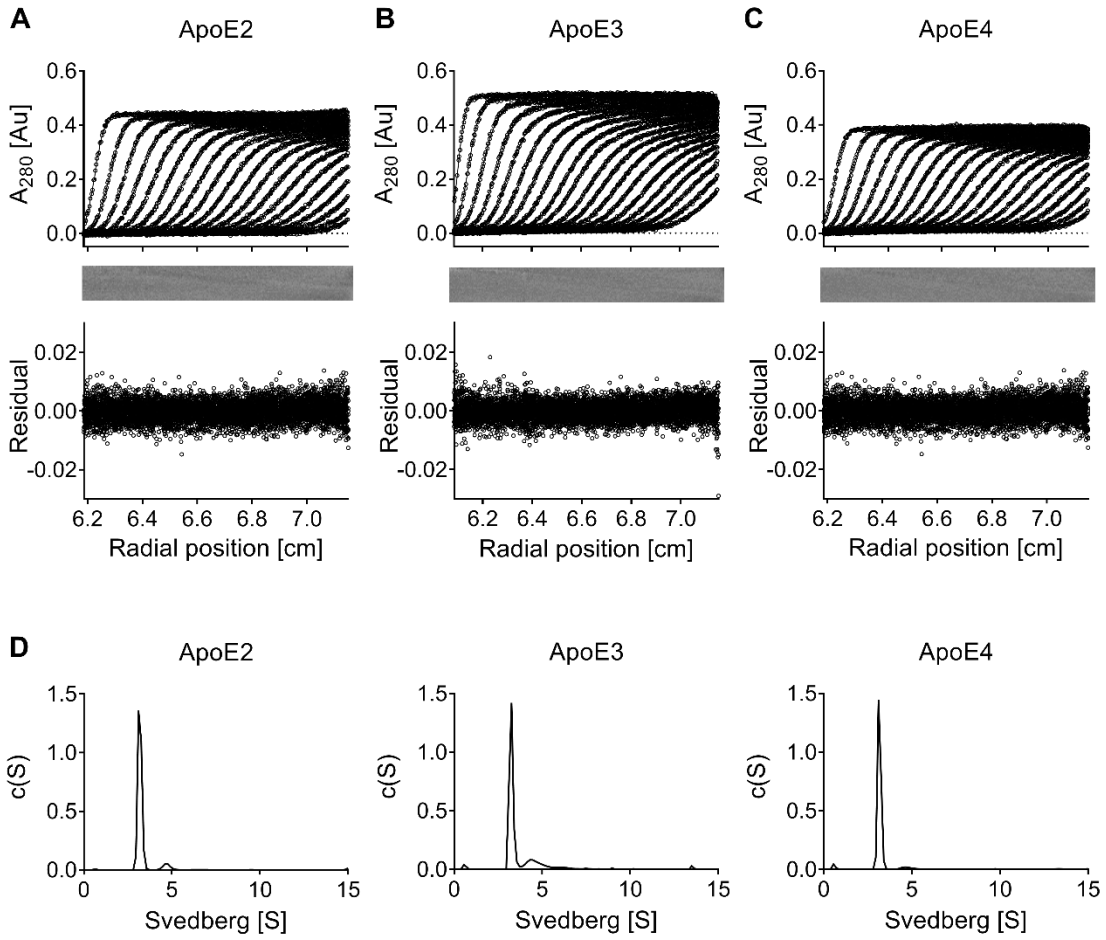

Figure 2.12. Sedimentation velocity of recombinant ApoE isoforms. Sedimentation velocity profiles of **(A)** ApoE2, **(B)** ApoE3 and **(C)** ApoE4 in SEC buffer are shown. The absorbance at 280 nm is plotted as a function of radial position. Curves were fitted to the Lamm equation with the SEDFIT program using the c(S) distribution function (upper panels). Grey scale of residual bitmap (medium panels) and residuals (bottom panels) plotted as a function of radial position attest of the quality of the fit. **(D)** Continuous c(S) size distributions of ApoE show no differences between all isoforms. One major species with a sedimentation coefficient at 3 S is detected for each isoform.

Table 2.9. Sedimentation analysis of recombinant ApoE isoforms in SEC buffer.

	f/f_0†	s* [S]	$s_{20,w}$# [S]	R_S [nm]	D x 10^{-7} [cm^2 s^{-1}]	Mw* [kDa]	Peak integration*	RMSD
ApoE2	1.75	3.19	5.09	5.72	2.50	122	~92%	0.0033
ApoE3	1.78	3.25	5.19	5.94	2.41	129	~75%	0.0031
ApoE4	1.79	3.17	5.06	5.92	2.42	126	~91%	0.0028

*Corresponding to the main sedimentation peak; †Best fitted friction ratio are used to calculate continuous size distribution; #Normalized to standard solution conditions of water at 20°C

Finally, small angle X-ray scattering (SAXS) was utilised to further investigate the shape of the ApoE isoforms in solution. All ApoE isoforms exhibit an identical scattering profile which suggest no difference in shape between ApoE isoforms (Figure 2.13). A Rg of 5.6 nm (56 Å) was calculated using the Guinier approximation and comes close to the hydrodynamic radius determined by gel filtration, SEC MALS and AUC. In the normalized Kratky representation, a compact, globular, monodispersed protein is observed as a near Gaussian peak with a maximum at 1.1 on the Y-axis and √3 on the X-axis (403). The presence of distinct maxima in the Kratky plots of all the ApoE isoforms indicate that they share a somewhat globular nature. However, the distinct shoulder found to the right of the main peak suggests that a portion of the protein is extended or polydispersed. This result is consistent with an extended multi-domain protein in which at least some of the domains, tethered by flexible linkers, have some freedom of movement with respect to the bulk of the protein (403). The pair distance distribution function fits to a maximal dimension (D_{max}) of approximately 19.5 nm (195 Å) and confirms elongation of ApoE in solution.

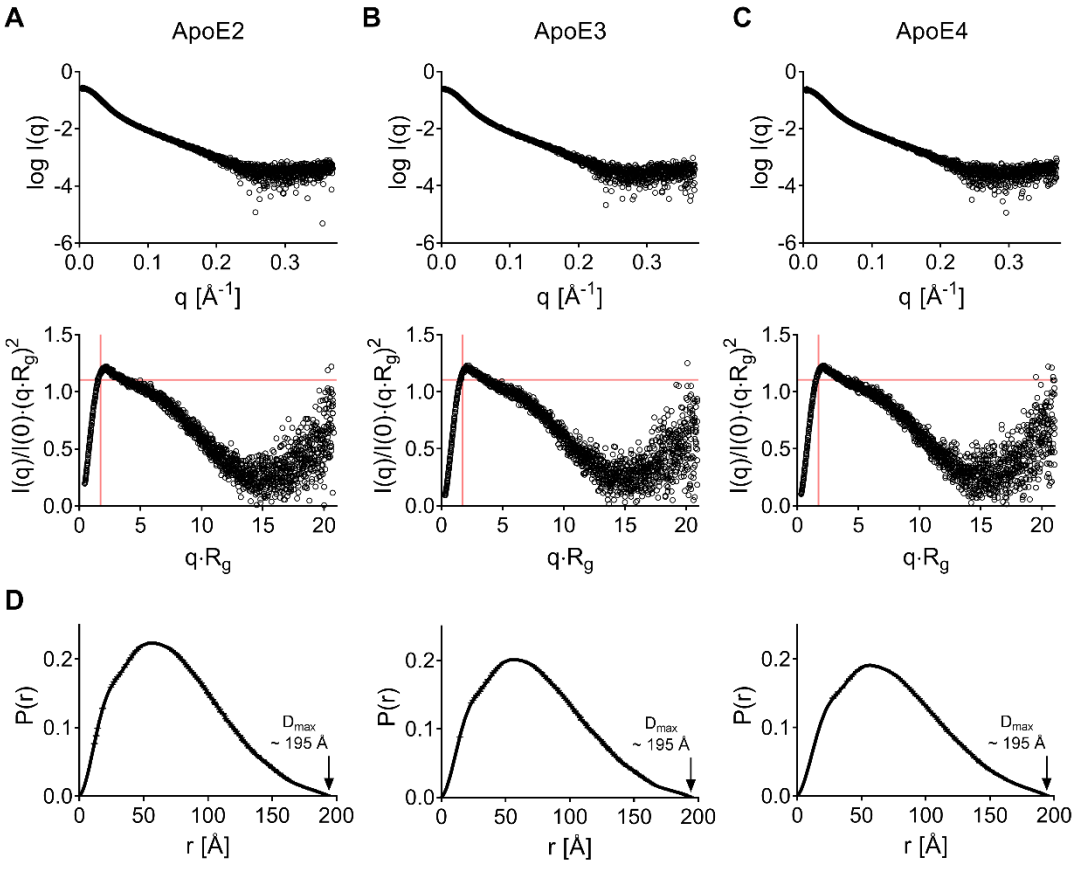

Figure 2.13. Small angle X-ray scattering experimental data of WT ApoE isoforms. X-ray scattering curves and the dimensionless Kratky plot for **(A)** ApoE2, **(B)** ApoE3 and **(C)** ApoE4 are shown, as well as **(D)** their corresponding pair distance distribution function P(r). The red cross-hair in the dimensionless Kratky plot denotes the Guinier-Kratky point (x= √3, y= 1.1), the peak position for an ideal globular particle.

Static and SAXS coupled with SEC (SEC-SAXS) was also performed with ApoE4$_{1-191}$ and ApoE4$_{mon}$. While ApoE4$_{1-191}$ remains monomeric and has stable Rg values at varying concentrations tested in the static measurements (Appendix Figure 2.25), a substantial concentration-dependent effect on Rg was observed in ApoE4$_{mon}$ (Figure 2.14). Estimation of the molecular weight (M_W) indicates that ApoE4$_{mon}$ is tetrameric at a concentration of 8 mg/mL and predominantly dimeric at lower concentrations. Similarly, the Rg values varied across the elution peak in SEC-SAXS (Appendix Figure 2.27B).

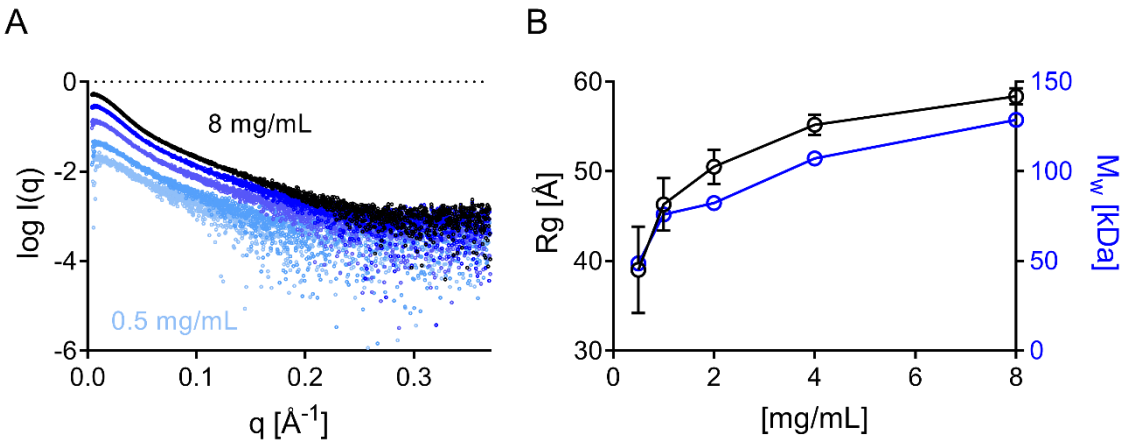

Figure 2.14. Scattering profile of ApoE4$_{mon}$ at different concentrations. (A) I(q) versus q as log-linear plots are shown for ApoE4$_{mon}$ at different concentrations (8, 4, 2, 1, 0.5 mg/mL; top to bottom scattering curve). **(B)** The estimated Rg from the Guinier approximation, as well as estimated M_W are shown as a function of protein concentration. The degree of fitting in the Guinier approximation decreases with decreased protein concentration due to increased noise and therefore results in erroneous Rg. The molecular weight M_W was estimated based on the method by Rambo *et al* (404).

Analysis of the SEC-SAXS sample demonstrated that ApoE4$_{1-191}$ is globular and monodisperse in solution and peaks near the Guinier-Kratky point (x= $\sqrt{3}$, y= 1.1) as seen in the Kratky representation (Figure 2.15A). A Rg of 2.3 nm (23 Å) was calculated by using the Guinier approximation and a maximal dimension of 7.3 nm (73 Å) was fitted in the P(r) analysis. These dimensions compare well to the dimensions of the amino terminal domain crystal structure (~6.7 nm in length, ~2.3 nm in width, PDB entry 1GS9).

The theoretical scattering pattern of a protein in solution can be calculated from its crystal structure. This can help to evaluate differences in the shape of the protein in solution to its structure in the crystal lattice (377). Computation of the theoretical scattering profile of the amino terminal domain crystal structure (PDB entry 1GS9) aligns well with the experimental scattering pattern (Figure 2.15A). This suggests that there are only small differences between ApoE4$_{1-191}$ in solution and in the crystal lattice.

ApoE4$_{mon}$ on the other hand is extended or polydispersed in nature and does not have its peak maximum at the Guinier-Kratky point (Figure 2.15B). Based on a Rg of 4.5 nm (45 Å), the molecular weight of the SEC-SAXS sample was estimated to be 62 kDa, suggesting dimerization of the protein. The theoretical scattering pattern of the deposited ApoE3 NMR structure (PDB entry 2L7B) that is monomeric and globular in nature does therefore not align with the experimental scattering profile (Figure 2.15B). Structural parameters of SAXS data, as well as SEC-SAXS frame selection are found in the Appendix.

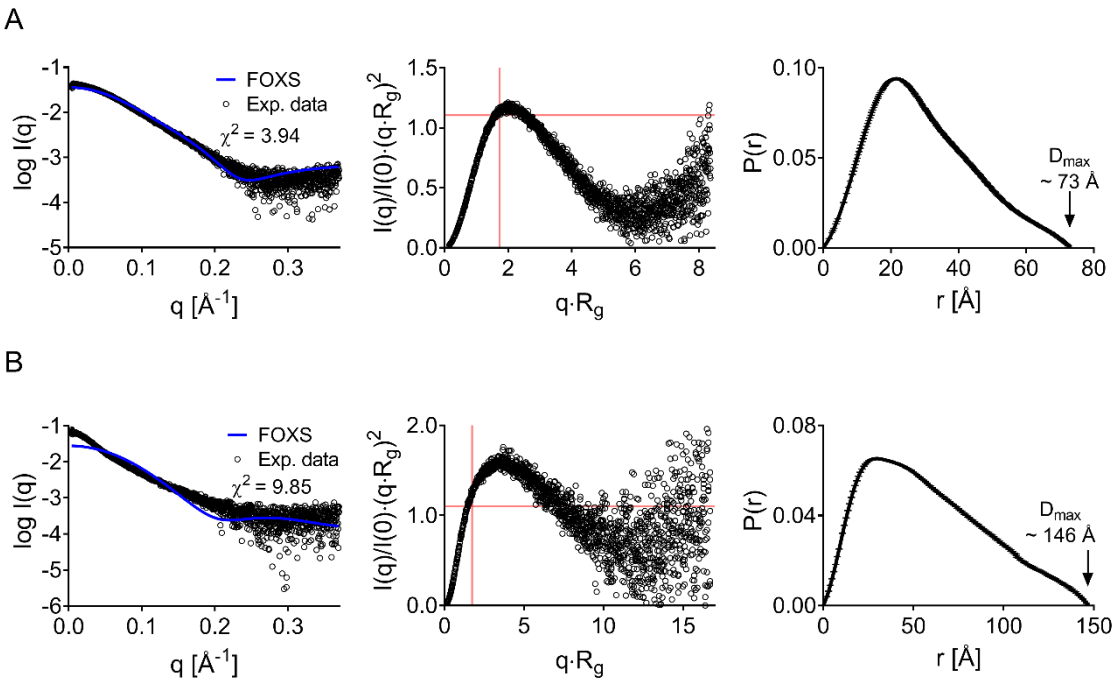

Figure 2.15. Small angle X-ray scattering experimental data of ApoE4$_{1-191}$ and ApoE4$_{mon}$. X-ray scattering curves (left), the dimensionless Kratky plot (middle) and the P(r) fit (right) are shown for **(A)** ApoE4$_{1-191}$ and **(B)** ApoE4$_{mon}$. Theoretical scattering profiles (in blue) were computed using the Fast X-ray Scattering (FOXS) web service (405). PDB entries 1GS9 and 2L7B were used to calculate theoretical scattering patterns of ApoE4$_{1-191}$ and ApoE4$_{mon}$ respectively. The quality of the fit χ^2 is included.

2.3.6 Crystallization trials

Several attempts were made to crystallize full length ApoE4 (see Methodology Section 2.2.16). Crystals grown with full length ApoE4 had similar morphology to crystals of ApoE4$_{1-191}$ (Figure 2.16A) and X-ray data collection of selected crystals revealed the amino terminal domain in the asymmetric unit. Analysis of crystals by SDS PAGE (not shown), as well as a stability test in solution confirmed degradation of full length ApoE4 in selected crystal conditions and its instability *in vitro* (Figure 2.16B). Notably, stability in solution could be increased by the addition of the mild detergent OG (Figure 2.16B). However, addition of OG, or the closely related OTG detergent only yielded crystals of the amino terminal domain (Figure 2.16C). Other additives such as heparin or Suramin that were shown to bind to ApoE4 (Chapter 3 and 4) did not yield

crystals of the full-length protein either (data not shown). Similar fragmentation was also observed with ApoE4$_{mon}$ (Figure 2.16D).

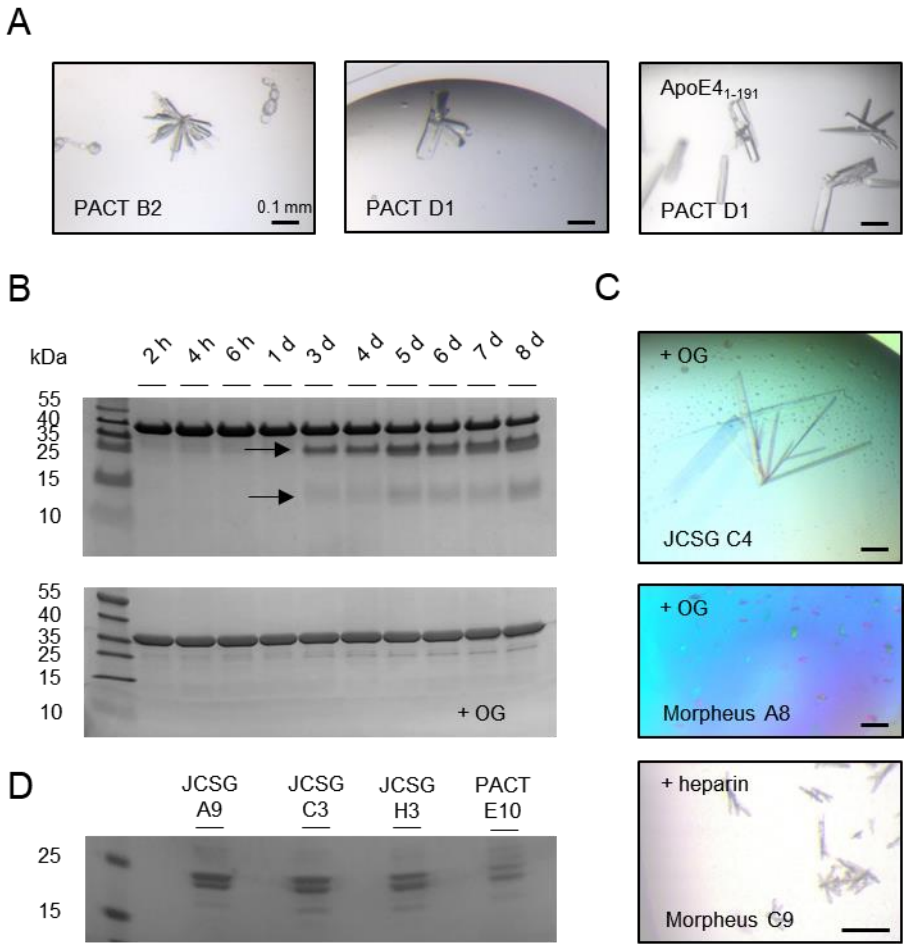

Figure 2.16. Crystallization trials of full length ApoE4. (A) Example crystals that were grown with full length ApoE4 in the PACT crystallization screen are shown and only consist of the amino terminal domain. Morphology of the crystals was identical or very similar to crystals grown with ApoE4$_{1-191}$. **(B)** ApoE4 degrades with time into ~22 kDa and ~12 kDa fragmentation products in solution at RT. Stability is drastically increased with the addition of 25 mM OG. **(C)** Example crystals grown in the presence of 25 mM OG, as well as 1 mg/mL heparin are shown. **(D)** ApoE4$_{mon}$ crystals were analysed by SDS PAGE and revealed degradation of the protein. The scale bar in each picture of panels **(A)** and **(C)** represents 0.1 mm. JCSG, PACT and Morpheus (Molecular Dimension) are commercially available crystallization screens. Constituents of the mother solutions PACT B2, D1, E10, and JCSG C4, A9, C3, H3, and Morpheus A8, C9 are found in the Appendix (Table 2.13).

The flexibility of a protein can influence crystallization success and flexible proteins may not form an ordered crystalline lattice. Flexibility can arise from the large movement of domains or loops, as well as due to solvent-exposed amino acid side chains such as from lysine residues. Chemical modification can reduce the surface entropy and therefore promote crystallization (384, 406). To test if crystallization of ApoE4 could be achieved by such residue modification, lysine and arginine residues were modified by reductive methylation and by chemical modification with 1,2-cyclohexanedione (CHD) (384, 385). Modification of residues was

performed on the heparin elution fractions after on-column digestion and modified proteins then purified by SEC. As can be seen on the gels in Figure 2.17A, ApoE4 has a slightly increased molecular weight after reductive methylation compared to unmethylated protein. This effect is more obvious in the modification of ApoE4 with CHD. Gelfiltration elution profiles were altered in both cases of modification with a shift to lower retention volumes (150 mL after lysine and 146 mL after arginine modification compared to 151 mL for unmodified protein, Figure 2.17B). Notably, a second elution peak with higher retention volume (187 mL) that contained modified ApoE4 was observed after arginine modification. A higher retention volume suggests a smaller size of the protein. Arginine modification may have moved the oligomeric state of ApoE4 to lower molecular weight species.

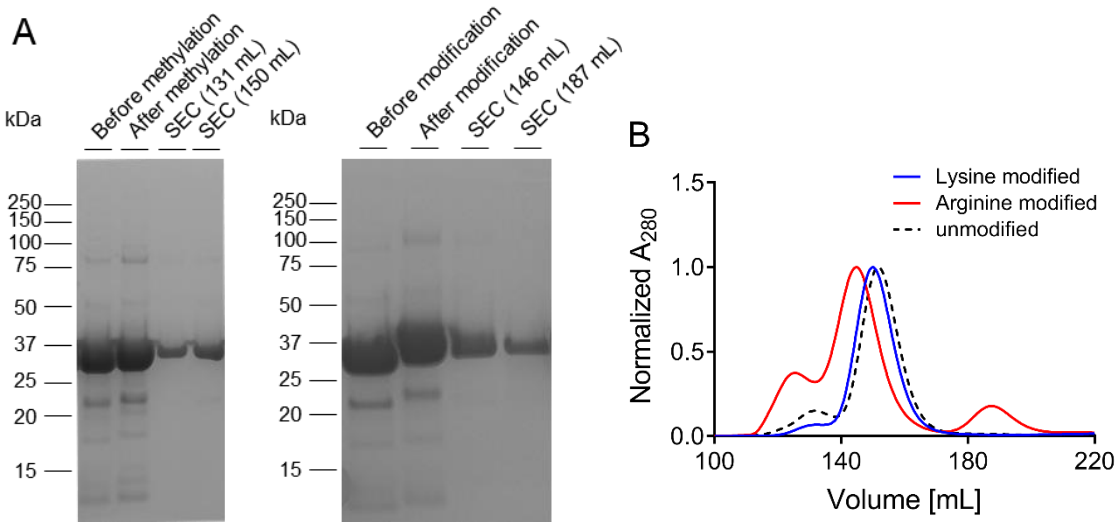

Figure 2.17. Modification of lysine residues by reductive methylation and arginine residues with CHD in ApoE4. (A) The left-hand gel shows electrophoresis of ApoE4 before and after reductive methylation of lysine residues. ApoE4 runs at a slightly higher apparent molecular weight after methylation. SEC fractions were highly pure and fractions at the major peak around 150 mL were pooled and concentrated. The right-hand gel demonstrates the effects of arginine modification with a notable increase in molecular weight of ApoE4 after chemical modification. A shoulder at 125 mL, as well as a major and a minor elution peak at 146 mL and 187 mL respectively were observed during SEC of arginine modified ApoE4. **(B)** The gelfiltration chromatograms of modified ApoE4 are compared to unmodified protein. The normalized absorbance at 280 nm is shown as a function of elution volume.

The Structure Screen (Molecular Dimension) condition C7 was identified in which a small crystal formed from lysine methylated ApoE4 (Figure 2.18A). Data collection at the synchrotron revealed however that the crystal was formed by the amino terminal domain. Arginine modification drastically influenced crystallization behaviour. While phase separation was predominantly observed in unmodified ApoE4 after mixing the protein with the mother solution (out of which the amino terminal domain eventually crystallized), arginine-modified ApoE4

precipitated with a dark colour and no crystals formed (Figure 2.18B). In a last effort, LCP crystallization was tested in collaboration with the Membrane Protein Lab (MPL, Imperial College at Diamond Lightsource), but unfortunately did not yield any crystals.

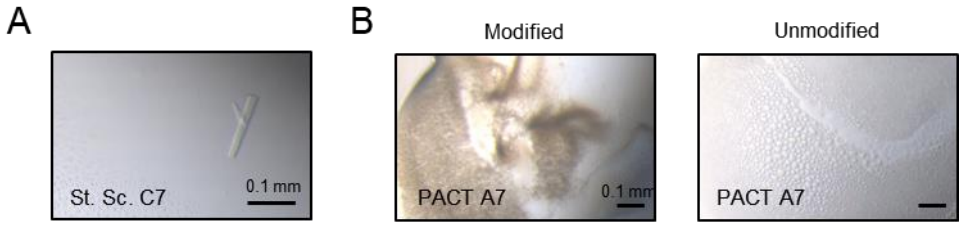

Figure 2.18. Crystallization of modified ApoE4. (A) A crystal of methylated ApoE4 was identified in the Structure Screen (St. Sc.) condition C7. **(B)** Arginine-modified ApoE4 behaved differently to unmodified protein. The example PACT A7 condition is compared. While modified ApoE4 precipitates with a brown colour, phase separation is seen in unmodified ApoE4. The scale bar represents 0.1 mm. St. Sc. and PACT (Molecular Dimension) are commercially available crystallization screens. Constituents of the mother solutions St. Sc. C7 and PACT A7 are found in the Appendix (Table 2.13).

As expected, $ApoE4_{1-191}$ readily crystalized and 62 conditions were identified in which protein crystals formed (ranging from low quality needles to high quality single crystals). A set of these crystals were sent to the synchrotron and the crystal obtained from the PACT A1 condition (Figure 2.19) diffracted to approximately 2.2 Å. Its structure was resolved by molecular replacement using a previous resolved structure (PDB entry 1GS9). Data collection, molecular replacement and structure refinement were performed by Dr Mark Roe (University of Sussex). The resolved crystal structure revealed a compact four-helix bundle that is similar to published structures (Figure 2.19) (212, 238). Residues at the amino (1 – 22) and carboxyl (163 – 191) termini, as well as residues connecting helix 2 and 3 are strongly disordered and did not allow any modelling. The structure perfectly aligns with 1GS9 with a root-mean-square deviation (RMSD) of atomic positions of 0.962 Å. Subtle differences to previously resolved structures are observed and involve Arg61, the residue implicated in mediating ApoE4 domain interaction (Chapter 1, Section 1.4.4). While Arg61 in truncated ApoE3 (PDB entry 1NFN) is buried in between helix 2 and 3 of the four-helix bundle, it seems to point away in truncated ApoE4 (PDB entry 1GS9, Figure 2.19). Here, the resolved structure confirms that surface exposed Arg61 in $ApoE4_{1-191}$ is flexible and is able to point towards both helices as found in ApoE3 amino terminal domain. Data collection and refinement statistics are found in the Appendix (Table 2.14).

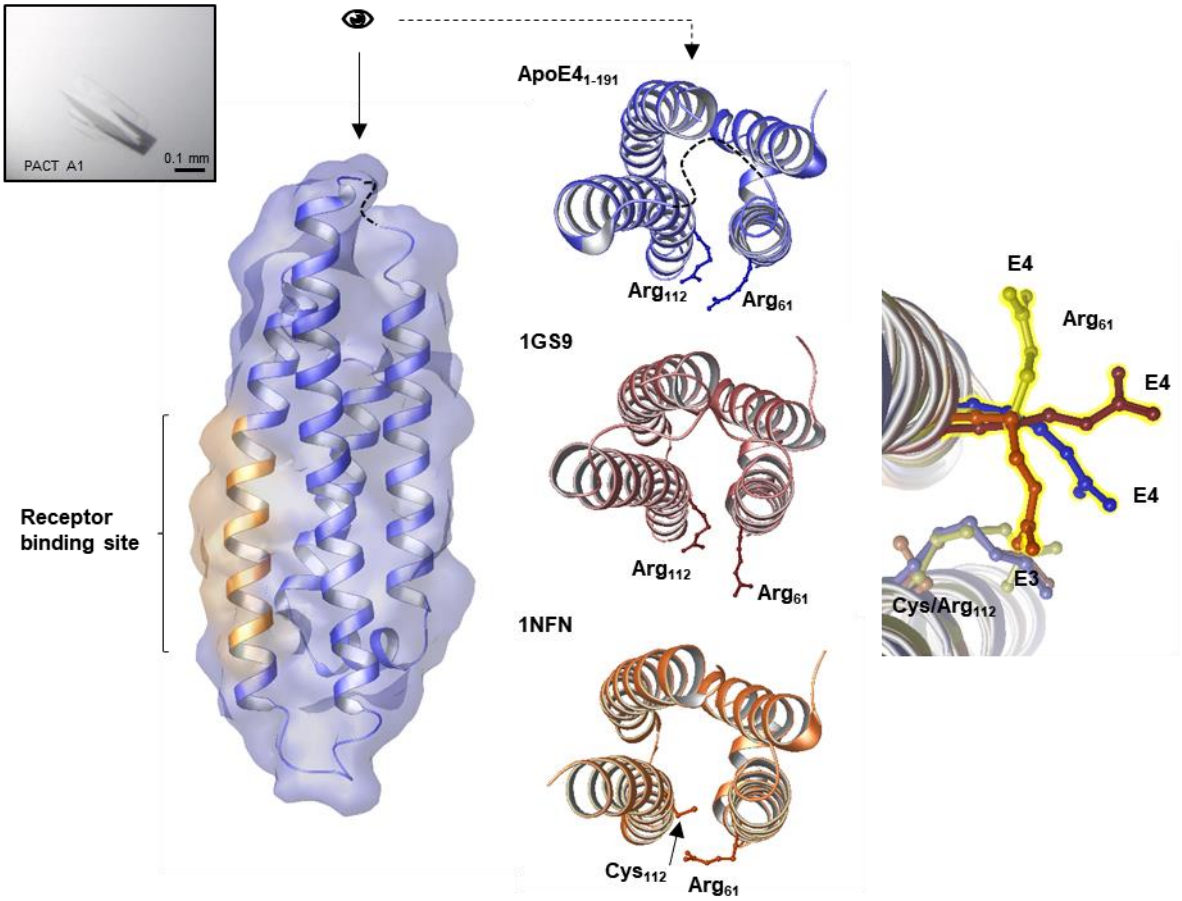

Figure 2.19. Crystal structure of ApoE4$_{1-191}$. The amino terminal domain forms a compact four-helix bundle (left Figure) that contains the receptor binding domain on helix 4 (highlighted in orange). Residues 82-84 that connect helix 2 and 3 could not be modelled due to weak electron density (indicated by dotted line). Comparison of this resolved structure with other amino terminal domains deposited in the protein data bank (middle and right figures) reveals high flexibility of Arg61. In ApoE3 (1NFN), Arg61 is buried between helix 2 and 3, while pointing away in ApoE4 (1GS9). Arg61 takes a similar conformation in this resolved structure as in ApoE3. Overlay of published structures (right figure; 1FNF in orange, 1GS9 in red, 1LE4 in yellow, resolved structure in blue) demonstrates conformation of Arg61 across resolved structures.

2.4 Discussion

The purification protocol developed as part of this thesis isolates ApoE isoforms in three steps under non-denaturing conditions. ApoE is expressed as a TRX fusion protein in Rosetta2(DE3) cells and, similar to previous observations, can only be produced over a short period of time (Figures 2.1 and 2.2) (369, 375) since longer expression times (> 6 h) result in lysis of the bacterial cells and low protein yields. Typically, 8 L were expressed as a main culture that yielded on average 10 mg of pure protein. Previous protocols report yields up to 20 mg of final product per 1 L of expression culture (375, 381). Compared to amounts of protein obtained here (~1.25 mg per 1 L culture), yields from the previous purification methods seem surprisingly high. In particular, since previous purification protocols involve additional steps including lipidation of ApoE with DMPC, ultracentrifugation in a potassium bromide gradient, extensive dialysis and delipidiation (375, 381). Other protocols that exclude these steps and purify ApoE solely by IMAC and SEC (under denaturing conditions) report yields up to 10 mg per 1 L expression culture (382). Identical amounts were obtained here with ApoE4$_{1\text{-}191}$ in a similar two-step purification process. Previous protocols purified ApoE under denaturing conditions (369, 375, 376, 381, 382). Chemical denaturation keeps ApoE in its monomeric state and prevents aggregation. This avoids elution of ApoE in the void volume of the size exclusion column and helps to separate it from other impurities (381). Chemical denaturation of ApoE was not performed in here developed purification protocol. Identical purity to previous methods was instead achieved by the inclusion of an additional purification step (i.e. HAC).

The lower yields of wild type ApoE isoforms compared to previous methods is likely due to loss of protein at the IMAC and HAC step. Although most TRX-ApoE eluted at high imidazole concentrations, some was also found to be present in the IMAC flow through and wash fractions (Figures 2.6 and 2.7). This suggests impaired binding or overloading of the TRX-ApoE fusion protein to the cobalt resin and partial elution at low imidazole concentrations (10 – 20 mM). Purifications were also tested with no imidazole and 5 mM imidazole in the lysis and IMAC binding buffer respectively, but also at these imidazole concentrations TRX-ApoE was found in the flow through and wash fractions (data not shown). A nickel resin could have been tested to capture TRX-ApoE since nickel resins have higher binding affinity for the six-histidine tag. This may prevent or reduce elution of TRX-ApoE at low imidazole concentrations. However, nickel resins have lower specificity compared to cobalt resins for the six-histidine tag that is likely to result in increased non-specific binding of other proteins and therefore in reduced purity (407). Nevertheless, final yields were limited by HAC. HiTrap Heparin HP columns (GE Healthcare) have a protein binding capacity of approximately 3 mg/mL medium (408). A 5 mL column as used in the purification established here will bind up to 15 mg of ApoE. Accounting for the loss of protein during HAC and SEC, final yields of approximately 10

mg are therefore explained due to limited binding capacity of the heparin column. Usage of a bigger heparin column is likely to have increased final protein yields.

Although the heparin column has only moderate protein binding capacity, its inclusion in the ApoE purification process was important. HAC substantially contributed to the purity of the final product and only functional (i.e. heparin binding) protein was selected. The intermediate HAC step however had to be adopted for ApoE2 that has reduced heparin binding affinity compared to ApoE3 and ApoE4 (Chapter 3).

Surprisingly, substantial concentration-dependent effects on the gel filtration elution profile were observed for $ApoE4_{mon}$ (Figure 2.8C). Elution peaks were very broad and applying the protein at lower concentrations resulted in a shift of the peak maximum to higher retention volumes. Static and SEC-SAXS measurements confirmed the concentration dependent effect on $ApoE4_{mon}$ size (Figure 2.14B). Suggestive is a monomer – dimer – tetramer equilibrium of $ApoE4_{mon}$. At high concentrations (> 8 mg/mL), the equilibrium is shifted towards the $ApoE4_{mon}$ tetramer, whereas dimers and monomers seem predominantly present at lower protein concentrations (0.5 – 8 mg/mL). This contradicts previous observations that a monomeric state persists up to concentrations of 15 mg/mL (243). Further characterization by complementary techniques such as AUC or SEC MALS should be performed in future to confirm results made in this thesis. Similar to ApoE2, $ApoE4_{mon}$ started to elute when washing the heparin column with SEC buffer (Figure 2.8B). This may be a result of $ApoE4_{mon}$ altered multimerization state. Heparin binding ability was shown to be dependent on ApoE oligomerization and monomeric, carboxyl-terminus truncated ApoE was shown to exhibit impaired binding to heparin (409, 410). Monomeric or dimeric forms of $ApoE4_{mon}$ will therefore have reduced heparin binding ability and elute at lower salt concentrations.

Characterization of wild type ApoE isoforms by gelfiltration (Figure 2.10), SEC MALS (Figure 2.11) and AUC (Figure 2.12) confirmed tetramerization of lipid-free ApoE isoforms in solution and hydrodynamic parameters determined here are well in accordance with previous results (195, 208, 378, 379). SAXS data on lipid-free ApoE has not been reported to date and adds to observations made with the other biophysical techniques. All ApoE isoforms resemble one another in solution in terms of size, shape and multimerization and their X-ray scattering data compares well to that of an elongated multi-domain protein that has a certain degree of flexibility (403).

Crystallization attempts of full length, lipid-free ApoE only yielded crystals of the amino terminal domain. ApoE's flexibility in solution as confirmed by SAXS (Figure 2.13) may hinder its assembly into a highly ordered crystal lattice. Modification of lysine and arginine residues (Figure 2.17), addition of small molecules or detergents, as well as LCP crystallization did not

produce any full-length ApoE4 protein crystals either. Crystals of full-length ApoE were previously yielded in complex with DPPC that diffracted to ~10 Å maximum resolution (221, 222). The diffraction data was used to create a low-resolution molecular envelope model that was confirmed by SAXS (411) (Chapter 1, Section 1.4.3). However, crystals diffracted only to low-resolution and the DPPC within the crystal resulted in strong diffuse scattering that would not allow for solving high-resolution data (221, 222). Additional strategies could be tested in future to increase crystallization success of the full-length protein. Fragmentation occurs at the flexible hinge region that is prone to proteolysis (196). Identification and mutation of critical residues in the hinge region could increase stability of ApoE in solution and therefore favour its crystallization. Chaperone-assisted crystallography could additionally be employed to decrease ApoE's intrinsic flexibility. Protein fusion partners such as TRX not only help proper folding of the target protein during recombinant expression, they can also aid with its crystallization. Several proteins were successfully crystallized as maltose binding protein (MBP) fusion partner and/or in the presence of designed ankyrin repeat proteins (DARPins) (412, 413). DARPins are genetically engineered antibody mimetic peptides that bind with high affinity to the target protein and may help to stabilize it in a certain conformation (412). ApoE with the right fusion partner may be stabilized in solution and lose some of its flexibility that may promote its assembly into a crystal.

Crystallization of the ApoE4 amino terminal domain confirmed high flexibility of the surface exposed Arg61 side chain. The ApoE4 domain interaction hypothesis was based in parts on observations made in the amino terminal high-resolution crystal structure that showed Arg61 to point away from the ApoE4 four-helix bundle (Chapter 1, Section 1.4.4). It has been suggested by Dong *et al* (238) that the altered conformation of Arg61 in ApoE4 enables its interaction with acidic residues located on the carboxyl terminus. In here resolved structure, Arg61 is buried between helix 2 and 3, identical to ApoE3 (Figure 2.19). This contradicts the observations that were made by Dong *et al* (238) and it therefore remains speculative whether Arg61 interacts with Glu255.

In conclusion, the purification process developed as part of this thesis yielded enough amounts of highly pure protein to perform biophysical characterization studies in solution and to set up crystallization trials. Selection of functional protein by use of a heparin column and the exclusion of non-denaturing conditions assures purification under mild conditions of native ApoE.

2.5 Appendix Chapter 2

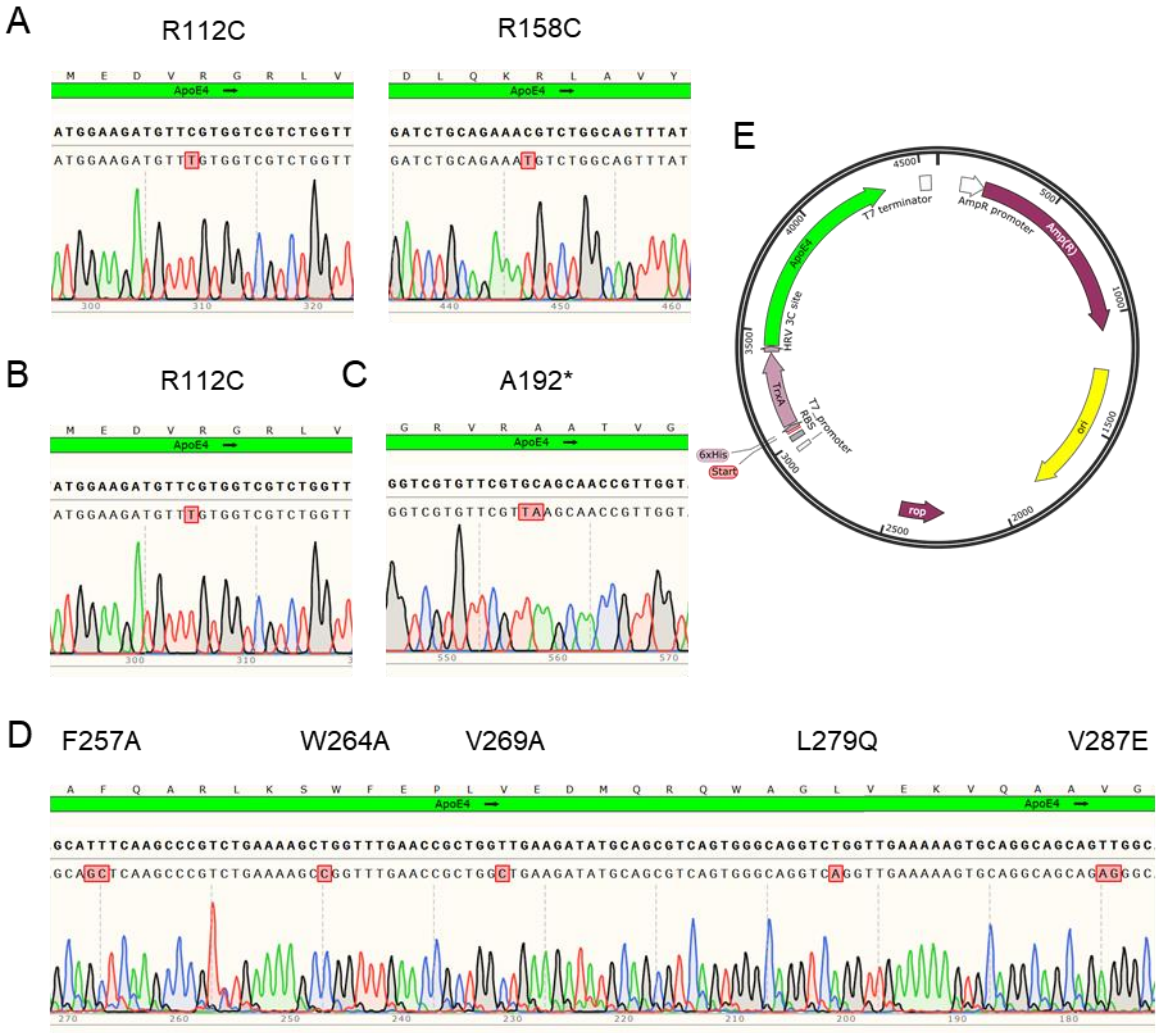

Figure 2.20. Sequencing results. Plasmid mutagenesis was confirmed by sequencing (Eurofins) and sequencing results were aligned with the ApoE4 DNA plasmid sequence in Snapgene version 4.2.6 (GSL Biotech). Sequencing chromatograms are shown below (green – adenine [A], red – thymine [T], black – guanine [G], blue – cytosine [C]). **(A)** ApoE2, **(B)** ApoE3, **(C)** ApoE4$_{1\text{-}191}$ and **(D)** ApoE4$_{mon}$. **(E)** The pET17b-TRX-ApoE4 plasmid map.

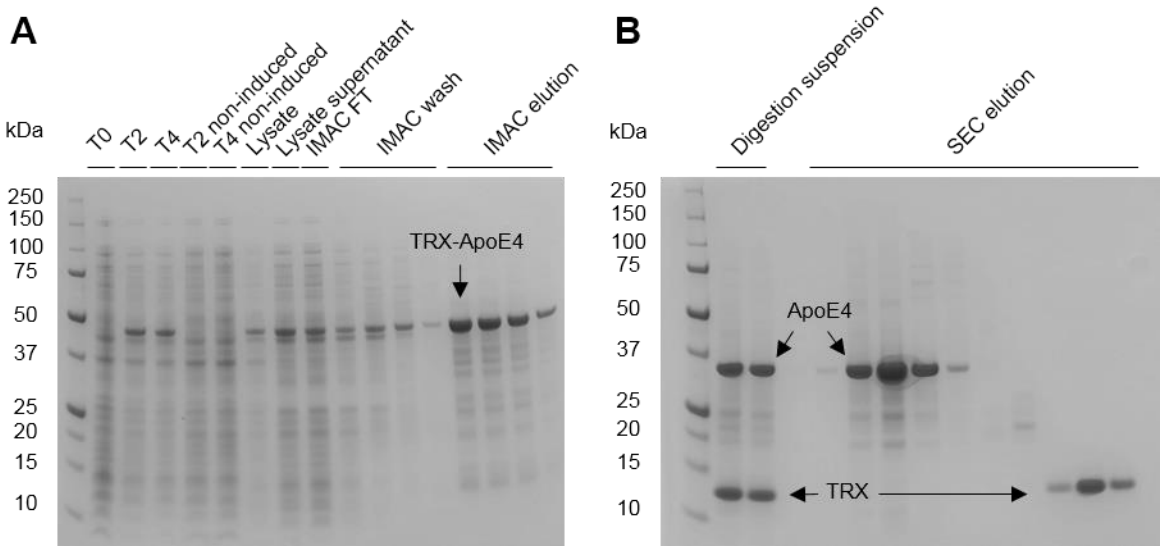

Figure 2.21. Purification of ApoE4 by a combination of IMAC and SEC. (A) Expression of ApoE4 is confirmed over 4 h (T0, T2, T4). A primary capture step by IMAC enriches ApoE4 and removes major impurities. ApoE4 shows good solubility and is found in the lysate supernatant after removal of the cell debris. Although most ApoE4 elutes at high imidazole concentration during the elution steps (IMAC elution), some is found in the flow through, as well as the wash fractions (IMAC FT and IMAC wash). The IMAC elution fractions were then pooled and the thioredoxin (TRX) protein removed by digestion with PreScission protease. **(B)** Digestion of the fusion protein was confirmed (digestion suspension) and the protein further purified by size exclusion chromatography (SEC). As seen in the elution fractions (SEC elution), ApoE4 is nicely separated from the TRX solubility tag by SEC, however, impurities are found to be co-eluting with ApoE4 resulting in moderate purity.

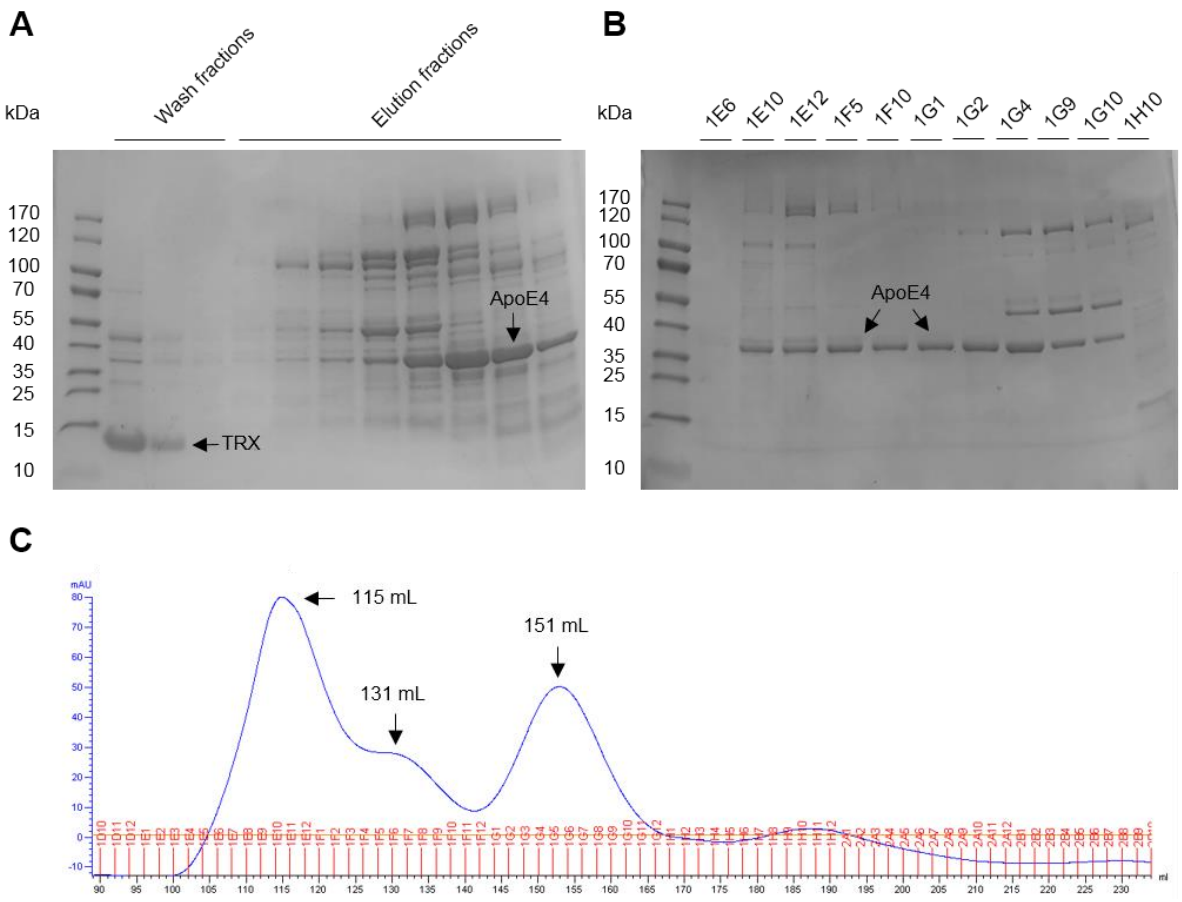

Figure 2.22. Purification of ApoE4 by a combination of HAC and SEC. (A) After lysis of the cells and removal of the cell debris, the lysate supernatant was directly applied to a heparin column and an on-column digestion was performed overnight. The next day, cleaved TRX was washed out (wash fractions) and ApoE4 eluted by increasing the salt concentration. Although the most pronounced observable band in the elution fractions is ApoE4, many other impurities are seen. **(B and C)** Purity improved by SEC, however, non-separable elution peaks are seen in the elution chromatogram. ApoE4 assumes different oligomeric states apparent from three major elution volumes (115 mL, 131 mL and 151 mL).

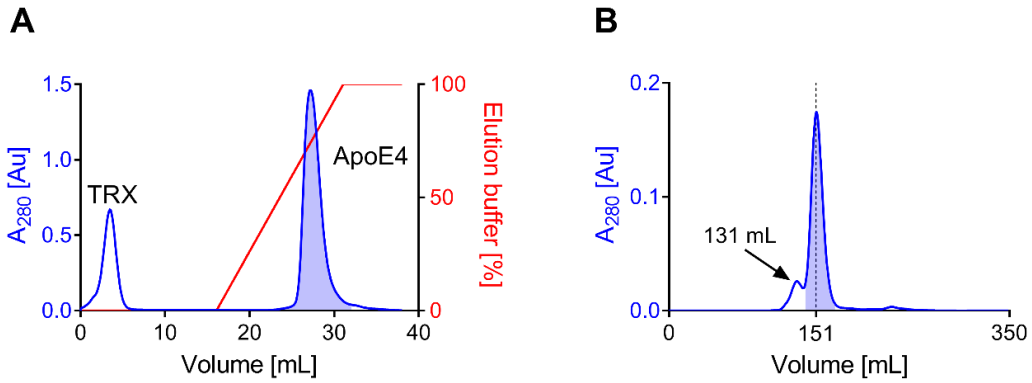

Figure 2.23. ApoE4 elution profiles. Example ApoE4 elution chromatograms are shown for **(A)** the heparin column and **(B)** the SEC column. The area under the curve highlighted in blue were ApoE4-containing fractions that were pooled for downstream processing. The absorbance at 280 nm is shown as a function of elution volume.

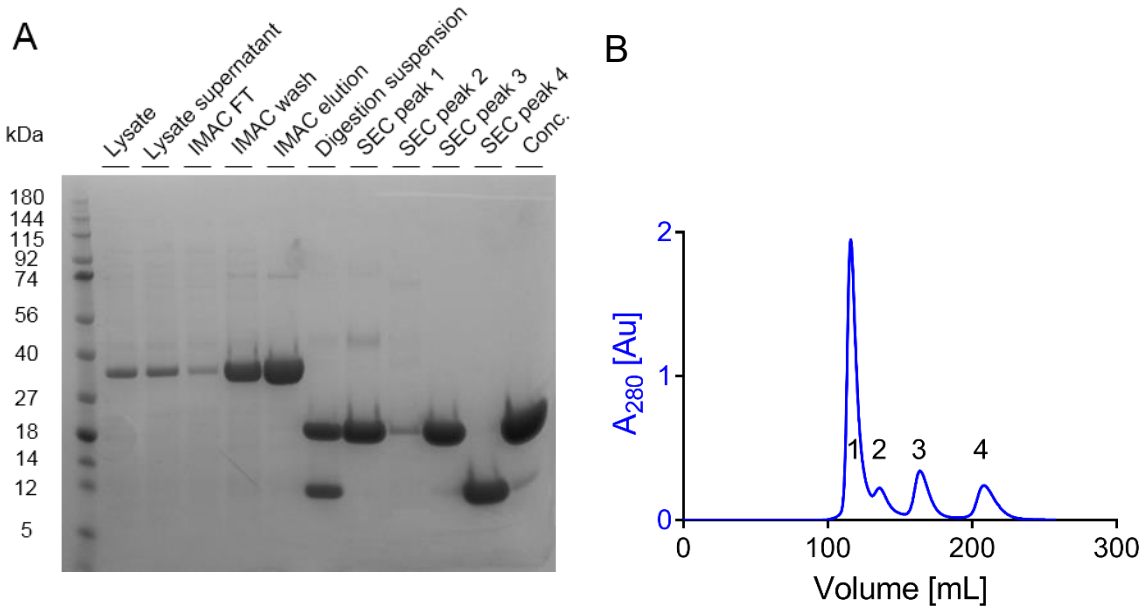

Figure 2.24. Purification of truncated ApoE4 by a combination of batch IMAC and SEC. (A) In a first purification procedure, ApoE4$_{1-191}$ was purified by capture on a cobalt resin, followed by SEC. After digestion overnight (digestion suspension), ApoE4$_{1-191}$ was applied to a HiLoad 26/600 Superdex 75 pg column (GE Healthcare). **(B)** Four elution peaks were observed. Peak 1 contains substantial amounts of aggregated ApoE4$_{1-191}$, peak 2 higher oligomeric species and peak 3 most of the monomeric ApoE4$_{1-191}$. The last peak consists of TRX. Although, TRX and ApoE4$_{1-191}$ were separated by SEC, some TRX was found to be present in the concentrate (conc.). Reverse IMAC to capture TRX resulted in great loss of ApoE4$_{1-191}$.

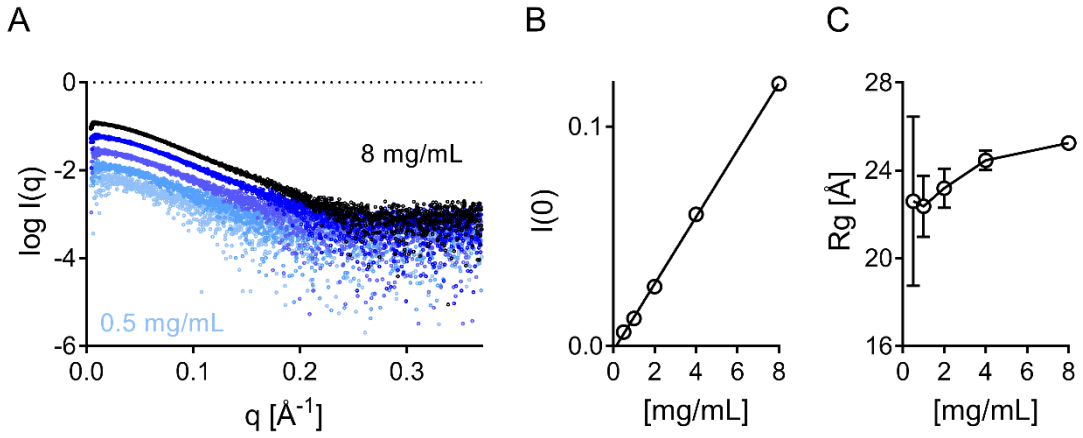

Figure 2.25. Scattering profile of ApoE4$_{1-191}$ at different protein concentrations. (A) I(q) versus q as log-linear plots are shown for ApoE4$_{1-191}$ at different concentrations (8, 4, 2, 1, 0.5 mg/mL; top to bottom scattering curve). **(B)** I(0), the intensity measured at zero angle (q= 0), is plotted as a function of protein concentration and demonstrates well behaviour of the sample. **(C)** The estimated Rg from the Guinier approximation as a function of protein concentration is shown.

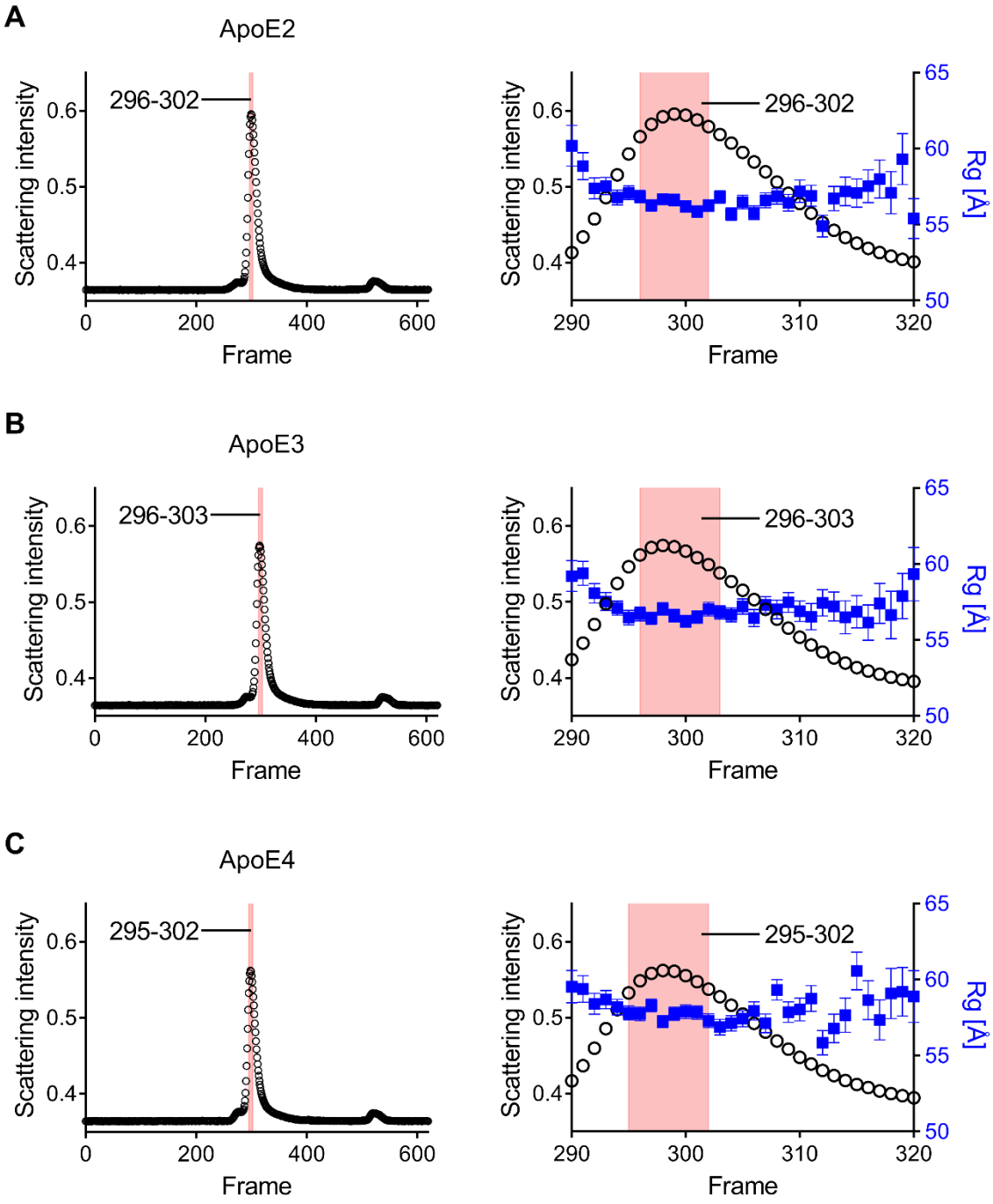

Figure 2.26. In-line SEC-SAXS frame selection for ApoE isoforms. Scattering profiles to curves **(A)** 296-302 (ApoE2), **(B)** 296-303 (ApoE3) and **(C)** 295-302 (ApoE4) were selected for analysis and averaging. The integral of scattering intensity as well as the Rg are plotted against the frame number.

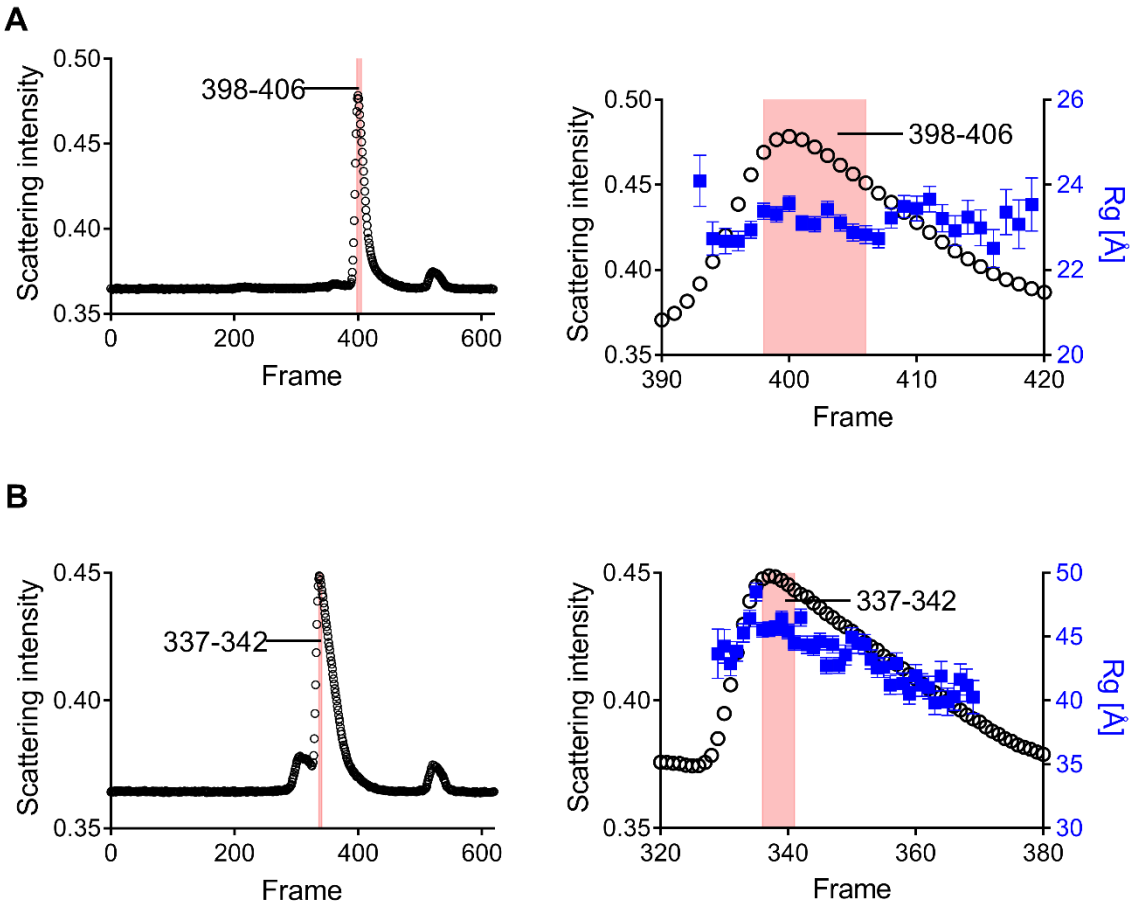

Figure 2.27. In-line SEC-SAXS frame selection for ApoE4$_{1\text{-}191}$ and ApoE4$_{mon}$. Scattering profiles to curves **(A)** 398-406 (ApoE4$_{1\text{-}191}$) and **(B)** 337-342 (ApoE4$_{mon}$) were selected for analysis and averaging. A broad elution peak for ApoE4$_{mon}$ is observed with a decrease in calculated Rg across the peak. The integral of scattering intensity as well as the Rg are plotted against the frame number.

Table 2.10. Structural parameters of ApoE SEC-SAXS data.

	ApoE2		ApoE3		ApoE4	
	ATSAS	**ScÅtter**	**ATSAS**	**ScÅtter**	**ATSAS**	**ScÅtter**
Gunier analysis						
Guinier Rg, (Å)	56.35 ± 0.15	56.34 ± 0.63	56.69 ± 0.14	56.81 ± 0.59	57.64 ± 0.15	57.69 ± 0.66
Gunier I(0), arbitrary units	0.2500 ± 0.0005	0.2759 ± 0.0004	0.2500 ± 0.0004	0.2494 ± 0.0003	0.2400 ± 0.0004	0.2395 ± 0.0063
P(r) analysis (manual)						
P(r) Rg, (Å)	58.20 ± 0.08	57.56 ± 1.88	58.56 ± 0.088	57.78 ± 1.88	59.33 ± 0.07	58.46 ± 1.33
P(r) I(0), arbitrary units	0.2785 ± 0.0004	0.2746 ± 0.0094	0.2511 ± 0.0003	0.2464 ± 0.0086	0.2411 ± 0.0003	0.2355 ± 0.0063
D_{max}, (Å)	194.5	194.5	195	195	195.5	195.5
q range, ($Å^{-1}$)	0.0089 - 0.2513	0.0083 - 0.2461	0.0056 - 0.2414	0.0054 - 0.2394	0.0058 - 0.235	0.0056 - 0.2351
GNOM total estimate	0.92	---	0.922	---	0.929	---
χ^2 (S_{k2})	---	1.17 (0.33)	---	0.88 (0.37)	---	1.02 (0.42)
P(r) analysis (Autognom)						
P(r) Rg, (Å)	58.48 ± 0.12	---	58.69 ± 0.11	---	59.52 ± 0.13	---
P(r) I(0), arbitrary units	0.2789 ± 0.0005	---	0.2515 ± 0.0004	---	0.2415 ± 0.0004	---
D_{max}, (Å)	204.68	---	203.65	---	207.92	---
q range, ($Å^{-1}$)	0.0054 – 0.1419	---	0.0054 – 0.1401	---	0.0056 – 0.1383	---
GNOM total estimate	0.896	---	0.899	---	0.856	---
M_W estimate						
Volume of correlation V_c, ($Å^2$) †	---	1062	---	1068	---	1103
M_W estimate (kDa)*	---	159 ± 5	---	160 ± 5	---	169 ± 4

Structural parameters. Parameters were calculated for comparison in ATSAS 2.8.2 and ScÅtter 3.1R.
† P(r) based V_c.
* Mass estimates based on P(r) Rg and V_c (404).

Table 2.11. Rg and I(0) of $ApoE4_{1-191}$ and $ApoE4_{mon}$ at different concentrations.

$ApoE4_{1-191}$ [mg/mL]	**Guinier Rg [Å]**	**I(0), arb. Units**
8	25.25 ± 0.29	0.120 ± 0.00025
4	24.47 ± 0.44	0.060 ± 0.00020
2	23.20 ± 0.89	0.027 ± 0.00020
1	22.37 ± 1.39	0.013 ± 0.00015
0.5	22.61 ± 3.85	0.006 ± 0.00020
$ApoE4_{mon}$ [mg/mL]	**Guinier Rg [Å]**	**I(0), arb. Units**
8	58.35 ± 0.92	0.552 ± 0.00110
4	55.19 ± 1.13	0.303 ± 0.00084
2	50.52 ± 1.91	0.136 ± 0.00072
1	46.32 ± 2.93	0.046 ± 0.00043
0.5	39.02 ± 4.83	0.020 ± 0.00039

Table 2.12. Structural parameters of $ApoE_{1-191}$ and $ApoE4_{mon}$ SEC-SAXS data.

	$ApoE4_{1-191}$		$ApoE4_{mon}$	
	ATSAS	**ScÅtter**	**ATSAS**	**ScÅtter**
Gunier analysis				
Guinier Rg, (Å)	23.22 ± 0.06	23.33 ± 0.19	45.38 ± 0.24	45.16 ± 1.38
Gunier I(0), arbitrary units	0.0420 ± 0.0001	0.0417 ± 0.0001	0.0660 ± 0.0002	0.0660 ± 0.0003
P(r) analysis (manual)				
P(r) Rg, (Å)	23.47 ± 0.041	22.65 ± 0.26	46.68 ± 0.11	45.56 ± 0.74
P(r) I(0), arbitrary units	0.0415 ± 0.0001	0.0415 ± 0.0006	0.0663 ± 0.0001	0.0649 ± 0.0015
D_{max}, (Å)	74	74	146.5	146.5
q range, ($Å^{-1}$)	0.0067 – 0.3379	0.0065 – 0.3384	0.0047 – 0.2461	0.0045 – 0.2461
GNOM total estimate	0.9	---	0.879	---
χ^2 (S_{k2})	---	0.89 (0.31)	---	0.82 (0.37)
P(r) analysis (Autognom)				
P(r) Rg, (Å)	23.37 ± 0.033	---	46.66 ± 0.15	---
P(r) I(0), arbitrary units	0.0414 ± 0.0001	---	0.0663 ± 0.0002	---
D_{max}, (Å)	73	---	144	---
q range, ($Å^{-1}$)	0.0085 – 0.344	---	0.0061 – 0.176	---
GNOM total estimate	0.856	---	0.807	---
M_W estimate				
Porod volume, ($Å^3$)	---	39460	---	131500
Volume of correlation V_c, ($Å^2$) †	---	253.1	---	588.4
M_W estimate (kDa)*	---	22.98	---	61.73

Structural parameters. Parameters were calculated for comparison in ATSAS 2.8.2 and ScÅtter 3.1R.
† P(r) based V_c.
* Mass estimates based on P(r) Rg and V_c (404).

Table 2.13. Crystal screen conditions.

Condition	Constituents
JCSG A9	0.2 M ammonium chloride, 20 % (w/v) PEG 3350
JCSG C3	0.2 M ammonium nitrate, 20 % (w/v) PEG 3350
JCSG C4	0.1 M HEPES pH 7.0, 10 % (w/v) PEG 6000
JCSG H3	0.1 M Bis-Tris pH 5.5, 25 % (w/v) PEG 3350
PACT A1	0.1 M SPG (succinic acid, sodium phosphate monobasic monohydrate, glycine) pH 4.0, 25 % (w/v) PEG 1500
PACT A7	0.2 M sodium chloride, 0.1 M sodium acetate pH 5.0, 20 % (w/v) PEG 6000
PACT B2	0.1 M MIB (sodium malonate dibasic monohydrate, imidazole, boric acid), 25 % (w/v) PEG 1500
PACT D1	0.1 M MMT (malic acid, MES monohydrate, Tris), 25 % (w/v) PEG 1500
PACT E10	0.02 M sodium/potassium phosphate, 20 % (w/v) PEG 3350
Structure Screen C7	0.1 M HEPES pH 7.5, 20 % (w/v) PEG 4000, 10 % (v/v) 2-propanol
Morpheus A8	0.06 M magnesium chloride hexahydrate, 0.06 M calcium chloride dihydrate, 0.1 M HEPES, 0.1M MOPS pH 7.5, 12.5 % (v/v) MPD, 12.5 % (w/v) PEG 1000, 12.5 % (w/v) PEG 3350
Morpheus C9	0.09 M sodium nitrate, 0.09 sodium phosphate dibasic, 0.09 M ammonium sulphate, 0.1 M Tris, 0.1 M bicine pH 8.5, 40% (v/v) PEG 500 MME, 20 % (w/v) PEG 20000

PEG - polyethylene glycol, MOPS - 3-(N-morpholino)propanesulfonic acid, MDP - 2-Methyl-2,4-pentanediol, PEG MME - polyethylene glycol methyl ether

Table 2.14. Data collection and refinement statistics of ApoE4$_{1-191}$.

Resolution range	37.74 - 2.16 (2.237 - 2.16)
Space group	P 2 21 21
Unit cell	28.4566 47.7983 122.967 90 90 90
Unique reflections	9409 (920)
Completeness (%)	97.48 (96.36)
Wilson B-factor	35.19
Reflections used in refinement	9344 (900)
Reflections used for R-free	438 (59)
R-work	0.2381 (0.3660)
R-free	0.2873 (0.4261)
Number of non-hydrogen atoms	1138
macromolecules	1084
solvent	54
Protein residues	137
RMS (bonds)	0.014
RMS (angles)	1.85
Ramachandran favored (%)	92.48
Ramachandran allowed (%)	5.26
Ramachandran outliers (%)	2.26
Rotamer outliers (%)	11.43
Clashscore	6.05
Average B-factor	45.39
macromolecules	45.23
solvent	48.69

3 DIFFERENTIAL BINDING OF APOE ISOFORMS TO HEPARIN INVESTIGATED BY SMALL ANGLE X-RAY SCATTERING

3.1 Introduction and Objectives

The main function of ApoE is maintaining lipid and cholesterol homeostasis in the brain and peripheral tissues and it does so by interacting with specific cell surface receptors and HSPGs (Chapter 1, Section 1.4.1 and 1.4.2). HSPGs are glycoproteins that contain covalently attached glycosaminoglycan (GAG) chains such as heparan sulphates (HS) and they are either membrane associated, secreted into the extracellular matrix or found in secretory vesicles (414). Heparin is a member of the GAG family of carbohydrates and is a highly sulphated form of HS (Figure 3.1) (414, 415). As outlined, HSPGs can enhance the uptake of ApoE-containing lipoproteins which is particularly important in the HSPG-LRP1 pathway of lipoprotein uptake or they can function as lipoprotein receptors in their own right (126).

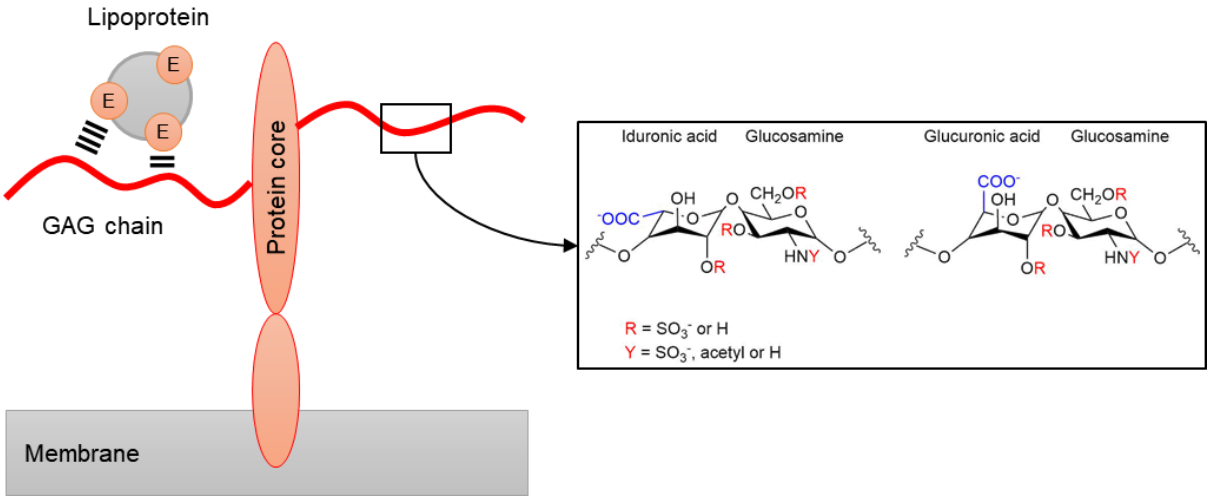

Figure 3.1. Heparan sulphate proteoglycans. HSPGs are glycoproteins that consist of a protein and one or more covalently attached GAG chains. GAGs are highly sulphated, linear polysaccharides and include for example HS and heparin. The inlet demonstrates the possible disaccharide subunits of heparin. Each disaccharide contains an uronic acid (Iduronic acid or Glucuronic acid) and a glucosamine component that can be modified (e.g. sulphated) at several positions. ApoE (E) as a constituent of lipoproteins interacts with the polyanionic GAGs through positively charged amino acids located in its heparin binding sites.

Binding of ApoE to HSPGs is mostly mediated by its heparin binding site located at the amino terminal domain (residues 136–147) and to a lesser extent by a second binding site at the carboxyl terminus that involves basic residues around lysine 233 (209, 210, 409, 416). Several studies have investigated the interaction of ApoE isoforms to heparin using surface plasmon resonance (SPR) (212, 213, 410, 416, 417). By passing defined amounts of ApoE over heparin-containing SPR sensor chips, binding affinities were determined to be in the nanomolar range and the interaction appears to be largely electrostatic, being sensitive to the

salt concentration (409, 417). Nuclear magnetic resonance (NMR) experiments demonstrate that Lys143 and Lys146 in the heparin binding region have low pK_a values of 9.5 and 9.2 respectively (typical pK_a of lysine side chain ~ 10.5) due to the high positive electrostatic potential in the vicinity of these residues that would favour deprotonation of the lysine ε-amino group (213, 409, 418) and mutagenesis studies have confirmed the importance of these residues for binding of ApoE to GAGs (213, 409). The binding kinetics are consistent with a two-step process where a fast initial electrostatic interaction is followed by a slower hydrophobic interaction (416). The binding is dependent on the ApoE oligomerization state and monomeric carboxyl-terminus truncated ApoE exhibits reduced binding to GAGs (409, 410). Lipidation state on the other hand does not seem to influence heparin binding affinity as assessed with DMPC complexed ApoE (410). Size of the heparin units on the other hand seems to influence binding affinity and small GAGs with less than six saccharide units do not interact with ApoE (212). Notably, ApoE4 was shown to exhibit up to 3-fold greater binding to GAGs with faster association rates compared to ApoE2 and ApoE3 due to an enhanced electrostatic initial interaction through its amino terminal domain (410, 416).

Structural information on the interaction of ApoE with GAG molecules such as heparin is limited. Far-UV circular dichroism (CD) studies suggest that there is no major structural change in secondary structure upon binding of ApoE to GAGs (410, 416), however, these techniques do not account for changes in tertiary or quaternary structure and conformation. In this chapter, the ApoE-heparin interaction was investigated using SAXS. Isoform-dependent differences in heparin binding affinity, as well as major structural changes that occur in ApoE upon heparin binding were identified. Additionally, the importance of critical lysine residues for the ApoE-heparin interaction are demonstrated.

3.2 Material and Methods

3.2.1 Materials

All materials were purchased from Sigma-Aldrich or Fisher Scientific and were the highest purity available. Heparin was purchased from Fisher Scientific (# 411210010) and Suramin from Sigma-Aldrich (# S2671).

3.2.2 Site directed mutagenesis

The ApoE4 (K143A, K146A) mutant was generated by site directed mutagenesis as described in Chapter 2, Section 2.2.2 using primers 5'-gtctggcaagccatctgcgtgcactgcgcaaacg-3' (K143A) and 5'-atctgcgtaaactgcgcgcacgtctgctgcgtgatg-3' (K146A). Sequencing results are presented in the Appendix (Figure 3.15).

3.2.3 Protein production and purification

ApoE isoforms and $ApoE4_{1-191}$ were produced and purified as described in Chapter 2, Sections 2.2.6 and 2.2.7.

3.2.4 Reductive methylation

Lysine residues in ApoE4 were modified by reductive methylation as described in Chapter 2, Section 2.2.10.

3.2.5 Heparin column binding studies

ApoE isoforms at 5 mg/mL in 20 mM HEPES, 150 mM NaCl, 10% (v/v) glycerol, pH 8.0 were loaded on a 5 mL HiTrap Heparin FF column (GE Healthcare) at a flow rate of 1.5 mL/min. The column was washed with 10 mL of 20 mM HEPES, 150 mM NaCl, 10% (v/v) glycerol, pH 8.0 and bound protein then eluted by applying a linear NaCl gradient of 0.15 – 1.0 M NaCl over 30 mL at a flow rate of 1.5 mL/min.

3.2.6 Small angle X-ray scattering

The following theoretical introduction to SAXS is mostly based on the review by Putnam *et al* (377). Additionally, the book on SAXS by Glatter and Kratky (419) and the webinars that are found online by Dr Thomas Grant (University at Buffalo, USA) (420) and Dr Alexey Kikhney (EMBL, Hamburg, Germany) (421) were used as a source.

In SAXS, a collimated, monochromatic beam of X-rays is directed through a sample that contains the protein of interest (Figure 3.2). Electrons oscillate under the influence of the electric field of the X-ray beam and emit secondary X-rays with the same wavelength as the incident beam, albeit out of phase (termed coherent X-ray scattering or Thomson scattering). SAXS is a contrast method and the scattering of the macromolecule in solution is derived from the difference in the average electron density of the sample containing the target molecule and

sample solvent. In practice, scattering of a buffer blank and the sample are collected and subtracted to yield the scattering of the pure macromolecule (Figure 3.2). The resulting scattering curve I(q) is radially symmetric (isotropic) due to random orientation of the particles in solution and is given as a function of momentum transfer. The momentum transfer is defined as:

$$q = \frac{4\pi sin\theta}{\lambda} \quad (3.1)$$

where 2θ is the scattering angle and λ is the wavelength of the incident X-ray beam. The unit of the momentum transfer q is therefore inverse angstroms [Å^{-1}]. In this thesis, scattering data was acquired at a wavelength of 1 Å and q ranging from 0 to 0.4 Å $^{-1}$. This corresponds to scattering angles 2θ of 0° to 3.6° respectively.

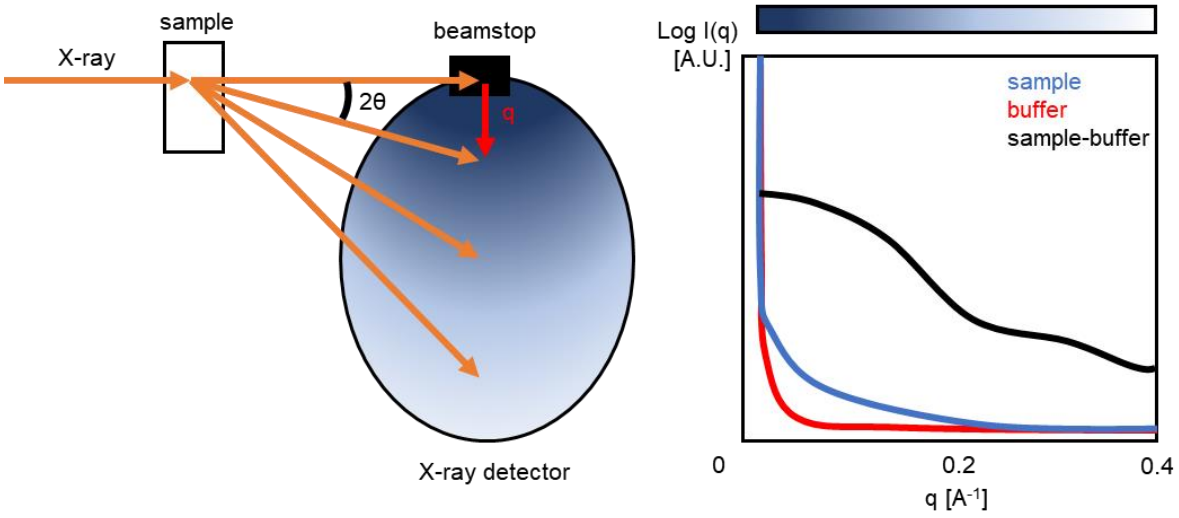

Figure 3.2. Experimental setup of SAXS data acquirement. A collimated, monochromatic X-ray beam is directed through a sample containing the target macromolecule. The intensities of the scattered X-rays are recorded by an X-ray detector. A beamstop prevents burning of the X-ray detector by the direct synchrotron beam (i.e. beam that is not scattered, zero angle). Intensities are then radially averaged and plotted as shown on the right as a function of momentum transfer (or scattering angle). The scattering intensity decreases with increasing scattering angle. Experimentally, scattering intensities of the buffer blank have to be subtracted from the sample to yield the pure scattering signal of the macromolecule.

The low-resolution portion (or low q range, ~ 0 – 0.2 Å^{-1}) contains information about the size of the particle. The parameter that is extracted from the low-resolution range is the radius of gyration (Rg). The Rg is the average of square centre-of-mass distances in the molecule and can be extracted by the Guinier approximation that is defined as:

$$I(q) = I(0)\, e^{-\frac{q^2 Rg^2}{3}} \quad (3.2)$$

$$\ln I(q) = \ln I(0) - \frac{q^2 Rg^2}{3} \quad (3.3)$$

where I(0) is the scattering intensity at zero angle. The scattering data will give a straight line in the Guinier plot (ln I(q) versus q^2) and is only valid over a q range of qRg < 1.3 for globular proteins. The Guinier plot additionally helps to assess the quality of the data and no linearity will exist for aggregated protein samples. The experimental setup of SAXS data collection does not allow for the direct measurement of scattering intensity at zero angle (Figure 3.2). Scattering intensity at zero angle, I(0) can be determined through linear extrapolation of the data in the Guinier plot. On an absolute scale, I(0) is the number of electrons in the protein sample and therefore can be used to determine the molecular weight. Similarly, intermediate q-vales can be used to obtain the cross-sectional radius (Rc) of an elongated macromolecule. Its definition is given in equation (3.4) and (3.5) and Rc is obtained from the slope of the linear portion of the plot ln qI(q) versus q^2.

$$qI(q) = I(0)\, e^{-\frac{q^2 Rc^2}{2}} \quad (3.4)$$

$$\ln qI(q) = \ln I(0) - \frac{q^2 Rc^2}{2} \quad (3.5)$$

Higher q-values (q ~ 0.2 – 0.4 $Å^{-1}$) contain details on the molecular shape of the sample and can visualize conformational changes. An excellent tool for the evaluation of folding and conformational change of the sample is the Kratky plot (q^2I(q) versus q). Often, the Kratky plot is normalized to the Rg and I(0) of the sample (Figure 3.3). Folded domains and globular proteins will peak at the Kratky-Guinier (x = √3, y = 1.1) point. Elongated or multidomain proteins have extended shoulders whereas unfolded samples will not reach baseline (Figure 3.3).

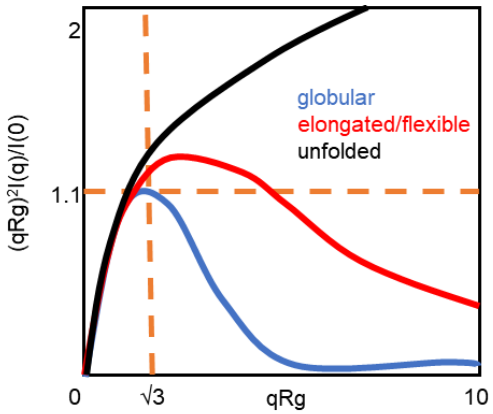

Figure 3.3. The Kratky representation. The normalized Kratky plot visualizes “foldedness” of the macromolecule.

The pair distance distribution function, P(r) represents the histogram (or probability) of distances between pairs of points within the particle (Figure 3.4). It is defined as:

$$P(r) = \gamma(r)\, r^2 \quad (3.6)$$

where γ(r) is a probability function that evaluates the probability to find a distance r within the molecule. P(r) is obtained by indirect Fourier transform. Trial P(r) functions are constructed for the sample and evaluated against the experimental scattering data. The P(r) function is typically constrained to be zero at r = 0 and r ≥ D_{max}, where D_{max} is the maximal linear dimensions in the scattering particle. The Rg and I(0) of the macromolecule can also be calculated from the P(r) function and unlike in the Guinier approximation uses the whole q range for their determination (377, 419).

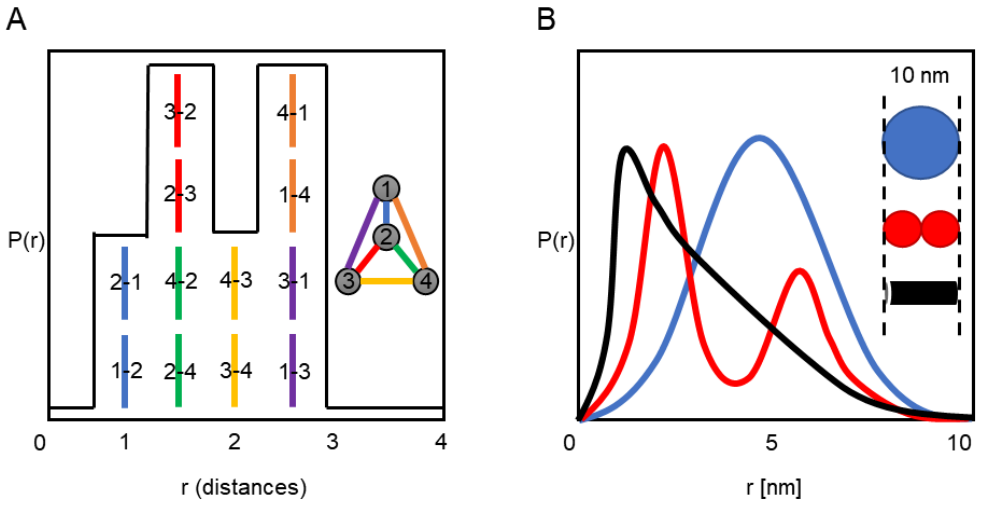

Figure 3.4. The pair distance distribution function. (A) The pair distance distribution function of a theoretical molecule with four atoms is shown. The P(r) function resolves the distances within the molecule (i.e. from atom to atom). **(B)** The P(r) function of three example bodies are shown that all have a maximal dimension of 10 nm. Figure 3.4A was adapted with permission from Cambridge University press: Putnam *et al*, Quarterly Reviews of Biophysics, 2007, 40(3):191-285 (377).

Proteins were buffer-exchanged into 20 mM HEPES, 300 mM NaCl, 1 mM TCEP, pH 8.0 by using Vivaspin 15 concentrators (Sartorius, MWCO 10000 Da). To determine ideal protein concentration for static measurements, scattering of ApoE at 8, 4, 2, 1 and 0.5 mg/mL protein in 20 mM HEPES, 300 mM NaCl, 1 mM TCEP, pH 8.0 was collected. Static SAXS experiments in the presence of heparin or Suramin were performed at an ApoE concentration of 4 mg/mL in 20 mM HEPES, 300 mM NaCl, 1 mM TCEP, pH 8.0 and final concentrations of 4, 12, 37, 110 and 330 µg/mL heparin or 4, 12, 37, 110 and 330 µM Suramin. SAXS data was collected on beamline B21 (Diamond Light Source, Oxford, UK) at an X-ray wavelength of 1 Å on a Pilatus 2M detector at a camera length of 4.036 m. Measurements were performed at 20°C and 28 x 1 sec frames were collected per sample. For size exclusion chromatography coupled

with SAXS (SEC-SAXS), ApoE at 10 mg/mL were delivered at 20°C and a flow rate of 0.16 mL/min via an in-line Agilent high performance liquid chromatography (HPLC) with a Shodex Kw-403 column and 20 mM HEPES, 300 mM NaCl, 1 mM TCEP, pH 8.0 as running buffer. For studies on the interaction of ApoE with heparin and Suramin, ApoE was pre-equilibrated with 1 mg/mL heparin or 1 mM Suramin and gel-filtered in 20 mM HEPES, 300 mM NaCl, 1 mM TCEP, pH 8.0. Measurements of each protein were also performed in 20 mM HEPES, 300 mM NaCl, 1 mM TCEP, 1 mg/mL heparin, pH 8.0. A total of 620 frames with 3 sec exposure per frame were recorded for each protein and the data processed using the B21 beamline in-house *pypeline* software and further analysed using the ATSAS data analysis 2.8.4 software.

3.2.7 Isothermal titration calorimetry

Proteins were dialysed against PBS + 0.01% (v/v) Triton X-100 overnight at 4˚C using 3.5 K Slide-A-Lyzer™ dialysis cassettes (ThermoFisher Scientific). Titration experiments were carried out on a Microcal PEAQ-ITC (Malvern) at 25˚C and a cell stirrer speed of 750 rpm. An initial 1 µL injection of 300 µM protein followed by an additional eighteen 2 µL injections were performed into the sample cell containing Suramin at 50 µM in PBS + 0.01% (v/v) Triton X-100 + 2% (v/v) DMSO. DMSO concentrations in the syringe and sample cell were matched. Injection of protein into PBS + 0.01% (v/v) Triton X-100 + 2% (v/v) DMSO was used as a control experiment and the integrated control heats were subtracted from the reaction heats. Data was analysed using the Microcal PEAQ-ITC analysis software version 1.1.0.1262.

3.2.8 Circular dichroism

Circular dichroic (CD) spectra were measured on a Jasco J-715 spectropolarimeter. Spectra were collected with the support of Ana Caroline-Raulin and Dr Youssra Al-Hilaly (Louise Serpell lab, University of Sussex). Proteins were extensively dialyzed against 20 mM sodium phosphate, pH 8.0 overnight at 4˚C using 3.5 K Slide-A-Lyzer™ dialysis cassettes (ThermoFisher Scientific) and far UV CD spectra were measured at 25 µM protein concentration and either 500 µM Suramin or 500 µg/mL heparin. The mean residue ellipticity ([Θ] mdeg cm^2 $dmol^{-1}$) at wavelength λ is calculated from the measured ellipticity Θ using equation (3.7).

$$[\Theta] = \frac{\Theta}{10.n.C.l} \quad (3.7)$$

with n is the number of peptide bonds in the protein, C the concentration of the sample in mol L^{-1} and l is the path length in cm. Temperature was maintained at 21°C. All spectra were collected in 0.01 cm path length clear quartz cuvettes (Starna Scientific, Essex, UK) in the wavelength range of 280-180 nm at a resolution of 0.1 nm and with a band-width of 1 nm. The scanning-speed was 50 nm/min and the response time 1 sec. Three spectra were acquired per sample, averaged and normalized by subtracting the buffer-only spectrum.

3.3 Results

3.3.1 Determination of ideal protein concentration for static SAXS measurements

To perform static SAXS measurements in the presence of ligands, the ideal protein concentration had to be determined, as well as the behaviour of the sample in solution. As demonstrated in Chapter 2, Section 2.3.5, a concentration-dependent effect on the Rg was identified for ApoE4$_{mon}$ which reflects a change in size and presumably oligomerization state. Such effects can make static SAXS measurements and downstream data analysis problematic. Scattering profiles were acquired of ApoE isoforms at varying concentration (Figure 3.5). No concentration-dependent effect was observed on the Rg value (Figure 3.5F, Appendix Table 3.2) and evaluation of the Guinier region shows no or minimal protein aggregation (Figure 3.5D, Appendix Figure 3.16). This suggests that ApoE retains its tetrameric state over the concentration range tested. A working concentration of 4 mg/mL was selected for static SAXS measurements in the presence of ligand as a good scattering signal was achieved while only moderate protein amounts were required.

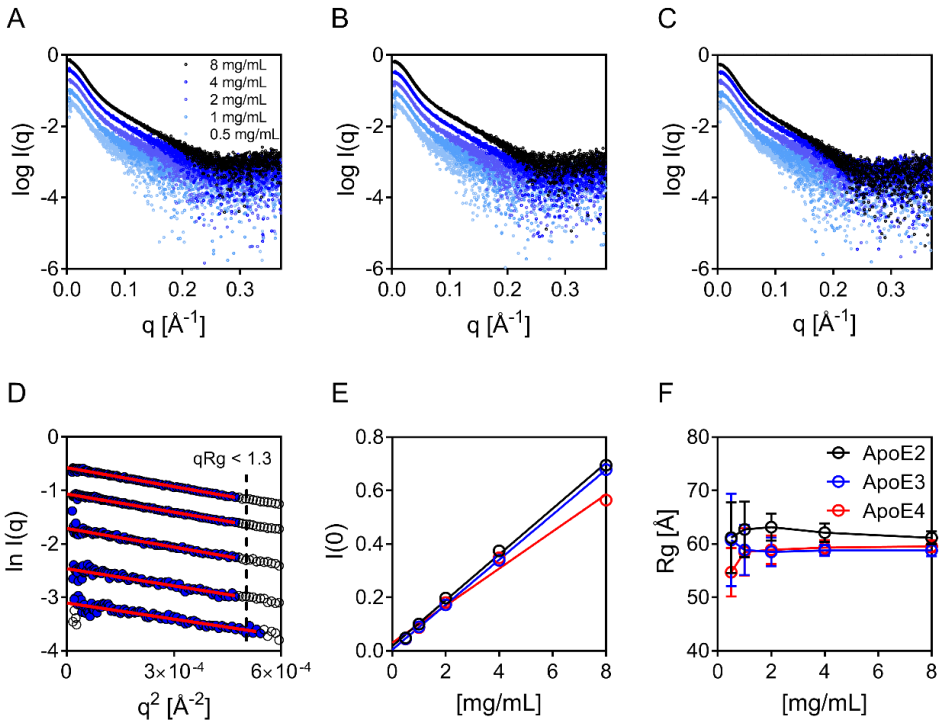

Figure 3.5. Scattering profile of ApoE isoforms at different concentrations. I(q) versus q as log-linear plots are shown for **(A)** ApoE2, **(B)** ApoE3 and **(C)** ApoE4 at different concentrations. **(D)** Example Guinier fits of ApoE4 at different concentration (red lines, 8 – 0.5 mg/mL from top to bottom) for qRg < 1.3 are shown. Filled blue symbols indicate data that was used for the Guinier fit. Fits for ApoE2 and ApoE3 are found in Appendix Figure 3.16. **(E)** I(0) is plotted as a function of protein concentration and demonstrates linearity. **(F)** The estimated Rg from the Guinier approximation is shown as a function of protein concentration.

3.3.2 Increase in size and mass of ApoE isoforms upon binding to heparin

SAXS profiles of all three ApoE isoforms were collected in the presence of increasing heparin concentrations. Static SAXS profiles collected in the absence of heparin confirm observations made in SEC-SAXS (Chapter 2, Section 2.3.5) and reflect a similar size, shape, Rg and Rc as determined by the Guinier approximation. Based on the Rg and Rc, an approximate co-axial length of ~ 192 Å was calculated for each isoform (Table 3.1).

Table 3.1. Approximated radius of gyration, cross-sectional radius and length of ApoE isoforms.

	Rg [Å]	Rc [Å]	L [Å]*
ApoE2	61.7 ± 0.8	27.1 ± 0.4	192.1
ApoE3	61.4 ± 0.7	26.9 ± 0.3	191.2
ApoE4	61.8 ± 0.5	27.0 ± 0.3	192.4

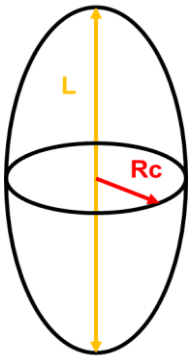

* Co-axial length was calculated using the formula $L = \sqrt{12}(Rg^2-Rc^2)$.

A concentration-dependent effect on the Rg, as well as on the cross-sectional radius Rc of ApoE isoforms was observed in the presence of heparin (Figure 3.6A and 3.6B). This effect was most pronounced for ApoE4 with an increase in Rg and Rc at the highest heparin concentration of +14 Å and +6 Å respectively. In comparison, the Rg of ApoE3 and ApoE2 increases by +11 Å and +10 Å, and the Rc by +5 Å and +3 Å respectively. Additionally, evaluation of the intensity at zero angle I(0) as determined by the Guinier fit confirms a concentration dependent effect of heparin on ApoE mass with the highest I(0) measured for ApoE4 (Figure 3.6C). These results suggest that ApoE4 binds with higher affinity to heparin than ApoE2 and ApoE3.

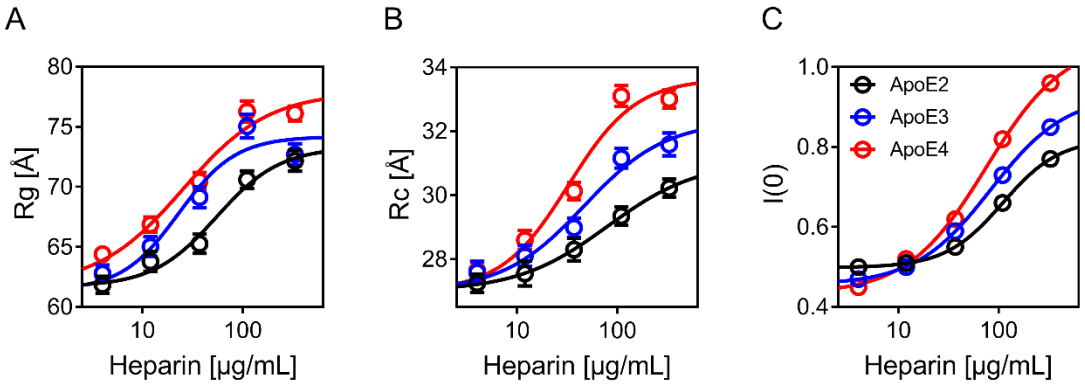

Figure 3.6. The effect of heparin on ApoE size. (A) The Rg, **(B)** the cross-sectional radius Rc and **(C)** the scattering intensity through zero angle I(0) as functions of heparin concentration for ApoE2, ApoE3 and ApoE4 determined by the Guinier approximation are shown.

To investigate the role of critical lysine residues that are involved in heparin binding, ApoE4 was subjected to reductive lysine methylation (Chapter 2, Section 2.3.6). Additionally, lysine residues that have previously been shown to be critical for heparin binding were mutated to alanine (K143A and K146A) (213, 409). Lysine methylation strongly reduced the concentration dependent effect of heparin on ApoE4 size and mass and mutation of the critical lysine residues completely abolished the effect (Figure 3.7). The absence of structural changes in the ApoE4 (K143A, K146A) mutant indicate that the observed changes in unmodified ApoE isoforms can be ascribed to a specific binding event and not due to background subtraction errors in the heparin containing samples. Mutation of the lysine residues that are located at the amino terminal of ApoE demonstrated the predominance of the amino terminus in heparin binding (409). Hence, binding of heparin to ApoE4$_{1\text{-}191}$ alone was confirmed (Appendix Figure 3.19).

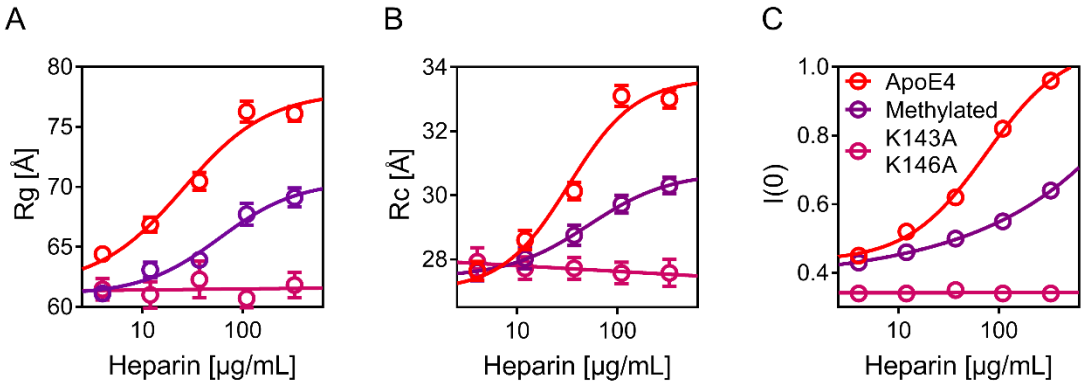

Figure 3.7. The effect of heparin on methylated ApoE4 and ApoE4 (K143A, K146A) size. (A) The Rg, **(B)** the cross-sectional radius Rc and **(C)** the scattering intensity through zero angle I(0) as functions of heparin concentration for ApoE4, methylated ApoE4 and ApoE4 (K143A, K146A) determined by the Guinier approximation are shown.

3.3.3 Heparin binding induces substantial conformational changes in ApoE

Comparison of the SAXS profiles using a structure similarity map (SSM) (422) allows for quantitation of the degree of a structural change. A decrease in structural and conformational similarity was observed with increasing heparin concentration when compared to the respective unbound states (Figure 3.8). The degree of structural alteration follows the order ApoE4 > ApoE3 > ApoE2 and is mitigated by lysine methylation. As expected, no structural change is observed for the ApoE4 (K143A, K146A) mutant with the defective heparin binding site.

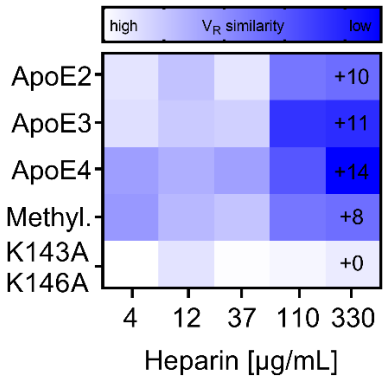

Figure 3.8. Comparison of heparin-induced conformational change of ApoE by a structure similarity map. The magnitude of the conformational changes in ApoE at different heparin concentrations depicted as SSM scored on the Volatility of Ratio (V_R) metric (422) is shown. Scores were assigned a gradient colour with white indicating high agreement and blue indicating low agreement. SAXS curves (q = 0.015 – 0.2) from heparin bound states were judged for agreement against their respective heparin-unbound states. Values at 330 µg/mL heparin denote change in Rg (+ Å).

Evaluation of the SAXS profiles in the normalized Kratky representation also confirmed the concentration dependent effect of heparin on ApoE shape (Figure 3.9A-C). As already confirmed in the SEC-SAXS measurements (Chapter 2, Section 2.3.5), ApoE isoforms share globular features. However, the shoulder to the right of the main peak seen in the unbound state of ApoE (i.e. at 0 µg/mL heparin) suggests that a portion of the protein is extended or polydispersed. Binding to increasing concentrations of heparin appears to reduce the magnitude of this shoulder implying an overall compaction and stabilization of ApoE by bringing its domains into closer proximity with each another. The importance of critical lysine residues in the ApoE-heparin interaction is again reflected in the normalized Kratky plots of the methylated ApoE4 and the ApoE4 (K143A, K146A) mutant (Figure 3.9D and 3.9E). Stabilization of the protein occurs to a lesser extent in methylated ApoE4 and no difference in conformation is seen in ApoE4 (K143A, K146A) across all heparin concentrations tested. A slight difference between the conformation of wild type and mutant ApoE4 (K143A, K146A) in the unbound state was however observed (Figure 3.9E). The ApoE4 mutant appears to adopt a more extended confirmation compared to wild type ApoE4 reflecting an involvement of Lys143 and Lys146 residues in ApoE quaternary structure. But, comparison of the far UV CD spectra of both proteins demonstrated no significant differences in secondary structure (Figure 3.9F).

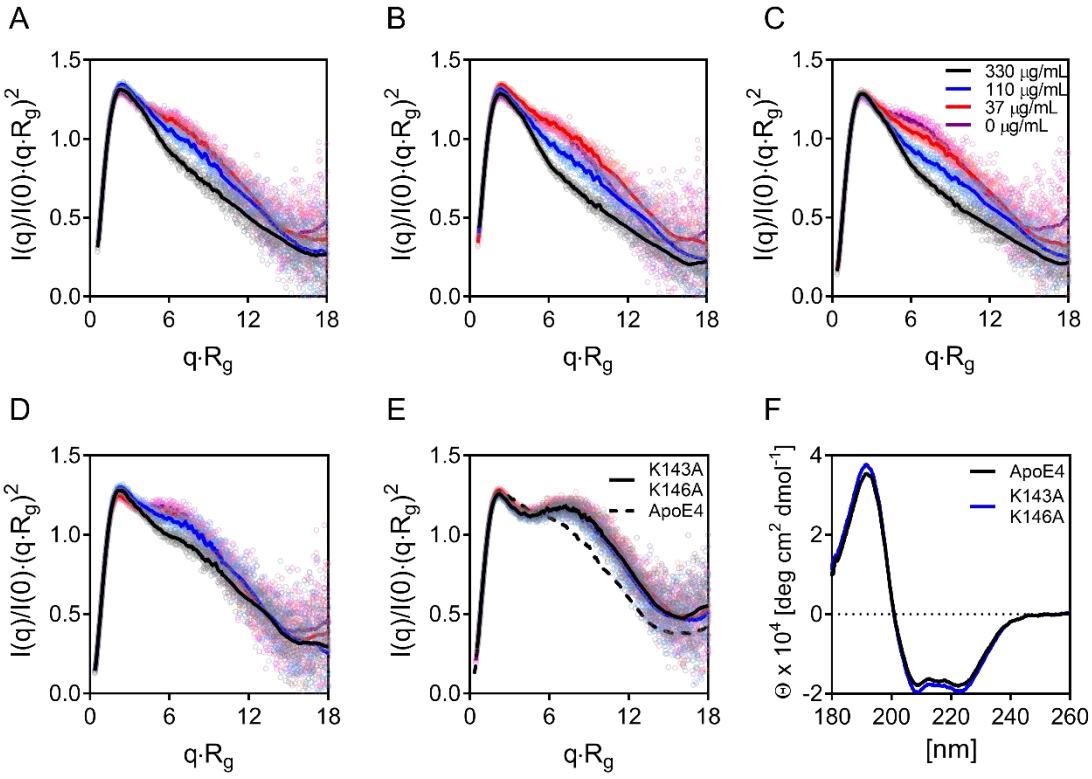

Figure 3.9. The effect of heparin on ApoE conformation. Smooth fits of the dimensionless Kratky representations for **(A)** ApoE2, **(B)** ApoE3, **(C)** ApoE4, **(D)** methylated ApoE4 and **(E)** ApoE4 (K143A, K146A) in the presence of different concentrations of heparin are shown. **(F)** Comparison of the wild type ApoE4 far UV CD spectrum with ApoE4 (K143A, K146A) mutant shows no difference in secondary structure.

3.3.4 Suramin binding promotes compaction of ApoE and induces similar structural changes as heparin

Heparin is a highly sulfonated polysaccharide that is member of the GAG family of carbohydrates. Native heparin has a molecular weight ranging from 3 to 30 kDa and consists of variably sulfonated repeating disaccharide units. The polydispersity and heterogeneity arising from the variable sulfonation of heparin makes its characterization, as well as fractionation challenging (415) and for this reason a more tractable heparin substitute was sought. Suramin, a sulfated naphtylamine has been reported to decrease the association of ApoE3 to the extracellular matrix of HepG2 cells (423–425), probably by antagonizing the ApoE-HSPG interaction.

SAXS was performed on ApoE in the presence of Suramin and substantial compaction of ApoE isoforms in a Suramin concentration dependent manner as assessed by the Rg and Rc was observed (Figure 3.10A, Appendix Figure 3.19F). The degree of compaction follows the order ApoE2 > ApoE3 > ApoE4 with a change in Rg of -10 Å for ApoE2 at the highest Suramin concentration. Reduction in size is also exhibited by methylated ApoE4 and ApoE4 (K143A,

K146A) mutant, however it was not as pronounced as wild type ApoE (Figures 3.10B and 3.10C). The SSM depicts the increasing compaction with increasing Suramin concentration in all three ApoE isoforms (Figure 3.10C), confirmed by the example normalized Kratky representation for ApoE4 (Figure 3.10D). On a molar basis the effect of Suramin on ApoE structure is significantly greater than that of heparin. Strong structural compaction is also exhibited by methylated ApoE4 upon binding to Suramin (Figure 3.10E) but is somewhat reduced in the heparin binding site ApoE4 (K143A, K146A) mutant (Figure 3.10F). These results suggest that additional residues besides the critical heparin binding lysine 143 and 146 are involved in Suramin binding.

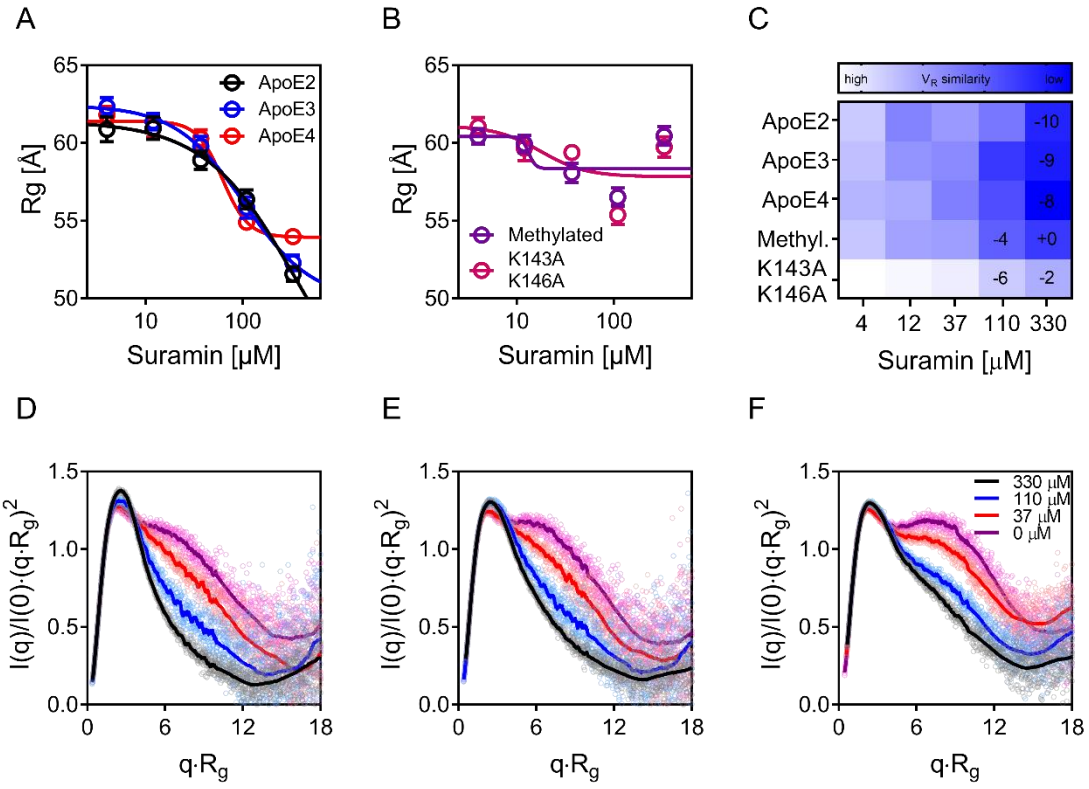

Figure 3.10. The effect of Suramin on ApoE size and conformation. Rg as a function of Suramin concentration for **(A)** wild type ApoE isoforms and **(B)** methylated ApoE4 and ApoE4 (K143A, K146A) is shown. **(C)** The magnitude of the conformational changes in ApoE at different Suramin concentrations is depicted as an SSM. Values denote change in Rg (- Å) at 330 µM Suramin. The smooth fits of the example dimensionless Kratky representations for **(D)** ApoE4, **(E)** methylated ApoE4 and **(F)** mutant ApoE4 (K143A, K 146A) confirm the effects on ApoE conformation.

3.3.5 Heparin and Suramin have different effects on the quaternary structure of ApoE and Suramin shows no specificity between the ApoE homologues

A pair-wise distance distribution function P(r) was calculated for SAXS profiles obtained at different heparin and Suramin concentrations. P(r) effectively represents the distribution of all pairwise distances within the particle. As all the measurements were made at the same protein concentration, changes in the integrated area under the distributions relate to the mass of the particle. With increasing heparin concentrations, the overall shape of the distribution functions does not change dramatically, rather the curves scale up (Figure 3.11A). This effect is consistent with heparin evenly coating the surface of the protein leading to increases in both mass and volume. In contrast, the integrated area under the distribution functions for ApoE treated with increasing concentrations of Suramin do not change significantly. Rather, the shape of the curve changes with a decrease in long and an increase in short distance vectors consistent with an overall compaction of the protein (Figure 3.11B). An interesting detail in the P(r) functions is a small shoulder to the left of the main peak at r ~ 25 Å. This population of short distance vectors may indicate the existence of a small domain that is discrete from the bulk of the protein. The shoulder disappears with increasing heparin or Suramin concentration suggesting that this domain may be pulled closer to the main body of the protein upon ligand binding.

The various ApoE isoforms show similar qualitative but different quantitative responses to heparin and Suramin. The calculated D_{max} in the presence of heparin followed the order ApoE4 > ApoE3 > ApoE2 and were concentration dependent (Figure 3.11A). Rg values determined from the P(r) function were similar to those obtained from the Guinier fit (Appendix Table 3.3). A Suramin concentration dependent decrease in D_{max} was also determined for all ApoE isoforms following the order ApoE2 > ApoE3 > ApoE4 (Figure 3.11B). Examples of the P(r) functions for ApoE3 are presented in Figure 3.11. The extended conformation of ApoE in its unbound state is demonstrated in its P(r) function which displays a D_{max} of ~200 Å.

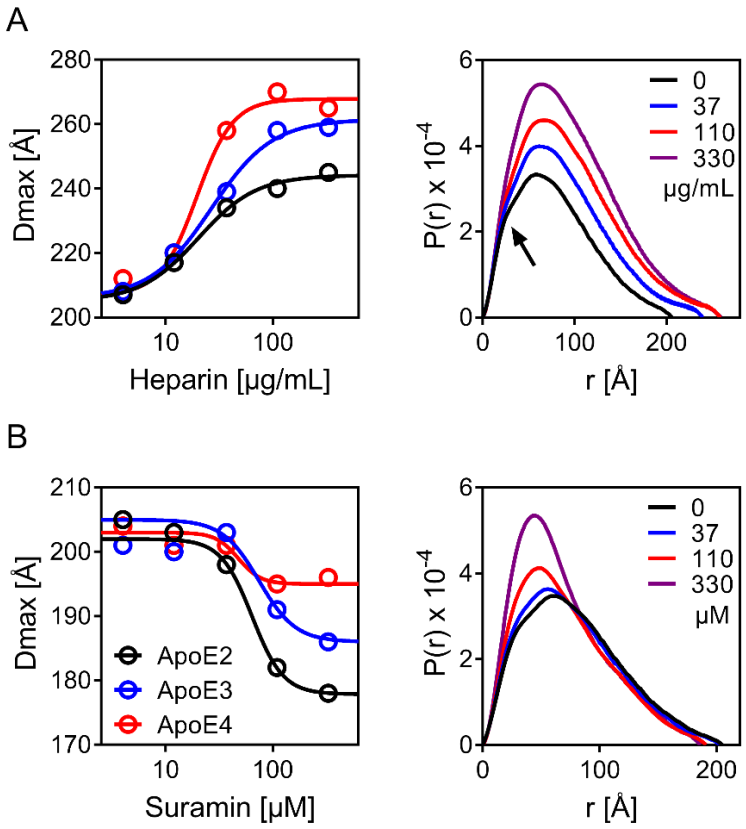

Figure 3.11. Pairwise distribution function of ApoE in the presence of heparin and Suramin. Fitted maximal dimension D_{max} of wild type ApoE isoforms as a function of **(A)** heparin and **(B)** Suramin concentration are shown, as well as example ApoE3 pairwise distribution functions (right plots).

To determine if this isoform dependent difference in heparin and Suramin binding is the result of altered binding affinity, Suramin binding was monitored by isothermal titration calorimetry (ITC). A substantial release of heat was measured when titrating ApoE into Suramin and similar binding affinities (ranging from 3.3-4.9 µM) were calculated for all three ApoE isoforms (Figure 3.12A). ApoE appears to possess two Suramin binding sites per monomer that are most likely located at the amino terminal domain and involve additional residues other than the critical lysine 143 and 146. Consistently, binding of Suramin to $ApoE4_{1-191}$ (Appendix Figure 3.19D and 3.19E) and the ApoE4 (K143A, K146A) mutant was confirmed (Figure 3.12A). It was not possible to measure the binding of heparin by ITC as its undefined molecular weight poses problems in determining the stoichiometry and hence the affinity. Nevertheless, the salt dependency of the ApoE-heparin interaction was confirmed and ApoE4 was observed to elute at a higher salt concentration from a heparin column compared to ApoE2 and ApoE3 (Figure 3.12C). This effect may arise from the additional arginine residue 112 in ApoE4 compared to ApoE3 that enhances the electrostatic interaction (410). It was of interest to determine the nature of the structural changes observed in the SAXS studies of ApoE binding to heparin and

Suramin. Far UV CD spectra of ApoE3 in the presence of heparin and Suramin indicated no secondary structural differences (Figure 3.12B) consistent with the possibility of tertiary and/or quaternary structural rearrangements.

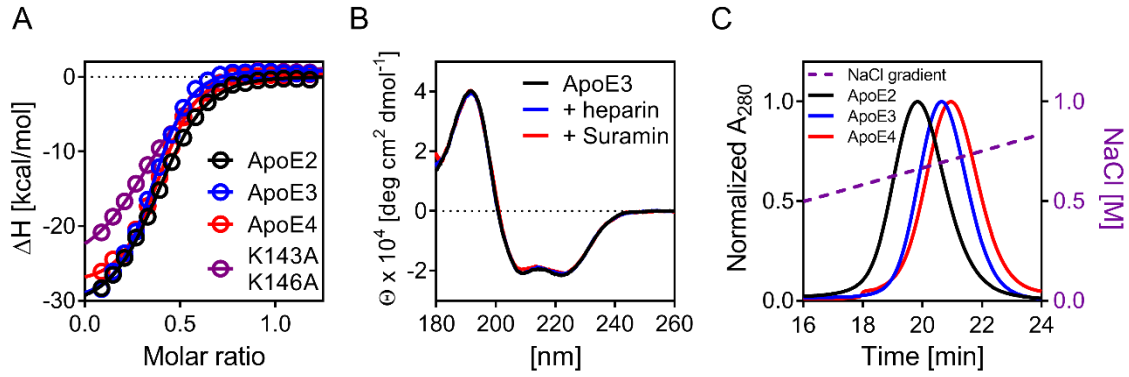

Figure 3.12. Suramin and heparin binding affinities to ApoE. (A) Binding affinity (K_d) values for the binding of Suramin to ApoE were determined by ITC. Normalized binding heats are presented with the solid line representing the nonlinear least square fits to a single-site binding model. Suramin binding affinities (± SD) of 4.9 ± 0.5 µM, 3.5 ± 0.5 µM, 3.3 ± 0.4 µM and 8.9 ± 1.6 µM were determined for ApoE2, ApoE3, ApoE4 and ApoE4 (K143A, K146A) respectively. Raw titration heats are presented in Appendix Figure 3.19. **(B)** Far UV CD spectroscopy demonstrates no change in secondary structure for ApoE3 in the presence of 500 µg/mL heparin or 500 µM Suramin. **(C)** The ApoE-heparin interaction is salt-dependent, with ApoE4 eluting from a heparin column at a higher salt concentration than ApoE2 and ApoE3 (only the elution from 0.5-0.8 M NaCl is shown out of the full 0.15-1.0 M NaCl gradient elution).

3.3.6 SAXS coupled with size exclusion chromatography reproduces the effects of heparin and Suramin on ApoE

Size exclusion chromatography coupled SAXS (SEC-SAXS) measurements were additionally performed to confirm observations made in the static measurements (Appendix Figures 3.17 and 3.18). Purity and monodispersity of the sample are essential for structural studies, as macromolecular aggregation affects SAXS data quality (377). As previously reported (251) and as observed by the Serpell lab (University of Sussex), ApoE4 has a propensity to form higher oligomeric species in solution under certain conditions. SEC-SAXS can be employed to exclude any ApoE aggregates that may have formed.

The SEC-SAXS measurements were performed in the presence of heparin and Suramin and data is in good agreement with the static measurements. Elution profiles reflecting the structural effects of ApoE interaction with heparin and Suramin are presented in Figure 3.13A. A lower retention volume and higher Rg's across the elution peak were measured in the presence of heparin, consistent with an increase in volume and size whereas pre-equilibration of ApoE with Suramin produced the opposite effect. Figure 3.13B presents example ApoE4 normalized Kratky plots and P(r) functions obtained from the SEC-SAXS measurements.

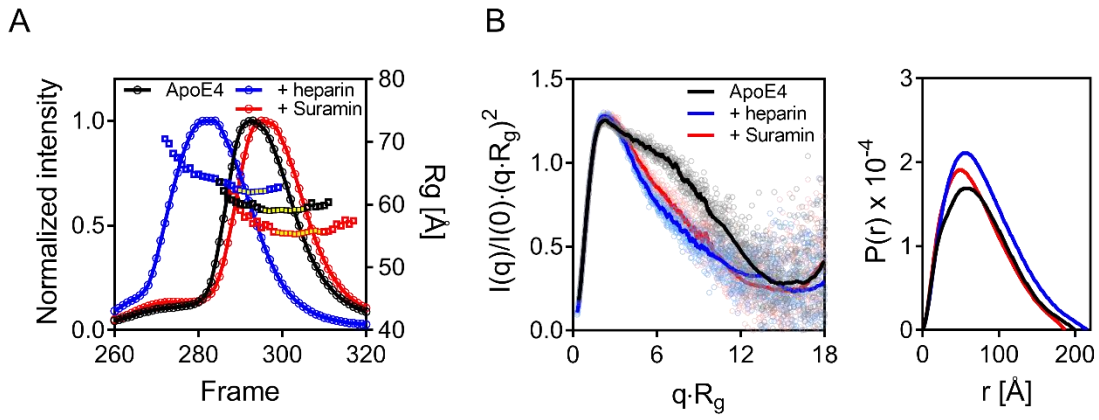

Figure 3.13. SEC-SAXS of ApoE4 in the presence of heparin and Suramin. The effects of heparin and Suramin on ApoE isoforms were reproduced in SEC-SAXS. **(A)** Example elution profiles of ApoE4 are shown. The normalized intensity (circles) and Rg (squares) are plotted as a function of frame number. Filtering ApoE4 through a column equilibrated with an additional 1 mg/mL heparin resulted in a decreased retention volume and an increased Rg. The opposite effect (compaction) is seen when ApoE4 has been pre-equilibrated with Suramin. **(B)** The smooth fits of the dimensionless Kratky representations (left) and ApoE4's respective P(r) functions (right) are presented and compare well to the static measurements.

Gel filtration of ApoE isoforms through the SEC column equilibrated in 1 mg/mL heparin resulted in only slightly different retention volumes and Rg values between ApoE isoforms (Appendix Figure 3.17). On the other hand, pre-equilibration of ApoE isoforms with heparin followed by SEC in the absence of heparin yielded the expected isoform dependent size difference with ApoE4 having larger Rg's across the elution peak and a lower retention volume (Figure 3.14A). This data is consistent with ApoE4 binding more heparin than ApoE2 and ApoE3. Lysine methylation under the same conditions resulted in a broadening of the elution peak with the peak maximum eluting at the identical volume as unbound ApoE4 (Figure 3.14B). In contrast, heparin binding had no effect on the elution profile and Rg values of the ApoE4 (K143A, K146A) mutant (Figure 3.14B).

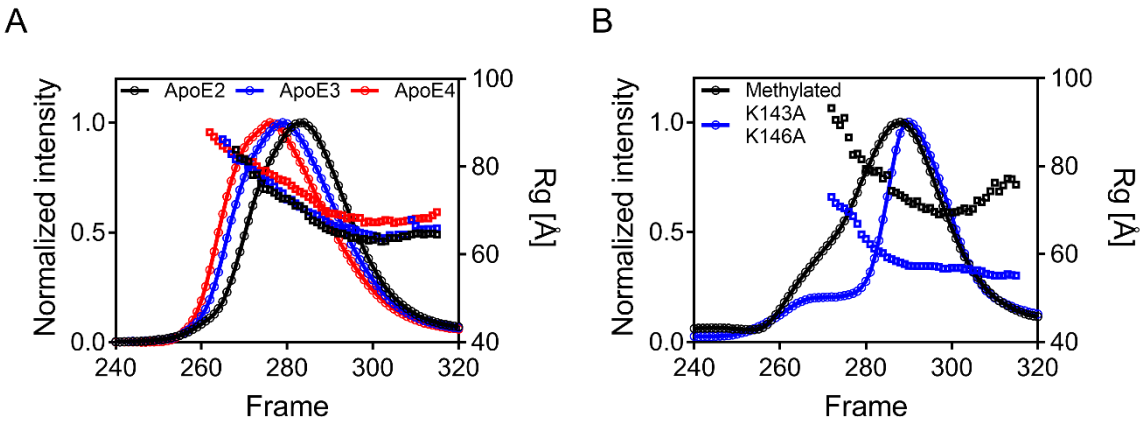

Figure 3.14. Comparison of SEC-SAXS elution profiles of ApoE isoforms in the presence of heparin. Elution profiles and Rg's across the peak of **(A)** wild type ApoE isoforms and **(B)** methylated, as well as ApoE4 (K143A, K146A) when pre-equilibrated with 1 mg/mL heparin and filtered through a column without heparin are shown.

3.4 Discussion

Substantial isoform-dependent conformational changes in ApoE upon heparin binding were identified. These effects are apparent in the SAXS profiles (Figure 3.9) but not in the far UV CD spectra (Figure 3.12B), indicating that they arise from changes in the ApoE tertiary and/or quaternary structure. In addition, the normalized Kratky plots reflect reduced flexibility and stabilization of ApoE by heparin. Analysis of ApoE size in terms of Rg, Rc and D_{max} by the Guinier approximation (Figure 3.6) and by the P(r) function (Figure 3.11A) demonstrated an increase in size (and hence mass) with increased heparin concentration, consistent with the binding of heparin to ApoE. The effect was greatest for ApoE4 which appears to be able to bind more avidly to GAG than either ApoE2 or ApoE3. The ApoE4-heparin interaction also appears to be higher affinity than that of the other two isoforms as it retains more bound polysaccharide after size exclusion column chromatography (Figure 3.14A) and binds more tightly to a heparin column (Figure 3.12C). This data is consistent with previous observations by Yamauchi *et al* (410) who have shown by SPR that the ionic interactions involved in HS binding of ApoE4 are three-fold greater than for ApoE3. The authors proposed that the additional arginine at site 112 in ApoE4 enhances the electrostatic potential of positively charged GAG binding residues (Lys143 and Lys146) leading to a stronger electrostatic interaction with heparin. In this study, the importance of Lys143 and Lys146 residues in the ApoE-heparin interaction was confirmed (213, 409, 418). Non-specific lysine methylation in ApoE4 strongly reduced its heparin binding capacity and mutation of the critical lysine residues Lys143 and Lys146 into alanine completely abolished the heparin binding by ApoE4 (Figures 3.7, 3.9D and 3.9E).

As heparin is a heterogeneous polysaccharide consisting of a mixture of GAGs (415), Suramin was used as model system to test its binding to ApoE isoforms. Suramin mimicked the effects of heparin on ApoE structure, promoting substantial compaction in a concentration-dependant fashion (Figures 3.10A and 3.10D). Effects of Suramin on the ApoE4 (K143A, K146A) mutant were still substantial, demonstrating that this ligand must interact with residues other than the heparin-binding Lys143 and Lys146 (Figures 3.10B and 3.10E). Binding stoichiometry by ITC was determined as two Suramin binding sites per ApoE monomer. Both binding sites are likely located on the amino terminus since binding of Suramin was confirmed to the amino terminal domain of ApoE4 by ITC (Appendix Figures 3.19D and 3.19E). The SAXS P(r) functions demonstrate the disappearance of a small domain(s) upon ApoE binding to both heparin and Suramin and far UV CD spectra indicate that these structural changes are tertiary/quaternary rather than secondary (Figures 3.11 and 3.12B). The data is consistent with a model in which the independently folded domains of ApoE come closer together upon ligand binding resulting

in compaction and stabilization. Similar structural reorganisations have previously been demonstrated for DNA binding proteins (426, 427).

In this study, recombinant protein was utilized that was produced in *E. coli*. As outlined in Chapter 2, Section 2.1, *E. coli* produced ApoE is not lipoprotein associated and hence heparin binding studies in this chapter were performed on lipid-free ApoE. ApoE is physiologically present on lipoprotein particles in the brain and actual amounts of lipid-free ApoE are expected to be small (Chapter 1, Section 1.4.2). It therefore remains to be determined if the isoform-dependent effect on heparin binding as observed here is retained when ApoE is complexed with lipids. Nevertheless, observations made here allow for broader conclusions.

ApoE's important role in the brain and its function in synaptic plasticity and neuronal repair have been outlined in Chapter 1, Section 1.4.2. ApoE and ApoE-containing lipoproteins are mostly secreted by astrocytes and microglia and are internalized by the interaction with the superfamily of LDLR proteins, as well as HSPGs (169, 173). In particular, during CNS inflammatory response, synthesis and secretion of ApoE is increased and ApoE is thought to promote regeneration by redistributing lipids and cholesterol (182–185, 188). HSPGs participate in the immune response and their expression, as well as secretion were shown to be upregulated around injury sites that help to capture ApoE-containing lipoproteins and other growth factors (192, 193). Differential binding of ApoE isoforms to GAGs as shown in this chapter may result in altered CNS immune response. Consistent with this hypothesis, increased activation, as well as release of pro-inflammatory cytokines by glial cells were shown in ApoE4 transgenic mice (307) which may be an effect of ApoE4's higher affinity to GAGs.

Several studies have additionally investigated the effects of ApoE isoforms on Aβ aggregation and plaque formation (284) and also the role of ApoE receptors, including HSPGs, in Aβ clearance and production (428, 429), but the mechanism whereby ApoE4 increases susceptibility to AD is still unknown. Recent research has shown that ApoE receptors and HSPGs are involved in synaptic signalling and plasticity, as well as in neurite outgrowth (173, 430, 431). In particular, HSPG-mediated neurite outgrowth is promoted by higher intracellular levels of ApoE3 rather than ApoE4 (432). Similarly, endosome recycling of ApoE receptors, as well as NMDA and AMPA receptors in the synapse appears to be reduced by ApoE4 resulting in altered glutamate receptor homeostasis (433). Altered binding and particularly dissociation of ApoE4 to HSPGs may slow down the release of lipoproteins, as well as recycling of synaptic receptors from the endosome compared to ApoE3 and ApoE2 and therefore influence synaptic plasticity. The structural data on the binding modes of ApoE to heparin presented in this chapter will help to elucidate the differential physiological effects of the three major ApoE isoforms in AD.

3.5 Appendix Chapter 3

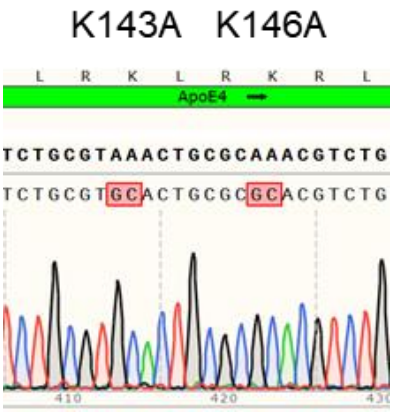

Figure 3.15. Sequencing results pET17B_ApoE4_K143A_K146A.

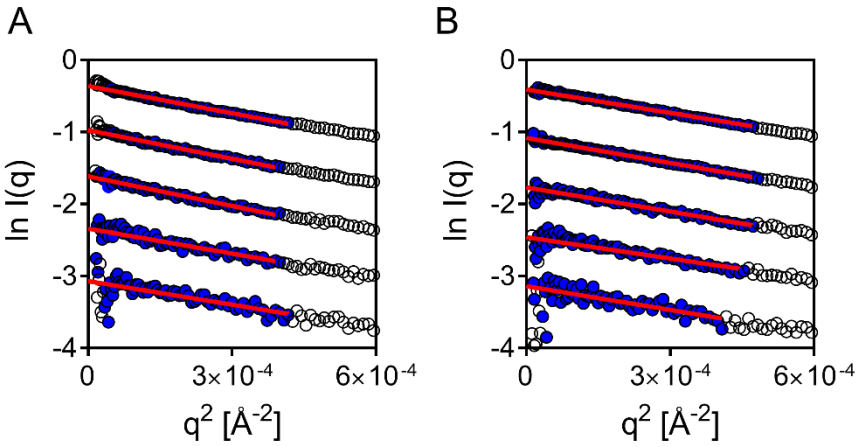

Figure 3.16. Guinier plot of ApoE2 and ApoE3 at varying concentration. Scattering in the Guinier representation is shown for **(A)** ApoE2 and **(B)** ApoE3 at 8, 4, 2, 1, and 0.5 mg/mL (top to bottom). Filled blue symbols indicate data that was used for the Guinier fit for qRg < 1.3.

Table 3.2. Guinier-derived Rg and I(0) of ApoE isoforms at different concentrations.

ApoE2 [mg/mL]	Guinier Rg [Å]	I(0), arb. Units
8	61.14 ± 1.21	0.695 ± 0.002
4	62.13 ± 1.75	0.375 ± 0.001
2	63.15 ± 2.54	0.197 ± 0.001
1	62.70 ± 5.21	0.100 ± 0.001
0.5	61.17 ± 6.60	0.049 ± 0.001
ApoE3 [mg/mL]	**Guinier Rg [Å]**	**I(0), arb. Units**
8	58.79 ± 1.07	0.678 ± 0.002
4	58.80 ± 1.06	0.339 ± 0.001
2	58.52 ± 2.68	0.172 ± 0.001
1	58.88 ± 4.69	0.090 ± 0.001
0.5	60.74 ± 8.68	0.045 ± 0.001
ApoE4 [mg/mL]	**Guinier Rg [Å]**	**I(0), arb. Units**
8	59.55 ± 1.09	0.564 ± 0.001
4	59.31 ± 1.35	0.348 ± 0.001
2	58.92 ± 2.68	0.181 ± 0.001
1	58.50 ± 4.41	0.087 ± 0.001
0.5	54.73 ± 4.53	0.045 ± 0.001

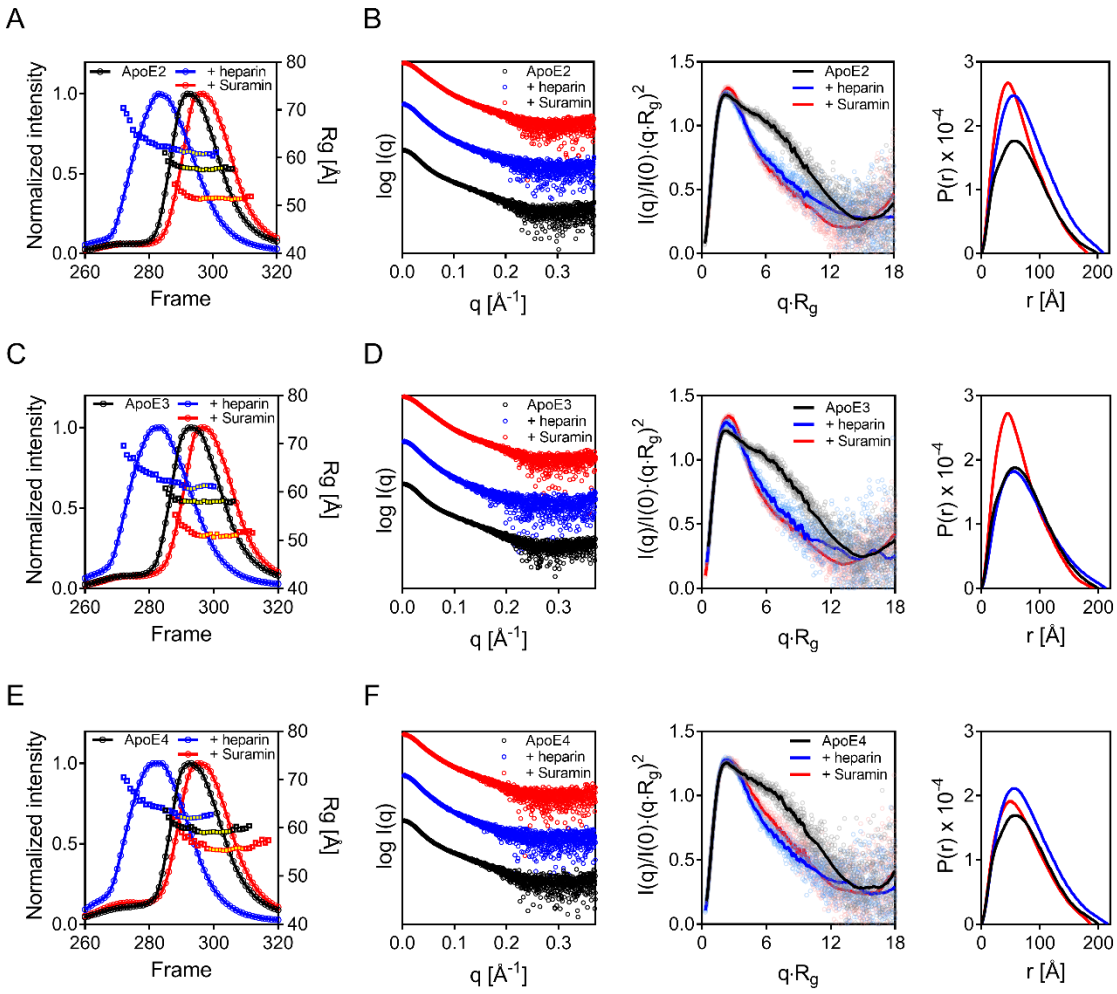

Figure 3.17. Comparison of SEC-SAXS data of wild type ApoE isoforms in the absence and in the presence of heparin and Suramin. ApoE isoforms were filtered through a Shodex Kw-403 column without ligand (black), pre-equilibrated with 1 mM Suramin (red) or additionally after supplementation with 1 mg/mL heparin to the SEC buffer (blue). The scattering intensities (circles) and radii of gyration Rg (squares) are plotted against the frame number in panels A, C and E. Profiles corresponding to curves **(A)** 291-303 (ApoE2), 290-298 (+ heparin) and 296-309 (+ Suramin), **(C)** 291-303 (ApoE3), 292-298 (+ heparin) and 296-307 (+ Suramin), **(E)** 296-305 (ApoE4), 290-296 (+ heparin) and 299-309 (+ Suramin) were averaged and used for analysis. These data points are depicted in yellow. Logarithmic intensity plots (left), their respective Kratky plots (middle) and P(r) functions (right) are presented for **(B)** ApoE2, **(D)** ApoE3 and **(F)** ApoE4. The Kratky plots indicate that the ApoE isoforms adopt an extended conformation in solution with a maximal dimension of ~200 Å. Suramin binding induces compaction of the ApoE isoforms such that ApoE elutes later from the SEC column with lower Rg values across the elution peak compared to native ApoE. Notably, Suramin has less compaction effect on ApoE4 when compared to ApoE2 and ApoE3. The lower retention volumes and higher Rg across the elution peak in the presence of heparin is consistent with heparin binding to ApoE. Heparin induces identical conformational changes as Suramin, but as it is a long polysaccharide it is expected to confer a larger hydrodynamic radius to ApoE isoforms.

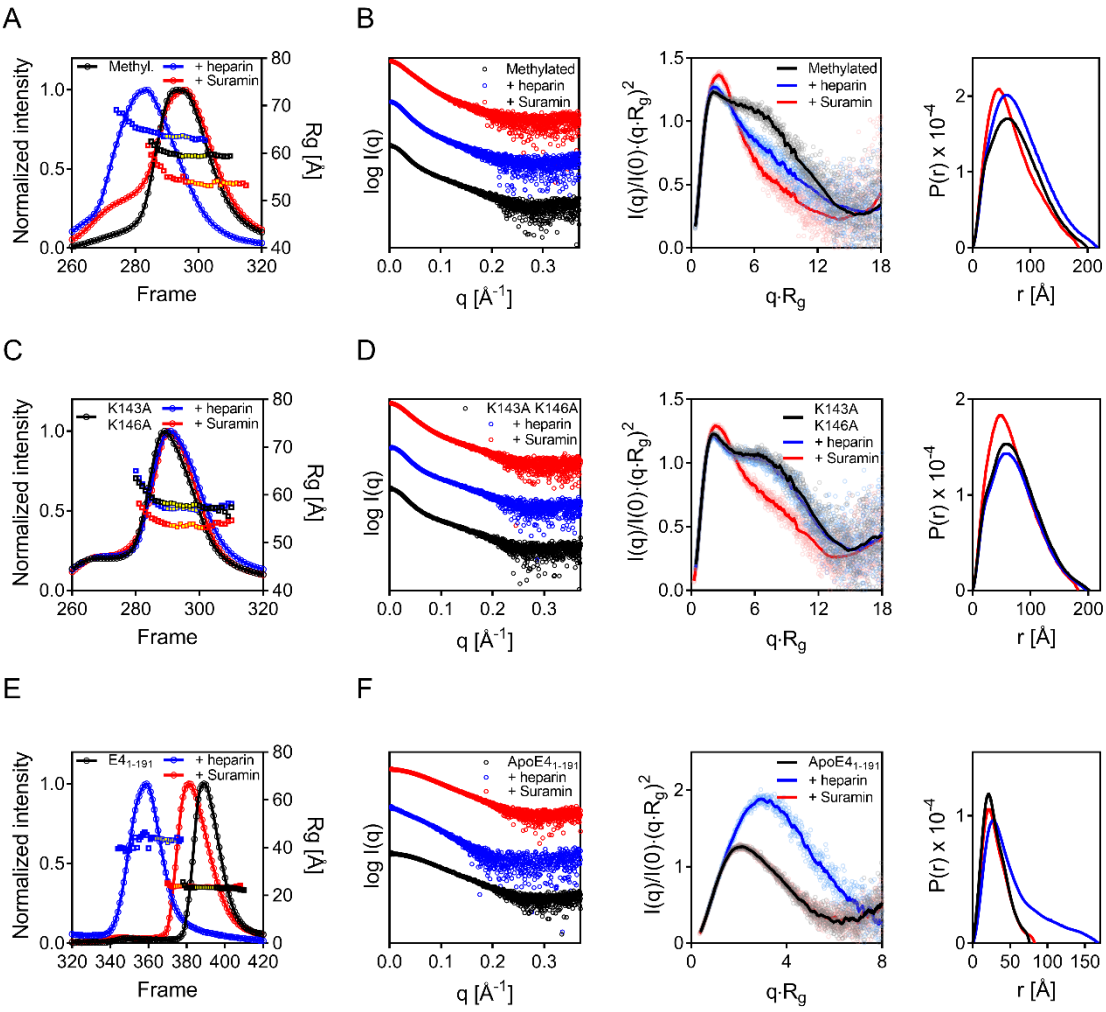

Figure 3.18. Comparison of SEC-SAXS data of methylated ApoE4, ApoE4 (K143A, K146A) and ApoE4$_{1-191}$ in the absence and presence of heparin and Suramin. The scattering intensities (circles) and the radii of gyration Rg (squares) are plotted against the frame number in panels A, C and E for proteins without (black), after pre-equilibration with 1 mM Suramin (red) and additionally after supplementation with 1 mg/mL heparin to the SEC buffer (blue). Profiles corresponding to curves **(A)** 295-302 (methylated ApoE4), 290-297 (+ heparin) and 297-312 (+ Suramin), **(C)** 289-299 (ApoE4 K143A K146A), 290-300 (+ heparin) and 291-301 (+ Suramin), **(E)** 385-395 (ApoE4$_{1-191}$), 364-374 (+ heparin) and 374-390 (+ Suramin) were averaged and used for analysis. These data points are depicted in yellow. Logarithmic intensity plots (left), their respective Kratky plots (middle) and P(r) functions (right) are presented for **(B)** methylated ApoE4, **(D)** ApoE4 (K143A K146A) and **(F)** ApoE4$_{1-191}$. **(B)** Methylated ApoE4 binds heparin and Suramin and adopts a similar conformation to wild type ApoE4, but the magnitude of the conformational change is diminished, presumably owing to impaired binding ability. **(D)** As expected, no conformational change and no effect on the elution profile is observed for ApoE4 (K143A K146A) mutant in the presence of heparin. On the other hand, binding of Suramin is still observed. **(F)** No change in ApoE4$_{1-191}$ flexibility as assessed in the Kratky plot is seen in the presence of Suramin. However, a lower retention volume is observed when the ApoE4 amino terminal domain is pre-equilibrated with Suramin. The data is consistent with a Suramin binding induced increase in hydrodynamic radius without perturbation of the ApoE4$_{1-191}$ conformation. The substantial increase in ApoE4$_{1-191}$ extension by heparin indicated by the Kratky representation is consistent with the binding of the flexible (and unfolded) polysaccharide to the amino terminal domain.

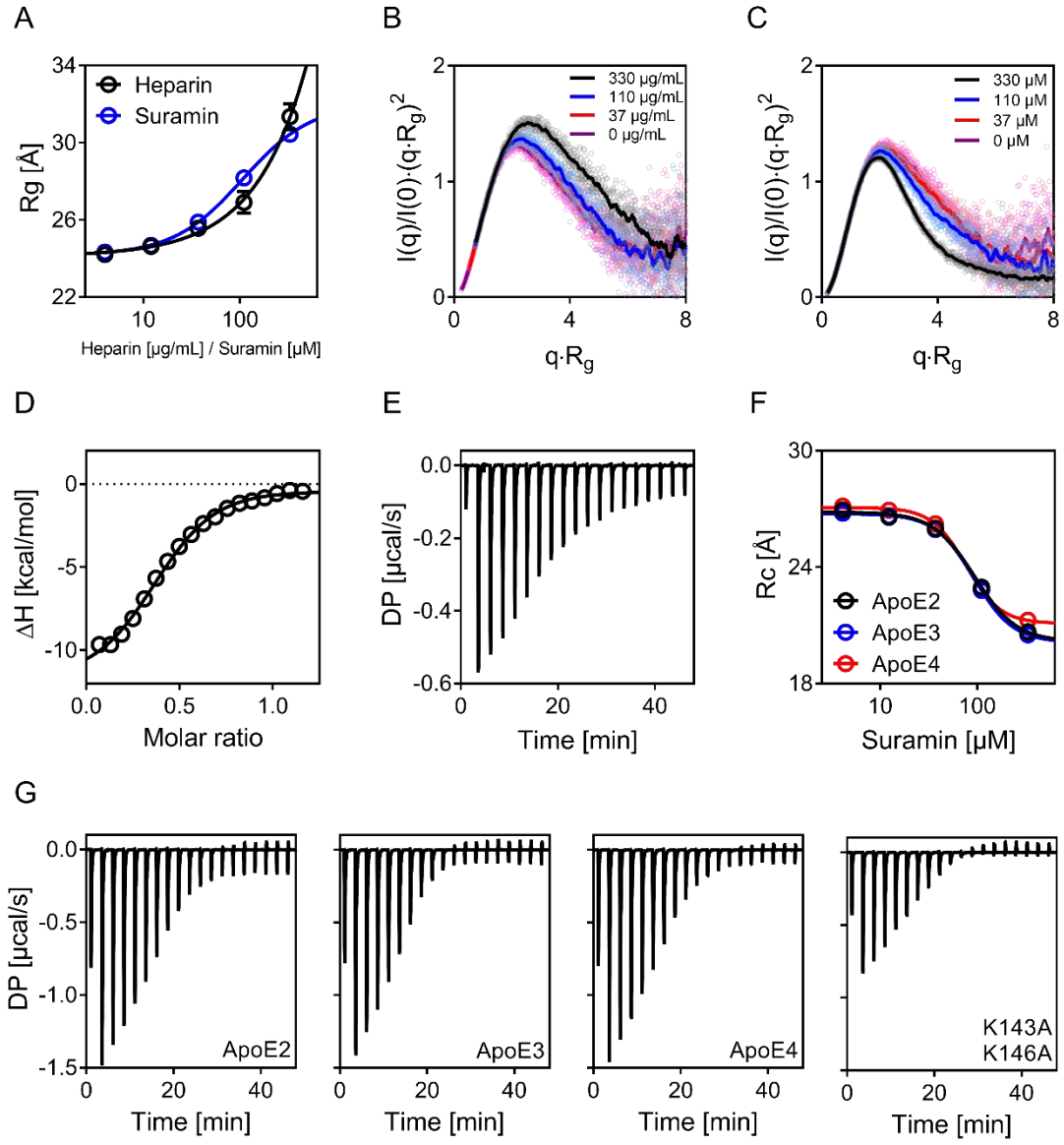

Figure 3.19. Static SAXS measurements of ApoE4$_{1-191}$ in the presence of heparin and Suramin and ITC titration heats. (A) ApoE4$_{1-191}$ change in Rg as a function of heparin and Suramin concentration is depicted. A concentration dependent increase in Rg is seen for both ligands. Normalized Kratky representations are for **(B)** heparin and **(C)** Suramin. **(D)** Presented are the normalized binding heats of the ApoE4$_{1-191}$ titration into Suramin with the solid line representing nonlinear least square fit using a single-site binding model. Suramin binding affinity (± SD) was determined to be 8 ± 1 µM with a stoichiometry *N* of 2. **(E)** Raw titration heats of 300 µM ApoE4$_{1-191}$ titrated into 50 µM Suramin are presented. **(F)** The concentration dependent effect of Suramin on wild type ApoE Rc is shown **(G)** Raw titration heats of 300 µM ApoE2, ApoE3, ApoE4 and mutant ApoE4 into 50 µM Suramin are shown. DP – differential power.

Table 3.3. Static SAXS parameters in the presence of heparin.

	ApoE2						
Heparin [µg/mL]	Guinier Rg [Å]	I(0), arb. Units	Pr Rg [Å]	Pr I(0), arb.units	D_{max} [Å]	q range [A^{-1}]	Gnom estimate
330	72.17 ± 0.86	0.77 ± 0.01	73.42 ± 0.32	0.76 ± 0.01	245	0.0075 - 0.2253	0.76
110	70.61 ± 0.73	0.66 ± 0.01	71.58 ± 0.40	0.65 ± 0.01	240	0.0079 - 0.23	0.57
37	65.27 ± 0.81	0.55 ± 0.01	67.51 ± 0.61	0.56 ± 0.01	234	0.0106 - 0.2347	0.70
12	63.80 ± 0.82	0.51 ± 0.01	64.64 ± 0.44	0.51 ± 0.01	217	0.0106 - 0.2253	0.76
4	61.85 ± 0.71	0.50 ± 0.01	62.99 ± 0.34	0.50 ± 0.01	207	0.011 - 0.2253	0.78
0	61.70 ± 0.82	0.46 ± 0.01	62.36 ± 0.33	0.46 ± 0.01	205	0.011 - 0.2253	0.78
	ApoE3						
Heparin [µg/mL]	Guinier Rg [Å]	I(0), arb. Units	Pr Rg [Å]	Pr I(0), arb.units	D_{max} [Å]	q range [A^{-1}]	Gnom estimate
330	72.71 ± 0.90	0.85 ± 0.01	75.57 ± 0.52	0.86 ± 0.01	259	0.0103 - 0.2309	0.74
110	75.05 ± 0.98	0.73 ± 0.01	75.45 ± 0.58	0.72 ± 0.01	258	0.0077 - 0.2216	0.63
37	69.14 ± 0.89	0.59 ± 0.01	69.97 ± 0.54	0.59 ± 0.01	239	0.0088 - 0.2253	0.69
12	65.04 ± 0.83	0.50 ± 0.01	65.76 ± 0.42	0.50 ± 0.01	220	0.0160 - 0.2436	0.74
4	62.79 ± 0.72	0.47 ± 0.01	63.84 ± 0.37	0.46 ± 0.01	208	0.0103 - 0.2253	0.78
0	61.40 ± 0.69	0.44 ± 0.01	62.89 ± 0.41	0.45 ± 0.01	206	0.0103 - 0.2253	0.78
	ApoE4						
Heparin [µg/mL]	Guinier Rg [Å]	I(0), arb. Units	Pr Rg [Å]	Pr I(0), arb.units	D_{max} [Å]	q range [A^{-1}]	Gnom estimate
330	76.11 ± 0.62	0.96 ± 0.01	77.98 ± 0.46	0.96 ± 0.01	265	0.0072 - 0.2253	0.75
110	76.28 ± 0.89	0.82 ± 0.01	78.49 ± 0.49	0.82 ± 0.01	270	0.0083 - 0.2253	0.72
37	70.47 ± 0.74	0.62 ± 0.01	73.17 ± 0.53	0.62 ± 0.01	258	0.0068 - 0.2207	0.74
12	66.86 ± 0.63	0.52 ± 0.01	67.72 ± 0.28	0.51 ± 0.01	220	0.0068 - 0.2196	0.63
4	64.40 ± 0.59	0.45 ± 0.01	65.40 ± 0.34	0.45 ± 0.01	212	0.0072 - 0.2031	0.78
0	61.78 ± 0.54	0.46 ± 0.01	63.40 ± 0.33	0.46 ± 0.01	208	0.0079 - 0.2253	0.78
	Methylated E4						
Heparin [µg/mL]	Guinier Rg [Å]	I(0), arb. Units	Pr Rg [Å]	Pr I(0), arb.units	D_{max} [Å]	q range [A^{-1}]	Gnom estimate
330	69.12 ± 0.78	0.64 ± 0.01	70.55 ± 0.41	0.64 ± 0.01	237	0.0077 - 0.2253	0.77
110	67.72 ± 0.92	0.55 ± 0.01	69.23 ± 0.45	0.55 ± 0.01	237	0.0095 - 0.2253	0.77
37	63.92 ± 0.61	0.50 ± 0.01	65.81 ± 0.44	0.50 ± 0.01	222	0.0083 - 0.2253	0.77
12	63.09 ± 0.63	0.46 ± 0.01	63.98 ± 0.34	0.46 ± 0.01	208	0.007 - 0.2184	0.79
4	61.13 ± 0.54	0.43 ± 0.01	62.72 ± 0.33	0.44 ± 0.01	202	0.0061 - 0.2236	0.79
0	60.75 ± 0.56	0.43 ± 0.01	62.20 ± 0.36	0.43 ± 0.01	203	0.0075 - 0.2365	0.78
	K143A K146A						
Heparin [µg/mL]	Guinier Rg [Å]	I(0), arb. Units	Pr Rg [Å]	Pr I(0), arb.units	D_{max} [Å]	q range [A^{-1}]	Gnom estimate
330	61.82 ± 1.05	0.34 ± 0.01	62.22 ± 0.47	0.34 ± 0.01	208	0.0091 - 0.2422	0.68
110	60.72 ± 0.79	0.34 ± 0.01	62.46 ± 0.55	0.34 ± 0.01	212	0.0111 - 0.2395	0.77
37	62.30 ± 1.52	0.35 ± 0.01	62.35 ± 0.48	0.35 ± 0.01	213	0.0102 - 0.2259	0.77
12	61.00 ± 1.10	0.34 ± 0.01	61.94 ± 0.48	0.34 ± 0.01	205	0.0115 - 0.2037	0.68
4	61.48 ± 0.89	0.34 ± 0.01	62.20 ± 0.40	0.34 ± 0.01	205	0.0091 - 0.2197	0.71
0	61.58 ± 0.89	0.34 ± 0.01	62.35 ± 0.50	0.34 ± 0.01	207	0.0088 - 0.2259	0.78
	$ApoE4_{1-191}$						
Heparin [µg/mL]	Guinier Rg [Å]	I(0), arb. Units	Pr Rg [Å]	Pr I(0), arb.units	D_{max} [Å]	q range [A^{-1}]	Gnom estimate
330	31.35 ± 0.67	0.130 ± 0.001	31.32 ± 0.30	0.110 ± 0.001	105	0.0248 - 0.2698	0.64
110	26.91 ± 0.56	0.098 ± 0.001	26.13 ± 0.23	0.085 ± 0.001	83	0.0281 - 0.2848	0.64
37	25.57 ± 0.30	0.081 ± 0.001	25.33 ± 0.16	0.080 ± 0.001	82	0.0208 - 0.3104	0.61
12	24.63 ± 0.26	0.079 ± 0.001	24.55 ± 0.17	0.078 ± 0.001	78	0.0181 - 0.3219	0.76
4	24.21 ± 0.25	0.076 ± 0.001	24.53 ± 0.18	0.075 ± 0.001	80	0.0177 - 0.3273	0.76
0	24.16 ± 0.23	0.078 ± 0.001	24.22 ± 0.15	0.078 ± 0.001	77	0.0152 - 0.3293	0.67

Table 3.4. Static SAXS parameters in the presence of Suramin.

	ApoE2						
Suramin [μM]	Guinier Rg [Å]	I(0), arb. Units	Pr Rg [Å]	Pr I(0), arb.units	D_{max} [Å]	q range [A^{-1}]	Gnom estimate
330	51.58 ± 0.47	0.55 ± 0.01	53.06 ± 0.30	0.55 ± 0.01	178	0.0130 - 0.2187	0.71
110	56.37 ± 0.62	0.49 ± 0.01	56.42 ± 0.26	0.49 ± 0.01	182	0.0088 - 0.2144	0.67
37	58.91 ± 0.59	0.49 ± 0.01	60.14 ± 0.33	0.48 ± 0.01	198	0.009 - 0.2017	0.73
12	60.96 ± 0.72	0.48 ± 0.01	61.66 ± 0.32	0.47 ± 0.01	203	0.0083 - 0.2211	0.76
4	60.88 ± 0.80	0.47 ± 0.01	61.89 ± 0.38	0.47 ± 0.01	205	0.0106 - 0.222	0.77
	ApoE3						
Suramin [μM]	Guinier Rg [Å]	I(0), arb. Units	Pr Rg [Å]	Pr I(0), arb.units	D_{max} [Å]	q range [A^{-1}]	Gnom estimate
330	52.30 ± 0.49	0.54 ± 0.01	54.09 ± 0.35	0.55 ± 0.01	186	0.0103 - 0.214	0.63
110	55.85 ± 0.68	0.47 ± 0.01	56.65 ± 0.33	0.47 ± 0.01	191	0.0106 - 0.2253	0.67
37	59.80 ± 0.63	0.46 ± 0.01	60.59 ± 0.44	0.46 ± 0.01	203	0.0106 - 0.2075	0.76
12	61.38 ± 0.52	0.45 ± 0.01	61.93 ± 0.32	0.45 ± 0.01	200	0.0066 - 0.2253	0.72
4	62.33 ± 0.60	0.46 ± 0.01	62.17 ± 0.30	0.45 ± 0.01	201	0.009 - 0.2209	0.79
	ApoE4						
Suramin [μM]	Guinier Rg [Å]	I(0), arb. Units	Pr Rg [Å]	Pr I(0), arb.units	D_{max} [Å]	q range [A^{-1}]	Gnom estimate
330	53.98 ± 0.39	0.58 ± 0.01	56.34 ± 0.33	0.59 ± 0.01	196	0.0095 - 0.2191	0.69
110	54.91 ± 0.43	0.46 ± 0.01	56.93 ± 0.39	0.47 ± 0.01	195	0.0095 - 0.2086	0.74
37	60.29 ± 0.57	0.48 ± 0.01	61.03 ± 0.30	0.48 ± 0.01	201	0.0083 - 0.2109	0.77
12	60.94 ± 0.55	0.45 ± 0.01	62.40 ± 0.27	0.45 ± 0.01	201	0.0086 - 0.2142	0.8
4	61.82 ± 0.53	0.46 ± 0.01	62.73 ± 0.29	0.45 ± 0.01	204	0.007 - 0.2213	0.78
	Methylated E4						
Suramin [μM]	Guinier Rg [Å]	I(0), arb. Units	Pr Rg [Å]	Pr I(0), arb.units	D_{max} [Å]	q range [A^{-1}]	Gnom estimate
330	60.45 ± 0.60	0.73 ± 0.01	61.85 ± 0.30	0.73 ± 0.01	206	0.007 - 0.2189	0.74
110	56.52 ± 0.59	0.48 ± 0.01	57.14 ± 0.21	0.48 ± 0.01	181	0.0061 - 0.2169	0.78
37	58.08 ± 0.62	0.44 ± 0.01	59.92 ± 0.29	0.44 ± 0.01	196	0.0099 - 0.2307	0.78
12	59.94 ± 0.56	0.43 ± 0.01	60.88 ± 0.30	0.43 ± 0.01	194	0.0068 - 0.2209	0.76
4	60.42 ± 0.50	0.43 ± 0.01	61.58 ± 0.25	0.43 ± 0.01	197	0.0052 - 0.222	0.8
	K143A K146A						
Suramin [μM]	Guinier Rg [Å]	I(0), arb. Units	Pr Rg [Å]	Pr I(0), arb.units	D_{max} [Å]	q range [A^{-1}]	Gnom estimate
330	59.74 ± 0.67	0.52 ± 0.01	62.67 ± 0.51	0.53 ± 0.01	224	0.0111 - 0.2173	0.71
110	55.38 ± 0.61	0.37 ± 0.01	56.87 ± 0.37	0.37 ± 0.01	189	0.0113 - 0.2342	0.76
37	59.39 ± 0.18	0.36 ± 0.01	59.94 ± 0.07	0.36 ± 0.01	199	0.0102 - 0.2328	0.85
12	59.67 ± 0.82	0.34 ± 0.01	61.18 ± 0.46	0.35 ± 0.01	202	0.0106 - 0.2279	0.78
4	61.05 ± 0.61	0.35 ± 0.01	61.84 ± 0.39	0.35 ± 0.01	204	0.01 - 0.2228	0.64
	$ApoE4_{1-191}$						
Suramin [μM]	Guinier Rg [Å]	I(0), arb. Units	Pr Rg [Å]	Pr I(0), arb.units	D_{max} [Å]	q range [A^{-1}]	Gnom estimate
330	30.44 ± 0.19	0.210 ± 0.001	31.15 ± 0.19	0.215 ± 0.001	111	0.0121 - 0.2618	0.74
110	28.17 ± 0.23	0.130 ± 0.001	28.60 ± 0.16	0.128 ± 0.001	95	0.0097 - 0.2832	0.74
37	25.89 ± 0.23	0.093 ± 0.001	25.69 ± 0.14	0.092 ± 0.001	80	0.0123 - 0.3079	0.65
12	24.68 ± 0.23	0.081 ± 0.001	25.03 ± 0.17	0.080 ± 0.001	82	0.0121 - 0.323	0.76
4	24.33 ± 0.27	0.081 ± 0.001	24.31 ± 0.16	0.079 ± 0.001	78	0.0168 - 0.3253	0.78

Values in the unbound state are found in Table 3.3.

Table 3.5. Parameters of SEC-SAXS data.

	ApoE2	**ApoE2 + heparin**	**ApoE2 + Suramin**
Guinier Rg [Å]	57.75 ± 0.12	61.06 ± 0.18	51.42 ± 0.09
I(0), arb. Units	0.22 ± 0.01	0.32 ± 0.01	0.28 ± 0.01
Pr Rg [Å]	59.36 ± 0.09	62.8 ± 0.1	53.57 ± 0.07
Pr I(0), arb.units	0.22 ± 0.01	0.32 ± 0.01	0.28 ± 0.01
D_{max} [Å]	200	210	183
q range [$Å^{-1}$]	0.0059 - 0.2921	0.0066 - 0.2698	0.007 - 0.2921
Gnom estimate	0.8	0.8	0.79
	ApoE3	**ApoE3 + heparin**	**ApoE3 + Suramin**
Guinier Rg [Å]	58.18 ± 0.15	60.88 ± 0.21	51.25 ± 0.1
I(0), arb. Units	0.24 ± 0.01	0.23 ± 0.01	0.28 ± 0.01
Pr Rg [Å]	59.7 ± 0.08	63.31 ± 0.12	53.21 ± 0.09
Pr I(0), arb.units	0.24 ± 0.01	0.24 ± 0.01	0.28 ± 0.01
D_{max} [Å]	200	213	193
q range [$Å^{-1}$]	0.0075 - 0.2921	0.0052 - 0.2921	0.0059 - 0.2921
Gnom estimate	0.83	0.77	0.74
	ApoE4	**ApoE4 + heparin**	**ApoE4 + Suramin**
Guinier Rg [Å]	59 ± 0.16	61.29 ± 0.21	55.57 ± 0.14
I(0), arb. Units	0.22 ± 0.01	0.27 ± 0.01	0.23 ± 0.01
Pr Rg [Å]	60.46 ± 0.1	63.68 ± 0.13	56.96 ± 0.09
Pr I(0), arb.units	0.22 ± 0.01	0.28 ± 0.01	0.23 ± 0.01
D_{max} [Å]	200	216	187
q range [$Å^{-1}$]	0.0052 - 0.2921	0.0075 - 0.2921	0.0066 - 0.2921
Gnom estimate	0.76	0.76	0.8
	Methylated E4	**Methylated E4 + heparin**	**Methylated E4 + Suramin**
Guinier Rg [Å]	59.48 ± 0.18	63.59 ± 0.21	53.36 ± 0.15
I(0), arb. Units	0.22 ± 0.01	0.27 ± 0.01	0.23 ± 0.01
Pr Rg [Å]	60.9 ± 0.1	64.91 ± 0.15	55.44 ± 0.10
Pr I(0), arb.units	0.22 ± 0.01	0.27 ± 0.01	0.23 ± 0.01
D_{max} [Å]	200	217	185
q range [$Å^{-1}$]	0.0066 ± 0.2881	0.0063 - 0.291	0.0097 - 0.2921
Gnom estimate	0.81	0.76	0.74
	K143A K146A	**K143A K146A + heparin**	**K143A K146A + Suramin**
Guinier Rg [Å]	58.13 ± 0.17	56.96 ± 0.16	53.68 ± 0.14
I(0), arb. Units	0.19 ± 0.01	0.18 ± 0.01	0.2 ± 0.1
Pr Rg [Å]	59.63 ± 0.1	59 ± 0.11	55.06 ± 0.78
Pr I(0), arb.units	0.19 ± 0.01	0.18 ± 0.01	0.2 ± 0.1
D_{max} [Å]	202	198	183
q range [$Å^{-1}$]	0.0077 - 0.2927	0.0073 - 0.3005	0.0048 - 0.2923
Gnom estimate	0.82	0.82	0.79
	$ApoE4_{1-191}$	**$ApoE4_{1-191}$ + heparin**	**$ApoE4_{1-191}$ + Suramin**
Guinier Rg [Å]	23.25 ± 0.05	41.78 ± 0.41	23.74 ± 0.05
I(0), arb. Units	0.05 ± 0.01	0.07 ± 0.01	0.05 ± 0.01
Pr Rg [Å]	23.55 ± 0.03	45.09 ± 0.44	24.32 ± 0.05
Pr I(0), arb.units	0.05 ± 0.01	0.07 ± 0.01	0.05 ± 0.01
D_{max} [Å]	76	168	83
q range [$Å^{-1}$]	0.0164 - 0.3426	0.0164 - 0.2253	0.0146 - 0.3364
Gnom estimate	0.78	0.61	0.78

4 A BIOPHYSICAL APPROACH TO THE IDENTIFICATION OF NOVEL APOE CHEMICAL PROBES

4.1Introduction and Objectives

Data suggest that ApoE4 may contribute to AD pathogenesis through both Aβ-dependent and Aβ-independent pathways (Chapter 1, Section 1.5). One underlying hypothesis is that a structural difference between ApoE isoforms may confer ApoE4's detrimental effects in AD. It has been suggested that the amino acid substitution in ApoE4 alters the protein structure such that either (i) a salt bridge forms between Arg61 and Glu255 resulting in ApoE4 domain interaction (237–239), (ii) that the Arg112 affects charge distribution in the receptor binding region (245) which would be consistent with observations made here on the isoform dependent difference in heparin binding ability, or (iii) that ApoE4 may oligomerize differently and as a result may form large, fibril like oligomers (Chapter 1, Section 1.4.4) (247, 251). Regardless of the mechanism by which the structural and therefore functional difference arises, a potential therapeutic strategy is to use small molecules to convert ApoE4 into an ApoE3-like protein and thereby abolish ApoE4's detrimental effects in AD (234) (Chapter 1, Section 1.6).

This therapeutic approach has been investigated based on the hypothesis of the ApoE4 intramolecular domain interaction that attributes ApoE4's neuropathological effects to the Arg61-Glu255 salt bridge (252). For example, targeted replacement mice in which Thr61 in mouse ApoE was substituted with an arginine to mimic presumed domain interaction (241), show cognitive impairment compared to wild type matched controls and generally have lower levels of pre- and post-synaptic markers such as synaptophysin in the hippocampus (434). Primary cultured astrocytes from these targeted replacement mice have lower levels of ApoE due to increased activation of the unfolded protein response pathways and degradation of the protein (435). Similarly, increased neuronal degradation of ApoE4 compared to ApoE3 was demonstrated in mouse neuroblastoma cells, human brain lysates and in mice expressing ApoE under control of the neuron-specific enolase promoter (324, 332, 333). It has been suggested that the increased rate of proteolytic cleavage of ApoE4 results in fragments that enter the cytosol and interfere with cytoskeletal components such as tau (324) and may disrupt mitochondrial function (336) (Chapter 1, Section 1.5.3). Some of these effects can be reversed by disrupting the ApoE4 presumed domain interaction either by site directed mutagenesis (i.e. substituting Arg61 with a threonine) or by the use of small molecule "structure correctors" (364).

The structure correctors series include disulfonates such as GIND-25 (Azocarmine G) (363) and molecules with a phthalazinone core structure including PH002 (246) (Chapter 1, Section 1.6). These compounds were initially identified *in silico* (GIND series), as well as by drug

screening (phthalazinone series) using a cell-based FRET system (246, 363). In the cell-based FRET assay, ApoE fused with a fluorescence protein at its carboxyl and amino terminus respectively was expressed in mouse neuroblastoma cells (246). As outlined in Chapter 1, Section 1.4.4, a greater FRET signal was observed in the ApoE4 fusion construct consistent with the domain interaction concept. A reduction in the FRET signal was interpreted as disruption of the domain interaction due to a ligand induced change in conformation (246). Most recently, the effects of PH002 were investigated in human iPSCs with ε4 genotype that were developed by Yadong Huang and colleagues (339). As outlined in Chapter 1, Section 1.5.3, lower numbers of GABAergic neurons were derived from ε4 iPSCs and neurons showed increased ApoE4 fragmentation, altered APP metabolism, as well as increased tau phosphorylation. Treatment with PH002 reversed all these effects in a concentration dependent manner (339).

Although PH002 and other structure correctors have beneficial effects in AD cellular models, they were shown to cause significant toxicity in mice (364). Alternative small molecules that bind to ApoE4 are lacking. The objective of this section was to validate biophysical assays to enable screening for novel ApoE chemical probes that preferentially bind to ApoE4 over ApoE2 and ApoE3. The biophysical assays that were optimised were an optical label-free assay (Corning® Epic®), microscale thermophoresis (MST) and isothermal titration calorimetry (ITC). The 707-compound NIH clinical collection was screened against human full length recombinant ApoE4, with the label-free assay being used as the primary screen and MST and ITC being used for confirmation (Figure 4.1). Taking the screening hits through the orthogonal MST and ITC assays, binding of six drugs, as well as a selected drug analogue was confirmed. All drugs are in clinical use and include the hormone L-Thyroxine and it's analogue Tafamidis, as well as the selective estrogen receptor modulators (SERMs) Clomiphene, Tamoxifen, Toremifene, and the non-steroidal anti-inflammatory drug (NSAID) Meclofenamic acid. Although the functional effects of these compounds on ApoE structure and function remain to be elucidated, this thesis chapter nevertheless demonstrates the feasibility of using biophysical assays to screen for molecules that interact with ApoE4.

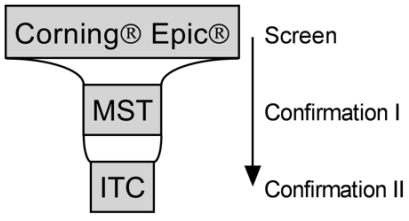

Figure 4.1. Summary of the screening strategy. Compounds are screened against full length human ApoE4 using the Corning® Epic® and hits then tested by MST and ITC. Hits are also evaluated by ITC against human full length ApoE2 and ApoE3 to determine selectivity.

4.2 Material and Methods

4.2.1 Materials

All materials were purchased from Sigma-Aldrich or Fisher Scientific and were the highest purity available. *N*-(3-Dimethylaminopropyl)-*N′*-ethylcarbodiimide hydrochloride (EDC, # 03450), Suramin (# S2671) and PH002 (# SML0461) were obtained from Sigma-Aldrich. Sulfo-*N*-hydroxysulfosuccinimide (sulfo-NHS, # 24510) and Azocarmine G (# 11444154) were purchased from Thermo Fisher Scientific. Corning® Epic® high sensitivity biochemical assay plates (# 5046) were retrieved from Corning®. Monolith NT.115 capillaries (# MO-K022) and the amine reactive Monolith protein labeling Kit RED-NHS (# MO-L001) were obtained from Nanotemper. The NIH clinical collection (NCC) was kindly provided by the National Institute of Health (NIH) and distributed by Evotec.

4.2.2 Protein production and purification

ApoE isoforms and ApoE4$_{1\text{-}191}$ were produced and purified as described in Chapter 2, Sections 2.2.6 and 2.2.7.

4.2.3 The Corning® Epic® label free technique

The Corning® Epic® technology is a label free technology that measures a change in wavelength of refracted light. The refractive index of a material is a dimensionless number that describes how light propagates through the material. It is defined as:

$$n = \frac{c}{v} \quad (4.1)$$

where *c* is the speed of light and *v* the phase velocity of light in the medium. The refractive index of a material determines how strong a ray of light is bent, or refracted, when it enters the material. The law of refraction (or Snell's law after Willebrord Snellius) states that the ratio of phase velocities is equivalent to the ratio of sines of the angles of incidence and refraction.

$$\frac{\sin\theta 1}{\sin\theta 2} = \frac{v1}{v2} = \frac{n2}{n1} \quad (4.2)$$

Snell's law implies that light is refracted perpendicularly when travelling from a medium with higher refractive index (e.g. water) to one with lower refractive index (e.g. air) (Figure 4.2). If the ray of light enters the medium with lower refractive index at a critical angle it is completely reflected (total internal reflection). However, the electromagnetic field in the second medium does not disappear and propagates along the boundary in form of an evanescent wave. This evanescent wave or field decays exponentially with increasing distance from the interface and has only a short penetration depth (150-200 nm) (436, 437).

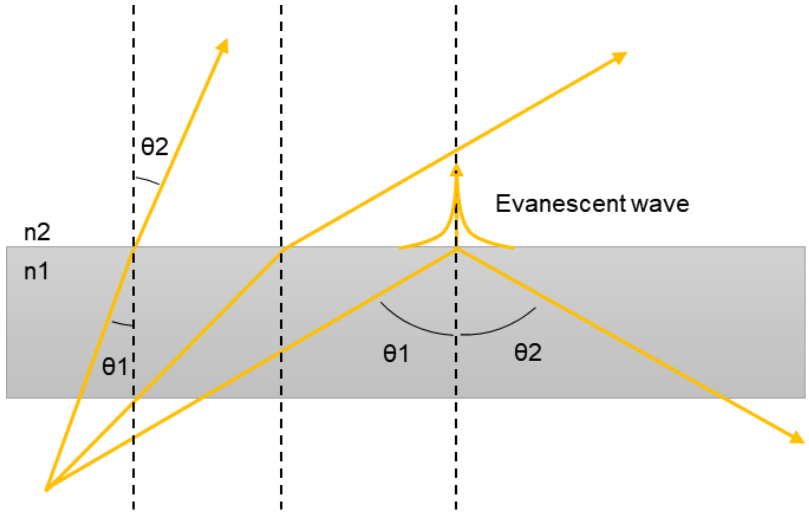

Figure 4.2. Snell's law. Light that travels from a medium with a higher refractive index n1 to a medium with a lower refractive index n2 is refracted at their boundaries. At a critical angle the light is internally reflected and creates an evanescent field that enters the medium with lower refractive index n2.

Each well of a Corning® Epic® plate contains an optical sensor (also referred as to resonant waveguide grating) that only reflects a narrow band of wavelengths when illuminated with broadband light. As outlined above, reflection of the light will create an evanescent field that enters the well of the Corning® Epic® plate. The wavelength of the reflected light depends on the local index of refraction at the surface of the biosensor; any change in the refractive index (e.g. by binding of an analyte to the target) will increase the local index of refraction and cause a shift in the resonant wavelength (Figure 4.3) (438, 439).

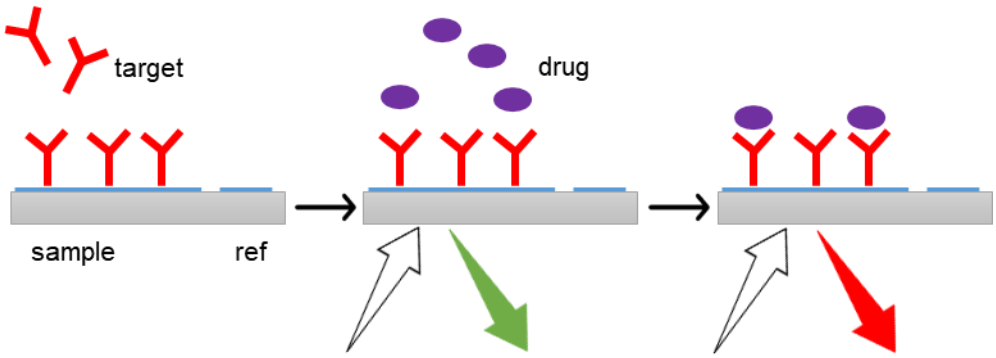

Figure 4.3. Principle of the Corning® Epic®. The target protein is immobilized on a chemistry surface via amine coupling. The well is then illuminated from below with broadband light and only a narrow band of wavelengths is reflected (here shown as green arrow or green light). Binding of analytes to the target will change the refractive index on the sample area and shift the wavelength of reflected light (here from green to red). An integral part of each well is the reference area (ref) that prevents binding of the target and filters out any physical effects such as temperature.

4.2.4 Activation of Corning® Epic® plates and immobilization of ApoE4

Corning® Epic® 384-well plates (# 5046) were activated with 200 mM EDC and 50 mM sulfo-NHS. For this, 400 mM EDC and 100 mM sulfo-NHS freshly dissolved in twice-distilled water were combined, vortexed and 15 µL of the mixture dispensed into each well of the Corning® Epic® plate. The plate was centrifuged at 87 x *g* at RT for 1 min, sealed and incubated at 26°C for 30 min. The plate was then washed three times with 15 µL twice-distilled water per well and protein then immobilized.

ApoE4 (5 µL) diluted to 300 µg/mL in 20 mM sodium citrate pH 5.6 were dispended into wells and incubated at 26°C for 1 h. The microplate was subsequently washed three times with PBS + 0.1% (v/v) Triton X-100 + 2% (v/v) DMSO (PBSTD) and remaining reactive groups on the biosensor then blocked by incubation with 50 mM ethanolamine in PBSTD for 5 min at RT. The plate was washed three times with PBSTD and after the final wash, 15 µL PBSTD were added to each well, sealed and placed into the Epic® reader for 1.5 h for thermal equilibration. To measure immobilization levels and/or to take the baseline before compound addition after thermal equilibration, 10-15 total points were recorded with 4 x 3 sec scans averaged per point. Immobilization levels were calculated through wells where no ApoE4 was added. The level of immobilization expressed in picometer (pm) was obtained by subtracting the response of wells with no ApoE4 from wells with protein.

To determine ideal immobilization conditions, binding of ApoE4 to the Corning® Epic® biosensor was tested in 20 mM sodium acetate pH 5.5, sodium citrate pH 6.0, sodium phosphate pH 6.5 and sodium phosphate buffer pH 7 at 100, 150 and 200 µg/mL. Refined pH screening was then performed in 20 mM sodium citrate buffer at pH 5.6, pH 5.8 and pH 6.0 at 100, 150 and 300 µg/mL.

4.2.5 Suramin binding curve on the Corning® Epic®

After thermal equilibration of the Corning® Epic® plate and baseline read (Section 4.2.4), the measurement was paused on the Epic® reader, the plate removed and Suramin added into the wells (total volume 30 µL) in triplicate at different concentrations, ranging from a control of 0 to 12 mM. The plate was sealed and placed back into the Epic® reader for 30 min. Binding shifts were then measured over 15-20 points in total with 4 x 3 sec scans averaged per point. Responses were measured as shifts in reflected wavelength and were expressed in pm.

To determine the correlation in between immobilization levels and shifts caused by Suramin, 5 µL ApoE4 in sodium citrate buffer pH 5.6 at different concentration (25, 50 and 300 µg/mL) was dispensed into each well of the Corning® Epic® plate. After immobilization, blocking and baseline read (Section 4.2.4), 15 µL of 2 mM Suramin in PBSTD was added as described above. PBSTD only was used as a negative control.

4.2.6 Screening plate test

Screening was performed with the aid of the FluidX-Xpp-721 (FluidX) automated liquid handling system. To assess reproducibility of the automated liquid handling system, plate tests were performed with Suramin at a final concentration of 150 µM randomly distributed across the plate. The plate layout is depicted in Figure 4.4. Suramin (2 µL) at 15 mM in neat DMSO was transferred into 98 µL of PBS + 0.1% (v/v) Triton X-100 (PBST) using the FluidX to yield intermediate 96-well plates. Suramin (15 µL) from intermediate plates was then transferred into the Corning® Epic® plate to a final volume of 30 µL using the automated liquid handling system. Additionally, Suramin at 150 µM and 5 mM was used as positive control. The plate was sealed, equilibrated in the Epic® reader for 30 min and response measured as described in 4.2.5.

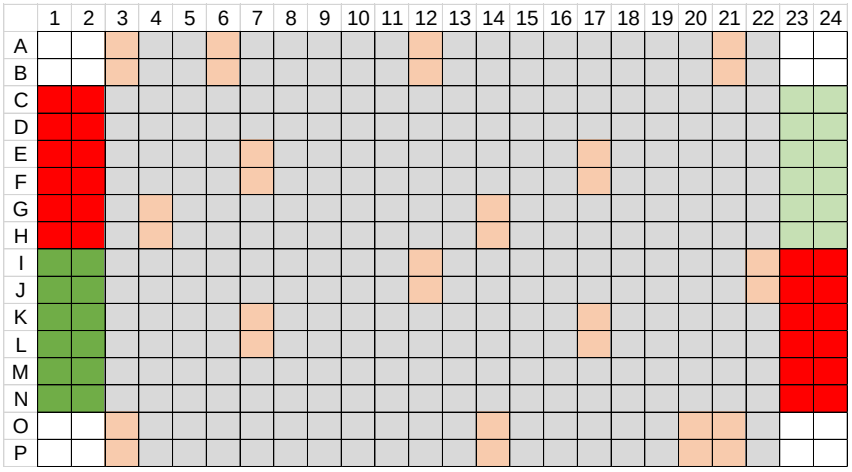

Figure 4.4. Plate test layout. Suramin at 5 mM (dark green) and 150 µM (bright green), as well as PBSTD (red) were used as positive and negative controls during screen. Immobilization levels were determined through wells where no ApoE4 was added (white). In the plate test, Suramin at 150 µM was randomly dispensed into the Corning® Epic® plate (orange). PBSDT (grey) was added to the remaining wells.

4.2.7 Screening

The NIH clinical collection that contains 707 compounds was screened against ApoE4. Screening was carried out at a compound concentration of 100 µM in two identical runs. Compounds at 10 mM in neat DMSO were diluted to 200 µM in PBS + 0.1% (v/v) Triton X-100 (resulting in 2% (v/v) DMSO) and then dispensed into the Epic® plate (total volume 30 µL) after having read the baseline. Plates were left for 30 min in the Epic® and binding shifts measured as described in section 4.2.5. Suramin at 5 mM and 150 µM was used as positive control; buffer only was used as negative control. Only plates with a Z'-factor above 0.5 were accepted. The Z'-factor is defined as:

$$Z' = 1 - \frac{3\left(\sigma_p + \sigma_n\right)}{\left|\mu_p - \mu_n\right|} \quad (4.3)$$

where σ is the standard deviation and μ the mean of the positive (p) and negative (n) control. The Z'-factor was calculated individually with the 150 μM and 5 mM Suramin positive control.

Screening data was extracted with the Epic® Analyzer (version 02-27-2015) and responses corrected for background signal. Only samples with ApoE4 immobilization levels > 1800 pm were included in data analysis. Median and median absolute deviation (MAD) for both screening runs were calculated separately and hit threshold arbitrarily set to 5 x MAD of the sample. Compounds with negative shifts were excluded as well as compounds with shifts ≥ 150 pm. Prioritized compounds that met hit criteria were tested in form of concentration response and were diluted 1:2 in neat DMSO, then transferred into PBS + 0.1% Triton X-100 as above and added into the wells (total volume 30 μL) in duplicate at different concentration, ranging from 0.2 to 100 μM.

4.2.8 Microscale thermophoresis

Thermophoresis describes the movement of particles in a temperature gradient. The velocity, v of particles is linear to the temperature gradient:

$$v = -D_T \Delta T \quad (4.4)$$

with thermal diffusion coefficient (or thermophoretic mobility) D_T and the temperature gradient ΔT. In steady state, thermophoresis is counterbalanced by mass diffusion. The depletion of macromolecules in the region of elevated temperature is quantified by the Soret coefficient S_T.

$$\frac{c_{hot}}{c_{cold}} = e^{-S_T \Delta T} \quad (4.5)$$

where c_{hot} and c_{cold} is the concentration of the macromolecule in a defined region at elevated and non-elevated temperature respectively. The Soret coefficient is the ratio of thermophoretic mobility D_T over diffusion coefficient D of the macromolecule.

$$S_T = \frac{D_T}{D} \quad (4.6)$$

An increase in temperature leads to depletion of solvated molecules and commonly movement of the molecules into colder regions. This solvent depletion is dependent on the interface between the molecules and the solvent. Binding of a ligand to the molecule will often induce changes in size, charge, as well as solvation and alter the molecule's thermophoretic behaviour. This allows for the analysis of binding events by MST. The macromolecule is labelled with a fluorescent dye (e.g. Alexa 647) and movement in solution monitored by measuring the fluorescence (Figure 4.5) (440–442).

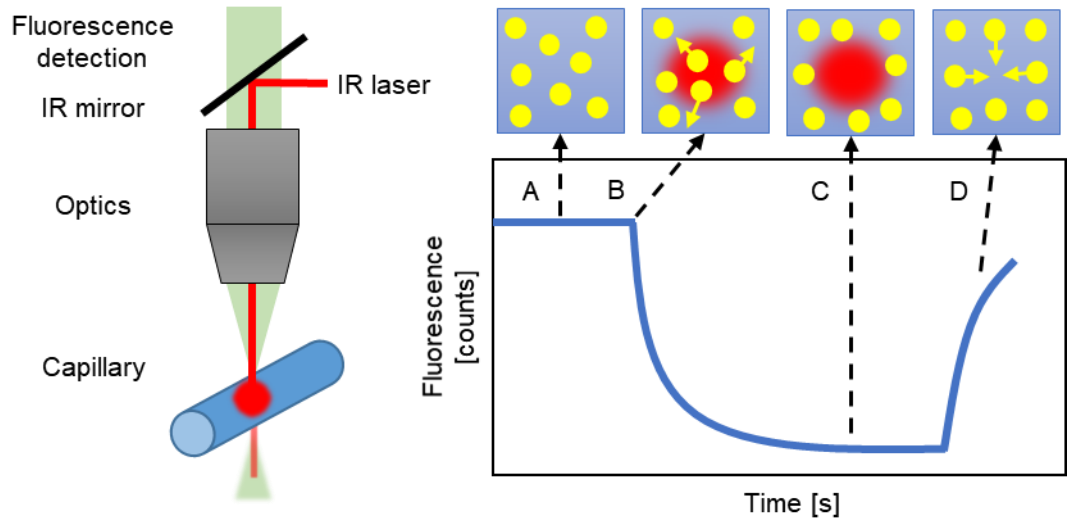

Figure 4.5. Microscale thermophoresis. The experimental setup of the MST experiment is shown on the left. MST is performed in a capillary and fluorescence excitement, as well as measurement of the labelled protein is measured through the same optics. An infrared (IR) laser is guided through the capillary and heats up a small sample volume that will induce movement of the molecules. Thermophoresis is therefore given as a change in fluorescence with time. A typical MST signal plot is shown on the right. (A) Initially, distribution of molecules (yellow circles) is homogenous in solution and a constant initial fluorescence is measured. (B) Application of the IR laser will heat up a small region within the capillary and induce thermophoresis. (C) In steady state, thermophoresis is counterbalanced by diffusion. (D) The IR laser is turned off which allows backdiffusion of the molecules. Figure adapted by permission from: Elsevier, Jerabek-Willemsen *et al*, Journal of Molecular Structure, 2014, 1077:101-113 (440).

ApoE4 was labelled in SEC buffer (Chapter 2, Section 2.2.6) using the Monolith NT-647 Protein Labeling Kit Red-NHS (Nanotemper) following the manufacturer's instruction and the labelling reaction was performed with 20 µM ApoE4 and 40 µM labelling dye. Labelled protein was centrifuged at 16000 x *g* for 5 min at RT before use and then diluted to 200 nM in 20 mM HEPES, 500 mM NaCl, 10% (v/v) glycerol, 0.1% Triton X-100 (MST buffer). Binding of hits identified by screening with the Corning® Epic® (Section 4.2.7) was first tested in 8-point concentration response assays. Compounds at 5 mM in neat DMSO were diluted 1:2 in DMSO and then transferred into MST buffer. Diluted compounds in MST buffer (4% (v/v) DMSO) were then combined with equal volumes of 200 nM labelled protein, resulting in a 2% (v/v) DMSO working concentration, 100 nM labelled ApoE4 and compound concentrations ranging from a control of 0 to 100 µM. The mixture was pulse centrifuged and incubated at RT for 5 min. Samples were then centrifuged at 16000 x *g* for 5 min and soaked into standard capillaries in duplicate. To achieve full binding curves of compounds, 12-point concentration responses were performed from 0.25 to 250 µM or 0.5 to 500 µM in triplicate. For this, compounds were diluted 1:2 in neat DMSO from 12.5 or 25 mM respectively, transferred into MST buffer and combined with equal volumes of 200 nM ApoE4. MST measurements were performed on the Monolith NT.115 (Nanotemper). Capillaries were thermally equilibrated at 25˚C for 5 min and

MST traces then collected at 20-40% LED excitation power and 20% IR power. Data were analysed on the integrated analysis software (MO affinity analyser version 2.2.4, Nanotemper). A sample denaturation test was performed for samples that altered initial fluorescence signal. The compound-ApoE4 mixture was centrifuged for 5 min at 16000 x *g* at RT and then mixed with equal volumes of 2 x denaturing buffer (4% SDS, 40 mM DTT). Samples were denatured at 95˚C for 5 min, soaked into capillaries and initial fluorescence measured. To test autofluorescence of compounds, compounds at 250 – 500 µM were mixed with 40 nM of NT-647 dye (Nanotemper) and fluorescence measured on the Monolith NT.115 (Nanotemper). Binding affinities as presented in Table 4.1 are the average of six independent experiments (± SD).

To determine optimal ApoE4 concentration and buffer for MST measurements used above, ApoE4 in PBS, PBS + 0.1% (v/v) Triton-X 100, SEC buffer and MST buffer was soaked into capillaries at 20, 40, 80 and 100 nM final concentration and capillary scans performed over time (0, 10 and 20 min) at 40% LED excitation power. To evaluate DMSO tolerance, thermophoresis of ApoE4 at 100 nM in MST buffer was tested at varying (v/v) DMSO concentrations (0, 1, 2, 4%) in quadruplicates. Capillaries were thermally equilibrated, and measurements performed as described above.

4.2.9 Isothermal titration calorimetry

Isothermal titration calorimetry (ITC) measures the heat change that occurs when two macromolecules (e.g. protein – ligand) interact. Depending on the type of reaction (exothermic versus endothermic) heat is released or absorbed. Measurements are performed at a constant temperature (isothermal) and the ligand is injected into the sample cell that contains the protein or vice versa. In ITC, heat changes are monitored by measuring the power required to keep a reference cell at equal temperature to the sample cell. The reference cell normally contains water or the sample buffer. Nearly all binding events are accompanied by a change in enthalpy Δ°H and all reactions will produce a calorimetric signal. ITC will therefore allow direct estimation of enthalpy changes in addition to the dissociation constant by the relation:

$$\Delta^\circ G = \Delta^\circ H - T\Delta^\circ S = -RT\ lnK_A = RT\ lnK_D \quad (4.7)$$

with Δ°G being the standard free energy, Δ°S the entropy, R the gas constant [8.314 J K^{-1} mol^{-1}], T the temperature (in kelvin), K_A and K_D the association and dissociation constant respectively. The right-hand version of the equation was obtained by the relation $K_A = K_D^{-1}$ (443, 444).

ITC titrations were performed as described in Chapter 3, Section 3.2.7. Hence, ApoE isoforms, as well as $ApoE4_{1\text{-}191}$ were dialysed against PBS + 0.01% (v/v) Triton X-100 overnight at 4˚C using 3.5 K Slide-A-Lyzer™ dialysis cassettes (ThermoFisher Scientific). ApoE, as well as

$ApoE4_{1-191}$ at 300 µM was injected into the cell containing compound at 25-50 µM in PBS + 0.01% (v/v) Triton X-100 + 2% (v/v) DMSO. DMSO concentrations in syringe and cell were matched. Titration experiments were carried out on a Microcal PEAQ-ITC (Malvern) at 25˚C and 750 rpm and consisted of a first (1 µL) injection followed by additional 18 (2 µL) injections. Injection of protein into PBS + 0.01% (v/v) Triton X-100 + 2% (v/v) DMSO was used as control experiment and integrated control heats were subtracted from the reaction heats. Data were analysed on the Microcal PEAQ-ITC analysis software version 1.1.0.1262 and data fitted for one set of sites. Binding affinities as presented in Table 4.1 are the average of two independent experiments (± SD).

4.3 Results

4.3.1 Corning® Epic® assay development

The binding of protein to the Corning® Epic® biosensors has to be optimised in order to achieve high levels of protein immobilization since low amounts of protein on the sensor will result in low and highly variable binding signals. Immobilization levels are obtained by comparing the response (in picometers, pm) of biosensors to which protein was added with sensors containing no protein. The immobilization response has to be in the range of 1500 – 3000 pm. Proteins are covalently bound to the biosensor via amine coupling and identification of the right pH for the immobilization procedure is necessary (Appendix Figure 4.18).

Binding of ApoE4 to the chemistry surface of the biosensor was tested in buffers with pH ranging from 5.5 – 7.0 (Figure 4.6A). The highest immobilization response was achieved in sodium acetate buffer pH 5.5 at an ApoE4 concentration of 200 µg/mL. However, ApoE4 visibly precipitated in sodium acetate buffer pH 5.5. Sodium acetate at low pH seems to affect ApoE4 conformation and altered elution pattern was confirmed by SEC (Appendix Figure 4.19). Therefore, ApoE4 immobilized to the biosensor in sodium acetate buffer pH 5.5 may be unfunctional. Good immobilization levels were still achieved in sodium citrate buffer pH 6.0 and variation of the pH to slightly lower values increased binding of ApoE4 to the biosensor without observing any precipitation. Increasing ApoE4 concentration to 300 µg/mL resulted in optimal protein immobilization (Figure 4.6B).

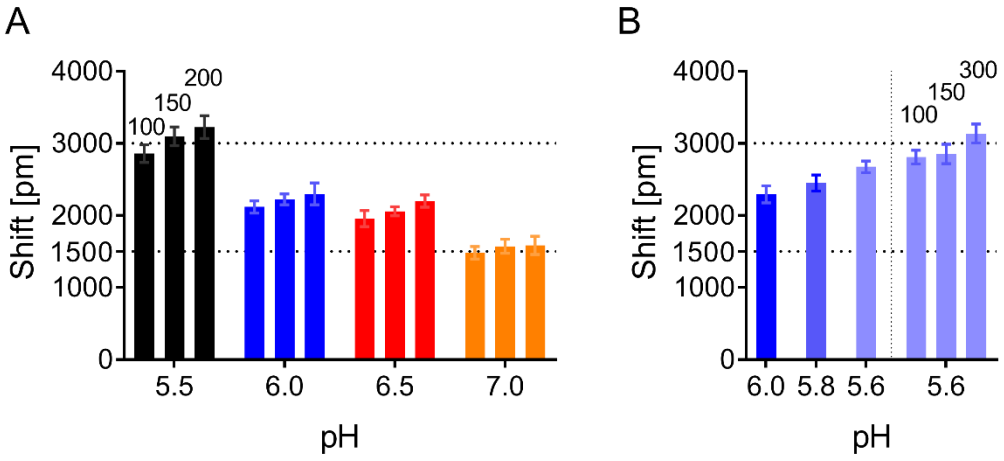

Figure 4.6. ApoE4 immobilization optimization. (A) ApoE4 immobilization levels on the Corning® Epic® biosensor in 20 mM sodium acetate pH 5.5, 20 mM sodium citrate pH 6.0, 20 mM sodium phosphate pH 6.5 or 20 mM sodium phosphate pH 7.0 to final concentrations of 100, 150 or 200 µg/mL are shown. An immobilization response < 1500 pm is considered low. **(B)** Binding of ApoE4 at 100 µg/mL in 20 sodium citrate pH 6.0, 5.8 and 5.6 is shown, as well as in 20 mM sodium citrate pH 5.6 at 100, 150 and 300 µg/mL. Each graph bar represents 12 wells measured for immobilization; standard deviation is expressed by error bars.

After having identified ideal immobilization conditions of ApoE4 to the biosensor (i.e. ApoE4 at 300 µg/mL in 20 mM sodium citrate buffer pH 5.6), the binding of ApoE4 structure correctors GIND-25 (or Azocarmine G) (361), PH002 (246) and EZ-482 (445) as well as Suramin were tested. Binding of Suramin to ApoE has not been described to date and was tested based on previous observations made that it interferes with the association of ApoE containing lipoproteins to the extracellular matrix of HepG2 cells (Chapter 3, Section 3.3.4). Only Suramin positively shifted the reflected wavelength, whereas PH002, as well as EZ-482 led to slight negative shifts which suggests binding of these compounds to the reference surface of the biosensor (Figure 4.7). No binding of GIND-25 was detected at concentrations used.

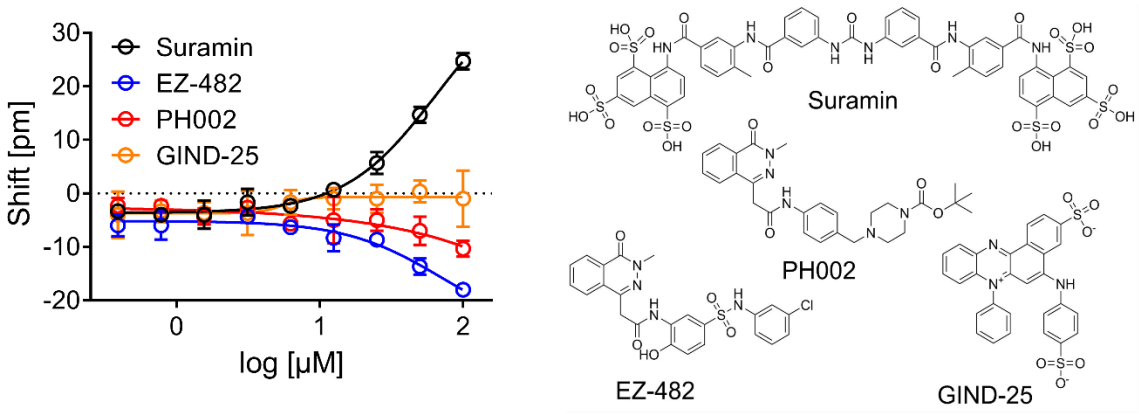

Figure 4.7. Selection of Suramin as positive control. Available ApoE4 modulators, as well as Suramin were tested by concentration response on the Corning® Epic® against ApoE4. Only Suramin positively shifted the wavelength suggesting binding, whereas negative shifts were observed for PH002 and EZ-482 which may indicate precipitation of compounds or binding to the reference surface of the biosensor. No binding was detected for GIND-25 at concentrations used. The data are expressed as mean of three independent experiments, the standard deviation (SD) is represented by the error bars.

Suramin was therefore selected as positive control and binding tested in the presence of DMSO, as well as the non-ionic detergent Triton X-100. Addition of detergents to assay buffers can help to stabilize proteins and particularly prevent compound aggregation during screening (446). Triton X-100 and DMSO did not affect the signal response and a DSMO concentration up to 2% (v/v) was well tolerated (Figure 4.8). Additionally, the influence of ApoE4 immobilization levels on the Suramin binding response was investigated. Varying amounts of ApoE4 were added to the biosensor and binding of Suramin at 1 mM tested (Figure 4.8D). As expected, decreased Suramin binding responses were measured the less ApoE4 was immobilized to the Corning® Epic® biosensor.

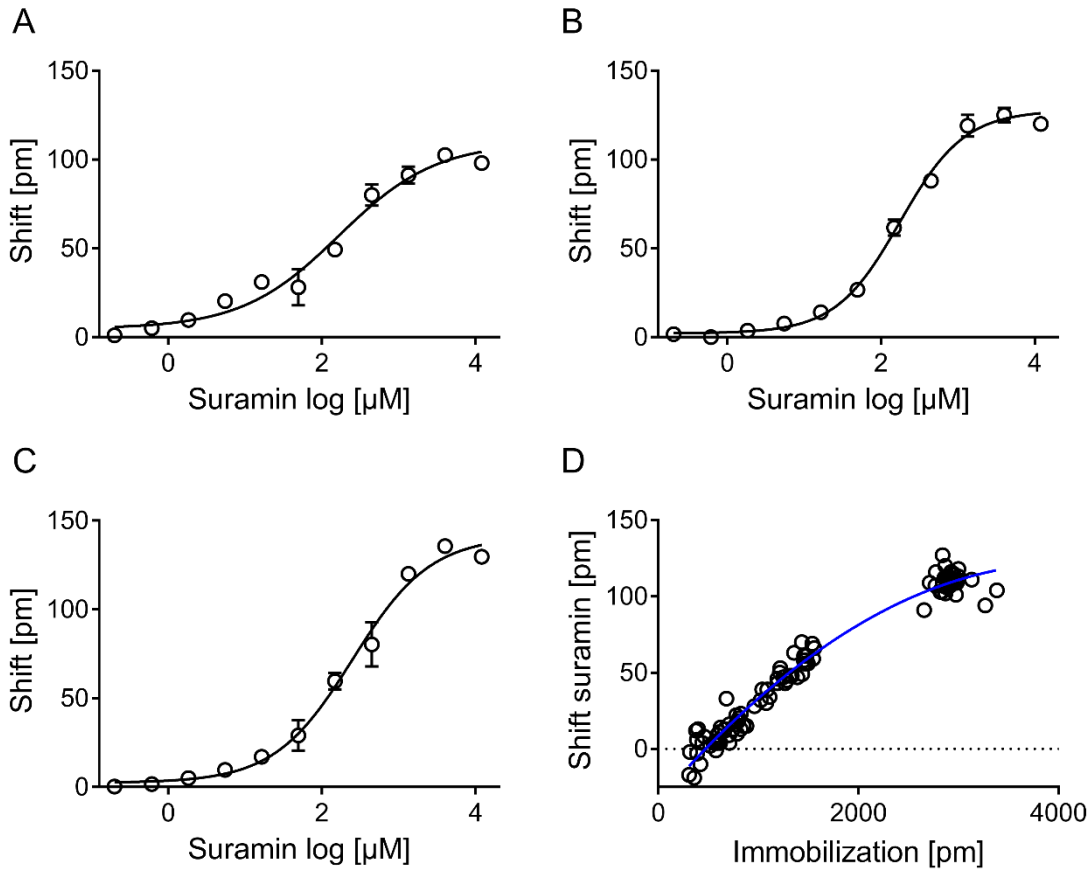

Figure 4.8. Suramin concentration response. The concentration response of Suramin is shown for buffers **(A)** PBS + 1% (v/v) DMSO, **(B)** PBS + 1% (v/v) DMSO + 0.1% (v/v) Triton X-100 and **(C)** PBS + 2% (v/v) DMSO + 0.1% Triton X-100. Suramin binding affinities of (± SD) 78 ± 21, 142 ± 25 and 184 ± 18 µM were calculated respectively (n= 3). **(D)** The response (in pm) caused by 1 mM Suramin is plotted as a function of ApoE4 immobilization levels (in pm). High immobilization levels (~3000 pm) result in good binding signals; lower levels of ApoE4 on the biosensor result in decreased signal.

A plate test was performed before compound screening to evaluate the signal-to-noise ratio. Suramin at 5 mM and 150 µM was selected as positive control as these concentrations resulted in approximately 100% and 50% binding signal respectively (Figure 4.8C). The plate test revealed excellent coupling of ApoE4 to the biosensor with average immobilization levels of 2700 pm (Figure 4.9C). Suramin at both concentrations gave a good signal-to-noise ratio (Figure 4.9A and 4.9B). The Corning® Epic® assay was therefore determined to be suitable for compound screening.

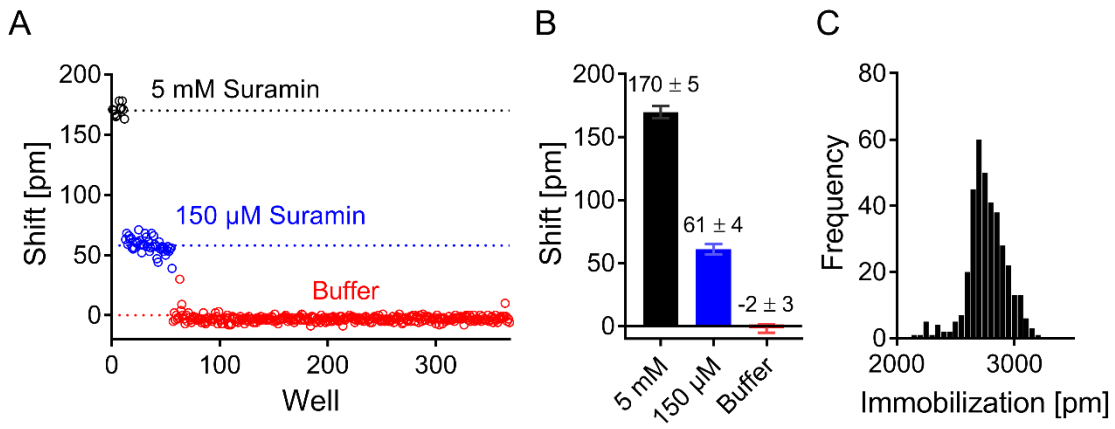

Figure 4.9. Screening plate test. (A) The response (in pm) of Suramin at 5 mM and 150 µM, as well as buffer only is shown for each well of the 384-well Corning® Epic® plate. **(B)** The average signal of Suramin at 5 mM (n= 12) and 150 µM (n= 12), as well as the buffer negative control (n= 24) is shown and demonstrates an excellent signal-to-noise ratio. **(C)** ApoE4 immobilization levels are normally distributed across the Corning® Epic® plate. Average immobilization (± SD) was 2739 ± 164 pm.

4.3.2 Secondary assays development

MST and ITC were selected as secondary assays to confirm binding of screening compounds. In MST, protein and ligand are soaked into glass capillaries and thermophoresis induced by applying an IR laser (Figure 4.5). Proteins can bind to the glass surface of the capillary which will result in non-homogeneous distribution of the protein and affect thermophoresis (Appendix Figure 4.20). Therefore, the MST assay buffer has to be optimized to prevent such association. In the case of ApoE4, addition of Triton X-100, as well as high salt concentration were necessary to stop binding to the capillary (Appendix Figure 4.21, Figure 4.10B). Labelling of ApoE4 with the NT-647 dye (Nanotemper) by amine coupling in SEC buffer was successful (Figure 4.10A) and DMSO concentrations up to 4% (v/v) were well tolerated for thermophoresis measurements (Figure 4.10C and 4.10D). Binding of Suramin was then tested and notably, Suramin altered the initial fluorescence measured before applying the IR laser (Figure 4.11A and 4.11C). It has to be evaluated if a change in the initial fluorescence induced by a ligand is the result of a binding event. Non-specific effects such as ligand-induced protein aggregation or loss of material have to be excluded. This is achieved by denaturing the protein and thus disrupting the protein-ligand interaction. The fluorescence intensity in the target and complex sample will be equal after denaturation. Similarly, auto-fluorescence of ligands has to be ruled out. Enhancement of the initial fluorescence by Suramin was found to be the result of a binding event as assessed by the denaturation test and test for auto-fluorescence (Figure 4.11B). MST raw traces are found in the Appendix (Figure 4.22). Binding of PH002 and EZ-482 could not be confirmed by MST. However, ligand-induced fluorescence was seen with GIND-25 (Appendix Figure 4.22).

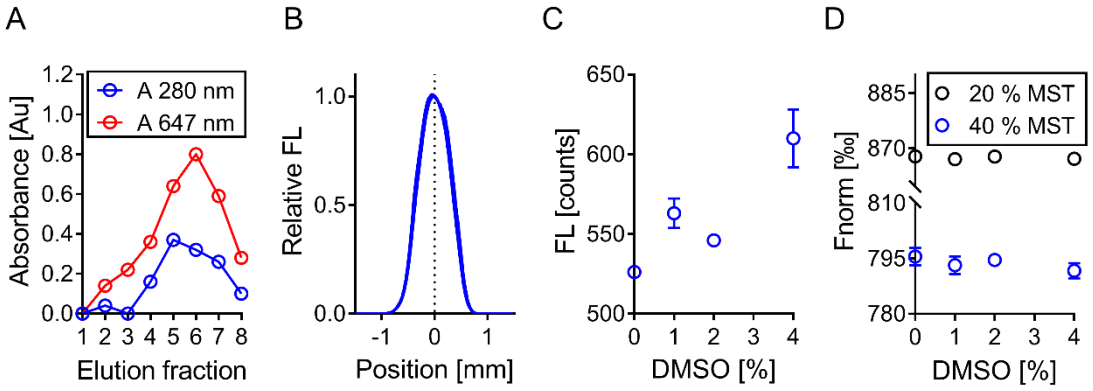

Figure 4.10. MST assay development. (A) After labelling of ApoE4 with the amine reactive dye, the protein was separated from free dye by SEC. The elution profile is shown as a function of absorbance at 280 nm (protein) and 647 nm (dye) versus elution fraction. Fractions 5-6 showed highest levels of ApoE4 and were pooled in this example for MST binding studies. **(B)** The fluorescence scan across four capillaries is shown. Relative fluorescence (FL) is normally distributed which suggests no binding of ApoE4 to the glass capillaries in the optimized MST buffer. **(C)** The initial measured FL is shown as a function of DMSO concentration. An increase in initial FL is visible at 4% (v/v) DMSO. **(D)** Thermophoresis (Fnorm) induced by 20% and 40% IR laser power is shown as a function of DMSO concentration. DMSO does not affect thermophoresis of ApoE4.

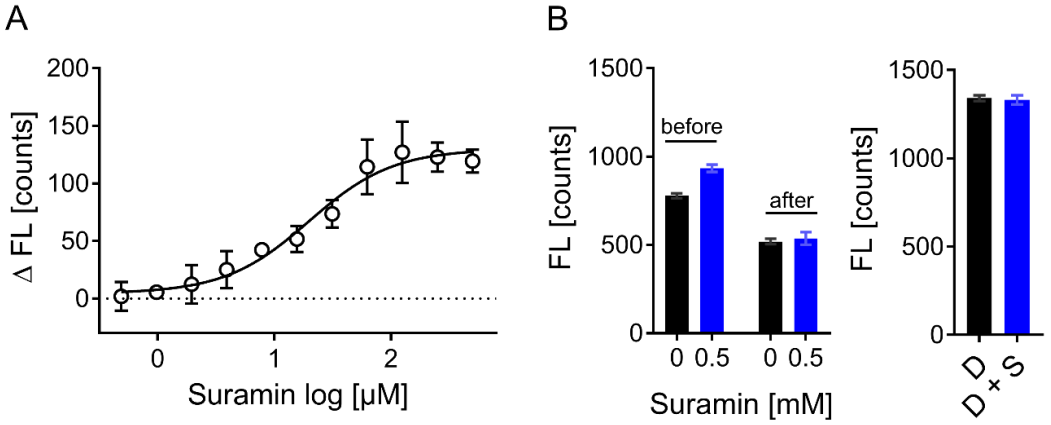

Figure 4.11. MST Suramin concentration response. (A) The initial fluorescence (FL) normalized to background (ΔFL) is shown as a function of Suramin concentration. Suramin enhances the initial FL in a concentration-dependent fashion. A mean binding affinity of (± SD) 28 ± 8 µM was calculated. **(B)** The Suramin-induced enhancement of FL is specific. Shown in the left panel is the FL before and after denaturing ApoE4 and the ApoE4-Suramin complex. The right panel demonstrates no autofluorescence of 500 µM Suramin (S) in the presence of 40 nM dye (D).

Lastly, binding of Suramin to ApoE4 was tested by ITC and the standard procedure (i.e. Suramin in syringe, ApoE4 in the sample cell) was evaluated against reverse ITC (i.e. ApoE4 in the syringe, Suramin in the sample cell). No difference in Suramin binding affinity was determined using both methods (Figure 4.12). Reverse ITC was selected as screening compounds that were identified (Section 4.3.3) had only moderate solubility. Because compound concentrations were kept low in the reverse procedure, their aggregation or precipitation from solution was avoided. Slight background heats were observed when injecting ApoE4 into buffer only that were subtracted during data analysis (Appendix Figure 4.23).

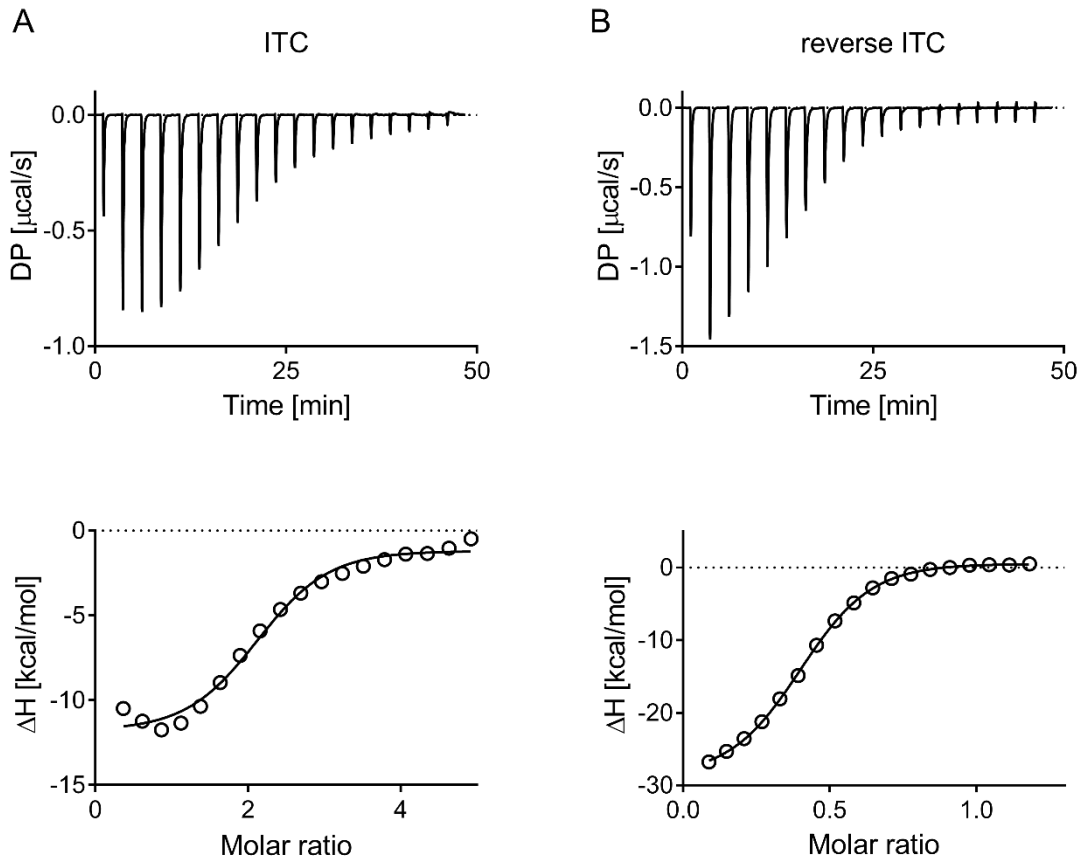

Figure 4.12. Binding of Suramin to ApoE4 evaluated by ITC. The upper panels show the raw titration heats, the lower panels are the normalized binding heats with the solid line representing nonlinear least square fits using the single-site binding model. **(A)** Injection of 500 µM Suramin into 20 µM ApoE4. **(B)** Injection of 300 µM ApoE4 into 50 µM Suramin. Binding affinities (± SD) of 5.0 ± 1.0 µM and 3.0 ± 0.4 µM were calculated respectively. DP – differential power (i.e. the power that is required to maintain the reference cell at equal temperature to the sample cell).

4.3.3 Screening identifies 59 compounds as ApoE4 binders

The NIH clinical collection (707 drugs) was screened against ApoE4 at 100 µM in two separate runs. The NIH clinical collection was selected as screening library due to the clinical history and diversity of compounds. Additionally, the small size of the library made the compound collection an optimal choice for a screening trial. Suramin was used as a positive control and at concentrations of 150 µM and 5 mM produced a mean response measured as shifts in reflected wavelength of 53 ± 11 and 146 ± 17 pm respectively (Figure 4.13A). All plates had a Z' above 0.5 (mean Z' values of 0.66 ± 0.05 and 0.82 ± 0.04 when using Suramin as a positive control at concentrations of 150 µM and 5 mM respectively) and were all included in data analysis (Figure 4.13B). Shift signals were normally distributed in both runs (Appendix Figure 4.24). Wells with low ApoE4 immobilization levels (< 1800 pm) were excluded from data analysis and in total, 5 wells out of 1920 had to be excluded (Figure 4.13C).

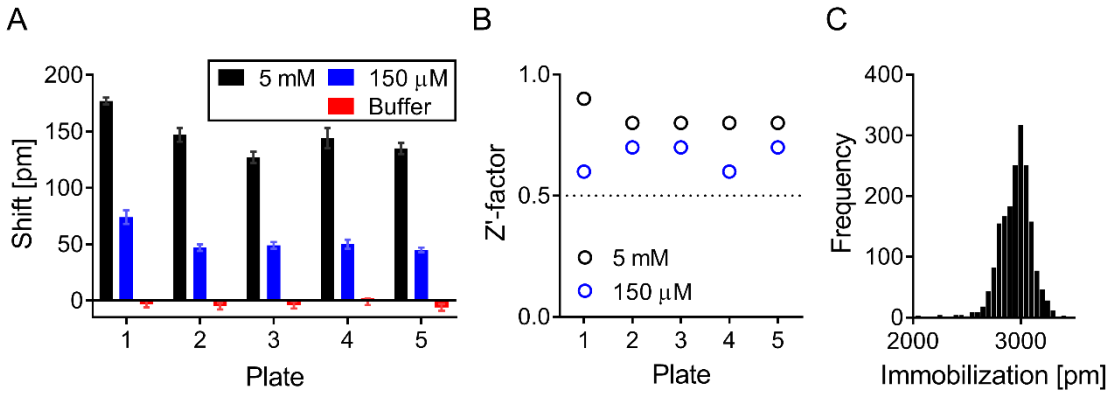

Figure 4.13. Screening statistics. Suramin at 5 mM and 150 µM was used as positive control and buffer as negative control during screen. **(A)** Suramin gave a mean shift (± SD) of 146 ± 17 pm and 53 ± 11 pm at 5 mM and 150 µM respectively. **(B)** Z'-factors across all plates were > 0.5. **(C)** The majority of wells had high ApoE4 immobilization levels with mean ± SD immobilization levels of 2921 ± 86 pm. Only five biosensors had low ApoE4 immobilization levels (< 1800 pm) and were excluded from data analysis.

Out of the 707-compounds screened, 59 compounds met the criterion to be considered a hit (i.e., response greater than 5-fold above the median absolute deviation of the sample median; Figure 4.14A). Due to a production issue which limited the availability of Corning® Epic® plates, 45 out of the 59 compounds were prioritized based on quantitative response and chemical attractiveness and tested by concentration response on the Corning® Epic®. Fourteen of these hits gave full or partial binding curves (Figure 4.14C and Appendix Figure 4.25) and were further evaluated in the secondary assays. Compounds were soluble and did not precipitate at 100 µM. Surprisingly, steroid-like compounds Ethylestrenol and Ethynylestradiol were initially identified as hits, however, gave no binding signal in the follow-up concentration-response study (data not shown).

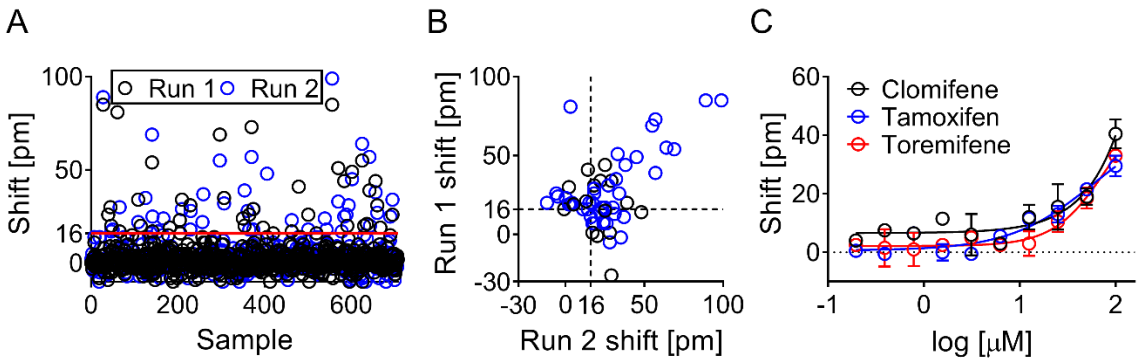

Figure 4.14. Screening and hit identification on the Corning® Epic®. (A) Hit threshold was set to five times the median absolute deviation (MAD) and a shift above 16 pm was considered a hit. In total 59 compounds met criteria to be considered a hit and their correlated shifts from both runs are shown in panel **(B)**. 45 of these hits indicated as blue circles in **(B)** were prioritized and tested by 10-point concentration response on the Corning® Epic® with a top concentration of 100 µM. 14 compounds returned with beginning binding curves and examples are shown in panel **(C)**. The remaining binding curves are found in Appendix Figure 4.25.

4.3.4 Evaluation of screening hits by MST and ITC confirms six drugs

The hits identified by the initial screening in the Corning® Epic® assay were next evaluated by MST. Three hits altered thermophoresis of ApoE4 in a concentration-dependent fashion and five altered the measured initial fluorescence (Figure 4.15). Affinities were determined to be in the micromolar range (Table 4.1) and some of these drugs such as Clomifene, Tamoxifen and Toremifene share structural features. One confirmed hit, Hydroxyzine pamoate, contained Pamoic acid as a counter ion. It was of interest to determine as to whether Hydroxyzine itself causes the quenching in initial fluorescence or Pamoic acid. Binding of Hydroxyzine dihydrochloride and Pamoic acid was therefore tested and Pamoic acid was found to be responsible for the response (Figure 4.15D). Quenching or enhancement of initial fluorescence by the hits was found to be binding-specific as assessed by the denaturation test and test for auto-fluorescence (Figure 4.16). Raw MST traces are found in the Appendix (Figure 4.26).

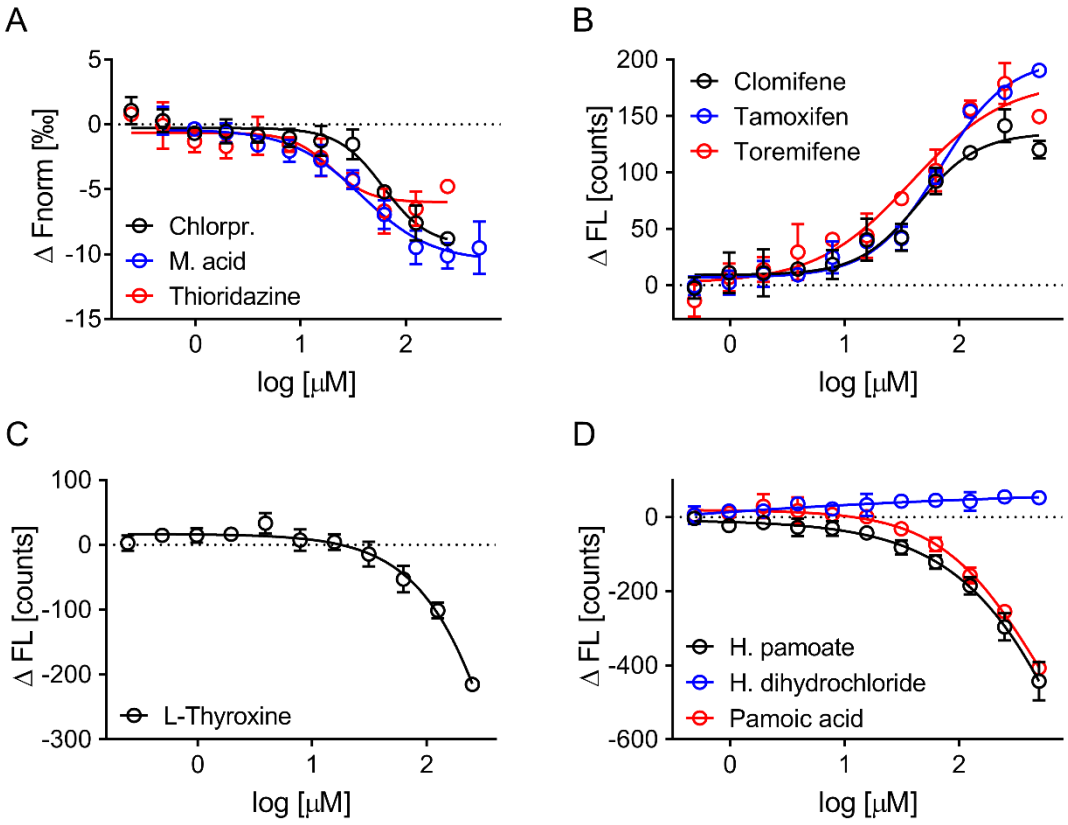

Figure 4.15. Hit confirmation by microscale thermophoresis. Hits were tested by concentration response from 500 or 250 µM. **(A)** Three out of these eight hits did alter thermophoresis without affecting the initial fluorescence (Chlorpromazine, Meclofenamic acid, Thioridazine), **(B)** three increased the initial fluorescence (Clomifene, Tamoxifen, Toremifene) and **(C and D)** two reduced the initial fluorescence (L-Thyroxine, Hydroxyzine pamoate) in a concentration dependant fashion. **(D)** Pamoic acid and not Hydroxyzine is responsible for the reduction in initial fluorescence. Data is expressed as the mean ± SD of three independent experiments.

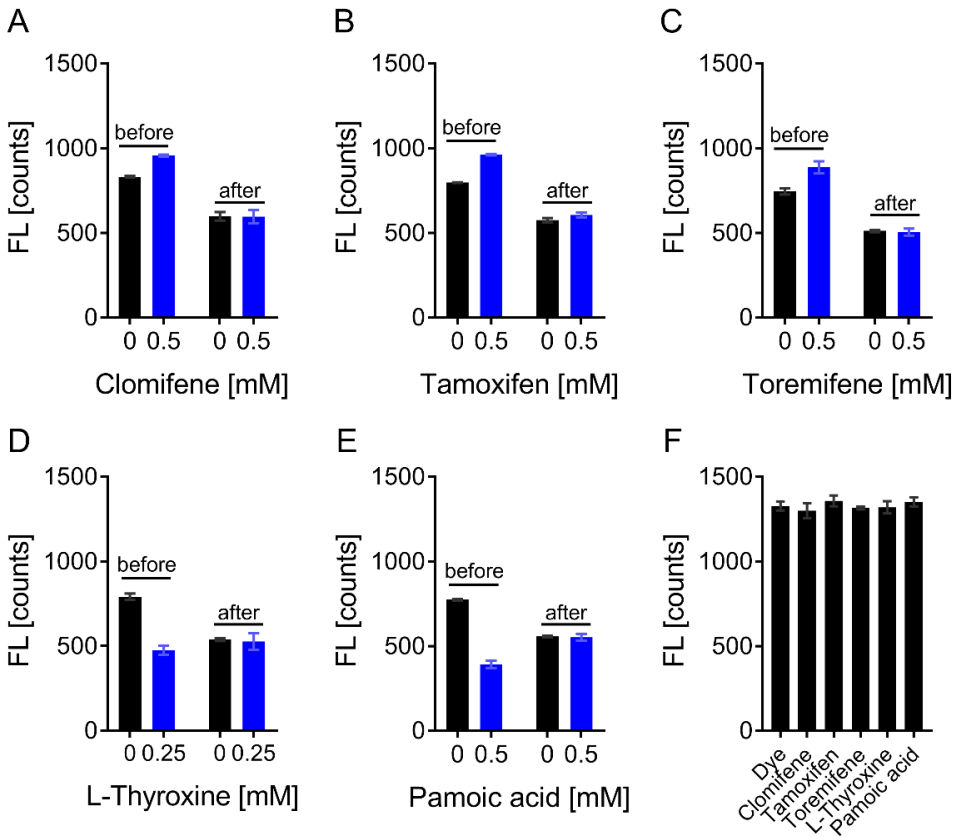

Figure 4.16. Microscale thermophoresis denaturation studies and compound auto-fluorescence. For compounds that altered initial fluorescence a denaturation test was performed, as well as tested for auto-fluorescence. Shown is the initial fluorescence before and after denaturation in the absence and presence of **(A)** Clomifene, **(B)** Tamoxifen, **(C)** Toremifene, **(D)** L-Thyroxine and **(E)** Pamoic acid. **(F)** Compounds were also tested for auto-fluorescence in the presence of fluorescence dye without protein. Compounds do not influence the fluorescence signal of the dye. Data are expressed as the mean ± SD of three independent experiments.

Finally, the eight hits identified by screening on the Corning® Epic® and confirmed by the orthogonal MST assay were tested by ITC and six drugs were confirmed (Figure 4.17 and Appendix Figure 4.28) whereas the binding of Thioridazine and Chlorpromazine to ApoE4 could not be confirmed. As already observed in the MST binding studies, some of the hits share structural features. Tafamidis that binds to the L-Thyroxine binding site in transthyretin (a transport protein of the thyroid hormone) (447) was therefore purchased and its binding to ApoE4 was confirmed (Figure 4.17B). Additionally, binding of all six hits and Tafamidis by ITC was tested against ApoE2 and ApoE3 and similar binding to all ApoE isoforms was observed (Appendix Figures 4.28 to 4.31). Interestingly, no binding of the hits to ApoE4$_{1\text{-}191}$ could be measured (Appendix Figure 4.32) which suggests the importance of tertiary/quaternary structure or that identified drugs bind to the carboxyl terminus of ApoE.

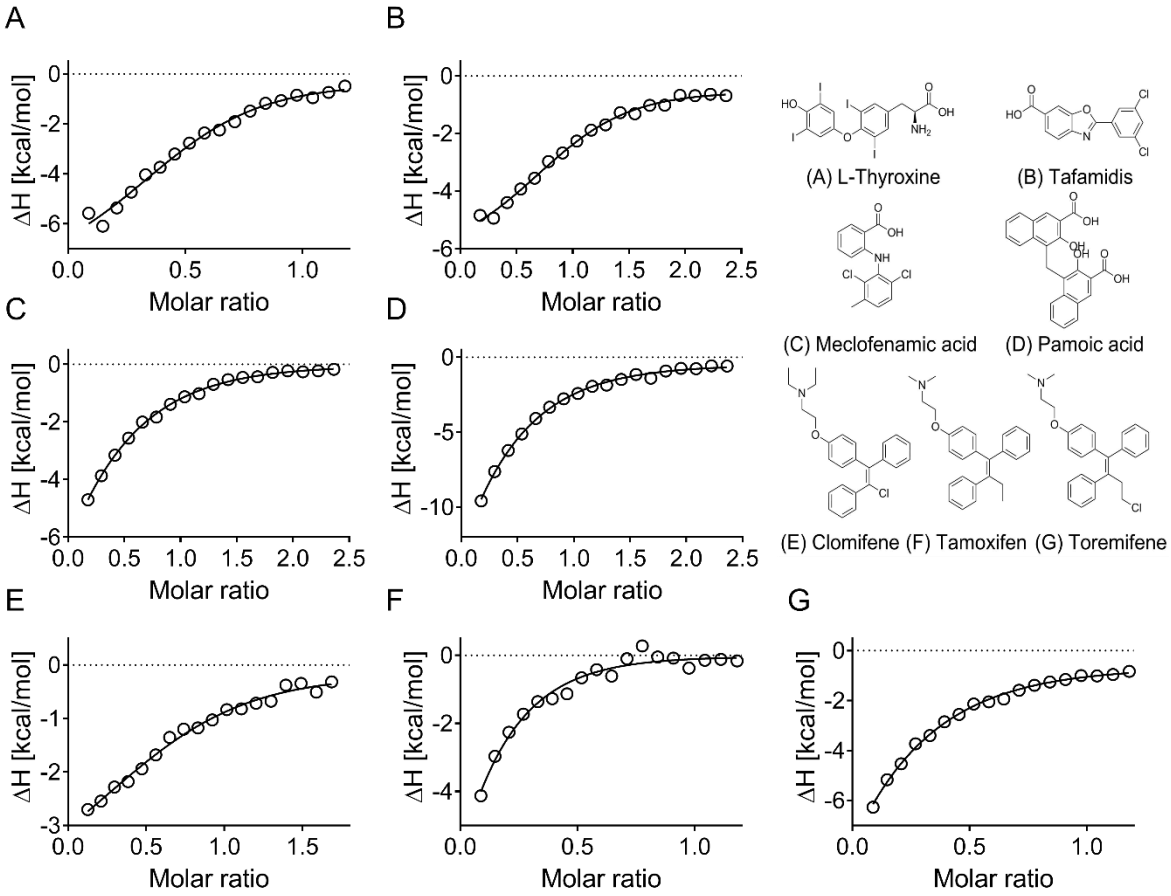

Figure 4.17. Hit confirmation by isothermal titration calorimetry. All eight hits successfully tested by MST were finally probed by ITC and six could be confirmed. Binding curves could not be fully resolved of a majority of hits due to binding affinities being in micromolar range. Binding to ApoE4 was confirmed for **(A)** L-Thyroxine, **(B)** its compound analogue Tafamidis, **(C)** Meclofenamic acid, **(D)** Pamoic acid, **(E)** Clomifene, **(F)** Tamoxifen and **(G)** Toremifene. Isotherms of raw titration are shown in Appendix Figure 4.28. Figures show the normalized binding heats with the solid line representing nonlinear least square fits using the single-site binding model.

Table 4.1. Binding affinities determined by MST and ITC.

	ApoE4		ApoE2	ApoE3
	MST [μM]	ITC [μM]	ITC [μM]	ITC [μM]
L-Thyroxine	✓	18 ± 12	33 ± 10	20 ± 3
Tafamidis	-	8 ± 2	6 ± 2	8 ± 1
Meclofenamic acid	51 ± 12	45 ± 13	47 ± 32	47 ± 9
Pamoic acid	✓	38 ± 4	55 ± 14	119 ± 50
Clomifene	44 ± 2	15 ± 10	67 ± 36	24 ± 9
Tamoxifen	67 ± 19	✓	✓	✓
Toremifene	44 ± 6	✓	✓	✓

✓ denotes that binding was confirmed, however, binding affinity could not be determined accurately.

4.4 Discussion

The aim of this study was to identify novel ApoE4 binders using a biophysical approach. Biophysical techniques have become key components of the drug discovery process and are routinely used for hit identification and/or confirmation (448). However, these techniques can be limited by the amount of protein required, sample preparation and throughput. The Corning® Epic® label-free assay measures a change in wavelength of refracted light when an analyte binds to a target that was immobilized on a biosensor (439). The technique is very sensitive and affinities in the nanomolar range can be determined. Micrograms of material is required and the 384-well plate format allows screening in an high throughput format. However, buffers must be well matched for additives and solvents that will otherwise result in artificial signals. Due to the limitations of individual biophysical methods, validation of hits by orthogonal assays, in the present study MST and ITC, are often used to increase the confidence in identifying protein-ligand interactions. MST monitors movement of molecules in a temperature gradient with this movement being tracked by a fluorophore that is covalently coupled to the molecule. The interaction of two molecules (e.g. drug binding to protein) will alter this movement and can therefore be used to detect binding (440). MST requires nanograms of material and thermophoresis curves can give information on unspecific effects such as ligand-induced protein aggregation. Although automated systems are available, the non-automated capillary-based system used in the present study only allows low throughput (up to 16 samples at a time) and additional validation steps may be required if extrinsic labelling is used. Finally, ITC can provide additional information on thermodynamic parameters and binding stoichiometry. High protein consumption and low throughput limit ITC to hit validation (448). It is for these various reasons that the Corning® Epic® was used for hit identification, and MST, as well as ITC used as orthogonal assays for hit validation (Figure 4.1).

Surprisingly, no binding of described structure correctors PH002 and EZ-482 to ApoE4 was observed during assay development. These compounds generally showed poor solubility that resulted in negative binding responses on the Corning® Epic® (Figure 4.7) and no change in thermophoresis (Appendix Figure 4.22 C-E). These results contradict previous observations that confirmed binding of PH002 and EZ-482 to recombinant, lipid-free ApoE by hydrogen−deuterium exchange and mass spectroscopy (HDX MS), as well as EPR (246, 445). As high concentrations of compounds were used in the previous studies, the observed binding effects may have been unspecific or due to compound aggregation.

The NIH clinical collection of 707 chemically-diverse drugs that all have a history of clinical use or entered clinical trials was screened against ApoE4. Suramin was used as a positive control, although it is neither a specific nor selective ApoE binder and has been shown to interact with many other proteins (449–451). Initially, 59 drugs were identified that bind to ApoE4 resulting

in a relatively high hit rate of 8%. MST proved a powerful secondary assay for confirmation studies and reduced the number of hits to eight compounds (1.1% hit rate). Using the MST, Pamoic acid was identified to be binding to ApoE4 instead of Hydroxyzine, which was the presumed “active” constituent of Hydroxyzine pamoate. Similar observations were made by Zhao *et al* (452) who screened for novel agonists of the orphan receptor GPR35. In their primary screen they identified Oxantel pamoate as an agonist for GPR35, however, subsequent testing with related compounds and Pamoic acid revealed the latter to be responsible for the agonist activity. Although Pamoic acid does not bind with high affinity to ApoE, these results, as well as those of Zhao and colleagues (452), emphasize how the counterion can be the active component and need to be tested in terms of screening (453).

Six out of eight drugs could be confirmed by ITC. All hits besides Pamoic acid are in clinical use and include a hormone (L-Thyroxine), three SERMs (Clomifene, Tamoxifen, Toremifene) and one NSAID (Meclofenamic acid). Binding of L-Thyroxine to ApoE has been previously reported using a radio-ligand binding assay (454, 455) with binding affinities in micromolar range. Interestingly, binding of L-Thyroxine in the radio-ligand assay was shown to be inhibited by Meclofenamic acid (455) which may suggest a shared binding site(s). In contrast to the previous studies (454, 455), no binding of L-Thyroxine, nor Meclofenamic acid could be confirmed to the amino terminal domain, however, binding of Tafamidis that shares chemical features of L-Thyroxine was confirmed. Notably, the interaction of SERMs to ApoE was observed. SERMs are agonists or antagonists of the estrogen receptor and have been considered as a possible treatment for women with AD. However, it is still a matter of debate if hormone therapy and SERMs have beneficial effects on cognitive function and clinical studies came to inconsistent results (456, 457).

The hits identified in the present study do not show selectivity for ApoE4 versus ApoE2 and ApoE3 and binding to all ApoE isoforms with similar affinities was confirmed by ITC. This indicates that ApoE isoforms share structural features and that compounds bind to conserved binding sites. Affinities are in the micromolar range (Table 4.1) and it was therefore not possible to accurately determine stoichiometry for a number of hits. This was most notable with Tamoxifen and Toremifene for which it was only possible to confirm binding by ITC but, the binding affinities could not be measured. Despite being non-selective, the identified compounds might alter ApoE function and may have beneficial effects such as on ApoE lipidation and expression, although this remains to be determined. Moreover, they provide chemical starting points for medicinal chemistry efforts for further optimization to attempt to identify isoform-selective binders.

4.5 Appendix Chapter 4

The target protein is immobilized to the Corning® Epic® biosensor via amine coupling. The biosensor surface is coated with a hydrophilic carboxymethylated polymer that is activated with the EDC crosslinker and sulfo-NHS (Figure 4.18). The free amines of the protein have to be uncharged to react with the activated ester (458). ApoE4's theoretical isoelectric point calculated by using the ProtParam webtool (459) is 5.65 and experimentally, ApoE isoforms focus with isoelectric points between pH 5.3 and 5.8 (109). Hence, ApoE4's overall charge will be neutral at pH 5.6 that will promote amine coupling to the biosensor.

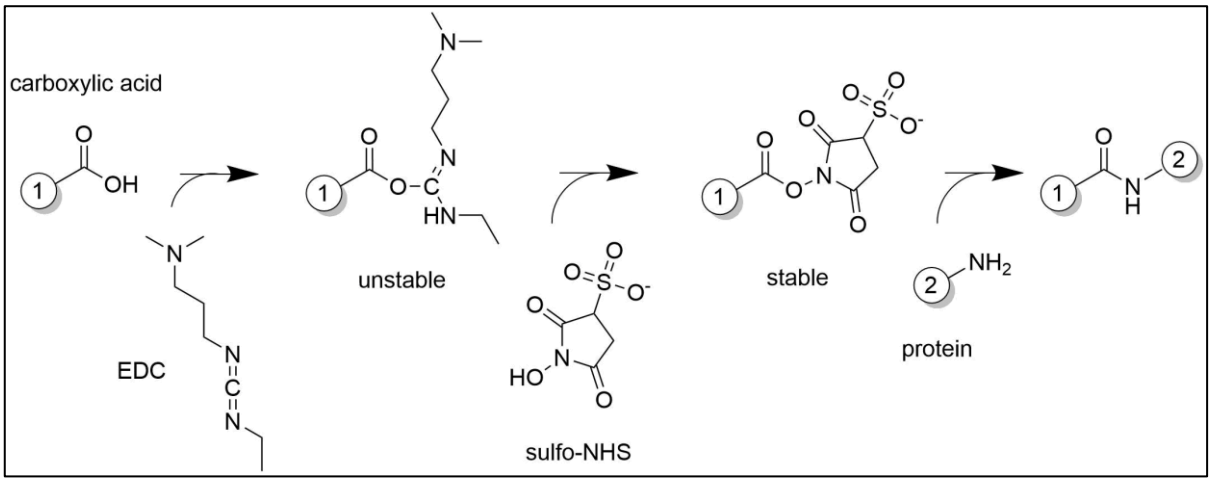

Figure 4.18. Amine coupling to the Corning® Epic® biosensor. The carboxyl moieties of the hydrophilic surface of the sensor are activated with EDC and sulfo-NHS to form stable amine-reactive sulfo-NHS esters. Protein is then covalently attached by its primary amine(s) (458).

As shown in Chapter 2, Section 2.3.6, ApoE4 is unstable in solution and degrades into ~22 kDa and ~10 kDa fragmentation products with time. It was therefore of interest to determine stability of ApoE4 in low pH buffers as ApoE4 was immobilized to the Corning® Epic® plates in 20 mM sodium citrate pH 5.6. ApoE4 visibly precipitated upon dilution into 20 mM sodium acetate pH 5.5 and notably, its elution pattern is altered in a sodium acetate buffer compared to sodium citrate and SEC buffer (Figure 4.19).

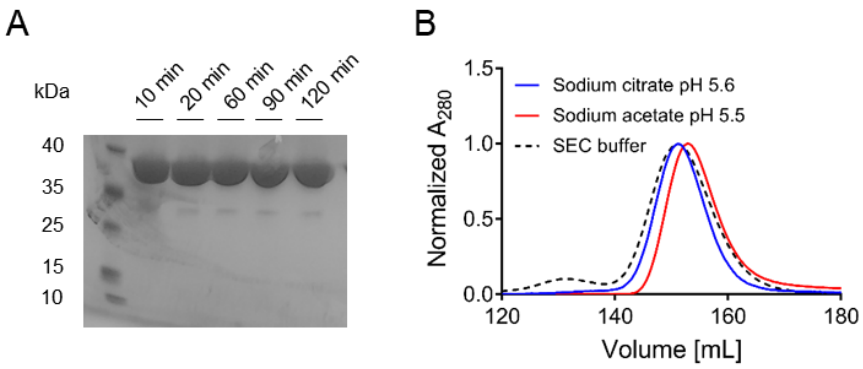

Figure 4.19. Stability and elution of ApoE4 at low pH. (A) Stability of ApoE4 at 1 mg/mL was tested in 20 mM sodium acetate buffer pH 5.5. No fragmentation is observed over 2 h. **(B)** Elution patterns of ApoE4 in 20 mM sodium acetate, 150 mM NaCl pH 5.5 and in 20 mM sodium citrate, 150 mM NaCl, pH 5.6 is compared. ApoE4 was delivered at 5 mg/mL. Sodium chloride was added to prevent unspecific binding of ApoE4 to the resin of the HiLoad 26/600 Superdex 200 pg (GE Healthcare) column. Elution of ApoE4 in sodium acetate pH 5.5 is shifted to a higher retention volume which suggests compaction of ApoE4.

It is crucial to optimise the MST assay buffer to prevent association of the protein to the glass surface of the capillary. Binding of proteins to the capillaries is identified during capillary scan. Homogenous distribution of the protein within the capillary will result in a bell-shaped fluorescence signal; inhomogeneous distribution on the other hand will result in distorted signals (Figure 4.20).

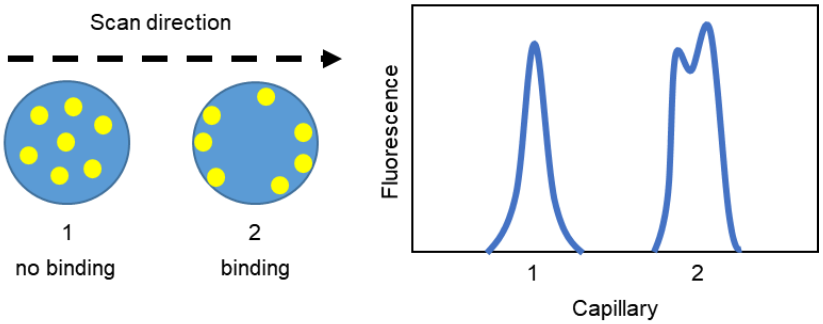

Figure 4.20. Protein association to MST capillaries. Capillaries are scanned from left to right and the fluorescence of the labelled protein is measured across the capillary. If the protein does not bind to the capillary, the fluorescence signal will be bell-shaped. Highest fluorescence signal is measured in the middle of the capillary in this case. If protein binds to the glass surface, the signal will be distorted due to inhomogeneous distribution of the protein.

Behaviour of ApoE4 in MST capillaries at varying concentrations (20, 40, 80 and 100 nM) was tested in PBS, PBS + 0.1% (v/v) Triton-X 100, SEC buffer (not shown) and a modified SEC buffer (20 mM HEPES, 500 mM NaCl, 10% (v/v) glycerol, ± 0.1% (v/v) Triton X-100, pH 8.0). Substantial binding to the capillaries was seen in PBS ± Triton X-100, whereas no binding in the modified SEC buffer with Triton X-100. Addition of detergent also increased the fluorescence signal. This suggests that ApoE4 in buffers without detergent bound to the test tubes during sample preparation and hence material was lost (Figure 4.21).

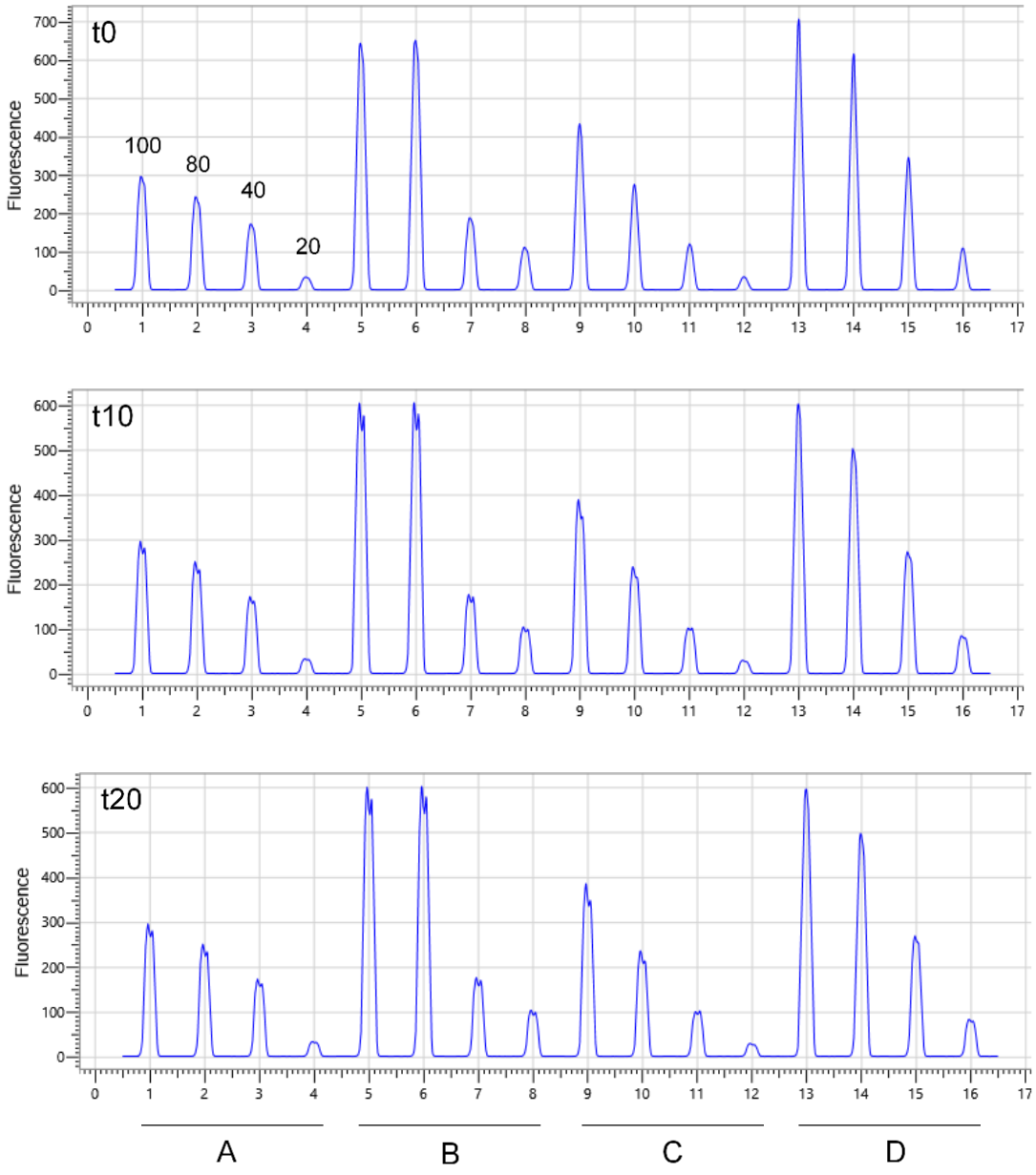

Figure 4.21. Scans of capillaries containing labelled ApoE4 in varying buffers. ApoE4 at 100, 80, 40 and 20 nM was left in standard MST capillaries over 20 min in **(A)** PBS, **(B)** PBS + 0.1% (v/v) Triton X-100, **(C)** 20 mM HEPES, 500 mM NaCl, 10% (v/v) glycerol, pH 8.0, or **(D)** 20 mM HEPES, 500 mM NaCl, 10% (v/v) glycerol, 0.1% (v/v) Triton X-100, pH 8.0 (MST assay buffer). Substantial binding to the capillaries over time was seen in buffers (A) – (C), no binding in buffer (D).

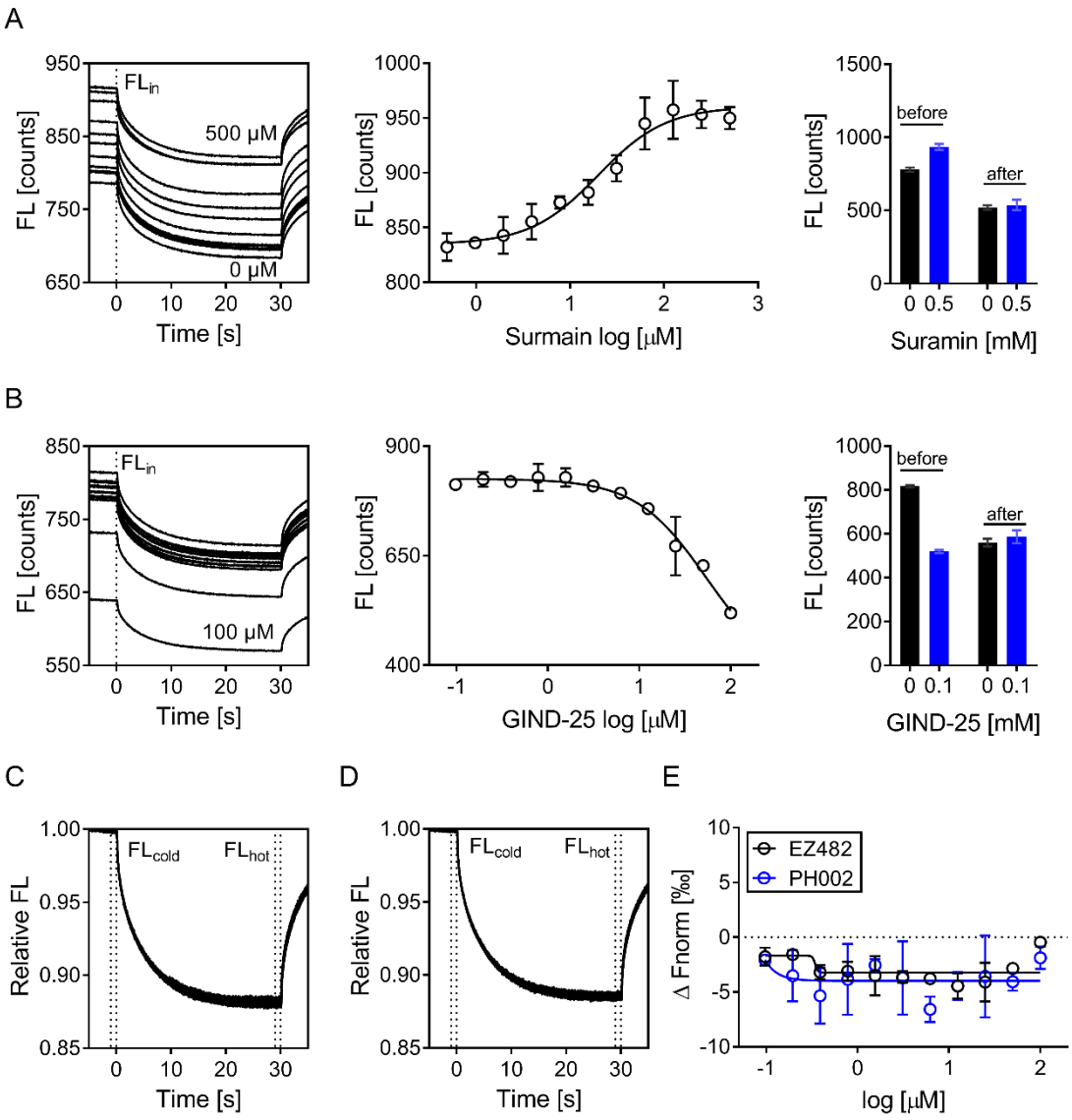

Figure 4.22. Suramin, GIND-25, PH002 and EZ482 MST traces. (A) Raw MST traces (left) in the presence of Suramin, the respective binding curve (middle) and the denaturation test (right) are shown. Suramin increased the initial fluorescence (FL_{in}) in a concentration dependent fashion. **(B)** Same plots are shown for GIND-25 that reduced the FL_{in} in a concentration dependent fashion. **(C)** Raw MST traces of PH002. **(D)** Raw MST traces of EZ482. PH002 and EZ482 did not alter FL_{in}, nor alter thermophoresis. Thermophoresis is calculated based on fluorescence measured before applying the IR laser (F_{cold}) and during steady state (F_{hot}). The normalized fluorescence ΔFnorm is the ratio F_{hot}/F_{cold} multiplied by a factor of 1000 (therefore yielding a fluorescence change in per thousand, ‰). **(E)** The normalized fluorescence is shown as a function of PH002 and EZ482 concentration. Data is expressed as the mean ± SD of three independent experiments.

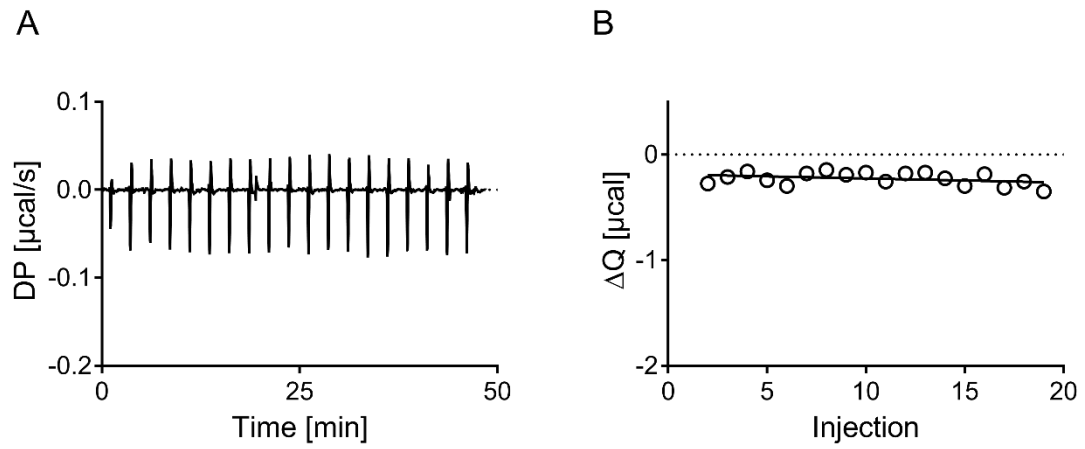

Figure 4.23. Titration of ApoE4 into buffer. (A) Shown are the raw isotherms of 300 µM ApoE4 titrated into PBS + 0.1% (v/v) Triton-X 100 + 2% (v/v) DMSO. **(B)** Integrated heats (µcal) are shown as a function of injection number. DP – differential power.

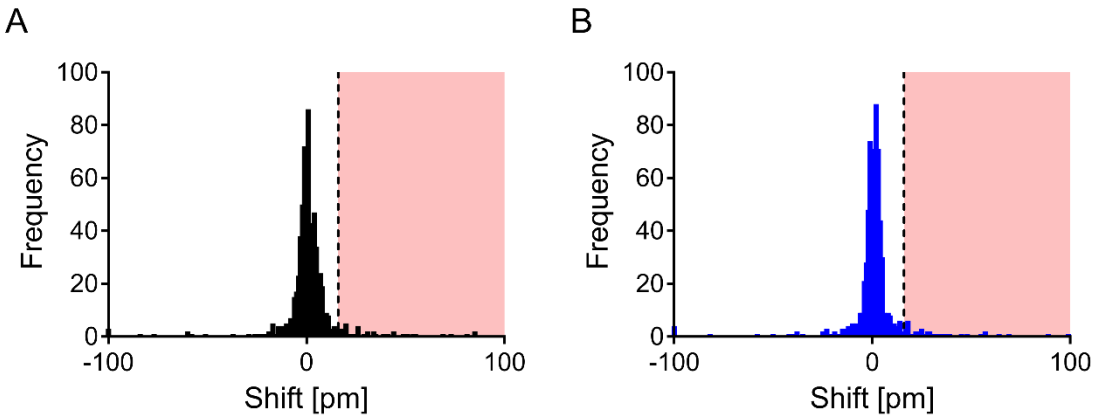

Figure 4.24. Screening response distribution. Shown is the number of compounds (frequency) as a function of response (in pm) for **(A)** screening run 1 and **(B)** screening run 2. Shift signals are normally distributed. Compounds with a response > 16 pm were considered a hit (red area).

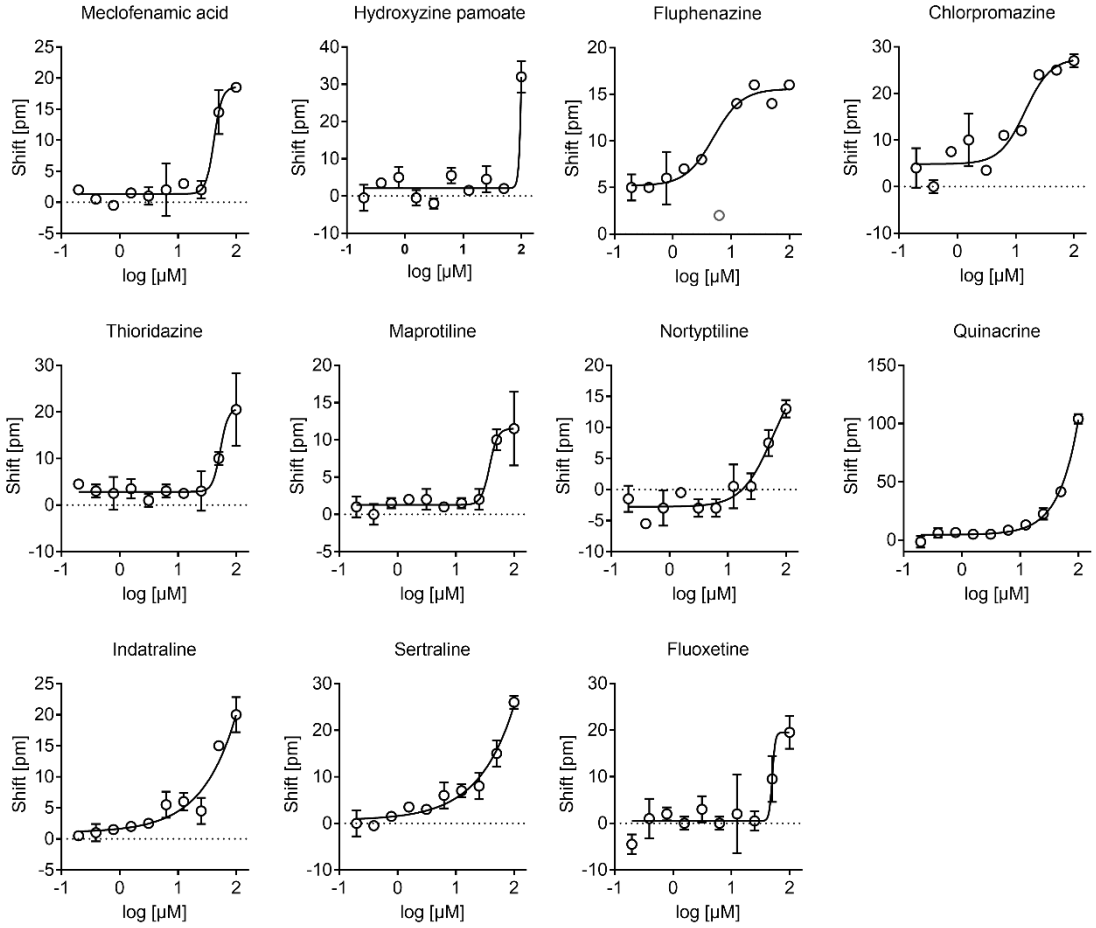

Figure 4.25. Confirmation of hits on the Corning® Epic®. Due to a production issue which limited the availability of Corning® Epic® plates, 45 out of the 59 compounds were prioritized based on quantitative response and chemical attractiveness and tested by concentration response on the Corning® Epic®. Fourteen of these hits gave full or partial binding curves that are shown here and in Figure 4.14C.

Hits were initially evaluated in form of 8-point concentration response by MST with a top concentration of 100 µM. If a compound did alter thermophoresis or initial fluorescence, the compound was obtained from a commercial vendor and re-tested in a 12-point concentration response. Out of the 14 compounds that were confirmed on the Corning® Epic®, three compounds did alter thermophoresis (Meclofenamic acid, Chlorpromazine, Thioridazine), three increased the initial fluorescence (Clomifene, Tamoxifen, Toremifene) and one decreased the initial fluorescence (Hydroxyzine pamoate). These compounds were purchased and re-confirmed by MST by 12-point concentration response as presented in Section 4.3.4 (Figure 4.15). Compounds that had to be excluded for evaluation on the Corning® Epic® due to plate production shortage (Section 4.3.3) were also tested by MST. Three compounds decreased the initial fluorescence (Figure 4.26) of which L-Thyroxine was eventually confirmed (Figure 4.15, Section 4.3.3).

In a secondary strategy, the hit threshold was decreased to three times the median absolute deviation of the sample median (hit threshold > 10 pm) to see if additional drugs could be identified by MST. None of the compounds significantly altered thermophoresis. One drug decreased the initial fluorescence, however, it could not be confirmed after repurchasing (Figure 4.26).

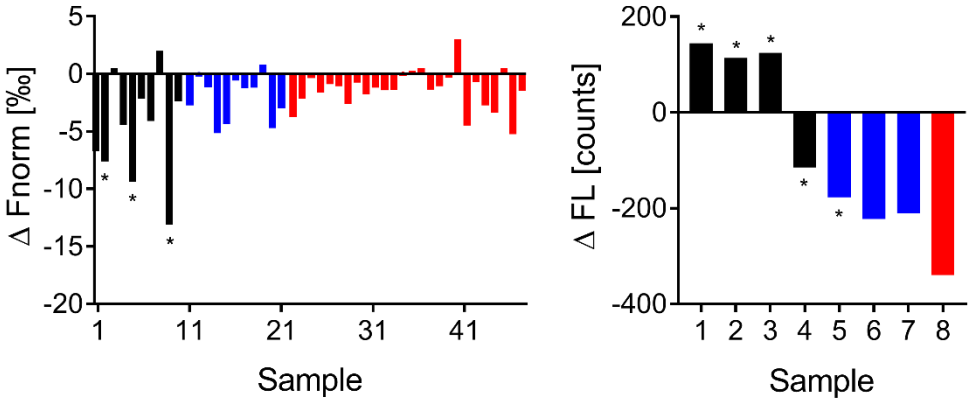

Figure 4.26. Evaluation of hits by MST. Shown is the mean signal of thermophoresis response (left panel) or initial fluorescence (right panel) of compounds at 100 µM from the 8-point concentration response. In black are the 14 compounds that were evaluated on the Corning® Epic® by concentration response. In blue are compounds that had to be excluded for evaluation on the Corning® Epic®. In red are novel compounds after setting the hit threshold to 3 x MAD. The asterisk (*) denotes hits that were eventually confirmed by 12-point concentration response and further evaluated by ITC.

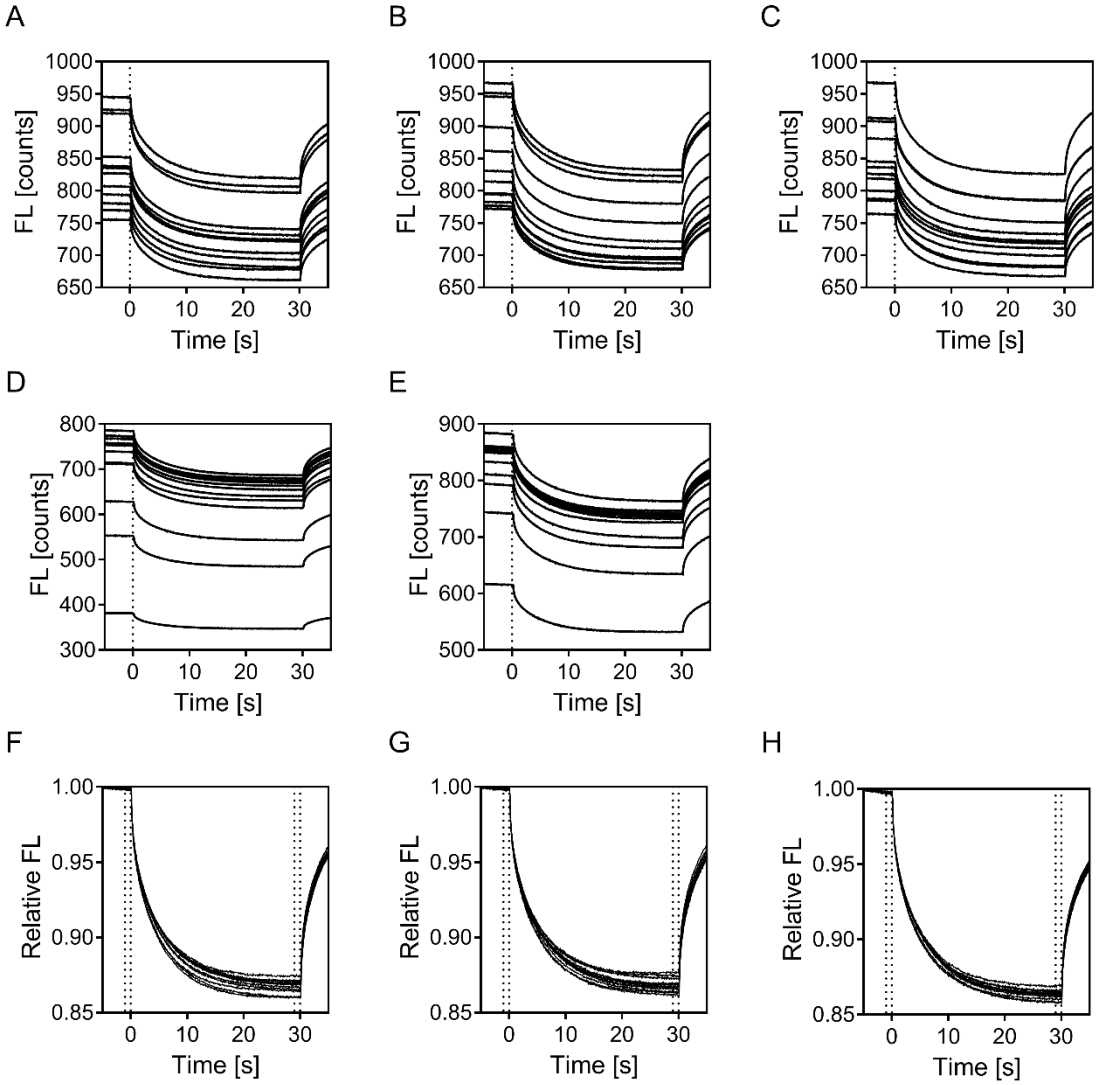

Figure 4.27. MST traces. Shown are the MST traces of **(A)** Clomifene, **(B)** Tamoxifen and **(C)** Toremifene that increased the measured initial fluorescence in a concentration-dependent fashion; **(D)** Pamoic acid and **(E)** L-Thyroxine that decreased the initial fluorescence; **(F)** Meclofenamic acid, **(G)** Chlormpromazine and **(H)** Thioridazine that altered thermophoresis. Fluorescence counts (FL) and thermophoresis (F_{norm}) are plotted as a function of time.

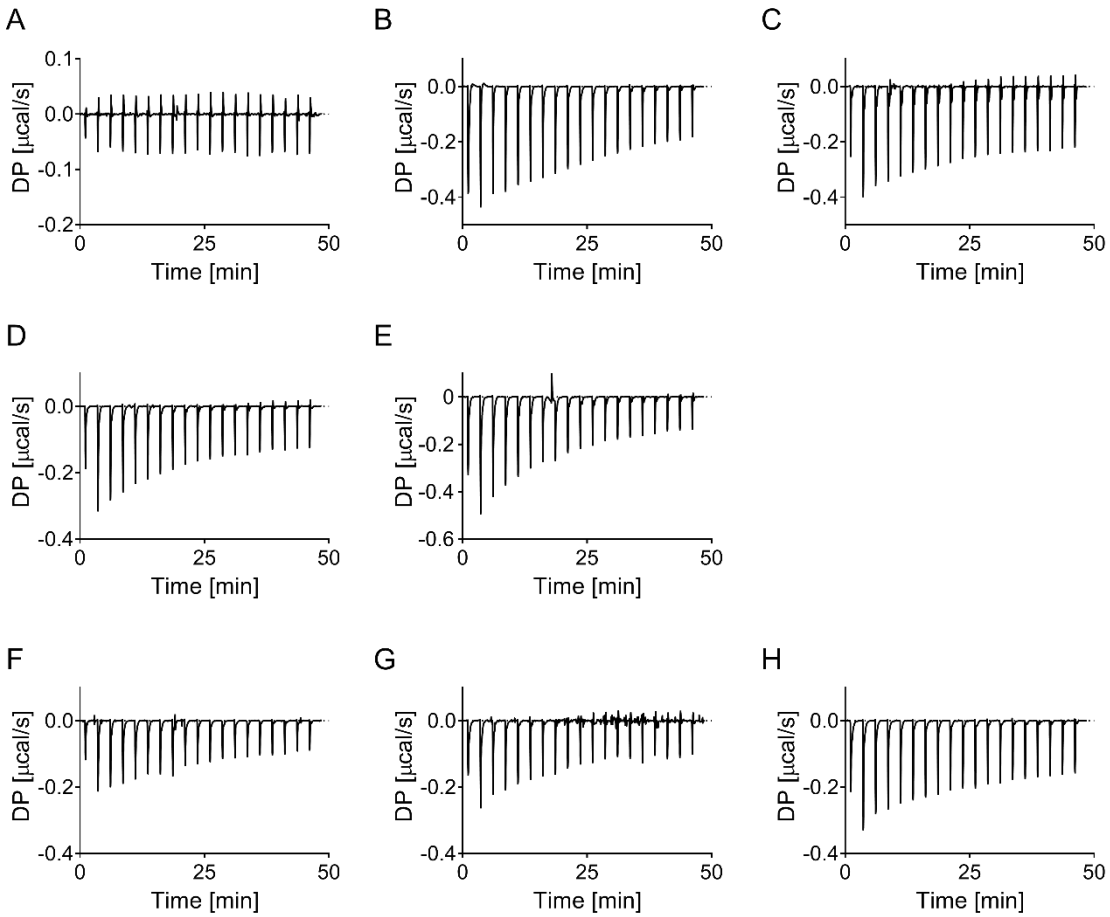

Figure 4.28. Isotherms of raw titration ApoE4. Shown are the isotherms of raw titration heat of 300 µM ApoE4 titrated into **(A)** PBS + 0.01% (v/v) Triton X-100 + 2% (v/v) DMSO, **(B)** 50 µM L-Thyroxine, **(C)** 25 µM Tafamidis, **(D)** 25 µM Meclofenamic acid, **(E)** 25 µM Pamoic acid, **(F)** 35 µM Clomifene, **(G)** 50 µM Tamoxifen and **(H)** 50 µM Toremifene.

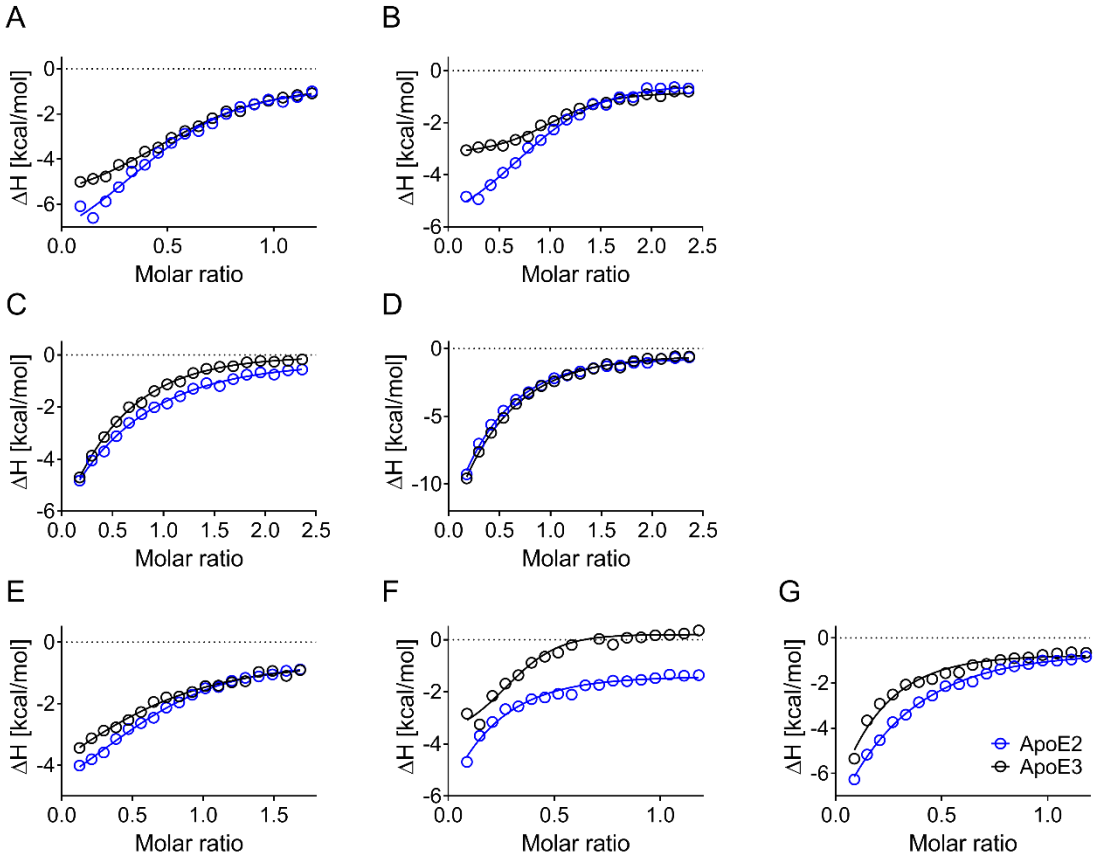

Figure 4.29. Hit confirmation by isothermal titration calorimetry. All confirmed hits were also tested against ApoE2 and ApoE3. Binding to ApoE2 and ApoE3 was confirmed for **(A)** L-Thyroxine, **(B)** its compound analogue Tafamidis, **(C)** Meclofenamic acid, **(D)** Pamoic acid, **(E)** Clomifene, **(F)** Tamoxifen and **(G)** Toremifene. Shown are the normalized binding heats with the solid line representing nonlinear least square fits using single-site binding model.

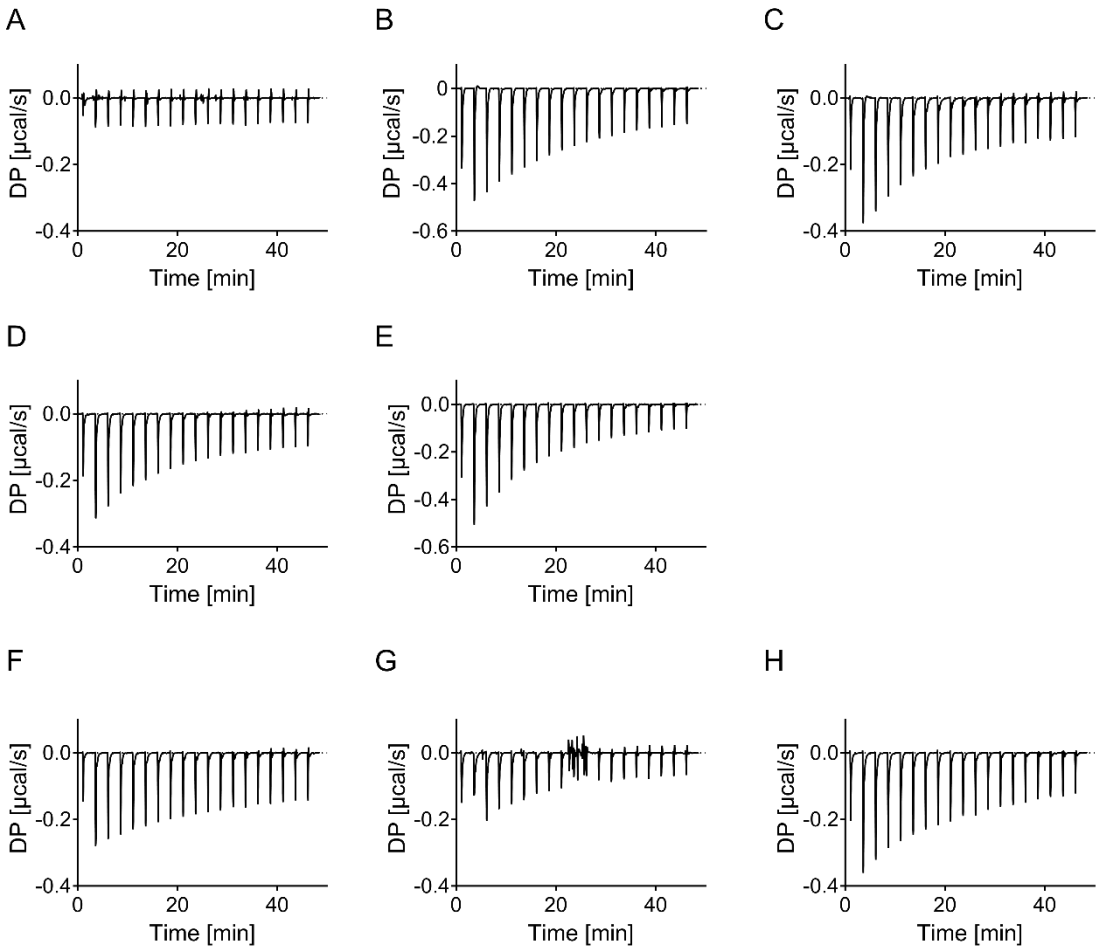

Figure 4.30. Isotherms of raw titration ApoE2. Shown are the isotherms of raw titration heat of 300 µM ApoE2 titrated into **(A)** PBS + 0.01% (v/v) Triton X-100 + 2% (v/v) DMSO, **(B)** 50 µM L-Thyroxine, **(C)** 25 µM Tafamidis, **(D)** 25 µM Meclofenamic acid, **(E)** 25 µM Pamoic acid, **(F)** 35 µM Clomifene, **(G)** 50 µM Tamoxifen and **(H)** 50 µM Toremifene.

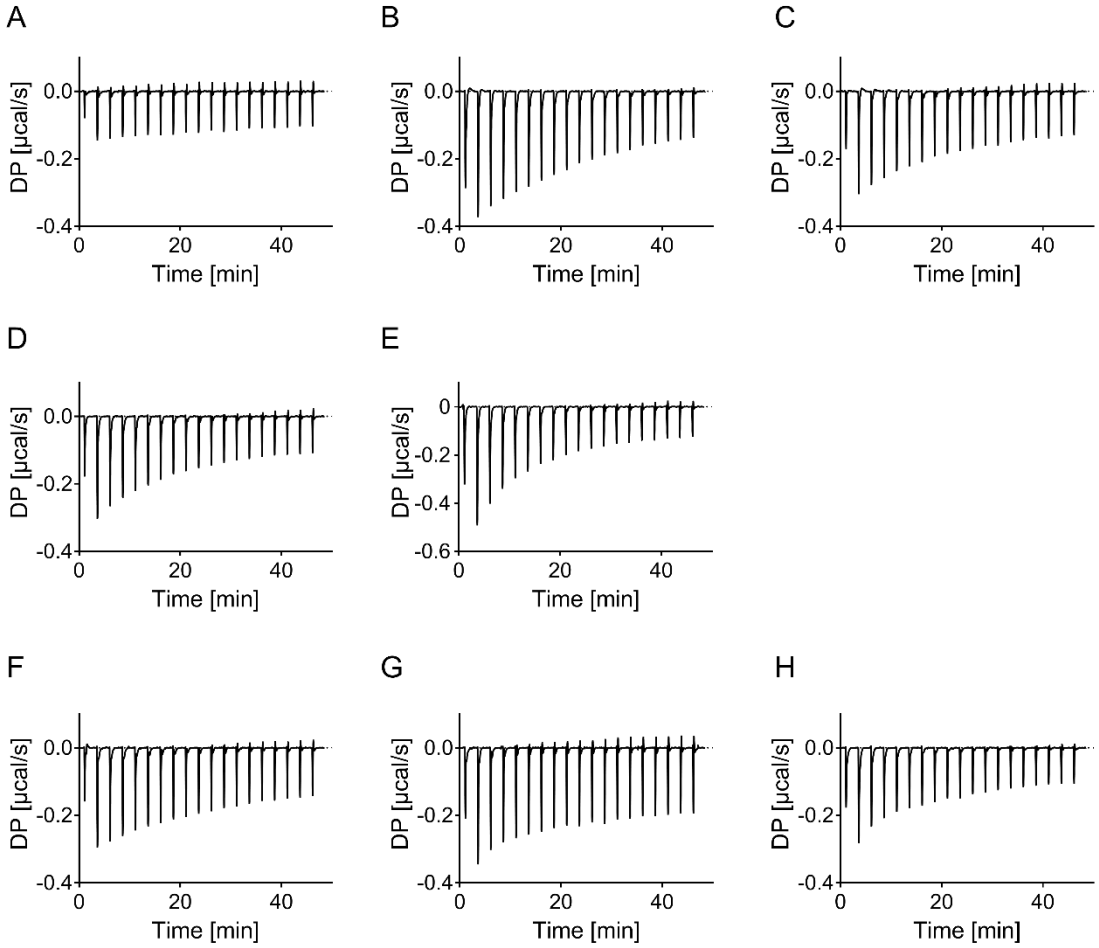

Figure 4.31. Isotherms of raw titration ApoE3. Shown are the isotherms of raw titration heat of 300 µM ApoE3 titrated into **(A)** PBS + 0.01% (v/v) Triton X-100 + 2% (v/v) DMSO, **(B)** 50 µM L-Thyroxine, **(C)** 25 µM Tafamidis, **(D)** 25 µM Meclofenamic acid, **(E)** 25 µM Pamoic acid, **(F)** 35 µM Clomifene, **(G)** 50 µM Tamoxifen and **(H)** 50 µM Toremifene.

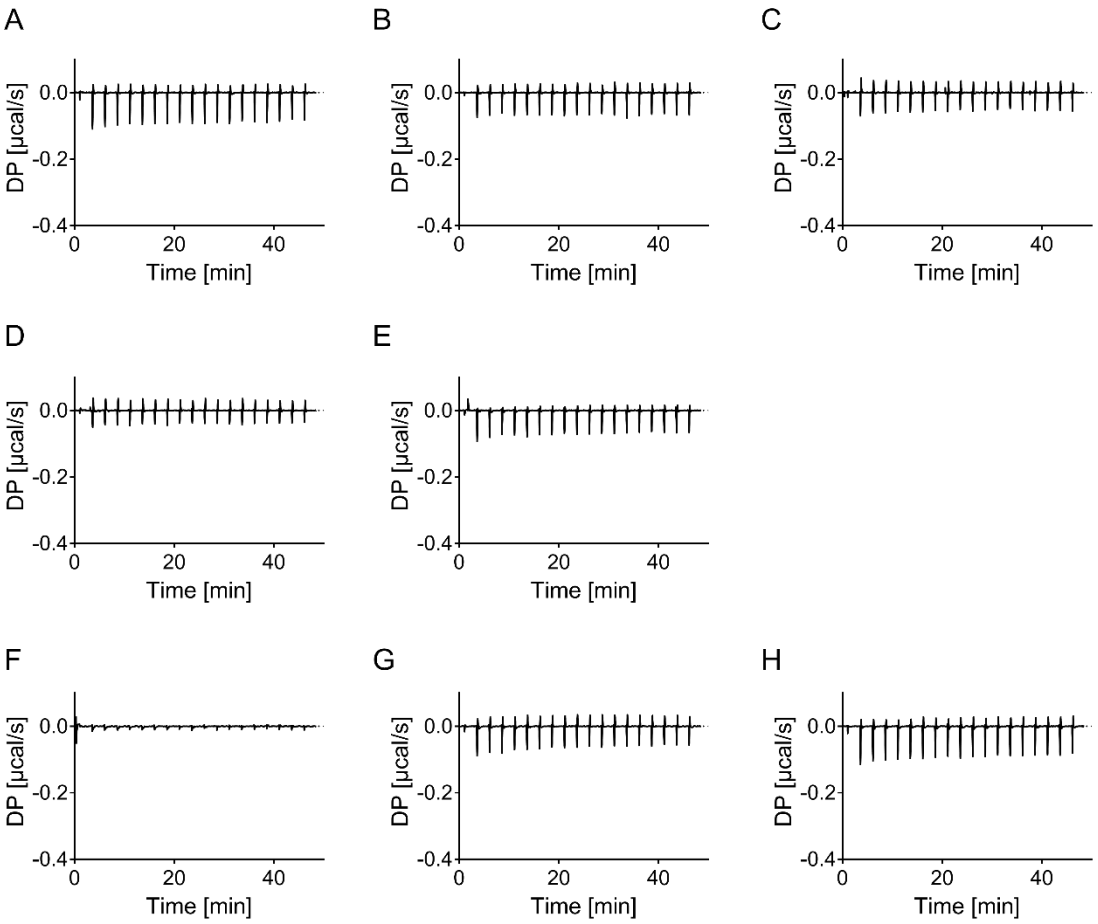

Figure 4.32. Isotherms of raw titration ApoE4$_{1-191}$. Shown are the isotherms of raw titration heat of 300 µM ApoE4$_{1-191}$ titrated into **(A)** PBS + 0.01% (v/v) Triton X-100 + 2% (v/v) DMSO, **(B)** 50 µM L-Thyroxine, **(C)** 25 µM Tafamidis, **(D)** 25 µM Meclofenamic acid, **(E)** 25 µM Pamoic acid, **(F)** 35 µM Clomifene, **(G)** 50 µM Tamoxifen and **(H)** 50 µM Toremifene.

5 CONCLUSIONS

As outlined in Chapter 1, the inheritance of the ε4 allele of the apolipoprotein E gene is an established risk factor for the late onset, most common form of AD and homozygote carriers of the ε4 allele have up to a 12-fold greater risk of developing AD than non-carriers (103–105, 460). ApoE is a component of lipoproteins and its primarily function is the transport of lipids and cholesterol in our body. ApoE recognizes specific receptors such as LDLR and LRP1 that mediate the uptake of lipoproteins (117). Internalization of lipoproteins is often enhanced by HSPGs that can also function as receptors by themselves (126). Three ApoE isoforms exist that differ at amino acid sites 112 and 158 by a cysteine-arginine interchange (114, 115). The difference in primary structure confers a functional difference although the exact mechanism by which ApoE4 increases the risk of developing AD remains elusive. A more thorough understanding of functional differences between ApoE isoforms is required such as functional differences in the ApoE-HSPG interaction.

The identification of small molecules that specifically interact with ApoE4 and that may alter its structure and function can be utilized to investigate ApoE biology. Such small molecules may also be of therapeutic value. Therefore, the central objective of this thesis was to study the ApoE-heparin interaction, identify any isoform-dependent differences in heparin binding and to screen for novel ApoE tool compounds. This research work provides novel findings on the ApoE-heparin interaction and identifies new drugs that bind, albeit non-selectively to the different ApoE isoforms. The thesis does answer the overarching hypothesis that a structural difference (i.e. amino acid interchange) results in a functional difference (i.e. altered heparin binding) between ApoE variants. However, biophysical techniques used to address the hypothesis did not identify differences in tertiary and/or quaternary structure between the proteins that are likely to be small. This may also be the reason why no specificity of screening compounds was observed against ApoE4 over ApoE2 and ApoE3. Nevertheless, drugs identified in this thesis are in clinical use and it may be worthwhile to evaluate their effects on ApoE biology and their use as therapeutic agents.

5.1 Chapter 2: Conclusions and future directions

In Chapter 2, a novel purification protocol of wild type ApoE2, ApoE3 and ApoE4, as well as the truncated $ApoE4_{1\text{-}191}$ and monomeric $ApoE4_{mon}$ variants under non-denaturing conditions was developed. Proteins were additionally compared in solution by complementary techniques including gel filtration, SEC MALS, AUC and SAXS, and crystallization trails of ApoE4 were conducted.

Highly pure protein is yielded in the newly developed protocol that selects functional protein by HAC. All ApoE isoforms resemble one another in solution in terms of structure and shape and have similar hydrodynamic properties. A Stokes radius R_S of 5.8 – 6.8 nm was calculated by gel filtration, SEC MALS and AUC, as well as a radius of gyration Rg of ~5.6 nm by SAXS; all of which are values similar to those reported in previous studies (195, 379). All biophysical techniques suggest an elongated tetrameric shape for ApoE in solution and SAXS additionally confirms intrinsic flexibility and/or polydispersity. This flexibility in combination with ApoE's intrinsic and/or proteolytic instability hindered its crystallization and only the amino terminal domain readily crystallized.

A prevailing hypothesis for ApoE4's increased risk of AD is the introduction of a salt bridge between Arg61 and Glu225 that is postulated to result in ApoE4's decreased stability, with the consequently increased fragmentation leading to cytotoxicity (252). This domain interaction is thought to give ApoE4 a more compact structure compared to ApoE2 and ApoE3. As outlined in Chapter 1, Section 1.4.4, there is indirect evidence for the ApoE4 domain interaction, but also suggestions for altered oligomerization behaviour or conformational changes within the receptor binding region due to the amino acid interchange in ApoE4. Large conformational changes in ApoE4 structure, such as a more compact shape compared to the two other isoforms are likely to be recognized in the biophysical techniques used in this thesis. However, no difference between ApoE isoforms was identified and all proteins behaved similar in terms of sedimentation and light scattering suggesting that there are no gross differences in secondary, tertiary and/or quaternary structure between ApoE2, ApoE3 and ApoE4; data that all suggest that under the conditions used in the present study the proposed ApoE4 intramolecular interaction does not occur. Direct proof of the Arg61 – Glu255 salt bridge in ApoE4 can only be obtained by a high-resolution crystal structure and the ApoE4 domain interaction hypothesis therefore remains inferential.

Although crystallization of full length ApoE4 was tested under various conditions, it would be of interest to further evaluate LCP in future. Preliminary LCP trials in collaboration with the Membrane Protein Lab (Imperial College) did not yield any crystals and focus was therefore shifted to in-solution structural techniques such as SAXS. However, as ApoE seems more stable in the presence of detergents, lipids and/or lipid surrogates LCP crystallization presents a promising approach to obtain a full-length crystal structure.

Interestingly, $ApoE4_{mon}$ is not entirely monomeric since dimeric, as well as tetrameric species are present particularly at higher protein concentrations which contradicts previous observations (243). Additionally, an elongated shape, polydispersity and/or intrinsic flexibility was confirmed by SAXS. This differs from the globular structure deduced by the NMR studies

(242). In future, it will be of interest to further investigate if additional residues other than the five residues that have been replaced in $ApoE4_{mon}$ are responsible for the oligomerization of ApoE.

5.2 Chapter 3: Conclusions and future directions

The ApoE-heparin and ApoE-Suramin interactions were investigated in Chapter 3 using SAXS and isoform-dependent differences were identified in their heparin binding ability, as well as substantial conformational changes upon ligand binding. ApoE4 binds with higher affinity to heparin compared to ApoE2 and ApoE3 that may be a result of an altered charge distribution in the receptor binding region due to the amino acid interchange at positions 112 and 158.

Previous studies using SPR have reported higher binding affinity of ApoE4 to heparin or HS compared to ApoE2 and ApoE3 (410). SAXS data collected in this thesis is consistent with an isoform-dependent difference in heparin binding and shows major structural changes when ApoE binds to the ligand. Heparin binding seems predominantly mediated by the amino terminal domain (residues 134-150) in the lipid-free protein as mutation of critical lysine residues in the receptor binding region abolishes the effects of heparin on ApoE size and conformation. The second heparin binding site located around Lys233 therefore seems to play a minor role in the heparin interaction.

As outlined in Chapter 1, Sections 1.4.1 and 1.4.2, HSPGs are glycoproteins that contain covalently attached GAGs such as heparin and are important receptors for the uptake of ApoE-containing lipoproteins. Differences in the ApoE-heparin (or ApoE-HSPG) interaction will likely result in altered lipoprotein metabolism and will influence the biological effects that ApoE has in the periphery and CNS such as on the immune response, neuron regeneration and growth. However, differences in lipoprotein metabolism between ApoE isoforms are subtle and particularly ApoE3 and ApoE4 seem equally efficient at clearing plasma cholesterol levels *in vivo* (461). Impaired HSPG binding affinity as in the case of ApoE2 can lead to the development of type III hyperlipoproteinemia. Affected individuals accumulate lipoprotein cholesterol and lipids in plasma which predisposes them to the premature development of atherosclerosis (Chapter 1, Section 1.4.1). However, less than 10% of ε2/ε2 homozygotic carriers develop overt type III hyperlipoproteinemia; most ε2/ε2 subjects, paradoxically, are normolipidemic or even hypocholesterolemic (135). Carriers of the ε4 allele on the other hand were shown to have higher LDL cholesterol levels compared to ε2 and ε3 individuals and ε4/ε4 homozygotes have a slightly increased risk to develop coronary disease compared to ε3/ε3 homozygotes (462). ApoE4 preferentially associates with large VLDLs compared to ApoE3 that preferably binds smaller HDLs and therefore promotes VLDL clearance from plasma (235–237). It has been suggested that accelerated ApoE4-mediated VLDL clearance results in downregulation

of LDLR and related receptors and therefore in an increase of plasma LDL levels (463). Lower levels of LDLR, LRP1 and related receptors in the liver may additionally be promoted by ApoE4's increased binding ability to HSPGs as shown in this thesis with heparin. For example, ApoE4-containing lipoproteins may be trapped in the endosomes due to slower dissociation of ApoE4 from HSPGs and therefore impair recycling of LDLRs back to the cell surface (Figure 5.1). Similarly, in the CNS where ApoE is the major apolipoprotein, higher binding affinity of ApoE4 to HSPGs may trap receptors such as NMDA and AMPA receptors (NMDAR and AMPAR) in synaptic endosomes resulting in altered glutamate receptor homeostasis (Figure 5.1) (433). Altered HSPG binding ability will also influence lipoprotein metabolism and clearance of the Aβ peptide in the brain. Unfortunately, it is still unclear how lipoprotein metabolism in the brain differs between ApoE isoforms and especially the role of HSPGs in the CNS needs further studying.

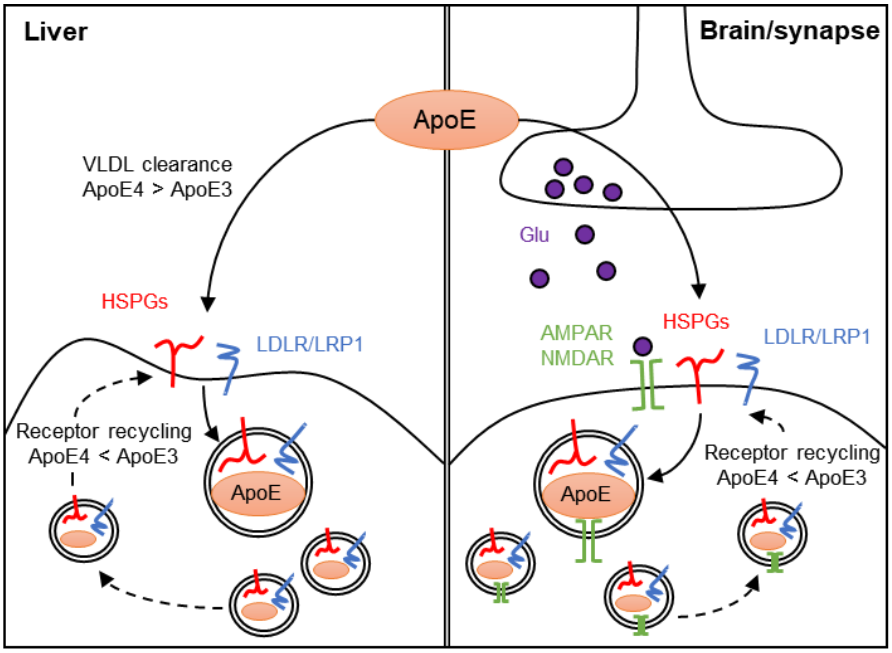

Figure 5.1. Proposed mechanism by which ApoE influences receptor homeostasis in liver and brain. ApoE containing VLDLs are cleared faster by ApoE4 in the liver (left) compared to ApoE3 due to preferred binding of ApoE4 for VLDLs and higher binding affinity of ApoE4 to HSPGs. Internalized ApoE-containing lipoproteins disengage in the endosome and receptors such as LDLR are recycled back to the cell surface. Due to ApoE4's altered binding to HSPGs, the recycling step is delayed compared to ApoE3 (and ApoE2) and the process stalled in the endosomes. Lower levels of ApoE receptors at the cell surface will result in accumulation of smaller lipoproteins such as LDLs and cholesterol. Similarly, in the synapse (right) recycling of glutamate receptors (AMPAR and NMDAR) trapped in the vesicle with ApoE4 is stalled resulting in altered glutamate (Glu) receptor homeostasis.

The exact mechanism for the altered heparin interaction between ApoE isoforms remains to be addressed. As mentioned, the ApoE amino terminal domain is largely responsible for heparin binding. Binding was only tested on ApoE4$_{1\text{-}191}$ in this thesis and it will be of interest to compare the interaction to the respective ApoE2 and ApoE3 amino terminal domains. If the

isoform dependent difference is still seen in the amino terminal domains, it suggests that the increased ApoE4 heparin binding is a result of altered charge distribution in the receptor binding region. On the other hand, if the amino terminal domains equally interact with heparin, this will indicate a role of ApoE tertiary and/or quaternary structure in the interaction. The assessment of further ApoE4 mutants in which the Arg112 is changed into other residues such as alanine, glutamic acid or lysine will additionally address the role of a positive charge at position 112.

Lastly, SAXS experiments were performed on lipid-free ApoE and it will be important to assess isoform dependent differences in lipidated or lipoprotein-associated ApoE in future. However, SAXS may not be the appropriate technique to investigate the heparin interaction with lipid-associated ApoE. SAXS is a contrast method and any additives such as detergents or lipid surrogates will increase noise and complicate data analysis. Nevertheless, as SAXS has successfully been employed on ApoE-DMPC complexes in previous studies (411) it is worth evaluating the heparin interaction on such complexes, particularly in conjunction with other biophysical techniques such as AUC.

5.3 Chapter 4: Conclusions and future directions

The screening in Chapter 4 identified novel ApoE binders by using three complementary biophysical assays. Hits identified include L-Thyroxine and its analogue Tafamidis, as well as the SERMs Clomiphene, Tamoxifen, Toremifene, and the NSAID Meclofenamic acid. Although none of the hits identified differentiated between ApoE isoforms, the methods used nevertheless provide a novel means of identifying compounds that may be useful in defining the physiological functions of ApoE. Identified drugs may also provide starting points for future attempts to develop molecules which interact selectively with ApoE4 and which might therefore be of therapeutic utility.

As determined in Chapter 2, ApoE isoforms resemble one another in terms of size and shape and structural differences must be small. Non-selective binding of compounds is therefore expected. Selectivity may however be of minor importance. In a therapeutic approach, identified drugs may only be used in ε4 positive carriers and modulation of the other isoforms (e.g. in heterozygotic patients such as ε3/ε4 carriers) may not pose a problem or be harmful.

The drugs identified are all in clinical use and their effects on ApoE biology in the brain (and periphery) remain to be investigated. Binding of L-Thyroxine to ApoE was previously demonstrated (454, 455) and the hormone was shown to increase ApoE expression and secretion in HTB14 astrocytes via activation of the thyroid receptor (464). Similar effects were also shown with steroid hormones. Progesterone and the synthetic progestin, Lynestrenol, at concentrations of 5-10 µM were demonstrated to induce ApoE secretion from human CCF-

STTG1 astrocytoma cells by activation of the LXR and progesterone receptor (465), and Estradiol increased ApoE levels in cultured mouse cortical neurons, as well as living mice via activation of the estrogen receptors respectively (466, 467). As outlined in Chapter 1, Section 1.6, a therapeutic strategy for AD includes increasing levels of lipidated and functional ApoE by activation of the LXR pathway. Therefore, it will be of interest in future to evaluate the effects of L-Thyroxine, as well as the SERMs Clomiphene, Tamoxifen and Toremifene on ApoE secretion in cellular models and to identify the pathways that lead to increased expression.

Characterizing the binding mode of the probes to ApoE remains to be addressed as well. No binding of hits was observed against $ApoE4_{1-191}$ which suggests that identified drugs either bind to the carboxyl terminus and/or that tertiary/quaternary structure of the full-length protein is required for binding. Due to the lack of a full length ApoE crystal structure, no computational approach can be used to identify the binding mode (e.g. by docking the compounds). However, this can be addressed experimentally, for example by hydrogen−deuterium exchange and mass spectroscopy (HDX MS). In HDX MS, proteins are equilibrated in deuterated water (D_2O) and certain hydrogens in the protein exchanged for deuterium (some hydrogens will exchange fast such as hydrogens from surface exposed residues, others including backbone hydrogens will exchange relatively slowly). Deuterium has a higher mass compared to hydrogen which can be monitored by MS. Ligands or inhibitors that bind to the protein will influence deuteration. The rate at which the protein is deuterated and where the hydrogen is exchanged for deuterium can be converted into conformational information that will give insights into the binding mode of the ligand (468). Similarly, Mondal *et al* (445) used HDX MS to investigate the effects of the modulator EZ-482 on ApoE structure. EZ-482 binds with similar affinity to the carboxyl terminus of ApoE3 and ApoE4, however, binding to ApoE4 is accompanied by a conformational reorganization of the amino terminus.

5.4 Limitations

The studies described in this these were performed *in vitro* using recombinant protein. *In vitro* work uses simple systems without the complexities and variabilities of the system in a living organism, such as the lipidation state of ApoE, and extrapolations to the *in vivo* situation should therefore be made with caution. For example, the heparin binding studies using SAXS in Chapter 3 suggest an isoform dependent difference, however, it is still not clear how ApoE3 and ApoE4 differ in terms of lipoprotein metabolism in humans and if the increased risk of ApoE4 to develop AD is a result of altered HSPG binding (461). SAXS studies were performed on lipid-free protein, however, ApoE is physiologically present on lipoproteins when interacting with its receptors and HSPGs. Although the observations reported in this thesis may not be directly physiologically relevant, they nevertheless provide clear hypotheses, such as an ApoE

isoform-specific difference in interaction with HPSGs, that can be tested under more functional and/or physiological conditions.

Similarly, the biophysical assays used to screen for novel ApoE binders are very simple systems that will not reflect the physiology of ApoE in the living organism. However, such biophysical (and biochemical) assays are good starting points for drug discovery efforts and to evaluate drug-target engagement before going into other *in vitro* cell based or *in vivo* animal models. In the case of this thesis work, screening was performed using the Corning® Epic® in which ApoE4 was immobilized to the biosensor surface via amine coupling. Coupling may have occurred at critical lysine residues located in the receptor binding region which may have affected functionality of the protein and influenced compound binding. Likewise, labelling of ApoE4 for MST measurements may have taken place at identical sites. The inclusion of ITC as a final assay in which no labelling or alteration of the protein is necessary was therefore appropriate. Triton X-100 detergent was added to all assay buffers to reduce compound aggregation and non-specific binding, as well as to keep ApoE in a more physiological conformation, similar to being associated to lipoproteins. However, it is not clear to what extent Triton X-100 influences ApoE structure or if ApoE isoforms differ structurally from each other in a lipid- or detergent-associated state. Despite the above discussed limitations, the biophysical assays used in this thesis remain a good system for identifying and characterizing ApoE binders and for generating initial data that may direct into further *in vitro* or *in vivo* studies.

6 REFERENCES

1. Alzheimer, A. (1907) [Über eine eigenartige Erkrankung der Hirnrinde] [Article in German]. *Allg. Zeitschrift fur Psychiatr. und Psych. Medizin*

2. Hyman, B. T., Phelps, C. H., Beach, T. G., Bigio, E. H., Cairns, N. J., Carrillo, M. C., Dickson, D. W., Duyckaerts, C., Frosch, M. P., Masliah, E., Mirra, S. S., Nelson, P. T., Schneider, J. A., Thal, D. R., Thies, B., Trojanowski, J. Q., Vinters, H. V., and Montine, T. J. (2012) National Institute on Aging–Alzheimer's Association guidelines for the neuropathologic assessment of Alzheimer's disease. *Alzheimer's Dement.* **8**, 1–13

3. Scheltens, P., Blennow, K., Breteler, M. M. B., de Strooper, B., Frisoni, G. B., Salloway, S., and Van der Flier, W. M. (2016) Alzheimer's disease. *Lancet*. **1**, 15056

4. Prince, M., Wimo, A., Guerchet, M., Ali, G.-C., Wu, Y.-T., and Prina, M. (2015) World Alzheimer Report 2015 - The Global Impact of dementia. *Alzheimer's Dis. Int.*

5. World Health Organization (2018) ICD-11: Dementia. [online] https://icd.who.int/browse11/l-m/en#/http%3A%2F%2Fid.who.int%2Ficd%2Fentity%2F546689346 (Accessed September 24, 2018)

6. World Health Organization (2018) ICD-11: Dementia due to Alzheimer's disease. [online] https://icd.who.int/browse11/l-m/en#/http%3A%2F%2Fid.who.int%2Ficd%2Fentity%2F795022044 (Accessed September 24, 2018)

7. Jack, C. R., Bennett, D. A., Blennow, K., Carrillo, M. C., Dunn, B., Haeberlein, S. B., Holtzman, D. M., Jagust, W., Jessen, F., Karlawish, J., Liu, E., Molinuevo, J. L., Montine, T., Phelps, C., Rankin, K. P., Rowe, C. C., Scheltens, P., Siemers, E., Snyder, H. M., Sperling, R., Elliott, C., Masliah, E., Ryan, L., and Silverberg, N. (2018) NIA-AA Research Framework: Toward a biological definition of Alzheimer's disease. *Alzheimer's Dement.* **14**, 535–562

8. Serrano-Pozo, A., Frosch, M. P., Masliah, E., and Hyman, B. T. (2011) Neuropathological alterations in Alzheimer disease. *Cold Spring Harb. Perspect. Med.* **1**, a006189

9. Glenner, G. G., and Wong, C. W. (1984) Alzheimer's disease and Down's syndrome: Sharing of a unique cerebrovascular amyloid fibril protein. *Biochem. Biophys. Res. Commun.* **122**, 1131–1135

10. Glenner, G. G., and Wong, C. W. (1984) Alzheimer's disease: Initial report of the purification and characterization of a novel cerebrovascular amyloid protein. *Biochem. Biophys. Res. Commun.* **120**, 885–890

11. Masters, C. L., Simms, G., Weinman, N. A., Multhaup, G., McDonald, B. L., and Beyreuther, K. (1985) Amyloid plaque core protein in Alzheimer disease and Down syndrome. *Proc. Natl. Acad. Sci. U. S. A.* **82**, 4245–9

12. Haass, C., Kaether, C., Thinakaran, G., and Sisodia, S. (2012) Trafficking and proteolytic processing of APP. *Cold Spring Harb. Perspect. Med.* **2**, a006270

13. Kang, J., Lemaire, H. G., Unterbeck, A., Salbaum, J. M., Masters, C. L., Grzeschik, K. H., Multhaup, G., Beyreuther, K., and Müller-Hill, B. (1987) The precursor of Alzheimer's disease amyloid A4 protein resembles a cell-surface receptor. *Nature*. **325**, 733–6

14. Dyrks, T., Weidemann, A., Multhaup, G., Salbaum, J. M., Lemaire, H. G., Kang, J., Müller-Hill, B., Masters, C. L., and Beyreuther, K. (1988) Identification, transmembrane

orientation and biogenesis of the amyloid A4 precursor of Alzheimer's disease. *EMBO J.* **7**, 949–57

15. Esch, F. S., Keim, P. S., Beattie, E. C., Blacher, R. W., Culwell, a R., Oltersdorf, T., McClure, D., and Ward, P. J. (1990) Cleavage of amyloid beta peptide during constitutive processing of its precursor. *Science*. **248**, 1122–4

16. Sisodia, S. S. (1992) Beta-amyloid precursor protein cleavage by a membrane-bound protease. *Proc. Natl. Acad. Sci. U. S. A.* **89**, 6075–9

17. Kuhn, P.-H., Wang, H., Dislich, B., Colombo, A., Zeitschel, U., Ellwart, J. W., Kremmer, E., Rossner, S., and Lichtenthaler, S. F. (2010) ADAM10 is the physiologically relevant, constitutive alpha-secretase of the amyloid precursor protein in primary neurons. *EMBO J.* **29**, 3020–32

18. De Strooper, B., Iwatsubo, T., and Wolfe, M. S. (2012) Presenilins and γ-secretase: structure, function, and role in Alzheimer Disease. *Cold Spring Harb. Perspect. Med.* **2**, a006304

19. Haass, C., Hung, A. Y., Schlossmacher, M. G., Teplow, D. B., and Selkoe, D. J. (1993) beta-Amyloid peptide and a 3-kDa fragment are derived by distinct cellular mechanisms. *J. Biol. Chem.* **268**, 3021–4

20. Sastre, M., Steiner, H., Fuchs, K., Capell, A., Multhaup, G., Condron, M. M., Teplow, D. B., and Haass, C. (2001) Presenilin-dependent gamma-secretase processing of beta-amyloid precursor protein at a site corresponding to the S3 cleavage of Notch. *EMBO Rep.* **2**, 835–41

21. Gu, Y., Misonou, H., Sato, T., Dohmae, N., Takio, K., and Ihara, Y. (2001) Distinct intramembrane cleavage of the beta-amyloid precursor protein family resembling gamma-secretase-like cleavage of Notch. *J. Biol. Chem.* **276**, 35235–8

22. Yan, R., Bienkowski, M. J., Shuck, M. E., Miao, H., Tory, M. C., Pauley, a M., Brashier, J. R., Stratman, N. C., Mathews, W. R., Buhl, a E., Carter, D. B., Tomasselli, a G., Parodi, L. a, Heinrikson, R. L., and Gurney, M. E. (1999) Membrane-anchored aspartyl protease with Alzheimer's disease beta-secretase activity. *Nature*. **402**, 533–7

23. Vassar, R., Bennett, B. D., Babu-Khan, S., Kahn, S., Mendiaz, E. a, Denis, P., Teplow, D. B., Ross, S., Amarante, P., Loeloff, R., Luo, Y., Fisher, S., Fuller, J., Edenson, S., Lile, J., Jarosinski, M. a, Biere, a L., Curran, E., Burgess, T., Louis, J. C., Collins, F., Treanor, J., Rogers, G., and Citron, M. (1999) Beta-secretase cleavage of Alzheimer's amyloid precursor protein by the transmembrane aspartic protease BACE. *Science*. **286**, 735–41

24. Sinha, S., Anderson, J. P., Barbour, R., Basi, G. S., Caccavello, R., Davis, D., Doan, M., Dovey, H. F., Frigon, N., Hong, J., Jacobson-Croak, K., Jewett, N., Keim, P., Knops, J., Lieberburg, I., Power, M., Tan, H., Tatsuno, G., Tung, J., Schenk, D., Seubert, P., Suomensaari, S. M., Wang, S., Walker, D., Zhao, J., McConlogue, L., and John, V. (1999) Purification and cloning of amyloid precursor protein beta-secretase from human brain. *Nature*. **402**, 537–40

25. Haass, C., Schlossmacher, M. G., Hung, A. Y., Vigo-Pelfrey, C., Mellon, A., Ostaszewski, B. L., Lieberburg, I., Koo, E. H., Schenk, D., and Teplow, D. B. (1992) Amyloid beta-peptide is produced by cultured cells during normal metabolism. *Nature*. **359**, 322–5

26. Seubert, P., Vigo-Pelfrey, C., Esch, F., Lee, M., Dovey, H., Davis, D., Sinha, S., Schlossmacher, M., Whaley, J., and Swindlehurst, C. (1992) Isolation and quantification of soluble Alzheimer's beta-peptide from biological fluids. *Nature*. **359**, 325–7

27. Shoji, M., Golde, T. E., Ghiso, J., Cheung, T. T., Estus, S., Shaffer, L. M., Cai, X. D., McKay, D. M., Tintner, R., and Frangione, B. (1992) Production of the Alzheimer amyloid beta protein by normal proteolytic processing. *Science*. **258**, 126–9

28. Näslund, J., Schierhorn, A., Hellman, U., Lannfelt, L., Roses, a D., Tjernberg, L. O., Silberring, J., Gandy, S. E., Winblad, B., and Greengard, P. (1994) Relative abundance of Alzheimer A beta amyloid peptide variants in Alzheimer disease and normal aging. *Proc. Natl. Acad. Sci. U. S. A.* **91**, 8378–82

29. Mori, H., Takio, K., Ogawara, M., and Selkoe, D. J. (1992) Mass spectrometry of purified amyloid beta protein in Alzheimer's disease. *J. Biol. Chem.* **267**, 17082–6

30. Jarrett, J. T., Berger, E. P., and Lansbury, P. T. (1993) The carboxy terminus of the beta amyloid protein is critical for the seeding of amyloid formation: implications for the pathogenesis of Alzheimer's disease. *Biochemistry*. **32**, 4693–7

31. Burdick, D., Soreghan, B., Kwon, M., Kosmoski, J., Knauer, M., Henschen, A., Yates, J., Cotman, C., and Glabe, C. (1992) Assembly and aggregation properties of synthetic Alzheimer's A4/beta amyloid peptide analogs. *J. Biol. Chem.* **267**, 546–54

32. Iwatsubo, T., Odaka, A., Suzuki, N., Mizusawa, H., Nukina, N., and Ihara, Y. (1994) Visualization of A beta 42(43) and A beta 40 in senile plaques with end-specific A beta monoclonals: evidence that an initially deposited species is A beta 42(43). *Neuron*. **13**, 45–53

33. Tanzi, R. E. (2012) The Genetics of Alzheimer Disease. *Cold Spring Harb. Perspect. Med.* **2**, 1–10

34. Cacace, R., Sleegers, K., and Van Broeckhoven, C. (2016) Molecular genetics of early-onset Alzheimer disease revisited. *Alzheimers. Dement.* **19**, 371–83

35. Alzheimer Disease & Frontotemporal Dementia Mutation Database [online] http://www.molgen.vib-ua.be/ADMutations (Accessed September 25, 2018)

36. Citron, M., Oltersdorf, T., Haass, C., McConlogue, L., Hung, a Y., Seubert, P., Vigo-Pelfrey, C., Lieberburg, I., and Selkoe, D. J. (1992) Mutation of the beta-amyloid precursor protein in familial Alzheimer's disease increases beta-protein production. *Nature*. **360**, 672–4

37. Suzuki, N., Cheung, T. T., Cai, X. D., Odaka, A., Otvos, L., Eckman, C., Golde, T. E., and Younkin, S. G. (1994) An increased percentage of long amyloid beta protein secreted by familial amyloid beta protein precursor (beta APP717) mutants. *Science*. **264**, 1336–40

38. Duff, K., Eckman, C., Zehr, C., Yu, X., Prada, C. M., Perez-tur, J., Hutton, M., Buee, L., Harigaya, Y., Yager, D., Morgan, D., Gordon, M. N., Holcomb, L., Refolo, L., Zenk, B., Hardy, J., and Younkin, S. (1996) Increased amyloid-beta42(43) in brains of mice expressing mutant presenilin 1. *Nature*. **383**, 710–3

39. Scheuner, D., Eckman, C., Jensen, M., Song, X., Citron, M., Suzuki, N., Bird, T. D., Hardy, J., Hutton, M., Kukull, W., Larson, E., Levy-Lahad, E., Viitanen, M., Peskind, E., Poorkaj, P., Schellenberg, G., Tanzi, R., Wasco, W., Lannfelt, L., Selkoe, D., and Younkin, S. (1996) Secreted amyloid beta-protein similar to that in the senile plaques of Alzheimer's disease is increased in vivo by the presenilin 1 and 2 and APP mutations linked to familial Alzheimer's disease. *Nat. Med.* **2**, 864–70

40. Jonsson, T., Atwal, J. K., Steinberg, S., Snaedal, J., Jonsson, P. V., Bjornsson, S., Stefansson, H., Sulem, P., Gudbjartsson, D., Maloney, J., Hoyte, K., Gustafson, A., Liu, Y., Lu, Y., Bhangale, T., Graham, R. R., Huttenlocher, J., Bjornsdottir, G., Andreassen, O. a., Jönsson, E. G., Palotie, A., Behrens, T. W., Magnusson, O. T., Kong, A.,

Thorsteinsdottir, U., Watts, R. J., and Stefansson, K. (2012) A mutation in APP protects against Alzheimer's disease and age-related cognitive decline. *Nature*. **488**, 96–9

41. Benilova, I., Gallardo, R., Ungureanu, A.-A., Castillo Cano, V., Snellinx, A., Ramakers, M., Bartic, C., Rousseau, F., Schymkowitz, J., and De Strooper, B. (2014) The Alzheimer disease protective mutation A2T modulates kinetic and thermodynamic properties of amyloid-β (Aβ) aggregation. *J. Biol. Chem.* **289**, 30977–89

42. Maloney, J. A., Bainbridge, T., Gustafson, A., Zhang, S., Kyauk, R., Steiner, P., van der Brug, M., Liu, Y., Ernst, J. A., Watts, R. J., and Atwal, J. K. (2014) Molecular mechanisms of Alzheimer disease protection by the A673T allele of amyloid precursor protein. *J. Biol. Chem.* **289**, 30990–1000

43. Terry, R. D., Masliah, E., Salmon, D. P., Butters, N., DeTeresa, R., Hill, R., Hansen, L. a., and Katzman, R. (1991) Physical basis of cognitive alterations in Alzheimer's disease: synapse loss is the major correlate of cognitive impairment. *Ann. Neurol.* **30**, 572–80

44. Giannakopoulos, P., Herrmann, F. R., Bussière, T., Bouras, C., Kövari, E., Perl, D. P., Morrison, J. H., Gold, G., and Hof, P. R. (2003) Tangle and neuron numbers, but not amyloid load, predict cognitive status in Alzheimer's disease. *Neurology*. **60**, 1495–500

45. Ingelsson, M., Fukumoto, H., Newell, K. L., Growdon, J. H., Hedley-Whyte, E. T., Frosch, M. P., Albert, M. S., Hyman, B. T., and Irizarry, M. C. (2004) Early Abeta accumulation and progressive synaptic loss, gliosis, and tangle formation in AD brain. *Neurology*. **62**, 925–31

46. Jack, C. R., Lowe, V. J., Weigand, S. D., Wiste, H. J., Senjem, M. L., Knopman, D. S., Shiung, M. M., Gunter, J. L., Boeve, B. F., Kemp, B. J., Weiner, M., and Petersen, R. C. (2009) Serial PIB and MRI in normal, mild cognitive impairment and Alzheimers disease: Implications for sequence of pathological events in Alzheimers disease. *Brain*. **132**, 1355–1365

47. Villemagne, V. L., Pike, K. E., Chételat, G., Ellis, K. A., Mulligan, R. S., Bourgeat, P., Ackermann, U., Jones, G., Szoeke, C., Salvado, O., Martins, R., O'Keefe, G., Mathis, C. A., Klunk, W. E., Ames, D., Masters, C. L., and Rowe, C. C. (2011) Longitudinal assessment of Aβ and cognition in aging and Alzheimer disease. *Ann. Neurol.* **69**, 181–92

48. Armstrong, R. A. (1994) beta-Amyloid (A beta) deposition in elderly non-demented patients and patients with Alzheimer's disease. *Neurosci. Lett.* **178**, 59–62

49. Lue, L. F., Kuo, Y. M., Roher, A. E., Brachova, L., Shen, Y., Sue, L., Beach, T., Kurth, J. H., Rydel, R. E., and Rogers, J. (1999) Soluble amyloid beta peptide concentration as a predictor of synaptic change in Alzheimer's disease. *Am. J. Pathol.* **155**, 853–62

50. McLean, C. A., Cherny, R. A., Fraser, F. W., Fuller, S. J., Smith, M. J., Beyreuther, K., Bush, A. I., and Masters, C. L. (1999) Soluble pool of Abeta amyloid as a determinant of severity of neurodegeneration in Alzheimer's disease. *Ann. Neurol.* **46**, 860–6

51. Näslund, J., Haroutunian, V., Mohs, R., Davis, K. L., Davies, P., Greengard, P., and Buxbaum, J. D. (2000) Correlation between elevated levels of amyloid beta-peptide in the brain and cognitive decline. *Jama*. **283**, 1571–1577

52. Walsh, D. M., Klyubin, I., Fadeeva, J. V, Cullen, W. K., Anwyl, R., Wolfe, M. S., Rowan, M. J., and Selkoe, D. J. (2002) Naturally secreted oligomers of amyloid β protein potently inhibit hippocampal long-term potentiation in vivo. *Nature*. **416**, 535–539

53. Gong, Y., Chang, L., Viola, K. L., Lacor, P. N., Lambert, M. P., Finch, C. E., Krafft, G. A., and Klein, W. L. (2003) Alzheimer's disease-affected brain: Presence of oligomeric

A ligands (ADDLs) suggests a molecular basis for reversible memory loss. *Proc. Natl. Acad. Sci.* **100**, 10417–10422

54. Kayed, R., Head, E., Thompson, J. L., McIntire, T. M., Milton, S. C., Cotman, C. W., and Glabe, C. G. (2003) Common structure of soluble amyloid oligomers implies common mechanism of pathogenesis. *Science*. **300**, 486–9

55. Lacor, P. N., Buniel, M. C., Chang, L., Fernandez, S. J., Gong, Y., Viola, K. L., Lambert, M. P., Velasco, P. T., Bigio, E. H., Finch, C. E., Krafft, G. A., and Klein, W. L. (2004) Synaptic targeting by Alzheimer's-related amyloid beta oligomers. *J. Neurosci.* **24**, 10191–200

56. Townsend, M., Shankar, G. M., Mehta, T., Walsh, D. M., and Selkoe, D. J. (2006) Effects of secreted oligomers of amyloid beta-protein on hippocampal synaptic plasticity: a potent role for trimers. *J. Physiol.* **572**, 477–92

57. Selkoe, D. J., and Hardy, J. (2016) The amyloid hypothesis of Alzheimer's disease at 25 years. *EMBO Mol. Med.* **8**, 595–608

58. Kosik, K. S., Joachim, C. L., and Selkoe, D. J. (1986) Microtubule-associated protein tau (tau) is a major antigenic component of paired helical filaments in Alzheimer disease. *Proc. Natl. Acad. Sci. U. S. A.* **83**, 4044–8

59. Nukina, N., and Ihara, Y. (1986) One of the antigenic determinants of paired helical filaments is related to tau protein. *J. Biochem.* **99**, 1541–4

60. Grundke-Iqbal, I., Iqbal, K., Tung, Y. C., Quinlan, M., Wisniewski, H. M., and Binder, L. I. (1986) Abnormal phosphorylation of the microtubule-associated protein tau (tau) in Alzheimer cytoskeletal pathology. *Proc. Natl. Acad. Sci. U. S. A.* **83**, 4913–7

61. Goedert, M., Spillantini, M. G., Jakes, R., Rutherford, D., and Crowther, R. A. (1989) Multiple isoforms of human microtubule-associated protein tau: sequences and localization in neurofibrillary tangles of Alzheimer's disease. *Neuron*. **3**, 519–26

62. Neve, R. L., Harris, P., Kosik, K. S., Kurnit, D. M., and Donlon, T. A. (1986) Identification of cDNA clones for the human microtubule-associated protein tau and chromosomal localization of the genes for tau and microtubule-associated protein 2. *Brain Res.* **387**, 271–80

63. Witman, G. B., Cleveland, D. W., Weingarten, M. D., and Kirschner, M. W. (1976) Tubulin requires tau for growth onto microtubule initiating sites. *Proc. Natl. Acad. Sci. U. S. A.* **73**, 4070–4

64. Binder, L. I., Frankfurter, A., and Rebhun, L. I. (1985) The distribution of tau in the mammalian central nervous system. *J. Cell Biol.* **101**, 1371–8

65. Dixit, R., Ross, J. L., Goldman, Y. E., and Holzbaur, E. L. F. (2008) Differential regulation of dynein and kinesin motor proteins by tau. *Science*. **319**, 1086–9

66. Wang, J., Xia, Y., Grundke-Iqbal, I., and Iqbal, K. (2013) Abnormal hyperphosphorylation of tau: sites, regulation, and molecular mechanism of neurofibrillary degeneration. *J. Alzheimers. Dis.* **33 Suppl 1**, S123-39

67. Drechsel, D. N., Hyman, a a, Cobb, M. H., and Kirschner, M. W. (1992) Modulation of the dynamic instability of tubulin assembly by the microtubule-associated protein tau. *Mol. Biol. Cell*. **3**, 1141–54

68. Brandt, R., Lee, G., Teplow, D. B., Shalloway, D., and Abdel-Ghany, M. (1994) Differential effect of phosphorylation and substrate modulation on tau's ability to promote microtubule growth and nucleation. *J. Biol. Chem.* **269**, 11776–11782

69. Illenberger, S., Zheng-fischho, Q., Preuss, U., Stamer, K., Baumann, K., Trinczek, B., Biernat, J., Godemann, R., and Mandelkow, E. E. (1998) The Endogenous and Cell Cycle-dependent Phosphorylation of tau Protein in Living Cells : Implications for Alzheimer ' s Disease. *Mol. Biol. Cell*. **9**, 1495–1512

70. Köpke, E., Tung, Y. C., Shaikh, S., Alonso, A. C., Iqbal, K., and Grundke-Iqbal, I. (1993) Microtubule-associated protein tau. Abnormal phosphorylation of a non-paired helical filament pool in Alzheimer disease. *J. Biol. Chem.* **268**, 24374–84

71. Alonso, A. C., Grundke-Iqbal, I., and Iqbal, K. (1996) Alzheimer's disease hyperphosphorylated tau sequesters normal tau into tangles of filaments and disassembles microtubules. *Nat. Med.* **2**, 783–7

72. Alonso, A. D., Grundke-Iqbal, I., Barra, H. S., and Iqbal, K. (1997) Abnormal phosphorylation of tau and the mechanism of Alzheimer neurofibrillary degeneration: sequestration of microtubule-associated proteins 1 and 2 and the disassembly of microtubules by the abnormal tau. *Proc. Natl. Acad. Sci. U. S. A.* **94**, 298–303

73. Alonso, A. C., Zaidi, T., Grundke-Iqbal, I., and Iqbal, K. (1994) Role of abnormally phosphorylated tau in the breakdown of microtubules in Alzheimer disease. *Proc. Natl. Acad. Sci. U. S. A.* **91**, 5562–6

74. Oddo, S., Vasilevko, V., Caccamo, A., Kitazawa, M., Cribbs, D. H., and LaFerla, F. M. (2006) Reduction of soluble Abeta and tau, but not soluble Abeta alone, ameliorates cognitive decline in transgenic mice with plaques and tangles. *J. Biol. Chem.* **281**, 39413–23

75. Santacruz, K., Lewis, J., Spires, T., Paulson, J., Kotilinek, L., Ingelsson, M., Guimaraes, A., DeTure, M., Ramsden, M., McGowan, E., Forster, C., Yue, M., Orne, J., Janus, C., Mariash, A., Kuskowski, M., Hyman, B., Hutton, M., and Ashe, K. H. (2005) Tau suppression in a neurodegenerative mouse model improves memory function. *Science*. **309**, 476–81

76. Wittmann, C. W., Wszolek, M. F., Shulman, J. M., Salvaterra, P. M., Lewis, J., Hutton, M., and Feany, M. B. (2001) Tauopathy in Drosophila: neurodegeneration without neurofibrillary tangles. *Science*. **293**, 711–4

77. Maeda, S., Sahara, N., Saito, Y., Murayama, S., Ikai, A., and Takashima, A. (2006) Increased levels of granular tau oligomers: An early sign of brain aging and Alzheimer's disease. *Neurosci. Res.* **54**, 197–201

78. Lasagna-Reeves, C. A., Castillo-Carranza, D. L., Sengupta, U., Sarmiento, J., Troncoso, J., Jackson, G. R., and Kayed, R. (2012) Identification of oligomers at early stages of tau aggregation in Alzheimer's disease. *FASEB J.* **26**, 1946–59

79. DeVos, S. L., Corjuc, B. T., Oakley, D. H., Nobuhara, C. K., Bannon, R. N., Chase, A., Commins, C., Gonzalez, J. A., Dooley, P. M., Frosch, M. P., and Hyman, B. T. (2018) Synaptic Tau Seeding Precedes Tau Pathology in Human Alzheimer's Disease Brain. *Front. Neurosci.* **12**, 267

80. Shafiei, S. S., Guerrero-Muñoz, M. J., and Castillo-Carranza, D. L. (2017) Tau oligomers: Cytotoxicity, propagation, and mitochondrial damage. *Front. Aging Neurosci.* **9**, 1–9

81. Mazanetz, M. P., and Fischer, P. M. (2007) Untangling tau hyperphosphorylation in drug design for neurodegenerative diseases. *Nat. Rev. Drug Discov.* **6**, 464–79

82. Perl, D. P. (2010) Neuropathology of Alzheimer's disease. *Mt. Sinai J. Med.* **77**, 32–42

83. Masliah, E., Terry, R. D., DeTeresa, R. M., and Hansen, L. A. (1989)

Immunohistochemical quantification of the synapse-related protein synaptophysin in Alzheimer disease. *Neurosci. Lett.* **103**, 234–9

84. DeKosky, S. T., Scheff, S. W., and Styren, S. D. (1996) Structural correlates of cognition in dementia: quantification and assessment of synapse change. *Neurodegeneration*. **5**, 417–21

85. Scheff, S. W., and Price, D. A. (1998) Synaptic density in the inner molecular layer of the hippocampal dentate gyrus in Alzheimer disease. *J. Neuropathol. Exp. Neurol.* **57**, 1146–53

86. Forner, S., Baglietto-Vargas, D., Martini, A. C., Trujillo-Estrada, L., and LaFerla, F. M. (2017) Synaptic Impairment in Alzheimer's Disease: A Dysregulated Symphony. *Trends Neurosci.* **40**, 347–357

87. Davies, P., and Maloney, A. J. (1976) Selective loss of central cholinergic neurons in Alzheimer's disease. *Lancet (London, England)*. **2**, 1403

88. Perry, E. K., Gibson, P. H., Blessed, G., Perry, R. H., and Tomlinson, B. E. (1977) Neurotransmitter enzyme abnormalities in senile dementia. Choline acetyltransferase and glutamic acid decarboxylase activities in necropsy brain tissue. *J. Neurol. Sci.* **34**, 247–65

89. White, P., Hiley, C. R., Goodhardt, M. J., Carrasco, L. H., Keet, J. P., Williams, I. E. I., and Bowen, D. M. (1977) Neocortical cholinergic neurons in elderly people. *Lancet (London, England)*. **1**, 668–71

90. Reisine, T. D., Yamamura, H. I., Bird, E. D., Spokes, E., and Enna, S. J. (1978) Pre- and postsynaptic neurochemical alterations in Alzheimer's disease. *Brain Res.* **159**, 477–81

91. Whitehouse, P. J., Price, D. L., Struble, R. G., Clark, A. W., Coyle, J. T., and Delon, M. R. (1982) Alzheimer's disease and senile dementia: loss of neurons in the basal forebrain. *Science*. **215**, 1237–9

92. Birks, J. (2006) Cholinesterase inhibitors for Alzheimer's disease. *Cochrane database Syst. Rev.* **15**, CD005593

93. McShane, R., Areosa Sastre, A., and Minakaran, N. (2006) Memantine for dementia. *Cochrane database Syst. Rev.* 10.1002/14651858.CD003154.pub5

94. World Health Organization (2018) ICD-11: Dementia due to Alzheimer disease with early onset. [online] https://icd.who.int/browse11/l-m/en#/http%3A%2F%2Fid.who.int%2Ficd%2Fentity%2F199015879 (Accessed September 28, 2018)

95. World Health Organization (2018) ICD-11: Dementia due to Alzheimer disease with late onset. [online] https://icd.who.int/browse11/l-m/en#/http%3A%2F%2Fid.who.int%2Ficd%2Fentity%2F1855418451 (Accessed January 15, 2019)

96. Goldman, J. S., Hahn, S. E., Catania, J. W., LaRusse-Eckert, S., Butson, M. B., Rumbaugh, M., Strecker, M. N., Roberts, J. S., Burke, W., Mayeux, R., Bird, T., and American College of Medical Genetics and the National Society of Genetic Counselors (2011) Genetic counseling and testing for Alzheimer disease: joint practice guidelines of the American College of Medical Genetics and the National Society of Genetic Counselors. *Genet. Med.* **13**, 597–605

97. Wingo, T. S., Lah, J. J., Levey, A. I., and Cutler, D. J. (2012) Autosomal recessive causes likely in early-onset Alzheimer disease. *Arch. Neurol.* **69**, 59–64

98. Gatz, M., Pedersen, N. L., Berg, S., Johansson, B., Johansson, K., Mortimer, J. A., Posner, S. F., Viitanen, M., Winblad, B., and Ahlbom, A. (1997) Heritability for Alzheimer's disease: the study of dementia in Swedish twins. *J. Gerontol. A. Biol. Sci. Med. Sci.* **52**, M117-25

99. Gatz, M., Reynolds, C. A., Fratiglioni, L., Johansson, B., Mortimer, J. A., Berg, S., Fiske, A., and Pedersen, N. L. (2006) Role of genes and environments for explaining Alzheimer disease. *Arch. Gen. Psychiatry*. **63**, 168–74

100. Lambert, J.-C., Heath, S., Even, G., Campion, D., Sleegers, K., Hiltunen, M., Combarros, O., Zelenika, D., Bullido, M. J., Tavernier, B., Letenneur, L., Bettens, K., Berr, C., Pasquier, F., Fiévet, N., Barberger-Gateau, P., Engelborghs, S., De Deyn, P., Mateo, I., Franck, A., Helisalmi, S., Porcellini, E., Hanon, O., European Alzheimer's Disease Initiative Investigators, de Pancorbo, M. M., Lendon, C., Dufouil, C., Jaillard, C., Leveillard, T., Alvarez, V., Bosco, P., Mancuso, M., Panza, F., Nacmias, B., Bossù, P., Piccardi, P., Annoni, G., Seripa, D., Galimberti, D., Hannequin, D., Licastro, F., Soininen, H., Ritchie, K., Blanché, H., Dartigues, J.-F., Tzourio, C., Gut, I., Van Broeckhoven, C., Alpérovitch, A., Lathrop, M., and Amouyel, P. (2009) Genome-wide association study identifies variants at CLU and CR1 associated with Alzheimer's disease. *Nat. Genet.* **41**, 1094–9

101. Lambert, J. C., Ibrahim-Verbaas, C. A., Harold, D., Naj, A. C., Sims, R., Bellenguez, C., DeStafano, A. L., Bis, J. C., Beecham, G. W., Grenier-Boley, B., Russo, G., Thorton-Wells, T. A., Jones, N., Smith, A. V., Chouraki, V., Thomas, C., Ikram, M. A., Zelenika, D., Vardarajan, B. N., Kamatani, Y., Lin, C. F., Gerrish, A., Schmidt, H., Kunkle, B., Dunstan, M. L., Ruiz, A., Bihoreau, M. T., Choi, S. H., Reitz, C., Pasquier, F., Cruchaga, C., Craig, D., Amin, N., Berr, C., Lopez, O. L., De Jager, P. L., Deramecourt, V., Johnston, J. A., Evans, D., Lovestone, S., Letenneur, L., Morón, F. J., Rubinsztein, D. C., Eiriksdottir, G., Sleegers, K., Goate, A. M., Fiévet, N., Huentelman, M. W., Gill, M., Brown, K., Kamboh, M. I., Keller, L., Barberger-Gateau, P., McGuiness, B., Larson, E. B., Green, R., Myers, A. J., Dufouil, C., Todd, S., Wallon, D., Love, S., Rogaeva, E., Gallacher, J., St George-Hyslop, P., Clarimon, J., Lleo, A., Bayer, A., Tsuang, D. W., Yu, L., Tsolaki, M., Bossù, P., Spalletta, G., Proitsi, P., Collinge, J., Sorbi, S., Sanchez-Garcia, F., Fox, N. C., Hardy, J., Deniz Naranjo, M. C., Bosco, P., Clarke, R., Brayne, C., Galimberti, D., Mancuso, M., Matthews, F., European Alzheimer's Disease Initiative (EADI), Genetic and Environmental Risk in Alzheimer's Disease, Alzheimer's Disease Genetic Consortium, Cohorts for Heart and Aging Research in Genomic Epidemiology, Moebus, S., Mecocci, P., Del Zompo, M., Maier, W., Hampel, H., Pilotto, A., Bullido, M., Panza, F., Caffarra, P., Nacmias, B., Gilbert, J. R., Mayhaus, M., Lannefelt, L., Hakonarson, H., Pichler, S., Carrasquillo, M. M., Ingelsson, M., Beekly, D., Alvarez, V., Zou, F., Valladares, O., Younkin, S. G., Coto, E., Hamilton-Nelson, K. L., Gu, W., Razquin, C., Pastor, P., Mateo, I., Owen, M. J., Faber, K. M., Jonsson, P. V., Combarros, O., O'Donovan, M. C., Cantwell, L. B., Soininen, H., Blacker, D., Mead, S., Mosley, T. H., Bennett, D. A., Harris, T. B., Fratiglioni, L., Holmes, C., de Bruijn, R. F., Passmore, P., Montine, T. J., Bettens, K., Rotter, J. I., Brice, A., Morgan, K., Foroud, T. M., Kukull, W. A., Hannequin, D., Powell, J. F., Nalls, M. A., Ritchie, K., Lunetta, K. L., Kauwe, J. S. K., Boerwinkle, E., Riemenschneider, M., Boada, M., Hiltuenen, M., Martin, E. R., Schmidt, R., Rujescu, D., Wang, L. S., Dartigues, J. F., Mayeux, R., Tzourio, C., Hofman, A., Nöthen, M. M., Graff, C., Psaty, B. M., Jones, L., Haines, J. L., Holmans, P. A., Lathrop, M., Pericak-Vance, M. A., Launer, L. J., Farrer, L. A., van Duijn, C. M., Van Broeckhoven, C., Moskvina, V., Seshadri, S., Williams, J., Schellenberg, G. D., and Amouyel, P. (2013) Meta-analysis of 74,046 individuals identifies 11 new susceptibility loci for Alzheimer's disease. *Nat. Genet.* **45**, 1452–8

102. Van Cauwenberghe, C., Van Broeckhoven, C., and Sleegers, K. (2016) The genetic landscape of Alzheimer disease: clinical implications and perspectives. *Genet. Med.* **18**,

421–30

103. Saunders, a M., Strittmatter, W. J., Schmechel, D., George-Hyslop, P. H., Pericak-Vance, M. a, Joo, S. H., Rosi, B. L., Gusella, J. F., Crapper-MacLachlan, D. R., and Alberts, M. J. (1993) Association of apolipoprotein E allele epsilon 4 with late-onset familial and sporadic Alzheimer's disease. *Neurology*. **43**, 1467–1472

104. Strittmatter, W. J., Saunders, a M., Schmechel, D., Pericak-Vance, M., Enghild, J., Salvesen, G. S., and Roses, a D. (1993) Apolipoprotein E: high-avidity binding to beta-amyloid and increased frequency of type 4 allele in late-onset familial Alzheimer disease. *Proc. Natl. Acad. Sci. U. S. A.* **90**, 1977–81

105. Corder, E. H., Saunders, a M., Strittmatter, W. J., Schmechel, D. E., Gaskell, P. C., Small, G. W., Roses, a D., Haines, J. L., and Pericak-Vance, M. a (1993) Gene dose of apolipoprotein E type 4 allele and the risk of Alzheimer's disease in late onset families. *Science*. **261**, 921–3

106. Shore, V. G., and Shore, B. (1973) Heterogeneity of human plasma very low density lipoproteins. Separation of species differing in protein components. *Biochemistry*. **12**, 502–7

107. Utermann, G. (1975) Isolation and partial characterization of an arginine-rich apolipoprotein from human plasma very-low-density lipoproteins: apolipoprotein E. *Hoppe. Seylers. Z. Physiol. Chem.* **356**, 1113–21

108. Utermann, G., Hees, M., and Steinmetz, A. (1977) Polymorphism of apolipoprotein E and occurrence of dysbetalipoproteinaemia in man. *Nature*. **269**, 604–7

109. Utermann, G., Langenbeck, U., Beisiegel, U., and Weber, W. (1980) Genetics of the apolipoprotein E system in man. *Am. J. Hum. Genet.* **32**, 339–47

110. Utermann, G., Steinmetz, A., and Weber, W. (1982) Genetic control of human apolipoprotein E polymorphism: comparison of one- and two-dimensional techniques of isoprotein analysis. *Hum. Genet.* **60**, 344–51

111. Zannis, V. I., and Breslow, J. L. (1980) Characterization of a unique human apolipoprotein E variant associated with type III hyperlipoproteinemia. *J. Biol. Chem.* **255**, 1759–62

112. Zannis, V. I., and Breslow, J. L. (1981) Human very low density lipoprotein apolipoprotein E isoprotein polymorphism is explained by genetic variation and posttranslational modification. *Biochemistry*. **20**, 1033–41

113. Zannis, V. I., Just, P. W., and Breslow, J. L. (1981) Human apolipoprotein E isoprotein subclasses are genetically determined. *Am. J. Hum. Genet.* **33**, 11–24

114. Weisgraber, K. H., Rall, S. C., and Mahley, R. W. (1981) Human E apoprotein heterogeneity. Cysteine-arginine interchanges in the amino acid sequence of the apo-E isoforms. *J. Biol. Chem.* **256**, 9077–9083

115. Rall, S. C., Weisgraber, K. H., and Mahley, R. W. (1982) Human apolipoprotein E. The complete amino acid sequence. *J. Biol. Chem.* **257**, 4171–8

116. Zannis, V. I., Breslow, J. L., Utermann, G., Mahley, R. W., Weisgraber, K. H., Havel, R. J., Goldstein, J. L., Brown, M. S., Schonfeld, G., Hazzard, W. R., and Blum, C. (1982) Proposed nomenclature of apoE isoproteins, apoE genotypes, and phenotypes. *J. Lipid Res.* **23**, 911–4

117. Mahley, R. W. (1988) Apolipoprotein E: cholesterol transport protein with expanding role in cell biology. *Science*. **240**, 622–30

118. Farrer, L. a, Cupples, L. A., Haines, J. L., Hyman, B., Kukull, W. a, Mayeux, R., Myers, R. H., Pericak-Vance, M. a, Risch, N., and van Duijn, C. M. (1997) Effects of Age, Sex, and Ethnicity on the Association Between Apolipoprotein E Genotype and Alzheimer Disease. *Jama*. **278**, 1349–1356

119. Lin, C. T., Xu, Y. F., Wu, J. Y., and Chan, L. (1986) Immunoreactive apolipoprotein E is a widely distributed cellular protein. Immunohistochemical localization of apolipoprotein E in baboon tissues. *J. Clin. Invest.* **78**, 947–58

120. Williams, D. L., Dawson, P. a, Newman, T. C., and Rudel, L. L. (1985) Synthesis of apolipoprotein E by peripheral tissues. Potential functions in reverse cholesterol transport and cellular cholesterol metabolism. *Ann. N. Y. Acad. Sci.* **454**, 222–9

121. Blue, M. L., Williams, D. L., Zucker, S., Khan, S. a, and Blum, C. B. (1983) Apolipoprotein E synthesis in human kidney, adrenal gland, and liver. *Proc. Natl. Acad. Sci. U. S. A.* **80**, 283–7

122. Elshourbagy, N. a, Liao, W. S., Mahley, R. W., and Taylor, J. M. (1985) Apolipoprotein E mRNA is abundant in the brain and adrenals, as well as in the liver, and is present in other peripheral tissues of rats and marmosets. *Proc. Natl. Acad. Sci. U. S. A.* **82**, 203–7

123. Zannis, V. I., Breslow, J. L., SanGiacomo, T. R., Aden, D. P., and Knowles, B. B. (1981) Characterization of the major apolipoproteins secreted by two human hepatoma cell lines. *Biochemistry*. **20**, 7089–96

124. Boyles, J. K., Pitas, R. E., Wilson, E., Mahley, R. W., and Taylor, J. M. (1985) Apolipoprotein E associated with astrocytic glia of the central nervous system and with nonmyelinating glia of the peripheral nervous system. *J. Clin. Invest.* **76**, 1501–1513

125. Pitas, R. E., Boyles, J. K., Lee, S. H., and Mahley, R. W. (1987) Astrocytes synthesize apolipoprotein E and metabolize apolipoprotein E-containing lipoproteins. *Biochim. Biophys. Acta*. **917**, 148–161

126. Mahley, R. W., and Ji, Z. S. (1999) Remnant lipoprotein metabolism: key pathways involving cell-surface heparan sulfate proteoglycans and apolipoprotein E. *J. Lipid Res.* **40**, 1–16

127. Jonas, A., and Phillips, M. C. (2008) Lipoprotein structure. in *Biochemistry of Lipids, Lipoproteins and Membranes*, 5th Ed. (Vance, D. E., and Vance, J. E. eds), pp. 485–506, Elsevier, **348**, 485–506

128. Fielding, C. J., and Fielding, P. E. (2008) Dynamics of lipoprotein transport in the circulatory system. in *Biochemistry of Lipids, Lipoproteins and Membranes*, 5th Ed. (Vance, D. E., and Vance, J. E. eds), pp. 533–553, Elsevier, 10.1016/B978-044453219-0.50021-0

129. Schneider, W. J. (2008) Lipoprotein receptors. in *Biochemistry of Lipids, Lipoproteins and Membranes*, 5th Ed. (Vance, D. E., and Vance, J. E. eds), pp. 555–578, Elsevier, 10.1016/B978-044453219-0.50022-2

130. Rader, D. J., and Hovingh, G. K. (2014) HDL and cardiovascular disease. *Lancet*. **384**, 618–625

131. Mahley, R. W., Weisgraber, K. H., Hussain, M. M., Greenman, B., Fisher, M., Vogel, T., and Gorecki, M. (1989) Intravenous infusion of apolipoprotein E accelerates clearance of plasma lipoproteins in rabbits. *J. Clin. Invest.* **83**, 2125–30

132. Shimano, H., Namba, Y., Ohsuga, J., Kawamura, M., Yamamoto, K., Shimada, M., Gotoda, T., Harada, K., Yazaki, Y., and Yamada, N. (1994) Secretion-recapture process

of apolipoprotein E in hepatic uptake of chylomicron remnants in transgenic mice. *J. Clin. Invest.* **93**, 2215–23

133. Fan, J., Ji, Z. S., Huang, Y., de Silva, H., Sanan, D., Mahley, R. W., Innerarity, T. L., and Taylor, J. M. (1998) Increased expression of apolipoprotein E in transgenic rabbits results in reduced levels of very low density lipoproteins and an accumulation of low density lipoproteins in plasma. *J. Clin. Invest.* **101**, 2151–64

134. Zhang, S. H., Reddick, R. L., Piedrahita, J. A., and Maeda, N. (1992) Spontaneous hypercholesterolemia and arterial lesions in mice lacking apolipoprotein E. *Science*. **258**, 468–71

135. Mahley, R. W., Huang, Y., and Rall, S. C. (1999) Pathogenesis of type III hyperlipoproteinemia (dysbetalipoproteinemia). Questions, quandaries, and paradoxes. *J. Lipid Res.* **40**, 1933–49

136. Rall, S. C., Newhouse, Y. M., Clarke, H. R. G., Weisgraber, K. H., McCarthy, B. J., Mahley, R. W., and Bersot, T. P. (1989) Type III hyperlipoproteinemia associated with apolipoprotein E phenotype E3/3. Structure and genetics of an apolipoprotein E3 variant. *J. Clin. Invest.* **83**, 1095–101

137. Horie, Y., Fazio, S., Westerlund, J. R., Weisgraber, K. H., and Rall, S. C. (1992) The functional characteristics of a human apolipoprotein E variant (cysteine at residue 142) may explain its association with dominant expression of type III hyperlipoproteinemia. *J. Biol. Chem.* **267**, 1962–8

138. Fazio, S., Lee, Y. L., Ji, Z. S., and Rall, S. C. (1993) Type III hyperlipoproteinemic phenotype in transgenic mice expressing dysfunctional apolipoprotein E. *J. Clin. Invest.* **92**, 1497–503

139. Ghiselli, G., Schaefer, E. J., Gascon, P., and Breser, H. B. (1981) Type III hyperlipoproteinemia associated with apolipoprotein E deficiency. *Science*. **214**, 1239–41

140. Mahley, R. W., and Hussain, M. M. (1991) Chylomicron and chylomicron remnant catabolism. *Curr. Opin. Lipidol.* **2**, 170–176

141. Mahley, R. W., Ji, Z. S., Brecht, W. J., Miranda, R. D., and He, D. (1994) Role of heparan sulfate proteoglycans and the LDL receptor-related protein in remnant lipoprotein metabolism. *Ann. N. Y. Acad. Sci.* **737**, 39–52

142. Mahley, R. W., and Huang, Y. (2007) Atherogenic remnant lipoproteins: Role for proteoglycans in trapping, transferring, and internalizing. *J. Clin. Invest.* **117**, 94–98

143. Kounnas, M. Z., Chappell, D. A., Wong, H., Argraves, W. S., and Strickland, D. K. (1995) The cellular internalization and degradation of hepatic lipase is mediated by low density lipoprotein receptor-related protein and requires cell surface proteoglycans. *J. Biol. Chem.* **270**, 9307–12

144. Mulder, M., Lombardi, P., Jansen, H., van Berkel, T. J., Frants, R. R., and Havekes, L. M. (1992) Heparan sulphate proteoglycans are involved in the lipoprotein lipase-mediated enhancement of the cellular binding of very low density and low density lipoproteins. *Biochem. Biophys. Res. Commun.* **185**, 582–7

145. Ji, Z. S., Brecht, W. J., Miranda, R. D., Hussain, M. M., Innerarity, T. L., and Mahley, R. W. (1993) Role of heparan sulfate proteoglycans in the binding and uptake of apolipoprotein E-enriched remnant lipoproteins by cultured cells. *J. Biol. Chem.* **268**, 10160–7

146. Ji, Z. S., Sanan, D. a, and Mahley, R. W. (1995) Intravenous heparinase inhibits remnant

lipoprotein clearance from the plasma and uptake by the liver: in vivo role of heparan sulfate proteoglycans. *J. Lipid Res.* **36**, 583–92

147. Wilsie, L. C., and Orlando, R. A. (2003) The low density lipoprotein receptor-related protein complexes with cell surface heparan sulfate proteoglycans to regulate proteoglycan-mediated lipoprotein catabolism. *J. Biol. Chem.* **278**, 15758–64

148. MacArthur, J. M., Bishop, J. R., Stanford, K. I., Wang, L., Bensadoun, A., Witztum, J. L., and Esko, J. D. (2007) Liver heparan sulfate proteoglycans mediate clearance of triglyceride-rich lipoproteins independently of LDL receptor family members. *J. Clin. Invest.* **117**, 153–64

149. Foley, E. M., Gordts, P. L. S. M., Stanford, K. I., Gonzales, J. C., Lawrence, R., Stoddard, N., and Esko, J. D. (2013) Hepatic remnant lipoprotein clearance by heparan sulfate proteoglycans and low-density lipoprotein receptors depend on dietary conditions in mice. *Arterioscler. Thromb. Vasc. Biol.* **33**, 2065–74

150. Gonzales, J. C., Gordts, P. L. S. M., Foley, E. M., and Esko, J. D. (2013) Apolipoproteins E and AV mediate lipoprotein clearance by hepatic proteoglycans. *J. Clin. Invest.* **123**, 2742–51

151. Söderberg, M., Edlund, C., Kristensson, K., and Dallner, G. (1990) Lipid compositions of different regions of the human brain during aging. *J. Neurochem.* **54**, 415–23

152. Dietschy, J. M., and Turley, S. D. (2004) Thematic review series: brain Lipids. Cholesterol metabolism in the central nervous system during early development and in the mature animal. *J. Lipid Res.* **45**, 1375–97

153. Dietschy, J. M. (2009) Central nervous system: cholesterol turnover, brain development and neurodegeneration. *Biol. Chem.* **390**, 287–93

154. Bauer, H.-C., Krizbai, I. A., Bauer, H., and Traweger, A. (2014) “You Shall Not Pass”-tight junctions of the blood brain barrier. *Front. Neurosci.* **8**, 392

155. Chobanian, A. V, and Hollander, W. (1962) Body cholesterol metabolism in man. I. The equilibration of serum and tissue cholesterol. *J. Clin. Invest.* **41**, 1732–7

156. Meaney, S., Hassan, M., Sakinis, A., Lütjohann, D., von Bergmann, K., Wennmalm, A., Diczfalusy, U., and Björkhem, I. (2001) Evidence that the major oxysterols in human circulation originate from distinct pools of cholesterol: a stable isotope study. *J. Lipid Res.* **42**, 70–8

157. Bloch, K., Berg, B. N., and Rittenberg, D. (1943) The biological conversion of cholesterol to cholic acid. *J Biol Chem*. **149**, 511–517

158. Quan, G., Xie, C., Dietschy, J. M., and Turley, S. D. (2003) Ontogenesis and regulation of cholesterol metabolism in the central nervous system of the mouse. *Dev. Brain Res.* **146**, 87–98

159. Pfrieger, F. W. (2003) Role of cholesterol in synapse formation and function. *Biochim. Biophys. Acta*. **1610**, 271–80

160. Koch, S., Donarski, N., Goetze, K., Kreckel, M., Stuerenburg, H. J., Buhmann, C., and Beisiegel, U. (2001) Characterization of four lipoprotein classes in human cerebrospinal fluid. *J. Lipid Res.* **42**, 1143–51

161. Xu, Q., Bernardo, A., Walker, D., Kanegawa, T., Mahley, R. W., and Huang, Y. (2006) Profile and regulation of apolipoprotein E (ApoE) expression in the CNS in mice with targeting of green fluorescent protein gene to the ApoE locus. *J. Neurosci.* **26**, 4985–94

162. Liu, M., Kuhel, D. G., Shen, L., Hui, D. Y., and Woods, S. C. (2012) Apolipoprotein E

does not cross the blood-cerebrospinal fluid barrier, as revealed by an improved technique for sampling CSF from mice. *Am. J. Physiol. Integr. Comp. Physiol.* **303**, R903–R908

163. Linton, M. F., Gish, R., Hubl, S. T., Bütler, E., Esquivel, C., Bry, W. I., Boyles, J. K., Wardell, M. R., and Young, S. G. (1991) Phenotypes of apolipoprotein B and apolipoprotein E after liver transplantation. *J. Clin. Invest.* **88**, 270–81

164. Stukas, S., Robert, J., Lee, M., Kulic, I., Carr, M., Tourigny, K., Fan, J., Namjoshi, D., Lemke, K., DeValle, N., Chan, J., Wilson, T., Wilkinson, A., Chapanian, R., Kizhakkedathu, J. N., Cirrito, J. R., Oda, M. N., and Wellington, C. L. (2014) Intravenously injected human apolipoprotein A-I rapidly enters the central nervous system via the choroid plexus. *J. Am. Heart Assoc.* **3**, e001156

165. Wahrle, S. E., Jiang, H., Parsadanian, M., Legleiter, J., Han, X., Fryer, J. D., Kowalewski, T., and Holtzman, D. M. (2004) ABCA1 is required for normal central nervous system ApoE levels and for lipidation of astrocyte-secreted apoE. *J. Biol. Chem.* **279**, 40987–93

166. Wahrle, S. E., Jiang, H., Parsadanian, M., Kim, J., Li, A., Knoten, A., Jain, S., Hirsch-Reinshagen, V., Wellington, C. L., Bales, K. R., Paul, S. M., and Holtzman, D. M. (2008) Overexpression of ABCA1 reduces amyloid deposition in the PDAPP mouse model of Alzheimer disease. *J. Clin. Invest.* **118**, 671–82

167. LaDu, M. J., Gilligan, S. M., Lukens, J. R., Cabana, V. G., Reardon, C. A., Van Eldik, L. J., and Holtzman, D. M. (1998) Nascent astrocyte particles differ from lipoproteins in CSF. *J. Neurochem.* **70**, 2070–81

168. DeMattos, R. B., Brendza, R. P., Heuser, J. E., Kierson, M., Cirrito, J. R., Fryer, J., Sullivan, P. M., Fagan, A. M., Han, X., and Holtzman, D. M. (2001) Purification and characterization of astrocyte-secreted apolipoprotein E and J-containing lipoproteins from wild-type and human apoE transgenic mice. *Neurochem. Int.* **39**, 415–25

169. Herz, J., and Bock, H. H. (2002) Lipoprotein receptors in the nervous system. *Annu. Rev. Biochem.* **71**, 405–34

170. Fryer, J. D., DeMattos, R. B., McCormick, L. M., O'Dell, M. A., Spinner, M. L., Bales, K. R., Paul, S. M., Sullivan, P. M., Parsadanian, M., Bu, G., and Holtzman, D. M. (2005) The low density lipoprotein receptor regulates the level of central nervous system human and murine apolipoprotein E but does not modify amyloid plaque pathology in PDAPP mice. *J. Biol. Chem.* **280**, 25754–25759

171. Liu, Q., Zerbinatti, C. V, Zhang, J., Hoe, H.-S., Wang, B., Cole, S. L., Herz, J., Muglia, L., and Bu, G. (2007) Amyloid precursor protein regulates brain apolipoprotein E and cholesterol metabolism through lipoprotein receptor LRP1. *Neuron*. **56**, 66–78

172. Kim, J., Castellano, J. M., Jiang, H., Basak, J. M., Parsadanian, M., Pham, V., Mason, S. M., Paul, S. M., and Holtzman, D. M. (2009) Overexpression of low-density lipoprotein receptor in the brain markedly inhibits amyloid deposition and increases extracellular A beta clearance. *Neuron*. **64**, 632–44

173. Cui, H., Freeman, C., Jacobson, G. A., and Small, D. H. (2013) Proteoglycans in the central nervous system: role in development, neural repair, and Alzheimer's disease. *IUBMB Life*. **65**, 108–20

174. Fu, Y., Zhao, J., Atagi, Y., Nielsen, H. M., Liu, C.-C., Zheng, H., Shinohara, M., Kanekiyo, T., and Bu, G. (2016) Apolipoprotein E lipoprotein particles inhibit amyloid-β uptake through cell surface heparan sulphate proteoglycan. *Mol. Neurodegener.* **11**, 37

175. Rapp, A., and Hüttinger, M. (2005) Role of chondroitin sulphate in the uptake of β-VLDL

by brain cells. *Eur. J. Neurosci.* **22**, 1400–1408

176. Nathan, B. P., Bellosta, S., Sanan, D. a, Weisgraber, K. H., Mahley, R. W., and Pitas, R. E. (1994) Differential effects of apolipoproteins E3 and E4 on neuronal growth in vitro. *Science*. **264**, 850–2

177. Nathan, B. P., Chang, K. C., Bellosta, S., Brisch, E., Ge, N., Mahley, R. W., and Pitas, R. E. (1995) The inhibitory effect of apolipoprotein E4 on neurite outgrowth is associated with microtubule depolymerization. *J. Biol. Chem.* **270**, 19791–9

178. Nathan, B. P., Jiang, Y., Wong, G. K., Shen, F., Brewer, G. J., and Struble, R. G. (2002) Apolipoprotein E4 inhibits, and apolipoprotein E3 promotes neurite outgrowth in cultured adult mouse cortical neurons through the low-density lipoprotein receptor-related protein. *Brain Res.* **928**, 96–105

179. Holtzman, D. M., Pitas, R. E., Kilbridge, J., Nathan, B., Mahley, R. W., Bu, G., and Schwartz, A. L. (1995) Low density lipoprotein receptor-related protein mediates apolipoprotein E-dependent neurite outgrowth in a central nervous system-derived neuronal cell line. *Proc. Natl. Acad. Sci. U. S. A.* **92**, 9480–4

180. Sun, Y., Wu, S., Bu, G., Onifade, M. K., Patel, S. N., LaDu, M. J., Fagan, a M., and Holtzman, D. M. (1998) Glial fibrillary acidic protein-apolipoprotein E (apoE) transgenic mice: astrocyte-specific expression and differing biological effects of astrocyte-secreted apoE3 and apoE4 lipoproteins. *J. Neurosci.* **18**, 3261–3272

181. Teter, B., Xu, P. T., Gilbert, J. R., Roses, A. D., Galasko, D., and Cole, G. M. (1999) Human apolipoprotein E isoform-specific differences in neuronal sprouting in organotypic hippocampal culture. *J. Neurochem.* **73**, 2613–6

182. Stoll, G., and Müller, H. W. (1986) Macrophages in the peripheral nervous system and astroglia in the central nervous system of rat commonly express apolipoprotein E during development but differ in their response to injury. *Neurosci. Lett.* **72**, 233–8

183. Ignatius, M. J., Gebicke-Härter, P. J., Skene, J. H., Schilling, J. W., Weisgraber, K. H., Mahley, R. W., and Shooter, E. M. (1986) Expression of apolipoprotein E during nerve degeneration and regeneration. *Proc. Natl. Acad. Sci. U. S. A.* **83**, 1125–9

184. Snipes, G. J., McGuire, C. B., Norden, J. J., and Freeman, J. a (1986) Nerve injury stimulates the secretion of apolipoprotein E by nonneuronal cells. *Proc. Natl. Acad. Sci. U. S. A.* **83**, 1130–4

185. White, F., Nicoll, J. A., and Horsburgh, K. (2001) Alterations in ApoE and ApoJ in relation to degeneration and regeneration in a mouse model of entorhinal cortex lesion. *Exp. Neurol.* **169**, 307–18

186. Iwata, A., Browne, K. D., Chen, X.-H., Yuguchi, T., and Smith, D. H. (2005) Traumatic brain injury induces biphasic upregulation of ApoE and ApoJ protein in rats. *J. Neurosci. Res.* **82**, 103–14

187. Horsburgh, K., Fitzpatrick, M., Nilsen, M., and Nicoll, J. A. (1997) Marked alterations in the cellular localisation and levels of apolipoprotein E following acute subdural haematoma in rat. *Brain Res.* **763**, 103–10

188. Chen, Y., Lomnitski, L., Michaelson, D. M., and Shohami, E. (1997) Motor and cognitive deficits in apolipoprotein E-deficient mice after closed head injury. *Neuroscience*. **80**, 1255–62

189. Du, Y., Chen, X., Wei, X., Bales, K. R., Berg, D. T., Paul, S. M., Farlow, M. R., Maloney, B., Ge, Y.-W., and Lahiri, D. K. (2005) NF-(kappa)B mediates amyloid beta peptide-stimulated activity of the human apolipoprotein E gene promoter in human astroglial

cells. *Brain Res. Mol. Brain Res.* **136**, 177–88

190. Lahiri, D. K. (2004) Apolipoprotein E as a target for developing new therapeutics for Alzheimer's disease based on studies from protein, RNA, and regulatory region of the gene. *J. Mol. Neurosci.* **23**, 225–33

191. Bales, K. R., Du, Y., Holtzman, D., Cordell, B., and Paul, S. M. (2000) Neuroinflammation and Alzheimer's disease: critical roles for cytokine/Abeta-induced glial activation, NF-kappaB, and apolipoprotein E. *Neurobiol. Aging*. **21**, 427-32; discussion 451–3

192. Properzi, F., Lin, R., Kwok, J., Naidu, M., van Kuppevelt, T. H., Ten Dam, G. B., Camargo, L. M., Raha-Chowdhury, R., Furukawa, Y., Mikami, T., Sugahara, K., and Fawcett, J. W. (2008) Heparan sulphate proteoglycans in glia and in the normal and injured CNS: expression of sulphotransferases and changes in sulphation. *Eur. J. Neurosci.* **27**, 593–604

193. Iseki, K., Hagino, S., Mori, T., Zhang, Y., Yokoya, S., Takaki, H., Tase, C., Murakawa, M., and Wanaka, A. (2002) Increased syndecan expression by pleiotrophin and FGF receptor-expressing astrocytes in injured brain tissue. *Glia*. **39**, 1–9

194. Farhy Tselnicker, I., Boisvert, M. M., and Allen, N. J. (2014) The role of neuronal versus astrocyte-derived heparan sulfate proteoglycans in brain development and injury. *Biochem. Soc. Trans.* **42**, 1263–9

195. Aggerbeck, L. P., Wetterau, J. R., Weisgraber, K. H., Wu, C. S., and Lindgren, F. T. (1988) Human apolipoprotein E3 in aqueous solution. II. Properties of the amino- and carboxyl-terminal domains. *J. Biol. Chem.* **263**, 6249–58

196. Wetterau, J. R., Aggerbeck, L. P., Rall, S. C., and Weisgraber, K. H. (1988) Human apolipoprotein E3 in aqueous solution. I. Evidence for two structural domains. *J. Biol. Chem.* **263**, 6240–8

197. Weisgraber, K. H., Innerarity, T. L., and Mahley, R. W. (1978) Role of lysine residues of plasma lipoproteins in high affinity binding to cell surface receptors on human fibroblasts. *J. Biol. Chem.* **253**, 9053–62

198. Mahley, R. W., Innerarity, T. L., Pitas, R. E., Weisgraber, K. H., Brown, J. H., and Gross, E. (1977) Inhibition of lipoprotein binding to cell surface receptors of fibroblasts following selective modification of arginyl residues in arginine-rich and B apoproteins. *J. Biol. Chem.* **252**, 7279–87

199. Weisgraber, K. H., Innerarity, T. L., and Mahley, R. W. (1982) Abnormal lipoprotein receptor-binding activity of the human E apoprotein due to cysteine-arginine interchange at a single site. *J. Biol. Chem.* **257**, 2518–21

200. Weisgraber, K. H. (1994) Apolipoprotein E: structure-function relationships. *Adv. Protein Chem.* **45**, 249–302

201. Lalazar, a, Weisgraber, K. H., Rall, S. C., Giladi, H., Innerarity, T. L., Levanon, A. Z., Boyles, J. K., Amit, B., Gorecki, M., and Mahley, R. W. (1988) Site-specific mutagenesis of human apolipoprotein E. Receptor binding activity of variants with single amino acid substitutions. *J. Biol. Chem.* **263**, 3542–5

202. Innerarity, T. L., Friedlander, E. J., Rall, S. C., Weisgraber, K. H., and Mahley, R. W. (1983) The receptor-binding domain of human apolipoprotein E. Binding of apolipoprotein E fragments. *J. Biol. Chem.* **258**, 12341–7

203. Weisgraber, K. H., Innerarity, T. L., Harder, K. J., Mahley, R. W., Milne, R. W., Marcel, Y. L., and Sparrow, J. T. (1983) The receptor-binding domain of human apolipoprotein

E. Monoclonal antibody inhibition of binding. *J. Biol. Chem.* **258**, 12348–54

204. Morrow, J. a, Arnold, K. S., Dong, J., Balestra, M. E., Innerarity, T. L., and Weisgraber, K. H. (2000) Effect of arginine 172 on the binding of apolipoprotein E to the low density lipoprotein receptor. *J. Biol. Chem.* **275**, 2576–80

205. Luo, C. C., Li, W. H., Moore, M. N., and Chan, L. (1986) Structure and evolution of the apolipoprotein multigene family. *J. Mol. Biol.* **187**, 325–340

206. Segrest, J. P., Jackson, R. L., Morrisett, J. D., and Gotto, A. M. (1974) A molecular theory of lipid-protein interactions in the plasma lipoproteins. *FEBS Lett.* **38**, 247–58

207. Sparrow, J. T., Sparrow, D. a, Fernando, G., Culwell, a R., Kovar, M., and Gotto, a M. (1992) Apolipoprotein E: phospholipid binding studies with synthetic peptides from the carboxyl terminus. *Biochemistry*. **31**, 1065–8

208. Westerlund, J. a, and Weisgraber, K. H. (1993) Discrete carboxyl-terminal segments of apolipoprotein E mediate lipoprotein association and protein oligomerization. *J. Biol. Chem.* **268**, 15745–50

209. Weisgraber, K. H., Rall, S. C., Mahley, R. W., Milne, R. W., Marcel, Y. L., and Sparrow, J. T. (1986) Human apolipoprotein E. Determination of the heparin binding sites of apolipoprotein E3. *J. Biol. Chem.* **261**, 2068–76

210. Cardin, A. D., Hirose, N., Blankenship, D. T., Jackson, R. L., Harmony, J. A., Sparrow, D. A., and Sparrow, J. T. (1986) Binding of a high reactive heparin to human apolipoprotein E: identification of two heparin-binding domains. *Biochem. Biophys. Res. Commun.* **134**, 783–9

211. Ji, Z. S., Fazio, S., and Mahley, R. W. (1994) Variable heparan sulfate proteoglycan binding of apolipoprotein E variants may modulate the expression of type III hyperlipoproteinemia. *J. Biol. Chem.* **269**, 13421–8

212. Dong, J., Peters-Libeu, C. a., Weisgraber, K. H., Segelke, B. W., Rupp, B., Capila, I., Hernáiz, M. J., LeBrun, L. a., and Linhardt, R. J. (2001) Interaction of the N-terminal domain of apolipoprotein E4 with heparin. *Biochemistry*. **40**, 2826–34

213. Libeu, C. P., Lund-Katz, S., Phillips, M. C., Wehrli, S., Hernáiz, M. J., Capila, I., Linhardt, R. J., Raffaï, R. L., Newhouse, Y. M., Zhou, F., and Weisgraber, K. H. (2001) New insights into the heparan sulfate proteoglycan-binding activity of apolipoprotein E. *J. Biol. Chem.* **276**, 39138–44

214. Innerarity, T. L., Pitas, R. E., and Mahley, R. W. (1979) Binding of arginine-rich (E) apoprotein after recombination with phospholipid vesicles to the low density lipoprotein receptors of fibroblasts. *J. Biol. Chem.* **254**, 4186–90

215. Windler, E., Chao, Y., and Havel, R. J. (1980) Determinants of hepatic uptake of triglyceride-rich lipoproteins and their remnants in the rat. *J. Biol. Chem.* **255**, 5475–80

216. Windler, E., and Havel, R. J. (1985) Inhibitory effects of C apolipoproteins from rats and humans on the uptake of triglyceride-rich lipoproteins and their remnants by the perfused rat liver. *J. Lipid Res.* **26**, 556–65

217. Shelburne, F., Hanks, H., Meyers, W., and Quarfordt, S. (1980) Effect of apoproteins on hepatic uptake of triglyceride emulsions in the rat. *J. Clin. Invest.* **65**, 652–658

218. Kowal, R. C., Herz, J., Weisgraber, K. H., Mahley, R. W., Brown, M. S., and Goldstein, J. L. (1990) Opposing effects of apolipoproteins E and C on lipoprotein binding to low density lipoprotein receptor-related protein. *J. Biol. Chem.* **265**, 10771–10779

219. Weisgraber, K. H., Mahley, R. W., Kowal, R. C., Herz, J., Goldstein, J. L., and Brown,

M. S. (1990) Apolipoprotein C-I modulates the interaction of apolipoprotein E with beta-migrating very low density lipoproteins (beta-VLDL) and inhibits binding of beta-VLDL to low density lipoprotein receptor-related protein. *J. Biol. Chem.* **265**, 22453–9

220. Sehayek, E., Lewin-Velvert, U., Chajek-Shaul, T., and Eisenberg, S. (1991) Lipolysis exposes unreactive endogenous apolipoprotein E-3 in human and rat plasma very low density lipoprotein. *J. Clin. Invest.* **88**, 553–560

221. Newhouse, Y., Peters-Libeu, C., and Weisgraber, K. H. (2005) Crystallization and preliminary X-ray diffraction analysis of apolipoprotein E-containing lipoprotein particles. *Acta Crystallogr. Sect. F. Struct. Biol. Cryst. Commun.* **61**, 981–4

222. Peters-Libeu, C. A., Newhouse, Y., Hatters, D. M., and Weisgraber, K. H. (2006) Model of biologically active apolipoprotein E bound to dipalmitoylphosphatidylcholine. *J. Biol. Chem.* **281**, 1073–1079

223. Drury, J., and Narayanaswami, V. (2005) Examination of Lipid-bound Conformation of Apolipoprotein E4 by Pyrene Excimer Fluorescence. *J. Biol. Chem.* **280**, 14605–14610

224. Hatters, D. M., Budamagunta, M. S., Voss, J. C., and Weisgraber, K. H. (2005) Modulation of apolipoprotein E structure by domain interaction: differences in lipid-bound and lipid-free forms. *J. Biol. Chem.* **280**, 34288–95

225. Hatters, D. M., Voss, J. C., Budamagunta, M. S., Newhouse, Y. N., and Weisgraber, K. H. (2009) Insight on the molecular envelope of lipid-bound apolipoprotein E from electron paramagnetic resonance spectroscopy. *J. Mol. Biol.* **386**, 261–271

226. Hatters, D. M., Peters-Libeu, C. a., and Weisgraber, K. H. (2006) Apolipoprotein E structure: insights into function. *Trends Biochem. Sci.* **31**, 445–454

227. Saito, H., Dhanasekaran, P., Baldwin, F., Weisgraber, K. H., Lund-Katz, S., and Phillips, M. C. (2001) Lipid binding-induced conformational change in human apolipoprotein E. Evidence for two lipid-bound states on spherical particles. *J. Biol. Chem.* **276**, 40949–54

228. Nguyen, D., Dhanasekaran, P., Phillips, M. C., and Lund-Katz, S. (2009) Molecular mechanism of apolipoprotein E binding to lipoprotein particles. *Biochemistry*. **48**, 3025–32

229. Mizuguchi, C., Hata, M., Dhanasekaran, P., Nickel, M., Phillips, M. C., Lund-Katz, S., and Saito, H. (2012) Fluorescence analysis of the lipid binding-induced conformational change of apolipoprotein E4. *Biochemistry*. **51**, 5580–8

230. Nguyen, D., Dhanasekaran, P., Nickel, M., Nakatani, R., Saito, H., Phillips, M. C., and Lund-Katz, S. (2010) Molecular basis for the differences in lipid and lipoprotein binding properties of human apolipoproteins E3 and E4. *Biochemistry*. **49**, 10881–9

231. Schneider, W. J., Kovanen, P. T., Brown, M. S., Goldstein, J. L., Utermann, G., Weber, W., Havel, R. J., Kotite, L., Kane, J. P., Innerarity, T. L., and Mahley, R. W. (1981) Familial dysbetalipoproteinemia. Abnormal binding of mutant apoprotein E to low density lipoprotein receptors of human fibroblasts and membranes from liver and adrenal of rats, rabbits, and cows. *J. Clin. Invest.* **68**, 1075–1085

232. Dong, L. M., Parkin, S., Trakhanov, S. D., Rupp, B., Simmons, T., Arnold, K. S., Newhouse, Y. M., Innerarity, T. L., and Weisgraber, K. H. (1996) Novel mechanism for defective receptor binding of apolipoprotein E2 in type III hyperlipoproteinemia. *Nat. Struct. Biol.* **3**, 718–22

233. Wilson, C., Mau, T., Weisgraber, K. H., Wardell, M. R., Mahley, R. W., and Agard, D. a (1994) Salt bridge relay triggers defective LDL receptor binding by a mutant

apolipoprotein. *Structure*. **2**, 713–8

234. Mahley, R. W., Weisgraber, K. H., and Huang, Y. (2006) Apolipoprotein E4: a causative factor and therapeutic target in neuropathology, including Alzheimer's disease. *Proc. Natl. Acad. Sci. U. S. A.* **103**, 5644–5651

235. Steinmetz, A., Jakobs, C., Motzny, S., and Kaffarnik, H. (1989) Differential distribution of apolipoprotein E isoforms in human plasma lipoproteins. *Arteriosclerosis*. **9**, 405–11

236. Gregg, R. E., Zech, L. a, Schaefer, E. J., Stark, D., Wilson, D., and Brewer, H. B. (1986) Abnormal in vivo metabolism of apolipoprotein E4 in humans. *J. Clin. Invest.* **78**, 815–21

237. Weisgraber, K. H. (1990) Apolipoprotein E distribution among human plasma lipoproteins: role of the cysteine-arginine interchange at residue 112. *J. Lipid Res.* **31**, 1503–11

238. Dong, L. M., Wilson, C., Wardell, M. R., Simmons, T., Mahley, R. W., Weisgraber, K. H., and Agard, D. a (1994) Human apolipoprotein E. Role of arginine 61 in mediating the lipoprotein preferences of the E3 and E4 isoforms. *J. Biol. Chem.* **269**, 22358–65

239. Dong, L. M., and Weisgraber, K. H. (1996) Human apolipoprotein E4 domain interaction. Arginine 61 and glutamic acid 255 interact to direct the preference for very low density lipoproteins. *J. Biol. Chem.* **271**, 19053–7

240. Xu, Q., Brecht, W. J., Weisgraber, K. H., Mahley, R. W., and Huang, Y. (2004) Apolipoprotein E4 domain interaction occurs in living neuronal cells as determined by fluorescence resonance energy transfer. *J. Biol. Chem.* **279**, 25511–25516

241. Raffai, R. L., Dong, L. M., Farese, R. V, and Weisgraber, K. H. (2001) Introduction of human apolipoprotein E4 "domain interaction" into mouse apolipoprotein E. *Proc. Natl. Acad. Sci. U. S. A.* **98**, 11587–91

242. Chen, J., Li, Q., and Wang, J. (2011) Topology of human apolipoprotein E3 uniquely regulates its diverse biological functions. *Proc. Natl. Acad. Sci. U. S. A.* **108**, 14813–14818

243. Zhang, Y., Vasudevan, S., Sojitrawala, R., Zhao, W., Cui, C., Xu, C., Fan, D., Newhouse, Y., Balestra, R., Jerome, W. G., Weisgraber, K., Li, Q., and Wang, J. (2007) A monomeric, biologically active, full-length human apolipoprotein E. *Biochemistry*. **46**, 10722–32

244. Frieden, C., and Garai, K. (2013) Concerning the structure of apoE. *Protein Sci.* **22**, 1820–1825

245. Frieden, C., and Garai, K. (2012) Structural differences between apoE3 and apoE4 may be useful in developing therapeutic agents for Alzheimer's disease. *Proc. Natl. Acad. Sci.* **109**, 8913–8918

246. Chen, H.-K. K., Liu, Z., Meyer-Franke, A., Brodbeck, J., Miranda, R. D., McGuire, J. G., Pleiss, M. a., Ji, Z.-S. S., Balestra, M. E., Walker, D. W., Xu, Q., Jeong, D. E., Budamagunta, M. S., Voss, J. C., Freedman, S. B., Weisgraber, K. H., Huang, Y., and Mahley, R. W. (2012) Small molecule structure correctors abolish detrimental effects of apolipoprotein E4 in cultured neurons. *J. Biol. Chem.* **287**, 5253–5266

247. Kara, E., Marks, J. D., Fan, Z., Klickstein, J. A., Roe, A. D., Krogh, K. A., Wegmann, S., Maesako, M., Luo, C. C., Mylvaganam, R., Berezovska, O., Hudry, E., and Hyman, B. T. (2017) Isoform and cell type-specific structure of Apolipoprotein E lipoparticles as revealed by a novel Forster Resonance Energy Transfer assay. *J. Biol. Chem.* **292**, jbc.M117.784264

248. Morrow, J. a, Segall, M. L., Lund-Katz, S., Phillips, M. C., Knapp, M., Rupp, B., and Weisgraber, K. H. (2000) Differences in stability among the human apolipoprotein E isoforms determined by the amino-terminal domain. *Biochemistry*. **39**, 11657–11666

249. Acharya, P., Segall, M. L., Zaiou, M., Morrow, J. a, Weisgraber, K. H., Phillips, M. C., Lund-Katz, S., and Snow, J. (2002) Comparison of the stabilities and unfolding pathways of human apolipoprotein E isoforms by differential scanning calorimetry and circular dichroism. *Biochim. Biophys. Acta*. **1584**, 9–19

250. Morrow, J. a., Hatters, D. M., Lu, B., Hochtl, P., Oberg, K. A., Rupp, B., and Weisgraber, K. H. (2002) Apolipoprotein E4 forms a molten globule. A potential basis for its association with disease. *J. Biol. Chem.* **277**, 50380–5

251. Hatters, D. M., Zhong, N., Rutenber, E., and Weisgraber, K. H. (2006) Amino-terminal Domain Stability Mediates Apolipoprotein E Aggregation into Neurotoxic Fibrils. *J. Mol. Biol.* **361**, 932–944

252. Huang, Y., and Mahley, R. W. (2014) Apolipoprotein E: Structure and function in lipid metabolism, neurobiology, and Alzheimer's diseases. *Neurobiol. Dis.* **72**, 3–12

253. Wisniewski, T., and Frangione, B. (1992) Apolipoprotein E: a pathological chaperone protein in patients with cerebral and systemic amyloid. *Neurosci. Lett.* **135**, 235–8

254. Namba, Y., Tomonaga, M., Kawasaki, H., Otomo, E., and Ikeda, K. (1991) Apolipoprotein E immunoreactivity in cerebral amyloid deposits and neurofibrillary tangles in Alzheimer's disease and kuru plaque amyloid in Creutzfeldt-Jakob disease. *Brain Res.* **541**, 163–6

255. Rebeck, G. W., Reiter, J. S., Strickland, D. K., and Hyman, B. T. (1993) Apolipoprotein E in sporadic Alzheimer's disease: allelic variation and receptor interactions. *Neuron*. **11**, 575–80

256. Schmechel, D. E., Saunders, A. M., Strittmatter, W. J., Crain, B. J., Hulette, C. M., Joo, S. H., Pericak-Vance, M. A., Goldgaber, D., and Roses, A. D. (1993) Increased amyloid beta-peptide deposition in cerebral cortex as a consequence of apolipoprotein E genotype in late-onset Alzheimer disease. *Proc. Natl. Acad. Sci. U. S. A.* **90**, 9649–53

257. Tiraboschi, P., Hansen, L. a, Masliah, E., Alford, M., Thal, L. J., and Corey-Bloom, J. (2004) Impact of APOE genotype on neuropathologic and neurochemical markers of Alzheimer disease. *Neurology*. **62**, 1977–83

258. Reiman, E. M., Chen, K., Liu, X., Bandy, D., Yu, M., Lee, W., Ayutyanont, N., Keppler, J., Reeder, S. a, Langbaum, J. B. S., Alexander, G. E., Klunk, W. E., Mathis, C. a, Price, J. C., Aizenstein, H. J., DeKosky, S. T., and Caselli, R. J. (2009) Fibrillar amyloid-beta burden in cognitively normal people at 3 levels of genetic risk for Alzheimer's disease. *Proc. Natl. Acad. Sci. U. S. A.* **106**, 6820–5

259. Morris, J. C., Roe, C. M., Xiong, C., Fagan, A. M., Goate, A. M., Holtzman, D. M., and Mintun, M. A. (2010) APOE predicts amyloid-beta but not tau Alzheimer pathology in cognitively normal aging. *Ann. Neurol.* **67**, 122–31

260. Rowe, C. C., Ellis, K. a., Rimajova, M., Bourgeat, P., Pike, K. E., Jones, G., Fripp, J., Tochon-Danguy, H., Morandeau, L., O'Keefe, G., Price, R., Raniga, P., Robins, P., Acosta, O., Lenzo, N., Szoeke, C., Salvado, O., Head, R., Martins, R., Masters, C. L., Ames, D., and Villemagne, V. L. (2010) Amyloid imaging results from the Australian Imaging, Biomarkers and Lifestyle (AIBL) study of aging. *Neurobiol. Aging*. **31**, 1275–83

261. Kantarci, K., Lowe, V., Przybelski, S. a., Weigand, S. D., Senjem, M. L., Ivnik, R. J., Preboske, G. M., Roberts, R., Geda, Y. E., Boeve, B. F., Knopman, D. S., Petersen, R.

C., and Jack, C. R. (2012) APOE modifies the association between Aβ load and cognition in cognitively normal older adults. *Neurology*. **78**, 232–40

262. Fleisher, A. S., Chen, K., Liu, X., Ayutyanont, N., Roontiva, A., Thiyyagura, P., Protas, H., Joshi, A. D., Sabbagh, M., Sadowsky, C. H., Sperling, R. a., Clark, C. M., Mintun, M. a., Pontecorvo, M. J., Coleman, R. E., Doraiswamy, P. M., Johnson, K. a., Carpenter, A. P., Skovronsky, D. M., and Reiman, E. M. (2013) Apolipoprotein E ε4 and age effects on florbetapir positron emission tomography in healthy aging and Alzheimer disease. *Neurobiol. Aging*. **34**, 1–12

263. Murphy, K. R., Landau, S. M., Choudhury, K. R., Hostage, C. A., Shpanskaya, K. S., Sair, H. I., Petrella, J. R., Wong, T. Z., Doraiswamy, P. M., and Alzheimer's Disease Neuroimaging Initiative (2013) Mapping the effects of ApoE4, age and cognitive status on 18F-florbetapir PET measured regional cortical patterns of beta-amyloid density and growth. *Neuroimage*. **78**, 474–80

264. LaDu, M. J., Falduto, M. T., Manelli, A. M., Reardon, C. A., Getz, G. S., and Frail, D. E. (1994) Isoform-specific binding of apolipoprotein E to beta-amyloid. *J. Biol. Chem.* **269**, 23403–6

265. Zhou, Z., Smith, J. D., Greengard, P., and Gandy, S. (1996) Alzheimer amyloid-beta peptide forms denaturant-resistant complex with type epsilon 3 but not type epsilon 4 isoform of native apolipoprotein E. *Mol. Med.* **2**, 175–80

266. Wisniewski, T., Golabek, A., Matsubara, E., Ghiso, J., and Frangione, B. (1993) Apolipoprotein E: binding to soluble Alzheimer's beta-amyloid. *Biochem. Biophys. Res. Commun.* **192**, 359–65

267. Strittmatter, W. J., Weisgraber, K. H., Huang, D. Y., Dong, L. M., Salvesen, G. S., Pericak-Vance, M., Schmechel, D., Saunders, A. M., Goldgaber, D., and Roses, A. D. (1993) Binding of human apolipoprotein E to synthetic amyloid beta peptide: isoform-specific effects and implications for late-onset Alzheimer disease. *Proc. Natl. Acad. Sci. U. S. A.* **90**, 8098–102

268. Sanan, D. A., Weisgraber, K. H., Russell, S. J., Mahley, R. W., Huang, D., Saunders, A., Schmechel, D., Wisniewski, T., Frangione, B., and Roses, A. D. (1994) Apolipoprotein E associates with beta amyloid peptide of Alzheimer's disease to form novel monofibrils. Isoform apoE4 associates more efficiently than apoE3. *J. Clin. Invest.* **94**, 860–9

269. LaDu, M. J., Pederson, T. M., Frail, D. E., Reardon, C. A., Getz, G. S., and Falduto, M. T. (1995) Purification of apolipoprotein E attenuates isoform-specific binding to beta-amyloid. *J. Biol. Chem.* **270**, 9039–42

270. Tokuda, T., Calero, M., Matsubara, E., Vidal, R., Kumar, A., Permanne, B., Zlokovic, B., Smith, J. D., Ladu, M. J., Rostagno, A., Frangione, B., and Ghiso, J. (2000) Lipidation of apolipoprotein E influences its isoform-specific interaction with Alzheimer's amyloid beta peptides. *Biochem. J.* **348 Pt 2**, 359–65

271. Yang, D. S., Smith, J. D., Zhou, Z., Gandy, S. E., and Martins, R. N. (1997) Characterization of the binding of amyloid-beta peptide to cell culture-derived native apolipoprotein E2, E3, and E4 isoforms and to isoforms from human plasma. *J. Neurochem.* **68**, 721–5

272. Chan, W., Fornwald, J., Brawner, M., and Wetzel, R. (1996) Native complex formation between apolipoprotein E isoforms and the Alzheimer's disease peptide A beta. *Biochemistry*. **35**, 7123–30

273. Ma, J., Yee, A., Brewer, H. B., Das, S., and Potter, H. (1994) Amyloid-associated

proteins α1-antichymotrypsin and apolipoprotein E promote assembly of Alzheimer β-protein into filaments. *Nature*. **372**, 92–94

274. Wisniewski, T., Castaño, E. M., Golabek, A., Vogel, T., and Frangione, B. (1994) Acceleration of Alzheimer's fibril formation by apolipoprotein E in vitro. *Am. J. Pathol.* **145**, 1030–5

275. Castano, E. M., Prelli, F., Wisniewski, T., Golabek, A., Kumar, R. a, Soto, C., and Frangione, B. (1995) Fibrillogenesis in Alzheimer's disease of amyloid beta peptides and apolipoprotein E. *Biochem. J.* **306 (Pt 2)**, 599–604

276. Webster, S., and Rogers, J. (1996) Relative efficacies of amyloid β peptide (Aβ) binding proteins in Aβ aggregation. *J. Neurosci. Res.* **66**, 58–66

277. Naiki, H., Gejyo, F., and Nakakuki, K. (1997) Concentration-dependent inhibitory effects of apolipoprotein E on Alzheimer's beta-amyloid fibril formation in vitro. *Biochemistry*. **36**, 6243–50

278. Wood, S. J., Chan, W., and Wetzel, R. (1996) Seeding of A beta fibril formation is inhibited by all three isotypes of apolipoprotein E. *Biochemistry*. **35**, 12623–8

279. Evans, K. C., Berger, E. P., Cho, C. G., Weisgraber, K. H., and Lansbury, P. T. (1995) Apolipoprotein E is a kinetic but not a thermodynamic inhibitor of amyloid formation: implications for the pathogenesis and treatment of Alzheimer disease. *Proc. Natl. Acad. Sci. U. S. A.* **92**, 763–7

280. Beffert, U., and Poirier, J. (1998) ApoE associated with lipid has a reduced capacity to inhibit beta-amyloid fibril formation. *Neuroreport*. **9**, 3321–3

281. Winkler, K., Scharnagl, H., Tisljar, U., Hoschützky, H., Friedrich, I., Hoffmann, M. M., Hüttinger, M., Wieland, H., and März, W. (1999) Competition of Abeta amyloid peptide and apolipoprotein E for receptor-mediated endocytosis. *J. Lipid Res.* **40**, 447–55

282. Goldgaber, D., Schwarzman, A. I., Bhasin, R., Gregori, L., Schmechel, D., Saunders, A. M., Roses, A. D., and Strittmatter, W. J. (1993) Sequestration of amyloid beta-peptide. *Ann. N. Y. Acad. Sci.* **695**, 139–43

283. Cerf, E., Gustot, A., Goormaghtigh, E., Ruysschaert, J.-M., and Raussens, V. (2011) High ability of apolipoprotein E4 to stabilize amyloid-β peptide oligomers, the pathological entities responsible for Alzheimer's disease. *FASEB J.* **25**, 1585–95

284. Kim, J., Basak, J. M., and Holtzman, D. M. (2009) The role of apolipoprotein E in Alzheimer's disease. *Neuron*. **63**, 287–303

285. Games, D., Adams, D., Alessandrini, R., Barbour, R., Berthelette, P., Blackwell, C., Carr, T., Clemens, J., Donaldson, T., and Gillespie, F. (1995) Alzheimer-type neuropathology in transgenic mice overexpressing V717F beta-amyloid precursor protein. *Nature*. **373**, 523–7

286. Bales, K. R., Verina, T., Dodel, R. C., Du, Y., Altstiel, L., Bender, M., Hyslop, P., Johnstone, E. M., Little, S. P., Cummins, D. J., Piccardo, P., Ghetti, B., and Paul, S. M. (1997) Lack of apolipoprotein E dramatically reduces amyloid beta-peptide deposition. *Nat. Genet.* **17**, 263–4

287. Holtzman, D. M., Bales, K. R., Wu, S., Bhat, P., Parsadanian, M., Fagan, a M., Chang, L. K., Sun, Y., and Paul, S. M. (1999) Expression of human apolipoprotein E reduces amyloid-beta deposition in a mouse model of Alzheimer's disease. *J. Clin. Invest.* **103**, R15–R21

288. Holtzman, D. M., Bales, K. R., Tenkova, T., Fagan, a M., Parsadanian, M., Sartorius,

L. J., Mackey, B., Olney, J., McKeel, D., Wozniak, D., and Paul, S. M. (2000) Apolipoprotein E isoform-dependent amyloid deposition and neuritic degeneration in a mouse model of Alzheimer's disease. *Proc. Natl. Acad. Sci. U. S. A.* **97**, 2892–7

289. Fagan, A. M., Watson, M., Parsadanian, M., Bales, K. R., Paul, S. M., and Holtzman, D. M. (2002) Human and murine ApoE markedly alters A beta metabolism before and after plaque formation in a mouse model of Alzheimer's disease. *Neurobiol. Dis.* **9**, 305–318

290. Dodart, J.-C., Marr, R. A., Koistinaho, M., Gregersen, B. M., Malkani, S., Verma, I. M., and Paul, S. M. (2005) Gene delivery of human apolipoprotein E alters brain Abeta burden in a mouse model of Alzheimer's disease. *Proc. Natl. Acad. Sci. U. S. A.* **102**, 1211–6

291. Hudry, E., Dashkoff, J., Roe, A. D., Takeda, S., Koffie, R. M., Hashimoto, T., Scheel, M., Spires-Jones, T., Arbel-Ornath, M., Betensky, R., Davidson, B. L., and Hyman, B. T. (2013) Gene Transfer of Human Apoe Isoforms Results in Differential Modulation of Amyloid Deposition and Neurotoxicity in Mouse Brain. *Sci. Transl. Med.* **5**, 212ra161-212ra161

292. Kanekiyo, T., Xu, H., and Bu, G. (2014) ApoE and Aβ in Alzheimer's disease: accidental encounters or partners? *Neuron*. **81**, 740–54

293. Saido, T., and Leissring, M. a (2012) Proteolytic degradation of amyloid β-protein. *Cold Spring Harb. Perspect. Med.* **2**, a006379

294. Iwata, N., Tsubuki, S., Takaki, Y., Watanabe, K., Sekiguchi, M., Hosoki, E., Kawashima-Morishima, M., Lee, H. J., Hama, E., Sekine-Aizawa, Y., and Saido, T. C. (2000) Identification of the major Abeta1-42-degrading catabolic pathway in brain parenchyma: suppression leads to biochemical and pathological deposition. *Nat. Med.* **6**, 143–50

295. Farris, W., Schütz, S. G., Cirrito, J. R., Shankar, G. M., Sun, X., George, A., Leissring, M. a., Walsh, D. M., Qiu, W. Q., Holtzman, D. M., and Selkoe, D. J. (2007) Loss of neprilysin function promotes amyloid plaque formation and causes cerebral amyloid angiopathy. *Am. J. Pathol.* **171**, 241–51

296. Farris, W., Mansourian, S., Chang, Y., Lindsley, L., Eckman, E. A., Frosch, M. P., Eckman, C. B., Tanzi, R. E., Selkoe, D. J., and Guenette, S. (2003) Insulin-degrading enzyme regulates the levels of insulin, amyloid beta-protein, and the beta-amyloid precursor protein intracellular domain in vivo. *Proc. Natl. Acad. Sci. U. S. A.* **100**, 4162–7

297. Leissring, M. A., Farris, W., Chang, A. Y., Walsh, D. M., Wu, X., Sun, X., Frosch, M. P., and Selkoe, D. J. (2003) Enhanced proteolysis of beta-amyloid in APP transgenic mice prevents plaque formation, secondary pathology, and premature death. *Neuron*. **40**, 1087–93

298. Marr, R. a, Rockenstein, E., Mukherjee, A., Kindy, M. S., Hersh, L. B., Gage, F. H., Verma, I. M., and Masliah, E. (2003) Neprilysin Gene Transfer Reduces Human Amyloid Pathology in Transgenic Mice. *J. Neurosci.* **23**, 1992–1996

299. Jiang, Q., Lee, C. Y. D., Mandrekar, S., Wilkinson, B., Cramer, P., Zelcer, N., Mann, K., Lamb, B., Willson, T. M., Collins, J. L., Richardson, J. C., Smith, J. D., Comery, T. A., Riddell, D., Holtzman, D. M., Tontonoz, P., and Landreth, G. E. (2008) ApoE promotes the proteolytic degradation of Abeta. *Neuron*. **58**, 681–93

300. Itagaki, S., McGeer, P. L., Akiyama, H., Zhu, S., and Selkoe, D. (1989) Relationship of microglia and astrocytes to amyloid deposits of Alzheimer disease. *J. Neuroimmunol.* **24**, 173–82

301. Pike, C. J., Cummings, B. J., and Cotman, C. W. (1995) Early association of reactive

astrocytes with senile plaques in Alzheimer's disease. *Exp. Neurol.* **132**, 172–9

302. Vehmas, A. K., Kawas, C. H., Stewart, W. F., and Troncoso, J. C. (2003) Immune reactive cells in senile plaques and cognitive decline in Alzheimer's disease. *Neurobiol. Aging*. **24**, 321–31

303. Frackowiak, J., Wisniewski, H. M., Wegiel, J., Merz, G. S., Iqbal, K., and Wang, K. C. (1992) Ultrastructure of the microglia that phagocytose amyloid and the microglia that produce beta-amyloid fibrils. *Acta Neuropathol.* **84**, 225–33

304. Koistinaho, M., Lin, S., Wu, X., Esterman, M., Koger, D., Hanson, J., Higgs, R., Liu, F., Malkani, S., Bales, K. R., and Paul, S. M. (2004) Apolipoprotein E promotes astrocyte colocalization and degradation of deposited amyloid-beta peptides. *Nat. Med.* **10**, 719–26

305. Zhao, L., Lin, S., Bales, K. R., Gelfanova, V., Koger, D., Delong, C., Hale, J., Liu, F., Hunter, J. M., and Paul, S. M. (2009) Macrophage-mediated degradation of beta-amyloid via an apolipoprotein E isoform-dependent mechanism. *J. Neurosci.* **29**, 3603–12

306. Aguzzi, A., Barres, B. A., and Bennett, M. L. (2013) Microglia: scapegoat, saboteur, or something else? *Science*. **339**, 156–61

307. Zhu, Y., Nwabuisi-Heath, E., Dumanis, S. B., Tai, L. M., Yu, C., Rebeck, G. W., and LaDu, M. J. (2012) APOE genotype alters glial activation and loss of synaptic markers in mice. *Glia*. **60**, 559–69

308. Cudaback, E., Li, X., Montine, K. S., Montine, T. J., and Keene, C. D. (2011) Apolipoprotein E isoform-dependent microglia migration. *FASEB J.* **25**, 2082–91

309. Sunderland, T., Linker, G., Mirza, N., Putnam, K. T., Friedman, D. L., Kimmel, L. H., Bergeson, J., Manetti, G. J., Zimmermann, M., Tang, B., Bartko, J. J., and Cohen, R. M. (2003) Decreased beta-amyloid1-42 and increased tau levels in cerebrospinal fluid of patients with Alzheimer disease. *JAMA*. **289**, 2094–103

310. Sunderland, T., Mirza, N., Putnam, K. T., Linker, G., Bhupali, D., Durham, R., Soares, H., Kimmel, L., Friedman, D., Bergeson, J., Csako, G., Levy, J. A., Bartko, J. J., and Cohen, R. M. (2004) Cerebrospinal fluid beta-amyloid1-42 and tau in control subjects at risk for Alzheimer's disease: the effect of APOE epsilon4 allele. *Biol. Psychiatry*. **56**, 670–6

311. Castellano, J. M., Kim, J., Stewart, F. R., Jiang, H., DeMattos, R. B., Patterson, B. W., Fagan, A. M., Morris, J. C., Mawuenyega, K. G., Cruchaga, C., Goate, A. M., Bales, K. R., Paul, S. M., Bateman, R. J., and Holtzman, D. M. (2011) Human apoE isoforms differentially regulate brain amyloid-β peptide clearance. *Sci. Transl. Med.* **3**, 89ra57

312. Bell, R. D., Sagare, A. P., Friedman, A. E., Bedi, G. S., Holtzman, D. M., Deane, R., and Zlokovic, B. V (2007) Transport pathways for clearance of human Alzheimer's amyloid beta-peptide and apolipoproteins E and J in the mouse central nervous system. *J. Cereb. blood flow Metab.* **27**, 909–18

313. Ito, S., Ohtsuki, S., and Terasaki, T. (2006) Functional characterization of the brain-to-blood efflux clearance of human amyloid-beta peptide (1-40) across the rat blood-brain barrier. *Neurosci. Res.* **56**, 246–52

314. Deane, R., Wu, Z., Sagare, A., Davis, J., Du Yan, S., Hamm, K., Xu, F., Parisi, M., LaRue, B., Hu, H. W., Spijkers, P., Guo, H., Song, X., Lenting, P. J., Van Nostrand, W. E., and Zlokovic, B. V. (2004) LRP/amyloid beta-peptide interaction mediates differential brain efflux of Abeta isoforms. *Neuron*. **43**, 333–44

315. Shibata, M., Yamada, S., Kumar, S. R., Calero, M., Bading, J., Frangione, B., Holtzman, D. M., Miller, C. A., Strickland, D. K., Ghiso, J., and Zlokovic, B. V. (2000) Clearance of Alzheimer's amyloid-ss(1-40) peptide from brain by LDL receptor-related protein-1 at the blood-brain barrier. *J. Clin. Invest.* **106**, 1489–99

316. Deane, R., Sagare, A., Hamm, K., Parisi, M., Lane, S., Finn, M. B., Holtzman, D. M., and Zlokovic, B. V (2008) apoE isoform – specific disruption of amyloid β peptide clearance from mouse brain. *J. Clin. Invest.* **118**, 4002–4013

317. Nishitsuji, K., Hosono, T., Nakamura, T., Bu, G., and Michikawa, M. (2011) Apolipoprotein E regulates the integrity of tight junctions in an isoform-dependent manner in an in vitro blood-brain barrier model. *J. Biol. Chem.* **286**, 17536–42

318. Bell, R. D., Winkler, E. A., Singh, I., Sagare, A. P., Deane, R., Wu, Z., Holtzman, D. M., Betsholtz, C., Armulik, A., Sallstrom, J., Berk, B. C., and Zlokovic, B. V (2012) Apolipoprotein E controls cerebrovascular integrity via cyclophilin A. *Nature*. **485**, 512–6

319. Rannikmae, K., Kalaria, R. N., Greenberg, S. M., Chui, H. C., Schmitt, F. A., Samarasekera, N., Al-Shahi Salman, R., and Sudlow, C. L. M. (2014) APOE associations with severe CAA-associated vasculopathic changes: collaborative meta-analysis. *J. Neurol. Neurosurg. Psychiatry*. **85**, 300–305

320. Thal, D. R., Ghebremedhin, E., Rüb, U., Yamaguchi, H., Del Tredici, K., and Braak, H. (2002) Two types of sporadic cerebral amyloid angiopathy. *J. Neuropathol. Exp. Neurol.* **61**, 282–93

321. Shinohara, M., Murray, M. E., Frank, R. D., Shinohara, M., DeTure, M., Yamazaki, Y., Tachibana, M., Atagi, Y., Davis, M. D., Liu, C.-C., Zhao, N., Painter, M. M., Petersen, R. C., Fryer, J. D., Crook, J. E., Dickson, D. W., Bu, G., and Kanekiyo, T. (2016) Impact of sex and APOE4 on cerebral amyloid angiopathy in Alzheimer's disease. *Acta Neuropathol.* **132**, 225–34

322. Mattsson, N., Zetterberg, H., Hansson, O., Andreasen, N., Parnetti, L., Jonsson, M., Herukka, S.-K., van der Flier, W. M., Blankenstein, M. A., Ewers, M., Rich, K., Kaiser, E., Verbeek, M., Tsolaki, M., Mulugeta, E., Rosén, E., Aarsland, D., Visser, P. J., Schröder, J., Marcusson, J., de Leon, M., Hampel, H., Scheltens, P., Pirttilä, T., Wallin, A., Jönhagen, M. E., Minthon, L., Winblad, B., and Blennow, K. (2009) CSF biomarkers and incipient Alzheimer disease in patients with mild cognitive impairment. *JAMA*. **302**, 385–93

323. Vemuri, P., Wiste, H. J., Weigand, S. D., Knopman, D. S., Shaw, L. M., Trojanowski, J. Q., Aisen, P. S., Weiner, M., Petersen, R. C., Jack, C. R., and Alzheimer's Disease Neuroimaging Initiative (2010) Effect of apolipoprotein E on biomarkers of amyloid load and neuronal pathology in Alzheimer disease. *Ann. Neurol.* **67**, 308–16

324. Brecht, W. J., Harris, F. M., Chang, S., Tesseur, I., Yu, G.-Q., Xu, Q., Dee Fish, J., Wyss-Coray, T., Buttini, M., Mucke, L., Mahley, R. W., and Huang, Y. (2004) Neuron-specific apolipoprotein e4 proteolysis is associated with increased tau phosphorylation in brains of transgenic mice. *J. Neurosci.* **24**, 2527–2534

325. Shi, Y., Yamada, K., Liddelow, S. A., Smith, S. T., Zhao, L., Luo, W., Tsai, R. M., Spina, S., Grinberg, L. T., Rojas, J. C., Gallardo, G., Wang, K., Roh, J., Robinson, G., Finn, M. B., Jiang, H., Sullivan, P. M., Baufeld, C., Wood, M. W., Sutphen, C., McCue, L., Xiong, C., Del-Aguila, J. L., Morris, J. C., Cruchaga, C., Fagan, A. M., Miller, B. L., Boxer, A. L., Seeley, W. W., Butovsky, O., Barres, B. A., Paul, S. M., and Holtzman, D. M. (2017) ApoE4 markedly exacerbates tau-mediated neurodegeneration in a mouse model of tauopathy. *Nature*. **549**, 523–527

326. Zhao, N., Liu, C.-C., Van Ingelgom, A. J., Linares, C., Kurti, A., Knight, J. A., Heckman, M. G., Diehl, N. N., Shinohara, M., Martens, Y. A., Attrebi, O. N., Petrucelli, L., Fryer, J. D., Wszolek, Z. K., Graff-Radford, N. R., Caselli, R. J., Sanchez-Contreras, M. Y., Rademakers, R., Murray, M. E., Koga, S., Dickson, D. W., Ross, O. A., and Bu, G. (2018) APOE ε2 is associated with increased tau pathology in primary tauopathy. *Nat. Commun.* **9**, 4388

327. Raber, J., Wong, D., Buttini, M., Orth, M., Bellosta, S., Pitas, R. E., Mahley, R. W., and Mucke, L. (1998) Isoform-specific effects of human apolipoprotein E on brain function revealed in ApoE knockout mice: increased susceptibility of females. *Proc. Natl. Acad. Sci. U. S. A.* **95**, 10914–9

328. Buttini, M., Orth, M., Bellosta, S., Akeefe, H., Pitas, R. E., Wyss-Coray, T., Mucke, L., and Mahley, R. W. (1999) Expression of human apolipoprotein E3 or E4 in the brains of Apoe-/- mice: isoform-specific effects on neurodegeneration. *J. Neurosci.* **19**, 4867–80

329. Andrews-Zwilling, Y., Bien-Ly, N., Xu, Q., Li, G., Bernardo, A., Yoon, S. Y., Zwilling, D., Yan, T. X., Chen, L., and Huang, Y. (2010) Apolipoprotein E4 causes age- and Tau-dependent impairment of GABAergic interneurons, leading to learning and memory deficits in mice. *J. Neurosci.* **30**, 13707–17

330. Leung, L., Andrews-Zwilling, Y., Yoon, S. Y., Jain, S., Ring, K., Dai, J., Wang, M. M., Tong, L., Walker, D., and Huang, Y. (2012) Apolipoprotein E4 causes age- and sex-dependent impairments of hilar GABAergic interneurons and learning and memory deficits in mice. *PLoS One*. **7**, e53569

331. Jones, P. B., Adams, K. W., Rozkalne, A., Spires-Jones, T. L., Hshieh, T. T., Hashimoto, T., von Armin, C. A. F., Mielke, M., Bacskai, B. J., and Hyman, B. T. (2011) Apolipoprotein E: isoform specific differences in tertiary structure and interaction with amyloid-β in human Alzheimer brain. *PLoS One*. **6**, e14586

332. Huang, Y., Liu, X. Q., Wyss-Coray, T., Brecht, W. J., Sanan, D. A., and Mahley, R. W. (2001) Apolipoprotein E fragments present in Alzheimer's disease brains induce neurofibrillary tangle-like intracellular inclusions in neurons. *Proc. Natl. Acad. Sci. U. S. A.* **98**, 8838–43

333. Harris, F. M., Brecht, W. J., Xu, Q., Tesseur, I., Kekonius, L., Wyss-Coray, T., Fish, J. D., Masliah, E., Hopkins, P. C., Scearce-Levie, K., Weisgraber, K. H., Mucke, L., Mahley, R. W., and Huang, Y. (2003) Carboxyl-terminal-truncated apolipoprotein E4 causes Alzheimer's disease-like neurodegeneration and behavioral deficits in transgenic mice. *Proc. Natl. Acad. Sci. U. S. A.* **100**, 10966–71

334. Nakamura, T., Watanabe, A., Fujino, T., Hosono, T., and Michikawa, M. (2009) Apolipoprotein E4 (1-272) fragment is associated with mitochondrial proteins and affects mitochondrial function in neuronal cells. *Mol. Neurodegener.* **4**, 35

335. Chang, S., ran Ma, T., Miranda, R. D., Balestra, M. E., Mahley, R. W., and Huang, Y. (2005) Lipid- and receptor-binding regions of apolipoprotein E4 fragments act in concert to cause mitochondrial dysfunction and neurotoxicity. *Proc. Natl. Acad. Sci. U. S. A.* **102**, 18694–9

336. Chen, H.-K., Ji, Z.-S., Dodson, S. E., Miranda, R. D., Rosenblum, C. I., Reynolds, I. J., Freedman, S. B., Weisgraber, K. H., Huang, Y., and Mahley, R. W. (2011) Apolipoprotein E4 Domain Interaction Mediates Detrimental Effects on Mitochondria and Is a Potential Therapeutic Target for Alzheimer Disease. *J. Biol. Chem.* **286**, 5215–5221

337. Mahley, R. W., and Huang, Y. (2012) Apolipoprotein E Sets the Stage: Response to Injury Triggers Neuropathology. *Neuron*. **76**, 871–885

338. Mahley, R. W., and Huang, Y. (2006) Apolipoprotein (apo) E4 and Alzheimer's disease: unique conformational and biophysical properties of apoE4 can modulate neuropathology. *Acta Neurol. Scand. Suppl.* **185**, 8–14

339. Wang, C., Najm, R., Xu, Q., Jeong, D., Walker, D., Balestra, M. E., Yoon, S. Y., Yuan, H., Li, G., Miller, Z. A., Miller, B. L., and Malloy, M. J. (2018) Gain of Toxic Apolipoprotein E4 Effects in Human iPSC-derived Neurons is Ameliorated by a Small-Molecule Structure Corrector. *Nat. Med.* 10.1038/s41591-018-0004-z

340. Yu, J.-T., Tan, L., and Hardy, J. (2014) Apolipoprotein E in Alzheimer's Disease: An Update. *Annu. Rev. Neurosci.* **37**, 79–100

341. Yamazaki, Y., Painter, M. M., Bu, G., and Kanekiyo, T. (2016) Apolipoprotein E as a Therapeutic Target in Alzheimer's Disease: A Review of Basic Research and Clinical Evidence. *CNS Drugs*. **30**, 773–89

342. Laffitte, B. A., Repa, J. J., Joseph, S. B., Wilpitz, D. C., Kast, H. R., Mangelsdorf, D. J., and Tontonoz, P. (2001) LXRs control lipid-inducible expression of the apolipoprotein E gene in macrophages and adipocytes. *Proc. Natl. Acad. Sci. U. S. A.* **98**, 507–12

343. Mak, P. A., Laffitte, B. A., Desrumaux, C., Joseph, S. B., Curtiss, L. K., Mangelsdorf, D. J., Tontonoz, P., and Edwards, P. A. (2002) Regulated Expression of the Apolipoprotein E/C-I/C-IV/C-II Gene Cluster in Murine and Human Macrophages. *J. Biol. Chem.* **277**, 31900–31908

344. Liang, Y., Lin, S., Beyer, T. P., Zhang, Y., Wu, X., Bales, K. R., DeMattos, R. B., May, P. C., Li, S. D., Jiang, X. C., Eacho, P. I., Cao, G., and Paul, S. M. (2004) A liver X receptor and retinoid X receptor heterodimer mediates apolipoprotein E expression, secretion and cholesterol homeostasis in astrocytes. *J. Neurochem.* **88**, 623–634

345. Shih, S. J., Allan, C., Grehan, S., Tse, E., Moran, C., and Taylor, J. M. (2000) Duplicated downstream enhancers control expression of the human apolipoprotein E gene in macrophages and adipose tissue. *J. Biol. Chem.* **275**, 31567–72

346. Lehmann, J. M., Kliewer, S. A., Moore, L. B., Smith-Oliver, T. A., Oliver, B. B., Su, J. L., Sundseth, S. S., Winegar, D. A., Blanchard, D. E., Spencer, T. A., and Willson, T. M. (1997) Activation of the nuclear receptor LXR by oxysterols defines a new hormone response pathway. *J. Biol. Chem.* **272**, 3137–40

347. Janowski, B. A., Willy, P. J., Devi, T. R., Falck, J. R., and Mangelsdorf, D. J. (1996) An oxysterol signalling pathway mediated by the nuclear receptor LXR alpha. *Nature*. **383**, 728–31

348. Donkin, J. J., Stukas, S., Hirsch-Reinshagen, V., Namjoshi, D., Wilkinson, A., May, S., Chan, J., Fan, J., Collins, J., and Wellington, C. L. (2010) ATP-binding cassette transporter A1 mediates the beneficial effects of the liver X receptor agonist GW3965 on object recognition memory and amyloid burden in amyloid precursor protein/presenilin 1 mice. *J. Biol. Chem.* **285**, 34144–54

349. Riddell, D. R., Zhou, H., Comery, T. A., Kouranova, E., Lo, C. F., Warwick, H. K., Ring, R. H., Kirksey, Y., Aschmies, S., Xu, J., Kubek, K., Hirst, W. D., Gonzales, C., Chen, Y., Murphy, E., Leonard, S., Vasylyev, D., Oganesian, A., Martone, R. L., Pangalos, M. N., Reinhart, P. H., and Jacobsen, J. S. (2007) The LXR agonist TO901317 selectively lowers hippocampal Abeta42 and improves memory in the Tg2576 mouse model of Alzheimer's disease. *Mol. Cell. Neurosci.* **34**, 621–8

350. Hong, C., and Tontonoz, P. (2014) Liver X receptors in lipid metabolism: opportunities for drug discovery. *Nat. Rev. Drug Discov.* **13**, 433–44

351. Bien-Ly, N., Gillespie, A. K., Walker, D., Yoon, S. Y., and Huang, Y. (2012) Reducing

human apolipoprotein E levels attenuates age-dependent Aβ accumulation in mutant human amyloid precursor protein transgenic mice. *J. Neurosci.* **32**, 4803–11

352. Laskowitz, D. T., Thekdi, A. D., Thekdi, S. D., Han, S. K. D., Myers, J. K., Pizzo, S. V., and Bennett, E. R. (2001) Downregulation of microglial activation by apolipoprotein E and apoE-mimetic peptides. *Exp. Neurol.* **167**, 74–85

353. Lynch, J. R., Tang, W., Wang, H., Vitek, M. P., Bennett, E. R., Sullivan, P. M., Warner, D. S., and Laskowitz, D. T. (2003) APOE genotype and an ApoE-mimetic peptide modify the systemic and central nervous system inflammatory response. *J. Biol. Chem.* **278**, 48529–33

354. Laskowitz, D. T., Fillit, H., Yeung, N., Toku, K., and Vitek, M. P. (2006) Apolipoprotein E-derived peptides reduce CNS inflammation: implications for therapy of neurological disease. *Acta Neurol. Scand. Suppl.* **185**, 15–20

355. Vitek, M. P., Christensen, D. J., Wilcock, D., Davis, J., Van Nostrand, W. E., Li, F. Q., and Colton, C. A. (2012) APOE-mimetic peptides reduce behavioral deficits, plaques and tangles in Alzheimer's disease transgenics. *Neurodegener. Dis.* **10**, 122–6

356. Sarantseva, S., Timoshenko, S., Bolshakova, O., Karaseva, E., Rodin, D., Schwarzman, A. L., and Vitek, M. P. (2009) Apolipoprotein E-mimetics inhibit neurodegeneration and restore cognitive functions in a transgenic Drosophila model of Alzheimer's disease. *PLoS One*. **4**, e8191

357. Sadowski, M., Pankiewicz, J., Scholtzova, H., Ripellino, J. a, Li, Y., Schmidt, S. D., Mathews, P. M., Fryer, J. D., Holtzman, D. M., Sigurdsson, E. M., and Wisniewski, T. (2004) A synthetic peptide blocking the apolipoprotein E/beta-amyloid binding mitigates beta-amyloid toxicity and fibril formation in vitro and reduces beta-amyloid plaques in transgenic mice. *Am. J. Pathol.* **165**, 937–48

358. Sadowski, M. J., Pankiewicz, J., Scholtzova, H., Mehta, P. D., Prelli, F., Quartermain, D., and Wisniewski, T. (2006) Blocking the apolipoprotein E/amyloid-beta interaction as a potential therapeutic approach for Alzheimer's disease. *Proc. Natl. Acad. Sci. U. S. A.* **103**, 18787–92

359. Kuszczyk, M. A., Sanchez, S., Pankiewicz, J., Kim, J., Duszczyk, M., Guridi, M., Asuni, A. A., Sullivan, P. M., Holtzman, D. M., and Sadowski, M. J. (2013) Blocking the interaction between apolipoprotein E and Aβ reduces intraneuronal accumulation of Aβ and inhibits synaptic degeneration. *Am. J. Pathol.* **182**, 1750–68

360. Liu, Q., Wu, W., Fang, C., Li, R., Liu, P., Lei, P., Hu, J., Sun, X., Zheng, Y., Zhao, Y., and Li, Y. (2011) Mapping ApoE/Aβ binding regions to guide inhibitor discovery. *Mol. Biosyst.* **7**, 1693–700

361. Ye, S., Huang, Y., Müllendorff, K., Dong, L., Giedt, G., Meng, E. C., Cohen, F. E., Kuntz, I. D., Weisgraber, K. H., and Mahley, R. W. (2005) Apolipoprotein (apo) E4 enhances amyloid beta peptide production in cultured neuronal cells: apoE structure as a potential therapeutic target. *Proc. Natl. Acad. Sci. U. S. A.* **102**, 18700–5

362. Brodbeck, J., McGuire, J., Liu, Z., Meyer-Franke, A., Balestra, M. E., Jeong, D. E., Pleiss, M., McComas, C., Hess, F., Witter, D., Peterson, S., Childers, M., Goulet, M., Liverton, N., Hargreaves, R., Freedman, S., Weisgraber, K. H., Mahley, R. W., and Huang, Y. (2011) Structure-dependent impairment of intracellular apolipoprotein E4 trafficking and its detrimental effects are rescued by small-molecule structure correctors. *J. Biol. Chem.* **286**, 17217–17226

363. Mahley, R. W., Weisgraber, K. H., and Huang, Y. (2011) ApoE4 domain interaction inhibitors and methods of use thereof

364. Mahley, R. W., and Huang, Y. (2012) Small-Molecule Structure Correctors Target Abnormal Protein Structure and Function: Structure Corrector Rescue of Apolipoprotein E4–Associated Neuropathology. *J. Med. Chem.* **55**, 8997–9008

365. Mahley, R. W. (2016) Central Nervous System Lipoproteins: ApoE and Regulation of Cholesterol Metabolism. *Arterioscler. Thromb. Vasc. Biol.* **36**, 1305–15

366. Pfaffinger, D., Edelstein, C., and Scanu, A. M. (1983) Rapid isolation of apolipoprotein E from human plasma very low density lipoproteins by molecular sieve high performance liquid chromatography. *J. Lipid Res.* **24**, 796–800

367. Morikawa, M., Fryer, J. D., Sullivan, P. M., Christopher, E. A., Wahrle, S. E., DeMattos, R. B., O'Dell, M. A., Fagan, A. M., Lashuel, H. A., Walz, T., Asai, K., and Holtzman, D. M. (2005) Production and characterization of astrocyte-derived human apolipoprotein E isoforms from immortalized astrocytes and their interactions with amyloid-beta. *Neurobiol. Dis.* **19**, 66–76

368. Thrift, R. N., Forte, T. M., Cahoon, B. E., and Shore, V. G. (1986) Characterization of lipoproteins produced by the human liver cell line, Hep G2, under defined conditions. *J. Lipid Res.* **27**, 236–50

369. Vogel, T., Weisgraber, K. H., Zeevi, M. I., Ben-Artzi, H., Levanon, A. Z., Rall, S. C., Innerarity, T. L., Hui, D. Y., Taylor, J. M., and Kanner, D. (1985) Human apolipoprotein E expression in Escherichia coli: structural and functional identity of the bacterially produced protein with plasma apolipoprotein E. *Proc. Natl. Acad. Sci. U. S. A.* **82**, 8696–700

370. Wernette-Hammond, M. E., Lauer, S. J., Corsini, A., Walker, D., Taylor, J. M., and Rall, S. C. (1989) Glycosylation of human apolipoprotein E. The carbohydrate attachment site is threonine 194. *J. Biol. Chem.* **264**, 9094–101

371. Xu, P. T., Schmechel, D., Qiu, H. L., Herbstreith, M., Rothrock-Christian, T., Eyster, M., Roses, a D., and Gilbert, J. R. (1999) Sialylated human apolipoprotein E (apoEs) is preferentially associated with neuron-enriched cultures from APOE transgenic mice. *Neurobiol. Dis.* **6**, 63–75

372. Yamauchi, K., Tozuka, M., Hidaka, H., Hidaka, E., Kondo, Y., and Katsuyama, T. (1999) Characterization of apolipoprotein E-containing lipoproteins in cerebrospinal fluid: effect of phenotype on the distribution of apolipoprotein E. *Clin. Chem.* **45**, 1431–8

373. Mancone, C., Amicone, L., Fimia, G. M., Bravo, E., Piacentini, M., Tripodi, M., and Alonzi, T. (2007) Proteomic analysis of human very low-density lipoprotein by two-dimensional gel electrophoresis and MALDI-TOF/TOF. *Proteomics*. **7**, 143–54

374. Lee, Y., Kockx, M., Raftery, M. J., Jessup, W., Griffith, R., and Kritharides, L. (2010) Glycosylation and sialylation of macrophage-derived human apolipoprotein E analyzed by SDS-PAGE and mass spectrometry: evidence for a novel site of glycosylation on Ser290. *Mol. Cell. Proteomics*. **9**, 1968–81

375. Morrow, J. a, Arnold, K. S., and Weisgraber, K. H. (1999) Functional characterization of apolipoprotein E isoforms overexpressed in Escherichia coli. *Protein Expr. Purif.* **16**, 224–230

376. Pillot, T., Barbier, A., Visvikis, A., Lozac'h, K., Rosseneu, M., Vandekerckhove, J., and Siest, G. (1996) Single-step purification of two functional human apolipoprotein E variants hyperexpressed in Escherichia coli. *Protein Expr. Purif.* **7**, 407–14

377. Putnam, C. D., Hammel, M., Hura, G. L., and Tainer, J. a (2007) X-ray solution scattering (SAXS) combined with crystallography and computation: defining accurate macromolecular structures, conformations and assemblies in solution. *Q. Rev. Biophys.*

40, 191–285

378. Chou, C.-Y., Lin, Y.-L., Huang, Y.-C., Sheu, S.-Y., Lin, T.-H., Tsay, H.-J., Chang, G.-G., and Shiao, M.-S. (2005) Structural variation in human apolipoprotein E3 and E4: secondary structure, tertiary structure, and size distribution. *Biophys. J.* **88**, 455–66

379. Barbier, A., Clement-Collin, V., Dergunov, A. D., Visvikis, A., Siest, G., and Aggerbeck, L. P. (2006) The structure of human apolipoprotein E2, E3 and E4 in solution: 1. Tertiary and quaternary structure. *Biophys. Chem.* **119**, 158–169

380. Garai, K., and Frieden, C. (2010) The association−dissociation behavior of the ApoE proteins: kinetic and equilibrium studies. *Biochemistry*. **49**, 9533–41

381. Newhouse, Y., and Weisgraber, K. H. (2011) Apolipoprotein E expression and purification. *Methods Mol. Biol.* **670**, 127–40

382. Argyri, L., Skamnaki, V., Stratikos, E., and Chroni, A. (2011) A simple approach for human recombinant apolipoprotein E4 expression and purification. *Protein Expr. Purif.* **79**, 251–257

383. Vallejo, L. F., and Rinas, U. (2004) Strategies for the recovery of active proteins through refolding of bacterial inclusion body proteins. *Microb. Cell Fact.* **3**, 11

384. Shaw, N., Cheng, C., and Liu, Z.-J. (2007) Procedure for reductive methylation of protein to improve crystallizability. *Protoc. Exch.* 10.1038/nprot.2007.287

385. Busby, T. F., and Gan, J. C. (1976) Chemical modifications of lysyl and arginyl residues of human plasma α1-antitrypsin. *Arch. Biochem. Biophys.* **177**, 552–560

386. Balbo, A., and Schuck, P. (2005) Analytical ultracentrifugation in the study of protein self-association and heterogeneous protein-protein interactions. *Protein-Protein Interact. A Mol. Cloning Man.*

387. Erickson, H. P. (2009) Size and shape of protein molecules at the nanometer level determined by sedimentation, gel filtration, and electron microscopy. *Biol. Proced. Online*. **11**, 32–51

388. Wyatt Technology Understanding Multi-Angle Static Light Scattering. [online] http://www.wyatt.com/library/theory/understanding-multi-angle-static-light-scattering.html (Accessed November 5, 2018)

389. Minton, A. P. (2016) Recent applications of light scattering measurement in the biological and biopharmaceutical sciences. *Anal. Biochem.* **501**, 4–22

390. Cole, J. L., Lary, J. W., P Moody, T., and Laue, T. M. (2008) Analytical ultracentrifugation: sedimentation velocity and sedimentation equilibrium. *Methods Cell Biol.* **84**, 143–79

391. Lebowitz, J., Lewis, M. S., and Schuck, P. (2002) Modern analytical ultracentrifugation in protein science: a tutorial review. *Protein Sci.* **11**, 2067–79

392. Schuck, P. (2000) Size-distribution analysis of macromolecules by sedimentation velocity ultracentrifugation and lamm equation modeling. *Biophys. J.* **78**, 1606–19

393. Laue, T. M., Shah, B. D., Ridgeway, T. M., and Pelletier, S. L. (1992) Computer-aided interpretation of analytical sedimentation data for proteins. in *Analytical ultracentrifugation in biochemistry and polymer science* (Harding, S. E., and Horton, J. C. eds), pp. 90–125, The Royal Society of Chemistry, Cambridge

394. McPherson, A., and Gavira, J. a. (2014) Introduction to protein crystallization. *Acta Crystallogr. Sect. FStructural Biol. Commun.* **70**, 2–20

395. Hampton Research (2001) Crystal Growth Techniques. *Solut. Cryst. Growth*. [online] https://hamptonresearch.com/growth_101_lit.aspx (Accessed April 30, 2015)

396. Landau, E. M., and Rosenbusch, J. P. (1996) Lipidic cubic phases: a novel concept for the crystallization of membrane proteins. *Proc. Natl. Acad. Sci. U. S. A.* **93**, 14532–5

397. Caffrey, M. (2015) A comprehensive review of the lipid cubic phase or in meso method for crystallizing membrane and soluble proteins and complexes. *Acta Crystallogr. Sect. F, Struct. Biol. Commun.* **71**, 3–18

398. Moraes, I., and Archer, M. (2015) Methods for the successful crystallization of membrane proteins. *Methods Mol. Biol.* **1261**, 211–30

399. Berman, H. M., Westbrook, J., Feng, Z., Gilliland, G., Bhat, T. N., Weissig, H., Shindyalov, I. N., and Bourne, P. E. (2000) The Protein Data Bank. *Nucleic Acids Res.* **28**, 235–42

400. Winn, M. D., Ballard, C. C., Cowtan, K. D., Dodson, E. J., Emsley, P., Evans, P. R., Keegan, R. M., Krissinel, E. B., Leslie, A. G. W., McCoy, A., McNicholas, S. J., Murshudov, G. N., Pannu, N. S., Potterton, E. A., Powell, H. R., Read, R. J., Vagin, A., and Wilson, K. S. (2011) Overview of the CCP4 suite and current developments. *Acta Crystallogr. Sect. D Biol. Crystallogr.* **67**, 235–242

401. LaVallie, E. R., DiBlasio, E. A., Kovacic, S., Grant, K. L., Schendel, P. F., and McCoy, J. M. (1993) A Thioredoxin Gene Fusion Expression System That Circumvents Inclusion Body Formation in the E. coli Cytoplasm. *Nat. Biotechnol.* **11**, 187–193

402. Schneider, C. A., Rasband, W. S., and Eliceiri, K. W. (2012) NIH Image to ImageJ: 25 years of image analysis. *Nat. Methods*. **9**, 671–5

403. Receveur-Brechot, V., and Durand, D. (2012) How random are intrinsically disordered proteins? A small angle scattering perspective. *Curr. Protein Pept. Sci.* **13**, 55–75

404. Rambo, R. P., and Tainer, J. A. (2013) Accurate assessment of mass, models and resolution by small-angle scattering. *Nature*. **496**, 477–81

405. Schneidman-Duhovny, D., Hammel, M., Tainer, J. A., and Sali, A. (2016) FoXS, FoXSDock and MultiFoXS: Single-state and multi-state structural modeling of proteins and their complexes based on SAXS profiles. *Nucleic Acids Res.* **44**, W424-9

406. Walter, T. S., Meier, C., Assenberg, R., Au, K.-F., Ren, J., Verma, A., Nettleship, J. E., Owens, R. J., Stuart, D. I., and Grimes, J. M. (2006) Lysine methylation as a routine rescue strategy for protein crystallization. *Structure*. **14**, 1617–22

407. Bornhorst, J. A., and Falke, J. J. (2000) Purification of proteins using polyhistidine affinity tags. in *Methods in Enzymology*, pp. 245–254, **326**, 245–254

408. Healthcare, G. (2014) HiTrap Heparin HP manual, Instructions 71-7004-00 AU

409. Saito, H., Dhanasekaran, P., Nguyen, D., Baldwin, F., Weisgraber, K. H., Wehrli, S., Phillips, M. C., and Lund-Katz, S. (2003) Characterization of the heparin binding sites in human apolipoprotein E. *J. Biol. Chem.* **278**, 14782–7

410. Yamauchi, Y., Deguchi, N., Takagi, C., Tanaka, M., Dhanasekaran, P., Nakano, M., Handa, T., Phillips, M. C., Lund-Katz, S., and Saito, H. (2008) Role of the N- and C-terminal domains in binding of apolipoprotein E isoforms to heparan sulfate and dermatan sulfate: a surface plasmon resonance study. *Biochemistry*. **47**, 6702–10

411. Peters-Libeu, C. A., Newhouse, Y., Hall, S. C., Witkowska, H. E., and Weisgraber, K. H. (2007) Apolipoprotein E*dipalmitoylphosphatidylcholine particles are ellipsoidal in solution. *J. Lipid Res.* **48**, 1035–44

412. Sennhauser, G., and Grütter, M. G. (2008) Chaperone-assisted crystallography with DARPins. *Structure*. **16**, 1443–53

413. Gumpena, R., Lountos, G. T., and Waugh, D. S. (2018) MBP-binding DARPins facilitate the crystallization of an MBP fusion protein. *Acta Crystallogr. Sect. F, Struct. Biol. Commun.* **74**, 549–557

414. Sarrazin, S., Lamanna, W. C., and Esko, J. D. (2011) Heparan sulfate proteoglycans. *Cold Spring Harb. Perspect. Biol.* **3**, 1–33

415. Jones, C. J., Beni, S., Limtiaco, J. F. K., Langeslay, D. J., and Larive, C. K. (2011) Heparin characterization: challenges and solutions. *Annu. Rev. Anal. Chem. (Palo Alto. Calif).* **4**, 439–65

416. Futamura, M., Dhanasekaran, P., Handa, T., Phillips, M. C., Lund-Katz, S., and Saito, H. (2005) Two-step mechanism of binding of apolipoprotein E to heparin: implications for the kinetics of apolipoprotein E-heparan sulfate proteoglycan complex formation on cell surfaces. *J. Biol. Chem.* **280**, 5414–22

417. Shuvaev, V. V., Laffont, I., and Siest, G. (1999) Kinetics of apolipoprotein E isoforms-binding to the major glycosaminoglycans of the extracellular matrix. *FEBS Lett.* **459**, 353–7

418. Lund-Katz, S., Zaiou, M., Wehrli, S., Dhanasekaran, P., Baldwin, F., Weisgraber, K. H., and Phillips, M. C. (2000) Effects of lipid interaction on the lysine microenvironments in apolipoprotein E. *J. Biol. Chem.* **275**, 34459–64

419. Glatter, O., and Kratky, O. (1982) *Small-Angle X-ray Scattering*, 1st Ed. (Glatter, O., and Kratky, O. eds), Academic Press, London, 10.1002/actp.1985.010360520

420. Grant, T. (2014) SAXS Part I: Introduction to Biological Small Angle Scattering. [online] https://www.youtube.com/watch?v=SevPRumWqsE (Accessed November 19, 2018)

421. Kikhney, A. G. (2013) WeNMR Lecture (part I) on SAXS. [online] https://www.youtube.com/watch?v=xjnOCvvPNms&t=3627s (Accessed November 19, 2018)

422. Hura, G. L., Budworth, H., Dyer, K. N., Rambo, R. P., Hammel, M., McMurray, C. T., and Tainer, J. a (2013) Comprehensive macromolecular conformations mapped by quantitative SAXS analyses. *Nat. Methods*. **10**, 453–4

423. Burgess, J. W., Gould, D. R., and Marcel, Y. L. (1998) The HepG2 extracellular matrix contains separate heparinase- and lipid-releasable pools of ApoE. Implications for hepatic lipoprotein metabolism. *J. Biol. Chem.* **273**, 5645–54

424. Burgess, J. W., Liang, P., Vaidyanath, C., and Marcel, Y. L. (1999) ApoE of the HepG2 cell surface includes a major pool associated with chondroitin sulfate proteoglycans. *Biochemistry*. **38**, 524–31

425. Burgess, J. W., and Marcel, Y. L. (2001) Dynamic and stable pools of apoE differ functionally at the HepG2 cell surface. *J. Lipid Res.* **42**, 1413–20

426. Brosey, C. A., Yan, C., Tsutakawa, S. E., Heller, W. T., Rambo, R. P., Tainer, J. A., Ivanov, I., and Chazin, W. J. (2013) A new structural framework for integrating replication protein A into DNA processing machinery. *Nucleic Acids Res.* **41**, 2313–27

427. Li, J., Rodriguez, J. P., Niu, F., Pu, M., Wang, J., Hung, L.-W., Shao, Q., Zhu, Y., Ding, W., Liu, Y., Da, Y., Yao, Z., Yang, J., Zhao, Y., Wei, G.-H., Cheng, G., Liu, Z.-J., and Ouyang, S. (2016) Structural basis for DNA recognition by STAT6. *Proc. Natl. Acad. Sci. U. S. A.* **113**, 13015–13020

428. Holtzman, D., and Herz, J. (2012) Apolipoprotein E and apolipoprotein receptors: normal biology and roles in Alzheimer's disease. *Cold Spring Harb. Perspect. Med.* **2**, a006312

429. Huynh, T.-P. V., Davis, A. A., Ulrich, J. D., and Holtzman, D. M. (2017) Apolipoprotein E and Alzheimer's disease: the influence of apolipoprotein E on amyloid-β and other amyloidogenic proteins. *J. Lipid Res.* **58**, 824–836

430. Lane-Donovan, C., and Herz, J. (2017) ApoE, ApoE Receptors, and the Synapse in Alzheimer's Disease. *Trends Endocrinol. Metab.* **28**, 273–284

431. Kim, J., Yoon, H., Basak, J., and Kim, J. (2014) Apolipoprotein E in synaptic plasticity and Alzheimer's disease: potential cellular and molecular mechanisms. *Mol. Cells*. **37**, 767–76

432. Ji, Z., Pitas, R. E., and Mahley, R. W. (1998) Differential Cellular Accumulation/Retention of Apolipoprotein E Mediated by Cell Surface Heparan Sulfate Proteoglycans. *J. Biol. Chem.* **273**, 13452–13460

433. Chen, Y., Durakoglugil, M. S., Xian, X., and Herz, J. (2010) ApoE4 reduces glutamate receptor function and synaptic plasticity by selectively impairing ApoE receptor recycling. *Proc. Natl. Acad. Sci. U. S. A.* **107**, 12011–6

434. Zhong, N., Scearce-Levie, K., Ramaswamy, G., and Weisgraber, K. H. (2008) Apolipoprotein E4 domain interaction: Synaptic and cognitive deficits in mice. *Alzheimer's Dement.* **4**, 179–192

435. Zhong, N., Ramaswamy, G., and Weisgraber, K. H. (2009) Apolipoprotein E4 domain interaction induces endoplasmic reticulum stress and impairs astrocyte function. *J. Biol. Chem.* **284**, 27273–80

436. Heavens, O. S., and Ditchburn, R. W. (1991) Ray Optics (1): Reflection and Refraction. in *Insight into Optics*, 1st Ed. (Heavens, O. S., and Ditchburn, R. W. eds), pp. 6–12, John Wiley & Sons, Chichester

437. Heavens, O. S., and Ditchburn, R. W. (1991) Electromagnetic Theory of Dielectric Media. in *Insight into Optics*, 1st Ed. (Heavens, O. S., and Ditchburn, R. W. eds), pp. 93–107, John Wiley & Sons, Chichester

438. Corning Inc (2013) Corning Epic BT System User Manual

439. Fang, Y. (2010) *Optical Guided-wave Chemical and Biosensors II* (Zourob, M., and Lakhtakia, A. eds), Springer Series on Chemical Sensors and Biosensors, Springer Berlin Heidelberg, Berlin, Heidelberg, 10.1007/978-3-642-02827-4

440. Jerabek-Willemsen, M., André, T., Wanner, R., Roth, H. M., Duhr, S., Baaske, P., and Breitsprecher, D. (2014) MicroScale Thermophoresis: Interaction analysis and beyond. *J. Mol. Struct.* **1077**, 101–113

441. Jerabek-Willemsen, M., Wienken, C. J., Braun, D., Baaske, P., and Duhr, S. (2011) Molecular interaction studies using microscale thermophoresis. *Assay Drug Dev. Technol.* **9**, 342–53

442. Duhr, S., and Braun, D. (2006) Thermophoretic depletion follows Boltzmann distribution. *Phys. Rev. Lett.* **96**, 168301

443. Bundle, D. R., and Sigurskjold, B. W. (1994) Determination of accurate thermodynamics of binding by titration microcalorimetry. *Methods Enzymol.* **247**, 288–305

444. Freire, E., Mayorga, O. L., and Straume, M. (1990) Isothermal titration calorimetry. *Anal. Chem.* **62**, 950A–959A

445. Mondal, T., Wang, H., DeKoster, G. T., Baban, B., Gross, M. L., and Frieden, C. (2016) ApoE: In Vitro Studies of a Small Molecule Effector. *Biochemistry*. 10.1021/acs.biochem.6b00324

446. Arkin, M. R., Glicksman, M. A., Fu, H., Havel, J. J., and Du, Y. (2012) Inhibition of Protein-Protein Interactions : Non- Cellular Assay Formats. in *Assay Guidance Manual*, pp. 1–30, Eli Lilly & Company and the National Center for Advancing Translational Sciences

447. Bulawa, C. E., Connelly, S., Devit, M., Wang, L., Weigel, C., Fleming, J. A., Packman, J., Powers, E. T., Wiseman, R. L., Foss, T. R., Wilson, I. A., Kelly, J. W., and Labaudinière, R. (2012) Tafamidis, a potent and selective transthyretin kinetic stabilizer that inhibits the amyloid cascade. *Proc. Natl. Acad. Sci. U. S. A.* **109**, 9629–34

448. Renaud, J.-P., Chung, C.-W., Danielson, U. H., Egner, U., Hennig, M., Hubbard, R. E., and Nar, H. (2016) Biophysics in drug discovery: impact, challenges and opportunities. *Nat. Rev. Drug Discov.* **15**, 679–98

449. Bojanowski, K., Lelievre, S., Markovits, J., Couprie, J., Jacquemin-Sablon, A., and Larsen, A. K. (1992) Suramin is an inhibitor of DNA topoisomerase II in vitro and in Chinese hamster fibrosarcoma cells. *Proc. Natl. Acad. Sci. U. S. A.* **89**, 3025–9

450. Zhang, Y.-L., Keng, Y.-F., Zhao, Y., Wu, L., and Zhang, Z.-Y. (1998) Suramin Is an Active Site-directed, Reversible, and Tight-binding Inhibitor of Protein-tyrosine Phosphatases. *J. Biol. Chem.* **273**, 12281–12287

451. Kloen, P., Jennings, C. L., Gebhardt, M. C., Springfield, D. S., and Mankin, H. J. (1994) Suramin inhibits growth and transforming growth factor-beta 1 (TGF-beta 1) binding in osteosarcoma cell lines. *Eur. J. Cancer*. **30A**, 678–82

452. Zhao, P., Sharir, H., Kapur, A., Cowan, A., Geller, E. B., Adler, M. W., Seltzman, H. H., Reggio, P. H., Heynen-Genel, S., Sauer, M., Chung, T. D. Y., Bai, Y., Chen, W., Caron, M. G., Barak, L. S., and Abood, M. E. (2010) Targeting of the orphan receptor GPR35 by pamoic acid: a potent activator of extracellular signal-regulated kinase and β-arrestin2 with antinociceptive activity. *Mol. Pharmacol.* **78**, 560–8

453. Neubig, R. R. (2010) Mind your salts: when the inactive constituent isn't. *Mol. Pharmacol.* **78**, 558–9

454. Benvenga, S., Cahnmann, H. J., Rader, D., Kindt, M., and Robbins, J. (1992) Thyroxine binding to the apolipoproteins of high density lipoproteins HDL2 and HDL3. *Endocrinology*. **131**, 2805–11

455. Benvenga, S., Cahnmann, H. J., and Robbins, J. (1993) Characterization of thyroid hormone binding to apolipoprotein-E: localization of the binding site in the exon 3-coded domain. *Endocrinology*. **133**, 1300–5

456. Henderson, V. W. (2007) The Role of Sex Steroids in Alzheimer's Disease: Prevention and Treatment. in *Treatment of the Postmenopausal Woman*, Third Edit, pp. 295–306, Elsevier, 10.1016/B978-012369443-0/50029-6

457. Yaffe, K. (2001) Estrogens, selective estrogen receptor modulators, and dementia: what is the evidence? *Ann. N. Y. Acad. Sci.* **949**, 215–22

458. Fischer, M. J. E. (2010) Amine Coupling Through EDC/NHS: A Practical Approach. in *Surface Plasmon Resonance*, pp. 55–73, Humana Press, **627**, 55–73

459. Gasteiger, E., Hoogland, C., Gattiker, A., Duvaud, S., Wilkins, M. R., Appel, R. D., and Bairoch, A. (2005) Protein Identification and Analysis Tools on the ExPASy Server. in *The Proteomics Protocols Handbook*, 1st Ed. (Walker, J. M. ed), pp. 571–607, Humana

Press

460. Nalbantoglu, J., Gilfix, B. M., Bertrand, P., Robitaille, Y., Gauthier, S., Rosenblatt, D. S., and Poirier, J. (1994) Predictive value of apolipoprotein E genotyping in Alzheimer's disease: results of an autopsy series and an analysis of several combined studies. *Ann. Neurol.* **36**, 889–95

461. Phillips, M. C. (2014) Apolipoprotein E isoforms and lipoprotein metabolism. *IUBMB Life*. **66**, 616–623

462. Bennet, A. M., Di Angelantonio, E., Ye, Z., Wensley, F., Dahlin, A., Ahlbom, A., Keavney, B., Collins, R., Wiman, B., de Faire, U., and Danesh, J. (2007) Association of apolipoprotein E genotypes with lipid levels and coronary risk. *JAMA*. **298**, 1300–11

463. Mahley, R. W. (2016) Apolipoprotein E: from cardiovascular disease to neurodegenerative disorders. *J. Mol. Med. (Berl).* **94**, 739–46

464. Roman, C., Fuior, E. V., Trusca, V. G., Kardassis, D., Simionescu, M., and Gafencu, A. V. (2015) Thyroid hormones upregulate apolipoprotein E gene expression in astrocytes. *Biochem. Biophys. Res. Commun.* **468**, 190–5

465. Fan, J., Shimizu, Y., Chan, J., Wilkinson, A., Ito, A., Tontonoz, P., Dullaghan, E., Galea, L. A. M., Pfeifer, T., and Wellington, C. L. (2013) Hormonal modulators of glial ABCA1 and apoE levels. *J. Lipid Res.* **54**, 3139–50

466. Srivastava, R. A., Srivastava, N., Averna, M., Lin, R. C., Korach, K. S., Lubahn, D. B., and Schonfeld, G. (1997) Estrogen up-regulates apolipoprotein E (ApoE) gene expression by increasing ApoE mRNA in the translating pool via the estrogen receptor alpha-mediated pathway. *J. Biol. Chem.* **272**, 33360–6

467. Nathan, B. P., Barsukova, A. G., Shen, F., McAsey, M., and Struble, R. G. (2004) Estrogen facilitates neurite extension via apolipoprotein E in cultured adult mouse cortical neurons. *Endocrinology*. **145**, 3065–73

468. Marcsisin, S. R., and Engen, J. R. (2010) Hydrogen exchange mass spectrometry: what is it and what can it tell us? *Anal. Bioanal. Chem.* **397**, 967–72

469. Weisgraber, K. H., Rall, S. C., Innerarity, T. L., Mahley, R. W., Kuusi, T., and Ehnholm, C. (1984) A novel electrophoretic variant of human apolipoprotein E. Identification and characterization of apolipoprotein E1. *J. Clin. Invest.* **73**, 1024–33

470. Wlodawer, A., Minor, W., Dauter, Z., and Jaskolski, M. (2008) Protein crystallography for non-crystallographers, or how to get the best (but not more) from published macromolecular structures. *FEBS J.* **275**, 1–21

471. Baldwin, R. L., and Rose, G. D. (2013) Molten globules, entropy-driven conformational change and protein folding. *Curr. Opin. Struct. Biol.* **23**, 4–10